Heyd-Scuseria-Ernzerhof Screened-Exchange Hybrid Functional for Complex Materials: All-Electron Implementation and Application

Martin Schlipf

RWTHAACHEN
UNIVERSITY

JÜLICH
FORSCHUNGSZENTRUM

Heyd-Scuseria-Ernzerhof Screened-Exchange Hybrid Functional for Complex Materials: All-Electron Implementation and Application

Von der Fakultät für Mathematik, Informatik und Naturwissenschaften der RWTH Aachen University zur Erlangung des akademischen Grades eines Doktors der Naturwissenschaften genehmigte Dissertation

vorgelegt von

Dipl. Phys. Martin Schlipf

aus

Freiburg im Breisgau

Berichter   Jun.-Prof. Dr. Marjana Ležaić

Univ.-Prof. Dr. Carsten Honerkamp

Tag der mündlichen Prüfung: 13. September 2012

This document was typeset with LaTeX, figures were created with TikZ and VESTA.

Heyd-Scuseria-Ernzerhof Screened-Exchange Hybrid Functional for Complex Materials: All-Electron Implementation and Application

Martin Schlipf

Abstract

The design of suitable materials for application in future devices requires a detailed understanding of their electronic and structural properties. The *ab initio* method density functional theory (DFT) has emerged as the most commonly applied technique based on its high accuracy predicting characteristics of a wide range of materials. The limits of the predictive power of DFT are set by the availability of precise approximations to the exchange-correlation functional. In this thesis, we developed a scheme to realize screened nonlocal potentials within the full-potential linearized augmented-plane-wave (FLAPW) method and applied it, in particular, to the screened Heyd-Scuseria-Ernzerhof (HSE) functional. Incorporating a certain fraction of nonlocal exchange, hybrid functionals improve on the conventional local functionals by partly correcting for the spurious self interaction. This self interaction is most prominent in materials with localized states, so that we expect an improved description of transition-metal and rare-earth compounds. The strong localization of the d and f electrons in these materials complicates a description by pseudopotential methods, so that they are particularly suited for the all-electron FLAPW scheme. The nonlocal exchange is computationally very demanding, hence, we discuss two approximations to improve the computation time of hybrid functional calculations: a spacial restriction of the nonlocal exchange and the employment of a smaller k-point mesh in the calculation of the nonlocal exchange. We demonstrate that both schemes are feasible for selected materials, but not in general for all materials.

Employing our implementation of hybrid functionals, we analyze the electronic, structural, and magnetic properties of the rare-earth compounds GdN, EuO, EuS, EuSe, and EuTe and compare to results of DFT+U calculations from the literature. We find that GdN is close to a semi-metal/semiconductor phase transition, which may explain that both states are observed experimentally. In the EuX series, we reproduce the major trends in the series, i.e., the opening of the band gap as well as the transition from a ferromagnetic to an antiferromagnetic ground state. In a systematic study of several simple cubic perovskites, we assess the improvement of the HSE hybrid functional over the local PBE functional concerning the prediction of the lattice constant and the band transitions. Finally, we analyze the ground state of $PbCrO_3$, where the experimental semiconducting ground state could not be reproduced in previous DFT calculations. We determine the relaxed structure for all possible space groups, which are accessible by a combination of tilting and Jahn-Teller distortion of the oxygen octahedra as well as a polar displacement. Depending on the Hubbard U employed in the calculation, we obtain two different energetically optimal structures. Both structures exhibit a band gap and a polar displacement indicating that $PbCrO_3$ may be multiferroic.

Contents

List of Figures

List of Tables

Introduction

The development of better devices is increasingly driven by the selective engineering of material properties. This trend promotes the research of the dependence of characteristic features on subtle changes in the composition of compounds, in the defect concentration, and in the stacking in heterostructures. Of particular interest are complex oxide materials which allow for various attractive properties by small changes in the electronic or ionic structure. Technological demand for more efficient computer chips draws attention to magnetoelectric materials in which a ferromagnetic order is controlled not only by a magnetic but also by an electric field. Vice versa, a ferroelectric order is subject to changes in the external magnetic field. Hence, materials which combine both orders, the so-called *multiferroics*,[1] recently gained a lot of interest.[2]

Spaldin and Pickett[3] illustrate a general guideline how to design these functional materials. The selection of an appropriate method is important. We employ density functional theory (DFT)[4,5] which is the most widely applied method in theoretical material design due to its high predictive power. As DFT is in principle an exact solution of the many-body Schrödinger equation it contains no adjustable parameters and is commonly referred to as *ab initio* or *first principles* method. Conceptually, DFT reduces the complexity of a system with N electrons from the $3N$-dimensional wavefunction to the 3-dimensional density. The Hohenberg and Kohn[4] theorem proves that this mapping is exact. However in practice, the part of the total-energy originating from the exchange and the correlation of electrons is too complex to calculate for any material with more than a few electrons. Thus, Kohn and Sham[5] introduced a fictitious non-interacting system, in which all many-body effects are subsumed in the *exchange-correlation functional*.

In the material design process, if the results of theory and experiment are not consistent, the applied methods have to be refined.[3] Within DFT, this includes the development of more sophisticated exchange-correlation functionals which is allegorically referred to as *Jacob's ladder*.[6] The first idea was the development of the local density approximation (LDA)[7–12] which is a pure functional of the density. Later, the accuracy of DFT was improved by including the gradient of the density in the generalized gradient approximation (GGA) functionals.[13–17] However, despite their success for a wide range of materials, these local exchange-correlation func-

tionals include an unphysical interaction of an electron with itself, the so-called *self-interaction*, which yields a systematic underbinding of strongly localized states. This – in connection with the difficulties to systematically improve local functionals – leads to the emergence of orbital dependent exchange-correlation functionals. Kümmel and Kronik[18] point out four classes of orbital dependent functionals: the meta-GGAs,[19] the self-interaction correction,[11] the hybrid functionals,[20] and the exact exchange with orbital-dependent correlation.[21] Within this thesis, we employ local and hybrid functionals. The consideration of the adiabatic connection between the non-interacting Kohn-Sham system and the full-interacting real one, inspired Becke[20] to construct hybrid functionals in which an empirically optimized fraction of nonlocal Hartree-Fock (HF) exchange replaces a corresponding part of local exchange.[20,22,23] Later, Perdew *et al.*[24] proposed a parameter-free PBE0 hybrid functional in which the mixing parameter is inferred from expanding the adiabatic-connection formula and from comparing to Møller-Plesset perturbation theory[25] afterwards. The inclusion of the HF exchange partly corrects the spurious self-interaction resulting in an improved description of localized states. The calculation of the nonlocal exchange leads to a high computational cost of hybrid functionals. Several ideas to reduce the computation time were proposed. Heyd *et al.*[26] suggested to apply a range separation to the exchange functional and to limit the nonlocal HF exchange to the short-range (SR) contribution, since the screening by the electrons limits the distance of the exchange interaction in real material. This reduces the computational cost of hybrid functional calculations in real space[26] as well as in reciprocal space[27] codes. Tran *et al.*[28] suggested to restrict the hybrid functionals to on-site contributions only, which would raise the speed of these calculations close to conventional calculations. Taking advantage of the small dispersion of the exchange energy, Paier *et al.*[27] introduced a downsampling of the k-point mesh. We discuss the effect of similar approximations in Chap. 6.

In this thesis, we develop an implementation of the Heyd-Scuseria-Ernzerhof (HSE) hybrid functional within the full-potential linearized augmented-plane-wave (FLAPW) method.[29] In this all-electron method,[30–32] the crystal is separated into muffin-tin (MT) spheres centered at the atomic sites and the interstitial region (IR). The basis functions are a product of numerical radial functions and spherical harmonics in the MT spheres which are linearly matched to the plane waves employed in the IR. The evaluation of the PBE0 functional within the FLAPW method was pioneered by Betzinger *et al.*,[33] projecting the wavefunction products necessary for the HF exchange onto an auxiliary product basis. In Chap. 5, we extend this scheme to any nonlocal potential which is a pure function of the distance and apply it to the screened HSE functional. We achieve a combination of the FLAPW method specifically tailored to accurately describe atomic-like states and the screened hybrid

functionals suited in particular for localized electrons.

This facilitates the description of rare-earth compounds where the strong localization of the 4*f* states causes difficulties for pseudopotential methods and common exchange-correlation functionals. In particular, we focus on the isostructural and isovalent GdN, EuO, EuS, EuSe, and EuTe (Chap. 7). In GdN, a vivid discussion in the literature focuses on the nature of the transition between Γ- and X-point. Indications for an insulating[34–38] or a semi-metallic[38–42] ground state have been obtained. We predict a semi-metallic state at low temperatures which changes into an insulating state upon small changes in the lattice constant.[29] The europium chalcogenides EuX (X = O, S, Se, Te) recently regained high interest. In particular the high spin polarization of EuO, which grows lattice matched on several typical semiconductors,[43–46] offers the prospect of efficient spin filters.[47,48] The Curie temperature of 69 K[49] increases by defects[50,51] or doping.[51–56] In this thesis, we investigate the fundamental properties of the EuX series (Chap. 7) and find an overall excellent agreement with experimental observations of structural and magnetic properties.

In the material design of multiferroic materials, the most investigated structure is the perovskite one, ABO_3. An ideal perovskite is characterized by a cubic arrangement of A-site atoms. The B-site atom in the center of the cube is surrounded by an octahedron of oxygen atoms.[a] This arrangement allows to design materials, where the A site drives ferroelectricity and the B site is magnetic as in the famous $BiFeO_3$.[57] Furthermore, in a concept referred to as *strain-engineering*, the properties of material are tuned by growing the material on a substrate with a small misfit in the lattice constant.[58] A particular interesting example is the switching from an antiferromagnetic (AFM) to a ferromagnetic (FM) arrangement in strained $EuTiO_3$ upon changing the polarization.[59] These properties require an accurate description of the structural properties of the chosen materials. However, it is known[60] that apart from an underestimation (overestimation) of the lattice constant of ferroelectrics, the local functional LDA (GGA) also show strong deviations for other structural parameters, such as c/a ratio of the tetragonal unit cells of the ferroelectric deformation. In this thesis, we investigate the performance of the HSE hybrid functional for a set of cubic perovskite materials and outline the improvement over LDA and GGA results (Chap. 8), in particular for lattice constants and band transitions.

Finally, we investigate the properties of $PbCrO_3$ (PCO) in Chap. 9. At first glance, the material is similar to $BiFeO_3$ with the lone pair of Pb which might drive ferroelectricity on the A site and the magnetic Cr ion on the B site. However, experiments around 1970 indicate[61–63] that PCO has a semiconducting cubic ground state structure with an AFM arrangement of Cr ions. More recently, the material has been revis-

---

[a]We note that structures with other anions exist, but we limit ourselves to the oxygen compounds.

ited and several interesting phenomena have been observed: a random displacement of the Pb ions,[64] a mixed valency of the Cr ions,[65] a non-collinear spin reorientation leading to weak ferromagnetism,[66] and a phase transition under compressive pressure that goes along with large volume collapse.[67] So far, DFT calculations were not able to reproduce any of the experimental results. All calculations predict a metallic ground state, which typically has a much smaller volume than the experimental one.[68–70] Only Ganesh and Cohen[70] found a state with a volume comparable to experiment, however their result is metallic and has a strong tetragonal distortion. In Chap. 9 we present our investigation based on an analysis of all possible space groups accessible by tilting and Jahn–Teller (JT) distortion of the oxygen octahedron. As a result, we find the first theoretically obtained insulating ground state. Our results indicate, that PCO is microscopically unstable against tilting of the oxygen octahedron. Furthermore, we obtain a displacement of the Pb atoms giving rise to a ferroelectric polarization.

This thesis is organized as follows. We start with a general introduction to DFT, the conventional exchange-correlation functionals, and their limitations in the chap:dft. In Chap. 3, we present the FLAPW method. We motivate the intermixing of a fraction of HF exchange in the hybrid functionals and discuss their implementation within the FLAPW method in Chap. 4. In the chap:impl, we replace the pure Coulomb interaction by a screened one as used in the HSE functional. In Chap. 6, we analyze different approximations that would allow a faster evaluation of the hybrid functional. Then we switch to the application of DFT to complex materials. In Chap. 7, we apply hybrid functionals to GdN and to the europium chalcogenides. An investigation of the performance of the HSE functional for perovskites is presented in Chap. 8. The detailed analysis of the perovskite PCO is contained in Chap. 9. Finally, we conclude the thesis in the chap:concl.

Density Functional Theory

> The underlying physical laws necessary for the mathematical theory of a large part of physics and the whole of chemistry are thus completely known, and the difficulty is only that the exact application of these laws leads to equations much too complicated to be soluble. It therefore becomes desirable that approximate practical methods of applying quantum mechanics should be developed, which can lead to an explanation of the main features of complex atomic systems without too much computation.
>
> Paul Dirac[71]

2.1   Significance of DFT

Since Dirac's well-known quote more than 80 years have passed and his statement is still as true as at his time. Nevertheless with the advent of computer assisted calculations, several numerical techniques for solving the many-particle Schrödinger equation became feasible. Density functional theory (DFT) is one of the most efficient methods to solve the Schrödinger equation, as it maps the complicated interacting many-body problem *exactly* to an equivalent non-interacting single-particle one.[72]

The impact of DFT for the theoretical investigation of complex molecules and solids manifested itself in the Nobel prize for Walter Kohn in 1998. In his Nobel lecture,[73] he highlighted two of the important contributions DFT made to the field of many-body quantum physics. On the one hand DFT simplified the understanding of these systems by reducing the complexity from the multiple-particle wavefunction

with $3N$ independent coordinates, where N is the number of electrons, to the density $n(\boldsymbol{r})$ which can be much easier visualized, analyzed, and hence comprehended. This reduction in complexity on the other hand made numerical calculations possible. Numerical DFT calculations grew significantly in popularity in the 1990s[72] once the balance between accuracy and computational cost was demonstrated. Nowadays, DFT is successfully used to investigate materials properties from first principles.

This chapter is structured as follows. In Sec. 2.2, we introduce the Hohenberg-Kohn theorem and the Kohn-Sham equations. In Sec. 2.3, we illustrate how the interacting many-body problem is mapped onto the non-interacting single-particle system. In the sec:exc, we introduce the most commonly used local exchange-correlation functionals. References 72–75 were used in the preparation of this chapter.

2.2 The theoretical foundations of DFT

As pointed out by Dirac,[71] the physics of condensed matter and molecules is entirely described by the Schrödinger equation of the system. Throughout this work, we use the Born-Oppenheimer approximation[76] to separate the slow motion of the heavy nuclei and the much faster electronic motion into separate Hamiltonians and limit ourselves to the electronic Hamiltonian

$$\mathcal{H} = T + V_{\text{ext.}} + V_{\text{ee}} \tag{2.1}$$

with the the kinetic energy

$$T = \sum_i \frac{p_i^2}{2} = -\sum_i \frac{\triangle_i}{2}, \tag{2.2}$$

the external potential

$$V_{\text{ext}} = \sum_i \sum_a \frac{Z_a}{\left| \boldsymbol{r}_i - \boldsymbol{R}_a \right|}, \tag{2.3}$$

and the electron-electron interaction

$$V_{\text{ee}} = -\frac{1}{2} \sum_{i \neq j} \frac{1}{\left| \boldsymbol{r}_i - \boldsymbol{r}_j \right|}. \tag{2.4}$$

The small letter $\boldsymbol{r}_i$ indicates the position of an electron, the capital letter $\boldsymbol{R}_a$ the position of an atom, and Z_a is its atomic number. Here and in the following atomic units are used (see Sec. A).[77,78]

The central concept of DFT theory is the mapping of this N electron system onto an equivalent single-particle system. The auxiliary single-electron system is constructed to reproduce the density $n(\boldsymbol{r})$ of the many-particle system, since the system

is entirely described by its electronic density. The cusps in the density indicate the position of the nuclei which determine the external potential and hence the Hamiltonian (Eq. (2.1)). Hohenberg and Kohn[4] confirmed this qualitative understanding for non-degenerate eigenstates via proof by contradiction. Assuming two different external potentials $V_{\text{ext.}}^{(1)}(\boldsymbol{r})$ and $V_{\text{ext.}}^{(2)}(\boldsymbol{r})$ with different ground-state wave functions $\Phi_1(\boldsymbol{r})$ and $\Phi_2(\boldsymbol{r})$ could yield the same ground-state density, we find that

$$\left\langle \Phi_1 \left| T + V_{\text{ext.}}^{(1)} + V_{\text{ee}} \right| \Phi_1 \right\rangle \leq \left\langle \Phi_2 \left| T + V_{\text{ext.}}^{(1)} + V_{\text{ee}} \right| \Phi_2 \right\rangle \quad \text{and} \tag{2.5}$$

$$\left\langle \Phi_1 \left| T + V_{\text{ext.}}^{(2)} + V_{\text{ee}} \right| \Phi_1 \right\rangle \geq \left\langle \Phi_2 \left| T + V_{\text{ext.}}^{(2)} + V_{\text{ee}} \right| \Phi_2 \right\rangle. \tag{2.6}$$

The contribution of the external potential depends only on the density, hence we get

$$\left\langle \Phi_1 \left| T + V_{\text{ee}} \right| \Phi_1 \right\rangle \leq \left\langle \Phi_2 \left| T + V_{\text{ee}} \right| \Phi_2 \right\rangle, \quad \left\langle \Phi_1 \left| T + V_{\text{ee}} \right| \Phi_1 \right\rangle \geq \left\langle \Phi_2 \left| T + V_{\text{ee}} \right| \Phi_2 \right\rangle. \tag{2.7}$$

These inequalities can only be fullfilled if the total energy is identical and hence the wave functions are identical or degenerate. From the wave function the external potential is defined by the inversion of the Schrödinger equation up to a constant

$$V_{\text{ext.}} = \sum_i \frac{\triangle_i \Phi(\boldsymbol{r})}{2\Phi(\boldsymbol{r})} - V_{\text{ee}}. \tag{2.8}$$

Levy[79] established a constrained search formalism which extends the Hohenberg-Kohn theorem for degenerate ground states.[72] The search is constrained to all wave functions which are antisymmetric and yield a density $n(r)$. The ground state energy is

$$E = \min_n \left(F[n] + \int \mathrm{d}^3 r \, V_{\text{ext.}}(\boldsymbol{r}) n(\boldsymbol{r}) \right). \tag{2.9}$$

As the energy contribution of the external potential depends only on the density (and not directly on the wave function), any wave function Φ which minimizes the universal functional $F[n]$

$$F[n] = \min_{\langle \Phi | \Phi \rangle = n} \left\langle \Phi \left| T + V_{\text{ee}} \right| \Phi \right\rangle \tag{2.10}$$

is a ground-state solution.

Kohn and Sham[5] applied the Hohenberg-Kohn theorem to a fictitious one-electron system with same density and the Hamiltonian

$$\mathcal{H}^{\text{KS}} = T_{\text{s}} + V_{\text{s}}^{\text{eff.}}(\boldsymbol{r}), \tag{2.11}$$

where the interaction with the other electrons and the external potential are condensed in an effective single-particle potential $V_{\text{s}}^{\text{eff.}}(\boldsymbol{r})$. The theoretical foundation
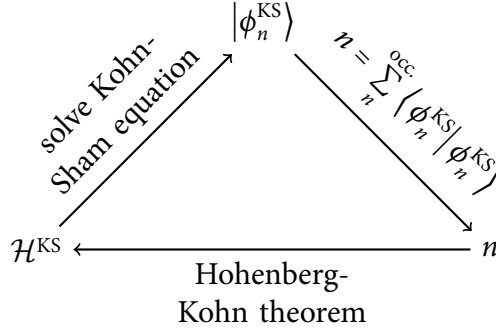
Figure 2.1: All information necessary to describe a physical system is contained equally in the Hamiltonian $\mathcal{H}$, the wave functions ϕ_n^{KS}, and the electronic density n.

of this mapping is presented in Sec. 2.3. The Kohn-Sham wave functions $\phi_n^{\text{KS}}(\boldsymbol{r})$ are the eigenfunctions of this Hamiltonian with the eigenvalue $\varepsilon_n^{\text{KS}}$

$$\mathcal{H}^{\text{KS}} \left| \phi_n^{\text{KS}} \right\rangle = \varepsilon_n^{\text{KS}} \left| \phi_n^{\text{KS}} \right\rangle . \tag{2.12}$$

Analogous to Eq. (2.10), the Kohn-Sham wave functions minimize the single particle kinetic energy under the constraint that they add up to the density[72]

$$T_{\text{s}}[n] = \min_{\langle \Phi_{\text{KS}} | \Phi_{\text{KS}} \rangle = n} \langle \Phi_{\text{KS}} | T | \Phi_{\text{KS}} \rangle , \tag{2.13}$$

with the Kohn-Sham wave function[a]

$$\left| \Phi_{\text{KS}} \right\rangle = \prod_n^{\text{occ.}} \left| \phi_n^{\text{KS}} \right\rangle . \tag{2.14}$$

This construction indicates, that in general the Kohn-Sham wave function and eigenvalue of the fictitious single-particle system do not represent the physical wave function and eigenvalue of the many-body system. Nevertheless, one commonly approximates the real values by their Kohn-Sham counterpart. For example the band gap of the real system can be approximated by the difference of Kohn-Sham eigenvalues.

Figure 2.1 illustrates how the Hohenberg-Kohn theorem and the Kohn-Sham equation can be used for practical DFT. The solution of the Kohn-Sham equation yields the wave functions and straightforward the density. As the density uniquely defines the Hamiltonian, we can iterate this loop until self consistency is achieved.

---

[a]In principle the Kohn-Sham wave function is the Slater determinant of the wave functions $\left| \phi_n^{\text{KS}} \right\rangle$. However, as we consider a non-interacting system, the simple product state yields equivalent results.

The total energy in DFT is minimized by the ground-state density. As shown above, the ground state wave function is a pure functional of the density

$$\left|\phi_n\right\rangle = \left|\phi_n[n]\right\rangle, \tag{2.15}$$

hence it is equivalent to formulate the energy either in terms of the density or in terms of the wave functions. In the following all contributions to the total energy are presented:

Kinetic energy The kinetic energy follows directly from the definition of the Kohn-Sham wave function in Eq. (2.13)

$$T_s[n] = \sum_n^{\text{occ.}} \left\langle \phi_n[n] \left| T \right| \phi_n[n] \right\rangle. \tag{2.16}$$

As the Kohn-Sham wave function is constructed to minimize this kinetic energy, the single particle kinetic energy is less than or equal to the real kinetic energy in Eq. (2.10). The functional dependence of the kinetic energy on the density n is non trivial and is evaluated by diagonalizing the Hamiltonian (see Sec. 3.1).

External potential The energy of a charge density in an external potential is straight-forward

$$E_{\text{ext}} = \int \mathrm{d}^3 r \, n(\boldsymbol{r}) V_{\text{ext.}}(\boldsymbol{r}). \tag{2.17}$$

If the exact ground-state density is known, this energy is identical for the real and the Kohn-Sham system by construction of the fictitious system.

Hartree energy The energy associated to the effective potential $V_{\text{ee}}^{\text{eff.}}$ is formally separated in several terms. The most prominent one, the classical Hartree energy U_{H} is evaluated directly from the density

$$U_{\text{H}}[n] = \frac{1}{2} \iint \mathrm{d}^3 r \, \mathrm{d}^3 r' \, \frac{n(\boldsymbol{r})n(\boldsymbol{r}')}{|\boldsymbol{r} - \boldsymbol{r}'|} \tag{2.18}$$

and corresponds to the Coulomb interaction of a charge density $n(\boldsymbol{r})$ with itself.

Exchange energy The exchange energy is formally defined as the difference of the real electron-electron interaction and the Hartree energy

$$E_{\text{x}}[n] = \left\langle \Phi[n] \left| V_{\text{ee}} \right| \Phi[n] \right\rangle - U_{\text{H}}[n]. \tag{2.19}$$

However, in practical calculations this term is typically approximated, as the direct evaluation is cumbersome.

Correlation energy The correlation energy $E_c[n]$ in DFT is defined as the difference of the energy of the real system and the previously mentioned energies. Naturally, in any real system this is extremely expensive if not impossible to evaluate. As for the exchange energy, approximations to this term are necessary.

In summary, we find the total energy of the Kohn-Sham system

$$E_{\text{tot}}[n] = T_s[n] + E_{\text{ext.}}[n] + U_H[n] + E_x[n] + E_c[n], \tag{2.20}$$

where the latter two terms are often subsumed in the so called *exchange-correlation* energy $E_{xc}[n]$. We will discuss the most common approaches to this functional in Sec. 2.4. The total energy in Eq. (2.20) is minimized under a constrained total number of electrons N

$$\int d^3r\, n(\boldsymbol{r}) = N. \tag{2.21}$$

Hence, we add this contraint with a Lagrange multiplier μ and solve the Euler-Lagrange equation

$$\frac{\delta}{\delta n}\left[E_{\text{tot}}[n(\boldsymbol{r})] - \mu\left(\int d^3r\, n(\boldsymbol{r}) - N\right)\right] = 0 \tag{2.22}$$

$$\frac{\delta T_s[n(\boldsymbol{r})]}{\delta n(\boldsymbol{r})} + V_{\text{ext.}}(\boldsymbol{r}) + \int d^3r'\, \frac{n(\boldsymbol{r}')}{|\boldsymbol{r} - \boldsymbol{r}'|} + V_{xc}(\boldsymbol{r}) = \mu, \tag{2.23}$$

with

$$V_{xc}(\boldsymbol{r}) = \frac{\delta E_{xc}[n(\boldsymbol{r})]}{\delta n(\boldsymbol{r})}. \tag{2.24}$$

Equation (2.23) defines the effective single-particle potential

$$V_s^{\text{eff.}}(\boldsymbol{r}) = V_{\text{ext.}}(\boldsymbol{r}) + \int d^3r'\, \frac{n(\boldsymbol{r}')}{|\boldsymbol{r} - \boldsymbol{r}'|} + V_{xc}(\boldsymbol{r}) \tag{2.25}$$

in the Kohn-Sham Hamiltonian Eq. (2.11). We identify μ as the chemical potential or Fermi energy E_F of the system.

2.3 Adiabatic connection formula

Harris and Jones[80] introduced the concept of the adiabatic connection to DFT, which provided important insight in the fundamental properties of the exchange-correlation functional.[20,80–82] Assume a λ-dependent Hamiltonian

$$\mathcal{H}_\lambda = T + \lambda V, \qquad 0 < \lambda < \infty, \tag{2.26}$$
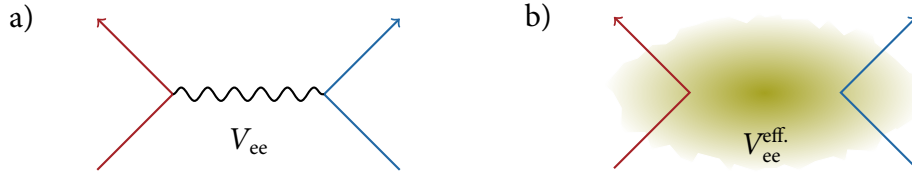
Figure 2.2: Example for the idea of the adiabatic connection in a interacting electron gas without external potential. a) The real system with the full electron-electron interaction V_{ee}. b) The fictitious system where the electron-electron interaction is replaced by an effective potential $V_{ee}^{eff.}$ that reproduces the same physics.

where λ determines the strength of the potential, then all eigenvalues and eigenfunctions depend on λ.[72] The wave functions depend only in second order on λ, as they are variational extrema. Hence, the energy derivative with respect to the coupling constant is

$$\frac{\mathrm{d}E_\lambda}{\mathrm{d}\lambda} = \langle \phi_\lambda | V | \phi_\lambda \rangle. \tag{2.27}$$

Integrating this yields the Hellmann-Feynman theorem[83–85]

$$E = E_{\lambda=1} = E_{\lambda=0} + \int_0^1 \mathrm{d}\lambda \, \langle \phi_\lambda | V | \phi_\lambda \rangle. \tag{2.28}$$

This idea is introduced in DFT by rewriting the universal functional as

$$F_\lambda[n] = \min_{\langle \Phi_\lambda | \Phi_\lambda \rangle = n} \langle \Phi_\lambda | T + \lambda V_{ee} | \Phi_\lambda \rangle, \tag{2.29}$$

so that we recover the physical system (Eq. (2.10)) for $\lambda = 1$ and the equation converts to the kinetic energy of the Kohn-Sham system (Eq. (2.13)) for $\lambda = 0$.[72] In this mapping the density $n(\mathbf{r})$ is independent of λ, so that the physical electron-electron interaction $V_{ee}(\mathbf{r}, \mathbf{r}')$ is replaced by an effective electron-electron interaction $V_{ee}^{eff.}(\mathbf{r})$ as illustrated by Fig. 2.2. The latter potential is a single particle potential, as required in the Kohn-Sham formalism.

Employing the Hellmann-Feynman theorem (Eq. (2.28)), we find that the universal functional is given as

$$\begin{aligned} F[n] &= \langle \Phi_{\lambda=0} | T | \Phi_{\lambda=0} \rangle + \int_0^1 \mathrm{d}\lambda \, \langle \Phi_\lambda | V_{ee} | \Phi_\lambda \rangle \\ &= T_s[n] + \int_0^1 \mathrm{d}\lambda \, \langle \Phi_\lambda | V_{ee} | \Phi_\lambda \rangle. \end{aligned} \tag{2.30}$$

Comparing the total energy of the physical system Eq. (2.9) and the Kohn-Sham system Eq. (2.20), we work out the following expression for the exchange-correlation energy

$$E_{xc}[n] = \int_0^1 d\lambda \, \langle \Phi_\lambda \, |V_{ee}| \, \Phi_\lambda \rangle - U_H[n]. \qquad (2.31)$$

Obviously, the Hartree energy depends linearly on the strength of the electron-electron interaction $U_{H,\lambda}[n] = \lambda U_H[n]$, so that it is straightforward to rewrite this equation as

$$E_{xc}[n] = \int_0^1 d\lambda \left(\langle \Phi_\lambda \, |V_{ee}| \, \Phi_\lambda \rangle - U_{H,\lambda}[n]/\lambda \right) =: \int_0^1 d\lambda \, E_{xc,\lambda}[n]. \qquad (2.32)$$

This is the so called *adiabatic connection formula*.[72] The exchange-correlation energy is expressed in terms of the Coulomb potential only. In practice this formula is not evaluated, but it is important for functional development. We will come back to this formula later in Chap. 4, when we introduce hybrid exchange-correlation functionals.

2.4   Local exchange-correlation functionals

In numerical DFT calculations the exchange-correlation energy is an approximated functional of the density, as an exact evaluation is not feasible. In this section, we introduce the most commonly used conventional exchange-correlation functionals. The simplest possible solution, the so-called local density approximation (LDA) is derived from the homogeneous electron gas, where the eigenstates are plane waves. Hence, the exchange energy is[74,75]

$$E_x = - \int_{|\boldsymbol{k}|<k_F} \frac{d^3k}{(2\pi)^3} \int_{|\boldsymbol{k}'|<k_F} \frac{d^3k'}{(2\pi)^3} \int d^3r \int d^3r' \frac{e^{-i\boldsymbol{k}\boldsymbol{r}} e^{-i\boldsymbol{k}'\boldsymbol{r}'} e^{i\boldsymbol{k}\boldsymbol{r}'} e^{i\boldsymbol{k}'\boldsymbol{r}}}{|\boldsymbol{r}-\boldsymbol{r}'|}, \qquad (2.33)$$

where $k_F = (3\pi^2 n_{\text{unif.}})^{1/3}$ is the Fermi wave vector corresponding to the uniform density $n_{\text{unif.}}$. Employing the symmetry of $\boldsymbol{k}$ and $\boldsymbol{k}'$ and substituting $\boldsymbol{u} = \boldsymbol{r} - \boldsymbol{r}'$, we obtain

$$E_x = - \int d^3r \int d^3u \frac{1}{u} \left(\int_{|\boldsymbol{k}|<k_F} \frac{d^3k}{(2\pi)^3} e^{i\boldsymbol{k}\boldsymbol{u}} \right)^2 =: \frac{1}{2} \int d^3r \, n_{\text{unif.}} \int d^3u \frac{n_x(\boldsymbol{u})}{u}, \qquad (2.34)$$

which defines the *exchange hole density*[74]

$$n_x(\boldsymbol{u}) = - \frac{2}{n_{\text{unif.}}} \left(\int_{|\boldsymbol{k}|<k_F} \frac{d^3k}{(2\pi)^3} e^{i\boldsymbol{k}\boldsymbol{u}} \right)^2 = - \frac{2}{n_{\text{unif.}}} \left[\frac{k_F^3}{2\pi^2} \frac{j_1(k_F u)}{k_F u} \right]^2, \qquad (2.35)$$
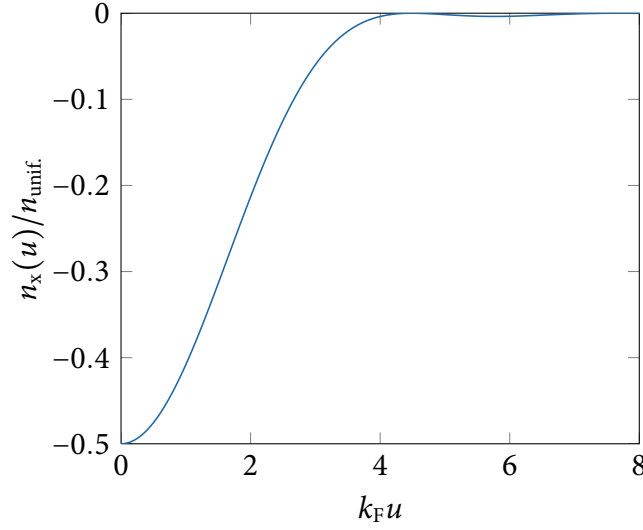
Figure 2.3: We show the LDA exchange hole n_x normalized to the uniform density $n_{unif.}$ as function of the dimensionless product of Fermi wave vector k_F and distance of two points u.

where $j_1(x)$ is a spherical Bessel function. As straightforward consequence of the Pauli exclusion principle, the exchange hole density repels exactly half of the density for small values of $k_F u$ (see Fig. 2.3). For large values of $k_F u$ the exchange density has hardly any impact on the energy. Solving the integral in Eq. (2.34) with the exchange hole density of Eq. (2.35), one finds[72,74]

$$E_x[n_{unif.}] = -\int d^3r \frac{3k_F}{4\pi} n_{unif.} = -\frac{3}{4}\left(\frac{3}{\pi}\right)^{\frac{1}{3}} \int d^3r\, n_{unif.}^{\frac{4}{3}} =: A_x \int d^3r\, n_{unif.}^{\frac{4}{3}}. \quad (2.36)$$

In the LDA, we apply these equations to non uniform densities $n(\mathbf{r})$

$$E_x = \frac{1}{2} \iint d^3r\, d^3u\, \frac{n(\mathbf{r}) n_x^{LDA}(\mathbf{r}, \mathbf{u})}{\mathbf{u}} = A_x \int d^3r\, n^{\frac{4}{3}}(\mathbf{r}). \quad (2.37)$$

This equation is formally similar to the Hartree energy Eq. (2.18). Thus, a natural interpretation of the exchange energy corresponding to the charge density is its Coulomb interaction with the surrounding exchange hole.[72]

The derivation of the correlation energy is more sophisticated than the exchange energy. Furthermore several LDA correlation functionals exist[75], which are based on the random phase approximation (RPA),[7,8] Quantum Monte Carlo (QMC) calculations,[9] or a parametrization of these QMC results.[10–12] Hence, we restrict ourselves to the description of the exchange and refer the interested reader to the literature.[72,74,75]

Next we turn to the generalized gradient approximation (GGA)[86] in which the reduced density gradient

$$s = |\nabla n| \, 2k_\mathrm{F} n \tag{2.38}$$

is taken into account. For solids typical values for s are between 0 and 1.[74] Consideration of the behavior of the exchange energy E_x under density scaling reveals, that the leading correction is quadratic in s

$$E_\mathrm{x}[n] = A_\mathrm{x} \int \mathrm{d}^3 r \, n^{\frac{4}{3}} \left(1 + \mu s^2 + \ldots \right) =: A_\mathrm{x} \int \mathrm{d}^3 r \, n^{\frac{4}{3}} F_\mathrm{x}(n, s), \tag{2.39}$$

where we introduced the *enhancement factor* F_x which has a different shape for different exchange functionals. Antoniewicz and Kleinman[87] demonstrated that the value of μ should be 10/81 for the limit of small s. In this work, we limit ourselves to the PBE GGA exchange functional,[14] which employs a roughly 1.8 times larger value of μ to reproduce the properties of the PW91 GGA exchange functional.[15] In contrast to more empirically motivated functionals, such as the BLYP functional,[16,17] the emphasis in the construction of the PBE exchange functional was the recovery of the uniform electron gas limit for small values of s which is satisfied by the LDA. Lieb and Oxford[88] established an upper limit for the local exchange-correlation energy. This limit was incorporated in the construction of the enhancement factor of the PBE exchange functional

$$F_\mathrm{x}(n, s) = 1 + \kappa - \frac{\kappa}{1 + \mu s^2}, \tag{2.40}$$

where $\kappa = 0.804$ satisfies the Lieb-Oxford bound and recovers the functional behavior of the PW91 functional.[15] A comparison of Eq. (2.37) and Eq. (2.39) reveals a useful expression for the enhancement factor F_x in terms of the exchange hole

$$F_\mathrm{x}(n, s) = \frac{1}{A_\mathrm{x} n^{\frac{1}{3}}} \int \mathrm{d}^3 u \, \frac{n_\mathrm{x}(\boldsymbol{r}, \boldsymbol{u})}{\boldsymbol{u}}. \tag{2.41}$$

We introduce dimensionless variables $y = k_\mathrm{F} u$ and $J_\mathrm{x} = n_\mathrm{x}/n$. Furthermore, we employ a spherical and a system average to obtain

$$F_\mathrm{x}(n, s) = -\frac{8}{9} \int_0^\infty \mathrm{d}y \, y J_\mathrm{x}(n, s). \tag{2.42}$$

Ernzerhof and Perdew[89] derived a numerical expression for the dimensionless exchange hole J_x for the PBE functional, which is the starting point for the local contribution of screened hybrid functionals (see Chap. 5).

2.5   Self-interaction error

Albeit local exchange-correlation functionals are extremely successful describing a variety of materials with high accuracy, they fail for some materials.[90] For heavy elements the GGA functionals tend to underperform the LDA functionals. While LDA yields accurate cohesive energies and lattice constants, GGA overestimate the lattice constant and underestimate the cohesive energy. A further problem is the qualitatively wrong description of the asymptotic behavior of the potential for large distances.[90] The local functionals exhibit an exponential decay, whereas the exact solution should decay as $1/r$. The third problem of local exchange correlation functionals is the neglect of van der Waals forces,[90] hence systems where the dispersion forces are responsible for the bonding are not described by local DFT. Moreover, local exchange-correlation functionals have difficulties describing systems with strongly localized electrons, e.g., the transition metal oxides.[90]

In this thesis, we focus in particular on the latter problem, which is attributed to the self-interaction error (SIE). The SIE is most obvious in a one-electron system, e.g. the H_2^+ molecule. It is straightforward, that there should be the correlation energy should vanish and the exchange energy should cancel the Hartree energy

$$E_c = 0, \qquad\qquad E_x = -U_H. \qquad\qquad (2.43)$$

However, the LDA and GGA functionals do not fulfill these relations for the one-electron system. For the simple case of one electron the SIE would be easy to correct, however this qualitative error persists in many-electron systems where no unique way to remove the SIE exists.[91] Perdew and Zunger[11] proposed an explicit removal of the one-electron SIE, which is referred to as *self-interaction correction*. However, in solids, removing the SIE self consistently is computationally very demanding. Filippetti and Spaldin[92] developed a faster implementation based on the approximation of the potential by a nonlocal, pseudopotentiallike projector.

Within the Hartree-Fock (HF) method,[93] the exact treatment of the exchange potential cancels the Hartree energy and correlation effects are neglected, so that both conditions of Eq. (2.43) are fulfilled. However, for systems with more than one electron correlations screen the bare Coulomb interaction, so that the HF method strongly overestimates its value.[94] The *GW* approximation[95] includes screening of the Coulomb potential resulting in accurate band energies. The disadvantages of the *GW* scheme are the high computational cost and the difficulties in achieving a self-consistent solution.[95] Due to these problems one commonly applies a non-self-consistent one-shot G_0W_0, which is thence starting point dependent. Within DFT we can go beyond the HF method including only a fraction of the nonlocal exchange in the exchange-correlation functionals, which will be extensively introduced

in Chap. 4 and Chap. 5. Recently, realizations of exact exchange and a treatment of the correlations within the RPA have been successfully applied to solids.[96] A different approach is the DFT+U method,[94] where an on-site Hubbard-like[97] term is incorporated to describe the exchange and correlation effects. This approach shares advantages and disadvantages of model Hamiltonian calculations. On the one hand, the impact on physical properties of a certain contribution is easily assessable, on the other hand, the appropriate size of the parameter – in this case value of the Hubbard U – is hard to determine. Although several techniques to determine the value of U consistently from first principles have been suggested,[98–100] in practice, U is often chosen to reproduce certain experimental observations, e.g., the band gap or the lattice constant.

The FLAPW Basis

3.1   Practical DFT – introduction of a basis

In the chap:dft, we have introduced the different contributions to the total energy in density functional theory (DFT). For the evaluation of the kinetic energy (cf. Eq. (2.13))

$$T_{\mathrm{s}}[n] = \sum_{n}^{\mathrm{occ.}} \left\langle \phi_n^{\mathrm{KS}}[n] \left| T \right| \phi_n^{\mathrm{KS}}[n] \right\rangle . \tag{3.1}$$

the Kohn-Sham wave functions $\phi_n^{\mathrm{KS}}[n]$ have to be known. However, the functional dependence of the Kohn-Sham wave function on the density is non trivial and only implicitly defined by the Kohn-Sham equation (2.12). We simplify this differential equation by introducing a basis $\chi_i(\boldsymbol{r})$

$$\sum_{j} \left\langle \chi_i \left| \mathcal{H}^{\mathrm{KS}} \right| \chi_j \right\rangle \left\langle \chi_j \left| \phi_n^{\mathrm{KS}} \right\rangle = \varepsilon_n^{\mathrm{KS}} \left\langle \chi_i \left| \phi_n^{\mathrm{KS}} \right\rangle . \tag{3.2}$$

With this ansatz, the problem is reduced to a matrix diagonalization for which fast numerical techniques have been developed. Nevertheless, in typical DFT realizations, the diagonalization of the Kohn-Sham Hamiltonian and hence, the evaluation of the kinetic energy, is the most time-consuming part of the calculation. In practice, we do not employ Eq. (3.1) to determine the kinetic energy, because the kinetic-energy operator is associated to a derivation of the wave functions. As for the numerical stable evaluation of derivatives larger values for the cutoff parameters

are necessary, it is more efficient to express the kinetic energy as

$$T_s[n] = \sum_n^{\text{occ.}} \left\langle \phi_n^{\text{KS}}[n] \left| \mathcal{H}^{\text{KS}} - V_s^{\text{eff.}} \right| \phi_n^{\text{KS}}[n] \right\rangle \tag{3.3}$$

$$= \sum_n^{\text{occ.}} \varepsilon_n^{\text{KS}} - \int \mathrm{d}^3 r \, n(\boldsymbol{r}) V_s^{\text{eff.}}(\boldsymbol{r}). \tag{3.4}$$

Extensive effort was spent in developing sophisticated implementations, which make practical DFT calculations feasible. Nowadays, in condensed matter physics the two most common techniques are pseudopotential methods[101,102] and all-electron methods.[103] For the sake of completeness, we mention that different approaches to solve the Kohn-Sham equation beside the introduction of a basis exist. In particular, in the KKR method[104,105] the Green's function of the crystal is calculated from Green's functions of isolated atoms via a Dyson equation. The details are discussed elsewhere.[106]

In the pseudopotential method only the valence electrons are treated with DFT. The effect of the core electrons and the nucleus is condensed in a pseudopotential, which is constructed using all-electron schemes.[107–110] Employing pseudopotentials permits the use of a plane-wave basis set with a moderate cutoff as the divergence of the potential near the nucleus disappears. In principle, the pseudopotential should be constructed for each investigated material separately. In practice, it turns out that the pseudopotential for a specific atom can be used for a wide range of materials. However, the pseudopotential method with a plane-wave basis set is not so well suited for materials with localized d- or especially f-electrons close to the Fermi energy.[111] For these materials atomic basis functions and the projector augmented wave (PAW) method[111] are more reliable.

In the all-electron methods one solves an atomic Schrödinger or Dirac equation to construct the radial part of the basis functions. The angular part is given by the spherical harmonics $Y_{lm}(\hat{\boldsymbol{r}})$. These basis functions are defined within spheres around the atoms, which are referred to as muffin-tin (MT) spheres.[103] The methods differ in the choice of overlapping[112] or non overlapping MT spheres. In the latter case, the basis functions within the MT spheres are augmented in the interstitial region (IR) in between.[103,113] Furthermore the basis set is either fixed for specific atoms, constructed once for the specific material or updated to the current potential after each self consistency iteration. In this work, we employ mostly the full-potential linearized augmented-plane-wave (FLAPW) method, which is described in detail below. A more extensive discussion is found in Ref. 114,115.

This chapter is organized as follows: In Sec. 3.2, we describe the construction of atomic basis functions common to most all-electron schemes. We focus in particular

on the augmentation with plane waves in the interstitial region (Sec. 3.3). A common extension of the basis to improve the description of semicore states are the so called *local orbitals*, which are introduced in Sec. 3.4.

3.2 Atomic basis functions

The divergence of the Coulomb potential at the nucleus constitutes a severe convergence problem for basis functions not specifically tailored to this potential. Hence, the basis in all-electron methods is ususaly constructed from solution of the atomic Schrödinger equation

$$\left[-\frac{p^2}{2} + V_a^{\text{eff.}}(\boldsymbol{r}) \right] \Psi_a(\boldsymbol{r}) = E\Psi_a(\boldsymbol{r}) \tag{3.5}$$

or atomic Dirac equation

$$\left[c\boldsymbol{\alpha} \cdot \boldsymbol{p} + (\beta - 1)c^2 + V_a^{\text{eff.}}(\boldsymbol{r}) \right] \Psi_a(\boldsymbol{r}) = E\Psi_a(\boldsymbol{r}). \tag{3.6}$$

In these equations $\boldsymbol{p}$ is the momentum operator, $V_a^{\text{eff.}}(\boldsymbol{r})$ the local effective potential at the atom a, E the energy eigenvalue, c the speed of light, α and β the Dirac matrices, and $\Psi_a(\boldsymbol{r})$ the wave function. In general, the wave function is a four component vector, but in the nonrelativistic case two components vanish and the spin-up and spin-down component are independent. For the remainder of this chapter, we will restrict the discussion to a scalar $\Psi_a(\boldsymbol{r})$ in the atomic Schrödinger equation. A more extensive discussion of the relativistic part can be found elsewhere.[114]

We make the ansatz $\Psi_a(\boldsymbol{r}) = R_{alm}(r)\, Y_{lm}(\widehat{\boldsymbol{r}})$. Inserting this in Eq. (3.5) yields

$$\left[-\frac{1}{2r^2}\frac{\mathrm{d}}{\mathrm{d}r}\left(r^2\frac{\mathrm{d}}{\mathrm{d}r} \right) + \frac{l(l+1)}{2r^2} + \sum_{l'm'} V_{al'm'}^{\text{eff.}}(r)\, Y_{l'm'}(\widehat{\boldsymbol{r}}) \right] R_{alm}\, Y_{lm}(\widehat{\boldsymbol{r}})$$
$$= E_{lm}R_{alm}\, Y_{lm}(\widehat{\boldsymbol{r}}), \quad (3.7)$$

where we inserted the spherical harmonic expansion of the effective potential. Near the atom, the potential is almost spherical, so that we can neglect all contributions $V_{a,l>0,m}^{\text{eff.}}$, so that the m dependence of the radial part disappears. If we define $u_{al}(r) = rR_{al}(r)$, Eq. (3.7) simplifies to

$$\left[-\frac{1}{2}\frac{\mathrm{d}^2}{\mathrm{d}r^2} + \frac{l(l+1)}{2r^2} + V_{a,00}^{\text{eff.}}(r) \right] u_{al}(r) = E_l u_{al}(r). \tag{3.8}$$

For a description of the entire crystal two possible techniques are common. Either one employs the atomic basis functions within overlapping spheres, so that the

atomic solutions describe the full wave functions, or the basis functions are combinations of atomic functions in the MT spheres and different functions in the IR. As the potential in the IR region is very smooth, plane waves will provide a precise description. In the next section, we illustrate how one combines these functions.

3.3   Augmented plane waves

Slater[103] introduced the simplest combination of a plane wave and atomic functions centered at the nuclei

$$\chi_{k+G}(r) = \begin{cases} \dfrac{1}{\sqrt{\Omega}}\, e^{i(k+G)\cdot r} & r \in \text{IR} \quad \text{and} \\ \sum\limits_{lm} a_{alm}^{k+G} u_{al}(r_a)\, Y_{lm}(\widehat{r}_a) & r \in \text{MT}(a), \end{cases} \tag{3.9}$$

where Ω is the volume of the unit cell, $r_a = r - R_a$, and R_a is the position of atom a. As a single plane wave is connected to multiple atomic functions, this basis is referred to as the *augmented-plane-wave* (APW) basis. The expansion coefficients a_{alm}^{k+G} ensure that the basis function is continuous at the boundary of the MT sphere. We determine these coefficients by expansion of the plane wave in terms of spherical harmonics

$$e^{ik\cdot r} = \sum_{lm} 4\pi i^l j_l(kr)\, Y_{lm}(\widehat{r}) Y_{lm}^*(\widehat{k}) \tag{3.10}$$

and comparison of coefficients of the same spherical harmonic. Employing the APW basis, Eq. (3.2) is rewritten as

$$\sum_{GG'} \left[\langle \chi_{k+G} | \mathcal{H}^{\text{KS}} | \chi_{k+G'} \rangle - \varepsilon_{nk}^{\text{KS}} \langle \chi_{k+G} | \chi_{k+G'} \rangle \right] \langle \chi_{k+G} | \phi_{nk}^{\text{KS}} \rangle = 0, \tag{3.11}$$

where we inserted the overlap matrix $\langle \chi_{k+G} | \chi_{k+G'} \rangle$, because the basis is not orthonormal. As it turns out, only if the energy E_l of the atomic solution coincides with the band energy $\varepsilon_{nk}^{\text{KS}}$, the APW method will be accurate enough.[114] Hence, one employs a self-consistency scheme inserting the resulting band energy as constraint into the determination of the atomic radial functions (Eq. (3.8)). Compared to a basis, which is independent of the parameter E_l, the additional self-consistency increases the computational demand of the APW method. Furthermore, if the function $u_{al}(r)$ has a very small value at the MT boundary, this may lead to numerical instabilities in the determination of the expansion coefficients a_{alm}^{k+G}.

To improve the variational freedom, Andersen[116] suggested to include a second radial function inside the MT spheres

$$
\chi_{\boldsymbol{k}+\boldsymbol{G}}(\boldsymbol{r}) = \begin{cases} \dfrac{1}{\sqrt{\Omega}}\, \mathrm{e}^{\mathrm{i}(\boldsymbol{k}+\boldsymbol{G})\cdot\boldsymbol{r}} & \boldsymbol{r}\in\mathrm{IR}\quad\text{and} \\[2ex] \displaystyle\sum_{p=1}^{2}\sum_{lm} a_{alm}^{p,\boldsymbol{k}+\boldsymbol{G}}\, u_{al}^{p}(r_a)\, \mathrm{Y}_{lm}(\widehat{\boldsymbol{r}}_a) & \boldsymbol{r}\in\mathrm{MT}(a). \end{cases} \tag{3.12}
$$

With these two radial functions the MT function can be matched to value and slope of the plane wave in the IR, so that we refer to this method as the linearized augmented-plane-wave (LAPW) technique. A suitable choice for the second radial function is the energy derivative of $u_{al}(r)$, i.e.

$$
u_{al}^{p=1}(r) = u_{al}(r) \quad\text{and}\qquad u_{al}^{p=2}(r) = \dot{u}_{al}(r). \tag{3.13}
$$

We obtain the energy derivative $\dot{u}_{al}(r)$ as the solution of the inhomogeneous differential equation which results from an energy derivative of Eq. (3.8)

$$
\left[-\frac{1}{2}\frac{\mathrm{d}^2}{\mathrm{d}r^2} + \frac{l(l+1)}{2r^2} + V_{a,00}^{\mathrm{eff.}}(r) \right] \dot{u}_{al}(r) = E_l \dot{u}_{al}(r) + u_{al}(r). \tag{3.14}
$$

The advantage of this particular choice is that the radial functions $u_{al}(r)$ and $\dot{u}_{al}(r)$ are orthogonal. Historically, the LAPW method was applied first to a constant interstitial potential. This limitation is not systematic, so that we incorporate the full potential in the IR. To distinguish between both methods, the latter is referred to as the full-potential LAPW (FLAPW) technique. The FLAPW method provides a highly accurate all-electron basis,[31,32,117] which has been successfully applied to a large variety of materials.

3.4   Local orbitals

In the FLAPW method, core and valence states are not orthogonal. Hence, for ill-suited systems the LAPW functions may incorrectly describe the high-lying core state instead of the envisaged valence states,[114] resulting in so called *ghost bands* that prevent a convergence of the self-consistency field cycle. An inclusion of these core states into the valence window is not possible, because the particular LAPW functions are necessary for the description of valence states with the same orbital moment.[115] However, it is possible to extend the basis by additional *local orbitals* (lo)

that are confined to a certain MT sphere[118]

$$
\chi_{\mathrm{lo}}(\boldsymbol{r}) = \begin{cases} 0 & \boldsymbol{r} \in \mathrm{IR} \quad \text{and} \\ \sum_{p=1}^{3} \sum_{lm} a_{alm}^{p,\mathrm{lo}} u_{al}^{p}(r_a)\, \mathrm{Y}_{lm}(\widehat{\boldsymbol{r}}_a) & \boldsymbol{r} \in \mathrm{MT}(a). \end{cases} \tag{3.15}
$$

In order that the basis function is nontrivial and vanishes at the MT boundary, a third radial function $u_{al}^{p=3}(r) = u_{al}^{\mathrm{lo}}(r)$ is required, which is obtained in the same fashion as the $u_{al}(r)$, but employing a different energy parameter E_l^{lo}. As additional constraint, we set $a_{alm}^{p=3,\mathrm{lo}}$ to zero and match the basis function to a "virtual" plane wave

$$
\mathrm{e}^{\mathrm{i}(\boldsymbol{k}+\boldsymbol{G}_{\mathrm{lo}})\cdot\boldsymbol{r}} . \tag{3.16}
$$

With this construction the expansion coefficients satisfy the periodic boundary conditions. Then, we adjust $a_{alm}^{p=3,\mathrm{lo}}$ such that the basis function vanishes at the boundary of MT sphere. As a consequence of the matching to a plane wave the basis function can be expressed in terms of a factor containing all $\boldsymbol{k}$-point dependence

$$
M_{\boldsymbol{G}_{\mathrm{lo}},m}(\boldsymbol{k}) = \mathrm{e}^{\mathrm{i}(\boldsymbol{k}+\boldsymbol{G}_{\mathrm{lo}})\cdot\boldsymbol{R}_a}\, \mathrm{Y}_{lm}^{*}(\widehat{\boldsymbol{k}+\boldsymbol{G}_{\mathrm{lo}}}) \tag{3.17}
$$

and a radial function $f_m^{\mathrm{lo}}(r)$

$$
\chi_{\boldsymbol{k}+\boldsymbol{G}_{\mathrm{lo}}}(\boldsymbol{r}) = \sum_{m=-l}^{l} M_{\boldsymbol{G}_{\mathrm{lo}},m}(\boldsymbol{k}) f_m^{\mathrm{lo}}(r). \tag{3.18}
$$

Michalicek *et al.*[119] discuss an improvement of the flexibility of the FLAPW basis by local orbitals with energy parameters of unoccupied states[120] or associated to higher energy derivatives. They find that in particular for systems with large MT radii or insulators with large band gaps a careful convergence of the basis by additional local orbitals may alter the outcome of the calculations significantly. In this thesis, if additional local orbitals are necessary to converge the results, we will employ unoccupied local orbitals where restrictions to the logarithmic derivative ensure that the constructed functions are orthogonal and the energy parameters increase with the number of nodes (for details see Ref. 121).

Orbital Dependent Functionals

4.1 Hybrid functionals

According to the Hohenberg and Kohn,[4] the density $n(r)$ of the system is sufficient to describe the properties of a system completely, so that the calculation of the ground state in density functional theory (DFT) is a three-dimensional problem whereas examining an N-particle system with a wave-function based scheme is a $3N$-dimensional one. Hence, DFT has become the most commonly applied technique to investigate ground-state properties of molecules and solids from first principles.[72] The accuracy of DFT originates in the fact that the largest contributions to the total energy can be calculated exactly. Only for the exchange-correlation energy, an analytical expression is unknown, but simple approximations, such as the local density approximation (LDA) and the generalized gradient approximation (GGA), provide an accurate prediction of electronic and structural ground-state properties. Albeit these local functionals have been successfully applied for wide range of materials, they systematically fail in some particular systems that we outlined in Sec. 2.5. The most prominent flaws of the local functionals that are the presence of a spurious self interaction[90] and the systematic underestimation of the band gap.[122,123]

Describing the exchange-correlation energy with an LDA or a GGA functional, even in a single-electron system the exchange-correlation and the Hartree contribution to the total energy do not cancel each other. As a consequence, these local functionals incorporate an unphysical self-interaction error (SIE),[90] which leads to a delocalization and is in particular important for localized d and f states. For more details see Sec. 2.5.

A common misconception is that the band gap, which is associated to excitation of the system, cannot be calculated by means of DFT. However, we can express the

band gap as

$$E_{\text{gap}} = \underbrace{E_{N+1} - E_N}_{\text{ionization energy}} - \underbrace{E_N - E_{N-1}}_{\text{electron affinity}},$$ (4.1)

for which only the ground-state energies of the $(N-1)$-, the N-, and the $(N+1)$-particle are necessary.[122,124] These can be evaluated in DFT, hence, the band gap is an accessible ground-state property of the system. Denoting the band gap obtained as differences of Kohn-Sham eigenvalues in the N-particle system by ε_{gap},[122] we can express the band gap as

$$E_{\text{gap}} = \varepsilon_{\text{gap}} + \Delta_{\text{xc}}$$ (4.2)

with the exchange-correlation discontinuity

$$\Delta_{\text{xc}} = \left.\frac{\delta E}{\delta n}\right|_{N+\delta} - \left.\frac{\delta E}{\delta n}\right|_{N-\delta},$$ (4.3)

which is associated to a tiny change δ in the number of particles.[123] However, for the local functionals the exchange discontinuity is zero, so that they underestimate the band gap of the system.

In contrast, the Hartree-Fock (HF) theory[93] provides a very accurate description of single atoms and ions, because it explicitly accounts for the self interaction, treats the exchange part exactly, and includes a derivative discontinuity. However, the HF theory is limited to atomic systems, because correlation effects, which are not included in the HF method, are important in larger molecules and solids, so that the chemical bonding is not accurately described.[20] As these correlation effects are captured well within the local exchange-correlation functionals, a combination of these techniques suggests itself. Becke[20] rationalized a intermixture of local exchange-correlation functionals with HF exchange considering the adiabatic connection between a noninteracting system and the fully interacting one (see Sec. 2.3) at a constant density

$$E_{\text{xc}}[n] = \int_0^1 \mathrm{d}\lambda\, E_{\text{xc},\lambda}[n],$$ (4.4)

where $E_{\text{xc}}[n]$ is the exchange-correlation energy, $E_{\text{xc},\lambda}[n]$ contains all exchange and correlation effects for a particular value of λ (see Eq. (2.32)), and λ determines the strength of the electron-electron interaction. On the one hand, the HF theory is exact in the noninteracting system, because all correlations effects are expressed by an effective potential. On the other hand, the local exchange-correlation functionals provide an accurate description of the fully interacting system. Hence, Becke[20] suggested the following linear approximation

$$E_{\text{xc},\lambda}[n] = (1-\lambda)E_{\text{x}}^{\text{HF}}[n] + \lambda E_{\text{xc}}^{\text{LDA}}[n],$$ (4.5)

where $E_x^{HF}[n]$ is the exchange energy of the HF method[a] and $E_{xc}^{LDA}[n]$ is the exchange-correlation energy of the LDA functional. Solving the integral in Eq. (4.4) with this approximation yields the half-and-half hybrid functional[20]

$$E_{xc}[n] = \frac{1}{2}E_x^{HF}[n] + \frac{1}{2}E_{xc}^{LDA}[n].$$ (4.6)

Becke later improved the accuracy of hybrid functionals by a semi-empirical approach, in which the mixture of local and nonlocal contribution was optimized for a benchmark set of molecules. Depending on the number of parameters in the optimization, these functionals are nowadays referred to as the B3X[23]

$$E_{xc}^{B3X} = E_{xc}^{LDA} + a\left(E_x^{HF} - E_x^{LDA}\right) + a_x\left(E_x^{X} - E_x^{LDA}\right) + a_c\left(E_c^{X} - E_c^{LDA}\right)$$ (4.7)

and B1X[22]

$$E_{xc}^{B1X} = E_{xc}^{X} + a\left(E_x^{HF} - E_x^{X}\right)$$ (4.8)

functional, where the X denotes the particular GGA functional.

Perdew *et al.*[24] motivated a particular choice of $a = 1/4$ in the B1X functional with X = PBE, which is referred to as the PBE0 functional. Assuming that the adiabatic connection integrand (Eq. (4.4)) can be expressed as

$$E_{xc,\lambda}^{PBE0}[n] = E_{xc,\lambda}^{PBE}[n] + \left(E_x^{HF} - E_x^{PBE}\right)(1 - \lambda)^m,$$ (4.9)

we obtain the exchange-correlation energy

$$E_{xc}^{PBE0}[n] = E_{xc}^{PBE} + \frac{1}{m}\left(E_x^{HF} - E_x^{PBE}\right).$$ (4.10)

Hence, the functional is identical to a B1X functional, if we choose $a = 1/m$. The advantage of this ansatz is that the expansion of Eq. (4.9) can be directly related to a Møller-Plesset pertubation expansion. For most materials, the fourth order Møller-Plesset pertubation, which corresponds to $m = 4$, yields very accurate atomization energies,[25] resulting in the value of $a = 1/4$.[24]

This chapter is organized as follows: In Sec. 4.2, we present the general approach to realize a nonlocal potential in DFT. We introduce an auxiliary basis particularly suited for the calculation of wave function products in the full-potential linearized augmented-plane-wave (FLAPW) method in Sec. 4.3. In Sec. 4.4, we outline the implementation of the HF exchange in the FLAPW method.[33,121]

---

[a]The correlation energy of the HF method is 0.

4.2   A generalized Kohn-Sham scheme

As discussed in Sec. 2.2, if a density $n(\boldsymbol{r})$ minimizes the total energy (Eq. (2.9)), then any many-body wave function $|\Phi\rangle$ that minimizes the universal functional (cf. Eq. (2.10))

$$F[n] = \min_{\langle\Phi|\Phi\rangle=n} \langle\Phi\,|\,T + V_{\mathrm{ee}}\,|\,\Phi\rangle \tag{4.11}$$

is a ground-state wave function of the system.[79] Here, V_{ee} is the electron-electron interaction. In a Kohn-Sham scheme, this complicated many-body interaction is expressed via the adiabatic connection (see Sec. 2.3) as an effective single-particle potential $V_{\mathrm{s}}^{\mathrm{eff.}}(\boldsymbol{r})$. Hence, the universal functional $F[n]$ reduces to the single-particle kinetic energy

$$T_{\mathrm{s}}[n] = \min_{\langle\Phi_{\mathrm{KS}}|\Phi_{\mathrm{KS}}\rangle=n} \langle\Phi_{\mathrm{KS}}\,|\,T\,|\,\Phi_{\mathrm{KS}}\rangle\,, \tag{4.12}$$

where $|\Phi_{\mathrm{KS}}\rangle$ is the many-body Kohn-Sham wave function. As the electrons are independent in a Kohn-Sham scheme, the many-body wave function can be expressed as product of single-particle wave functions $|\phi_n^{\mathrm{KS}}\rangle$ that solve the Kohn-Sham equation (2.12).

In hybrid functionals, the electron-electron exchange is not expressed in terms of an effective potential, but rather calculated exactly. Hence, we introduce a generalized Kohn-Sham (gKS) scheme, where the universal functional (Eq. (4.11)) retains part of the exchange

$$F[n] = \min_{\langle\Phi_{\mathrm{gKS}}|\Phi_{\mathrm{gKS}}\rangle=n} \langle\Phi_{\mathrm{gKS}}\,|\,T + a V_{\mathrm{x}}^{\mathrm{HF}}\,|\,\Phi_{\mathrm{gKS}}\rangle \tag{4.13}$$

with the factor $a = 1/4$ for the hybrid functionals employed in this thesis. In principle, for interacting electrons, the many-body wavefunction $|\Phi_{\mathrm{gKS}}\rangle$ cannot be written as a product state. To overcome this problem, one commonly approximates

$$\left|\Phi_{\mathrm{gKS}}\right\rangle \approx \left|\Phi_{\mathrm{KS}}\right\rangle. \tag{4.14}$$

With this approximation, the hybrid functionals can be calculated by small modification to the Kohn-Sham equation

$$\mathcal{H}^{\mathrm{gKS}}\left|\phi_n\right\rangle = \mathcal{H}^{\mathrm{KS}}\left|\phi_n\right\rangle - a\left(\sum_m^{\mathrm{occ.}} \left\langle\phi_m\,|\,v\,|\,\phi_m\phi_n\right\rangle + V_{\mathrm{x}}^{\mathrm{PBE}}\left|\phi_n\right\rangle\right) = \varepsilon_n^{\mathrm{gKS}}\left|\phi_n\right\rangle, \tag{4.15}$$

where $\mathcal{H}^{\mathrm{KS}}$ is the Kohn-Sham Hamiltonian (Eq. (2.11)), v is the Coulomb potential, and the nonlocal matrix element is calculated as

$$\left\langle\phi_m|v|\phi_m\phi_n\right\rangle = \phi_m(\boldsymbol{r}) \int \mathrm{d}^3 r' \frac{\phi_m^*(\boldsymbol{r}')\phi_n(\boldsymbol{r}')}{|\boldsymbol{r} - \boldsymbol{r}'|}. \tag{4.16}$$

We draw attention to the change of sign in Eq. (4.15), which originates in the exchange, i.e.

$$V_\mathrm{x}^\mathrm{HF} \propto -\frac{1}{|\boldsymbol{r} - \boldsymbol{r}'|}. \tag{4.17}$$

4.3   The mixed product basis

In practice, we calculate the Hamiltonian (Eq. (4.15)) expanding the wave functions in the FLAPW basis (cf. Chap. 3). For the evaluation of the nonlocal potential, we employ an auxiliary basis to represent products of wave functions.[33,125] We construct this basis so that the accuracy of the FLAPW basis is retained. In the calculation of products of the FLAPW basis functions, the angular part of the muffin-tin (MT) contribution is analytically given as

$$\mathrm{Y}_{lm}^*(\widehat{\boldsymbol{r}})\,\mathrm{Y}_{l'm'}(\widehat{\boldsymbol{r}}) = \sum_{LM} G_{lm,l'm',LM}\,\mathrm{Y}_{LM}(\widehat{\boldsymbol{r}}) \tag{4.18}$$

with the Gaunt coefficient

$$G_{lm,l'm',LM} = \int \mathrm{d}\Omega\, \mathrm{Y}_{lm}^*(\widehat{\boldsymbol{r}})\,\mathrm{Y}_{l'm'}(\widehat{\boldsymbol{r}})\mathrm{Y}_{LM}^*(\widehat{\boldsymbol{r}}). \tag{4.19}$$

We point out that only Gaunt coefficients with $|l - l'| \le L \le l + l'$ and $M = m' - m$ are nonzero. Nevertheless, we obtain several radial functions to any particular combination of L and M. These radial functions exhibit a high degree of linear dependence, which allows us to reduce the number of basis functions significantly.[121] Finally, we obtain

$$M_{qI}^\mathrm{MT}(\boldsymbol{r}) = M_I(|\boldsymbol{r} - \boldsymbol{R}_I|)\,\mathrm{Y}_I(\widehat{\boldsymbol{r}-\boldsymbol{R}_I})\,\mathrm{e}^{\mathrm{i}\boldsymbol{q}\cdot\boldsymbol{R}_I}, \tag{4.20}$$

where $M_I(r)$ is a radial function, $\boldsymbol{R}_I$ is the center of the MT sphere, and $\boldsymbol{q}$ a reciprocal vector in the Brillouin zone (BZ). The index I is summarizing the atom a, the angular momentum quantum number L, and the magnetic quantum number M.

In the interstitial region (IR), the product of two plane waves can be expressed as

$$\mathrm{e}^{-\mathrm{i}(\boldsymbol{k}+\boldsymbol{G})\cdot\boldsymbol{r}}\,\mathrm{e}^{\mathrm{i}(\boldsymbol{k}'+\boldsymbol{G}')\cdot\boldsymbol{r}} = \mathrm{e}^{\mathrm{i}(\boldsymbol{q}+\boldsymbol{G})\cdot\boldsymbol{r}}, \tag{4.21}$$

where $\boldsymbol{G} = \boldsymbol{G} - \boldsymbol{G}$ and $\boldsymbol{q} = \boldsymbol{k}' - \boldsymbol{k}$. Hence, the construction of basis functions for the IR is straightforward

$$M_{qI}^\mathrm{IR}(\boldsymbol{r}) = \frac{1}{\sqrt{\Omega}}\,\mathrm{e}^{\mathrm{i}(\boldsymbol{q}+\boldsymbol{G}_I)\cdot\boldsymbol{r}} \tag{4.22}$$

with the volume of the unit cell Ω. We refer to the basis $\{M_{qI}(\boldsymbol{r})\}$, which combines the MT basis $\{M_{qI}^\mathrm{MT}(\boldsymbol{r})\}$ and the IR $\{M_{qI}^\mathrm{IR}(\boldsymbol{r})\}$ one, as the *mixed product basis* (MPB).

4.4   Hybrid functionals in FLAPW

Analogous to the local functionals (cf. Chap. 3), we transform the generalized Kohn-Sham equation (Eq. (4.15) from a differential equation to a linear one by introducing the FLAPW basis

$$\sum_{G'} \langle \chi^\sigma_{k+G} | \mathcal{H}^{\mathrm{gKS}} | \chi^\sigma_{k+G'} \rangle \langle \chi^\sigma_{k+G'} | \phi^\sigma_{nk} \rangle = \varepsilon^\sigma_{nk} \langle \chi^\sigma_{k+G} | \phi^\sigma_{nk} \rangle . \tag{4.23}$$

Note, that we explicitly included indices for spin σ and wave vector $\mathbf{k}$ for the wave and basis functions. Furthermore, the Hamiltonian is diagonal in spin space, because we exclude spin-orbit coupling. We limit the discussion to the consideration of the additional nonlocal contribution in hybrid functionals

$$V^{\sigma,\mathrm{NL}}_{\mathrm{x},GG'}(\mathbf{k}) = -\sum_m^{\mathrm{occ.}} \sum_{\mathbf{q}}^{\mathrm{BZ}} \langle \chi^\sigma_{k+G} \phi^\sigma_{mq} | v | \phi^\sigma_{mq} \chi^\sigma_{k+G'} \rangle, \tag{4.24}$$

which is the most complex and computationally most expensive term, because it involves the calculation of $N_G^2 \times N_q \times N^\sigma_{\mathrm{occ.}}$ six-dimensional integrals for every $\mathbf{k}$ point and spin channel. Here, N_G is the number of basis functions, N_q is the number of $\mathbf{k}$ points in the BZ, and $N^\sigma_{\mathrm{occ.}}$ is the number of occupied states in the spin channel σ. To reduce the computational demand, it is advantageous to evaluate the nonlocal potential in terms of the wave functions[b]

$$V^{\sigma,\mathrm{NL}}_{\mathrm{x},nn'}(\mathbf{k}) = -\sum_m^{\mathrm{occ.}} \sum_{\mathbf{q}}^{\mathrm{BZ}} \langle \phi^\sigma_{nk} \phi^\sigma_{mq} | v | \phi^\sigma_{mq} \phi^\sigma_{n'k} \rangle, \tag{4.25}$$

because we can introduce a cutoff for the number of bands $N_{\mathrm{b}} \leq N_G$. An accurate convergence of the employed number of bands is the most important additional convergence parameter introduced by hybrid functionals. Next, we introduce the MPB described in the sec:mixbas

$$V^{\sigma,\mathrm{NL}}_{\mathrm{x},nn'}(\mathbf{k}) = -\sum_{m\mathbf{q}} \sum_{IJ} \langle \phi^\sigma_{nk} | \phi^\sigma_{mk-q} M_{qI} \rangle v_{IJ}(\mathbf{q}) \langle M_{qJ} \phi^\sigma_{mk-q} | \phi^\sigma_{n'k} \rangle \tag{4.26}$$

with the Coulomb matrix

$$v_{IJ}(\mathbf{q}) = \iint \mathrm{d}^3 r \, \mathrm{d}^3 r' \, \tilde{M}^*_{qI}(\mathbf{r}) v(\mathbf{r}, \mathbf{r}') \tilde{M}_{qJ}(\mathbf{r}'). \tag{4.27}$$

---

[b]Wave and basis functions are related to each other via the eigenvectors of the generalized Kohn-Sham equation. [121]
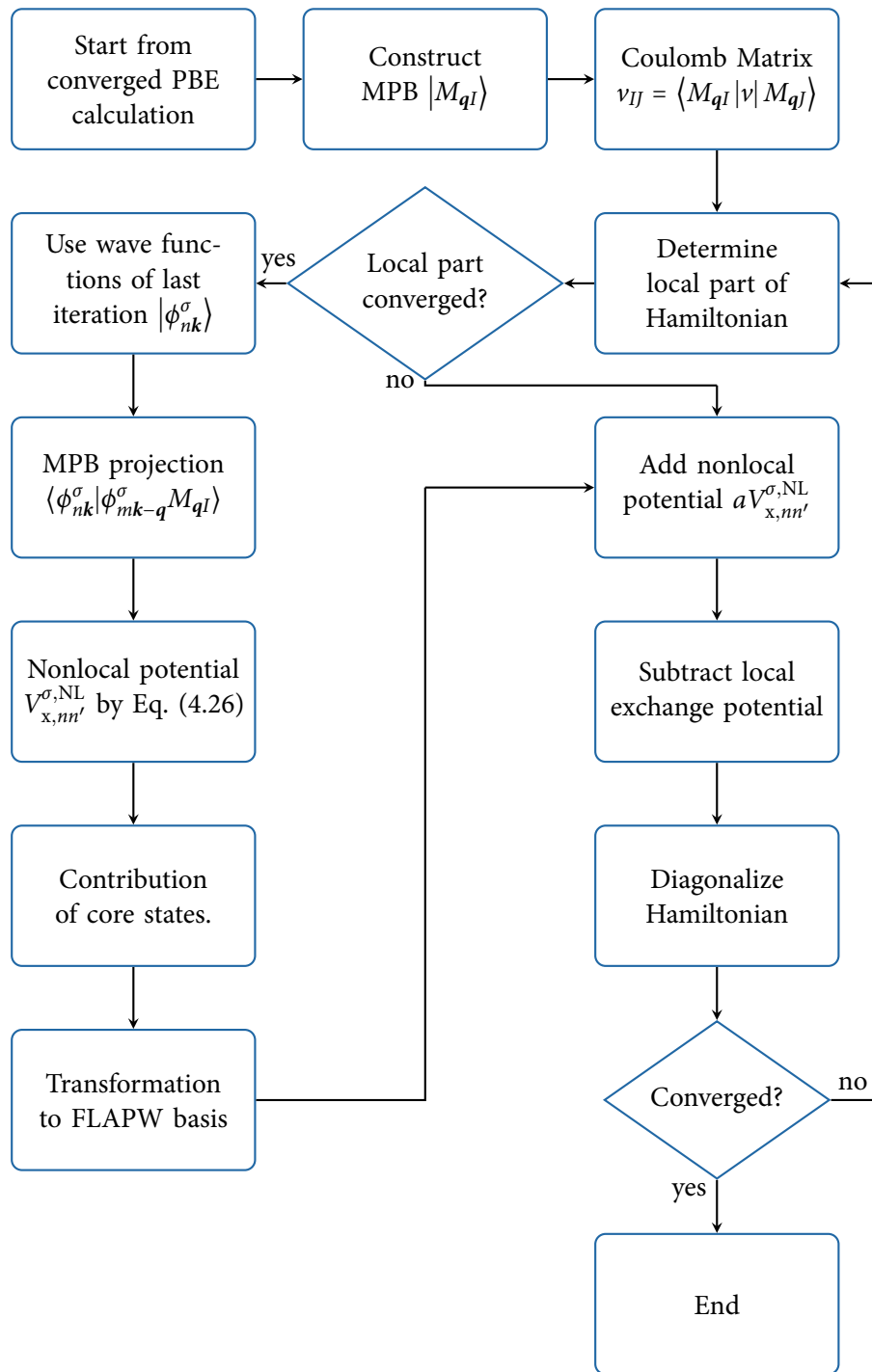
Figure 4.1: Flowchart of a PBE0 calculation within `Fleur`. The detailed description is given in the text.

Equation (4.26) corresponds to a vector-matrix-vector multiplication, for which efficient numerical algorithms have been developed. One advantage of this approach is that the same MPB can be employed over the full self-consistent field run so that the Coulomb matrix has to be calculated only once at the beginning of the self consistency. Betzinger *et al.*[33] optimized the Coulomb matrix by choosing linear combinations of MPB functions, such that the multipole moment of all but one basis function per combination of L and M disappears. If the multipole moment vanishes, only on-site terms in Eq. (4.26) contribute to the nonlocal potential so that a sparse-matrix technique becomes feasible.

The necessary computation time to achieve self consistency is further improved by separating evaluation of nonlocal and local potential. Compared to the contributions of electrostatic and kinetic energy, the nonlocal potential $V_{\mathrm{x},nn'}^{\sigma,\mathrm{NL}}$ is a small quantity. Hence, we converge the large contributions first before we reevaluate the nonlocal potential. Betzinger *et al.*[33] showed that this scheme leads to a reduction of the required number of self-consistency cycles by a factor of three to four. In Fig. 4.1, we illustrate schematically the order of events in a typical PBE0 calculation as implemented in `Fleur`.[126] We start the calculation from a converged calculation (typically PBE), because we need the wave functions to create an accurate MPB. With this MPB, we evaluate the Coulomb matrix according to Eq. (4.27). Then, we evaluate the local parts of the Hamiltonian as in a PBE calculation. If the density is converged with respect to the local potential, we switch to the calculation of the nonlocal potential. As we start from a converged calculation, this requirement is fulfilled in the first iteration. To evaluate the nonlocal potential, we employ the Kohn-Sham wave functions of the last iteration. Then, we project products of these wave functions onto the MPB. Equation (4.26) defines the vector-matrix-vector multiplication, which be perform to obtain the nonlocal potential. The summation over all occupied states in Eq. (4.25) includes the core states, which are evaluated as on-site integrals of the form

$$\iint_{\mathrm{MT}} \mathrm{d}^3 r\, \mathrm{d}^3 r'\, \frac{\phi_{n\mathbf{k}}^{\sigma,*} \phi_{\mathrm{core}}^* \phi_{\mathrm{core}} \phi_{n'\mathbf{k}}^{\sigma}}{|\mathbf{r} - \mathbf{r}'|}. \tag{4.28}$$

We transform from the wave functions to the FLAPW basis and add the nonlocal potential to the Hamiltonian. We subtract $a = {}^1/_4$ of the PBE exchange and diagonalize the Hamiltonian to obtain the wave functions and the new density. Then, we iterate this scheme until self consistency is achieved.

Screened Hybrid Functionals

5.1   Motivation for a screened exchange potential

In the chap:pbe0, we introduced hybrid functionals, which incorporate a certain fraction of bare Hartree-Fock (HF) exchange in the exchange-correlation functional (Eq. (2.32)). Becke[20] motivated this inclusion of nonlocal exchange by the adiabatic connection (see Sec. 2.3). Perdew *et al.*[24] argued that a fraction of $1/4$ is the optimum choice of HF exchange. Since then, hybrid functionals have been successfully applied to describe the electronic and structural properties of a rather large number of materials.[127–130] However, the computational effort of these functionals is significantly larger than the one necessary for conventional local functionals, in particular, because of the long-range nature of the Coulomb potential in calculation the HF exchange. To facilitate the calculation of materials with more than a few atoms per unit cell, a need for computationally less expensive realizations arose.

In real system, polarization effects screen the interactions between distant electrons, so that the contribution of the long-range (LR) exchange disappears. This prompted Heyd *et al.*[26] to separate the PBE0 hybrid functional[24] into long-range and short-range contributions. As approximation to the correlation effects, which screen the long-range interactions, only the short-range (SR) component of the HF exchange is incorporated in the exchange-correlation energy

$$E_{\text{xc}} = E_{\text{xc}}^{\text{PBE}} + a \left(E_{\text{x}}^{\text{HF,SR}} - E_{\text{x}}^{\text{PBE,SR}} \right). \tag{5.1}$$

In comparison to Eq. (4.10), the same mixing parameter $a = 1/4$ is adopted, whereas the modification to the exchange-correlation energy of the PBE functional[14] is only

applied to the SR component, effectively reducing the computational effort within the basis of localized Gaussian functions. Heyd *et al.*[26] used the error function $\text{erf}(x)$ and its complement $\text{erfc}(x) = 1 - \text{erf}(x)$ to decompose the Coulomb interaction $v(r)$ into a long-range (LR) and a short-range (SR) part

$$v(r) = \frac{1}{r} = \frac{\text{erf}(\omega r)}{r} + \frac{\text{erfc}(\omega r)}{r} = v^{\text{LR}}(r) + v^{\text{SR}}(r), \quad (5.2)$$

where ω is an adjustable screening parameter. A screened hybrid functional with this particular range separation is nowadays referred to as Heyd-Scuseria-Ernzerhof (HSE) functional. The screening parameter was optimized[26] with respect to a benchmark data set of molecules, which yielded $\omega = 0.15$. Krukau *et al.*[131] later refined this value for solids to a value of $\omega = 0.11$. To differentiate between the different screening parameters, the corresponding functionals are labeled HSE03 and HSE06 for $\omega = 0.15$ and $\omega = 0.11$, respectively. Throughout this work, we have employed only the HSE06 realization. The HSE functional was implemented within Gaussian[26,132] and plane-wave[27] basis sets and in the following, we present our approach its implementation within the full-potential linearized augmented-plane-wave (FLAPW) method.[29]

A screened exchange functional based on the Yukawa potential was recently implemented in FLAPW by Tran and Blaha.[133] Our approach is more general, as it is suited to treat any nonlocal potential $v(r)$, which is a pure function of the distance r. Hence, we could employ our method to implement the LC-ωPBE[134] functional, where the HF exchange is included only for the LR part, or the HISS[135] functional, in which the nonlocal potential is employed for intermediate distances.

5.2   Implementation

In Chap. 4, we discussed the implementation of the PBE0 functional within the FLAPW method by Betzinger *et al.*.[33] They used an auxiliary product basis $\{M_{qI}(\boldsymbol{r})\}$, which consists of two types of functions, namely

$$M_{qI}^{\text{MT}}(\boldsymbol{r}) = R_I(|\boldsymbol{r} - \boldsymbol{r}_I|) \, Y_I(\widehat{\boldsymbol{r} - \boldsymbol{r}_I}) \, e^{i\boldsymbol{q}\boldsymbol{r}_I} \quad (5.3)$$

within the muffin-tin sphere centered at $\boldsymbol{r}_I$ and

$$M_{qI}^{\text{IR}}(\boldsymbol{r}) = \frac{1}{\sqrt{\Omega}} \, e^{i(\boldsymbol{q}+\boldsymbol{G}_I)\boldsymbol{r}} \quad (5.4)$$

in the interstitial region (IR). Here the Bloch vector $\boldsymbol{q}$ and the index I label the basis function, where I indicates the atom, the angular momentum quantum number l and

the magnetic quantum number m within the MT sphere and the reciprocal lattice vector $\boldsymbol{G}$ in the IR. Ω is the volume of the unit cell of the crystal. $R_I(r)$ is a numerical radial function that is built from FLAPW basis functions. For further details refer to Sec. 4.3 or the articles of Friedrich *et al.*[125] and Betzinger *et al.*.[33] We refer to this auxiliary basis as the *mixed product basis* (MPB).

With the introduction of the MPB the nonlocal exchange potential is given by (see Eq. (4.26))

$$V_{\text{x},nn'}^{\sigma,\text{NL}}(\boldsymbol{k}) = -\sum_m^{\text{occ.}} \sum_{\boldsymbol{q}}^{\text{BZ}} \sum_{IJ} \langle \phi_{n\boldsymbol{k}}^\sigma | \phi_{m\boldsymbol{k}-\boldsymbol{q}}^\sigma M_{\boldsymbol{q},I} \rangle v_{IJ}(\boldsymbol{q}) \langle M_{\boldsymbol{q},J} \phi_{m\boldsymbol{k}-\boldsymbol{q}}^\sigma | \phi_{n'\boldsymbol{k}}^\sigma \rangle \tag{5.5}$$

with the wavefunction $\phi_{n\boldsymbol{k}}^\sigma$, the spin index σ, the band indices m and n, and the Coulomb matrix

$$v_{IJ}(\boldsymbol{q}) = \iint \mathrm{d}^3 r\, \mathrm{d}^3 r' \, \frac{\tilde{M}_{\boldsymbol{q},I}^*(\boldsymbol{r}) \tilde{M}_{\boldsymbol{q},J}(\boldsymbol{r}')}{|\boldsymbol{r} - \boldsymbol{r}'|}. \tag{5.6}$$

It seems to be straightforward to replace the Coulomb potential in Eq. (5.6) with the screened Coulomb potential as defined in Eq. (5.2). However, the computational cost of this ansatz is much larger than the evaluation of the Coulomb potential in the PBE0 functional, as we can construct the MPB such that the matrix Eq. (5.6) is sparse. This construction is an intrinsic property of the Coulomb potential and cannot be transferred to screened interactions. Furthermore, the direct evaluation of Eq. (5.6) is cumbersome for potentials which have more complex expansions in Legendre polynomials than the Coulomb potential.

Hence, we chose a different approach to calculate the SR nonlocal exchange potential. Figure 5.1 compares the bare and the screened Coulomb potential, $v(r)$ and $v^{\text{SR}}(r)$, which occur in the nonlocal exchange integral in the PBE0 and the HSE functional, respectively. The distance r is measured in units of Bohr radii a_0. Both potentials show a divergent behavior for $r \to 0$, however the difference $v^{\text{LR}}(r)$ remains finite. As the description of the divergence near the origin requires a large cutoff to be accurately described by a Fourier transformation, we expect a faster convergence of the LR potential, where this divergence is not present.

To utilize the faster convergence of the LR potential, we calculate the HSE exchange potential as

$$V_{\text{xc}}^{\text{HSE}} = V_{\text{xc}}^{\text{PBE}} - a V_{\text{x}}^{\text{PBE,SR}} + a \left(V_{\text{x}}^{\text{NL}} - V_{\text{x}}^{\text{NL,LR}} \right), \tag{5.7}$$

with the local exchange-correlation potentials $V_{\text{xc}}^{\text{PBE}}$ and $V_{\text{x}}^{\text{PBE,SR}}$, which are the functional derivative of the corresponding local exchange-correlation energies $E_{\text{xc}}^{\text{PBE}}$ and $E_{\text{x}}^{\text{PBE,SR}}$, and the nonlocal exchange potential in parentheses, which consists of the bare Coulomb potential V_{x}^{NL} and the LR component $V_{\text{x}}^{\text{NL,LR}}$.
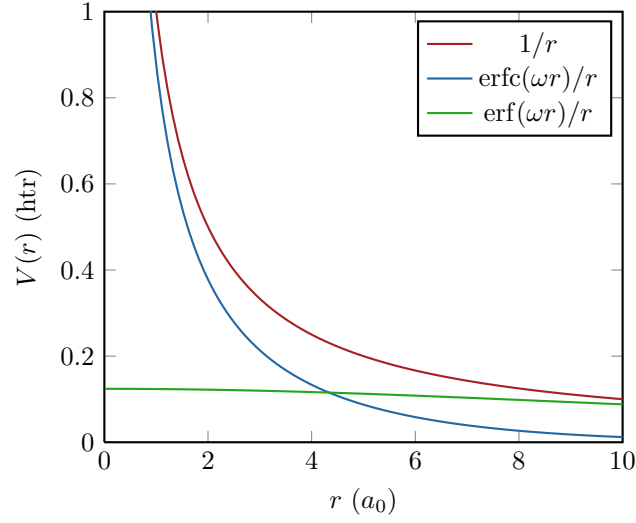
Figure 5.1: The bare (red) and the screened (blue) Coulomb potential show the same divergent behavior near the origin, whereas their difference (green) is a smooth function and has a finite limit. To describe the divergence near the origin requires a large reciprocal cutoff. Without this divergence, the Fourier transform of the difference converges much faster.[29]

The local exchange-correlation energies are functionals of the density[14,89] (cf. Eq. (2.39))

$$E_x = \int d^3r\, n(\boldsymbol{r}) \varepsilon_x^{LDA}(n) F_x(s) \tag{5.8}$$

with the reduced density gradient[a] s, the LDA exchange energy density ε_x^{LDA}, and the enhancement factor F_x. Ernzerhof and Perdew[89] derived the enhancement factor $F_x(s)^{PBE}$ for the PBE functional as integral over the PBE exchange hole $J^{PBE}(s, y)$

$$F_x(s)^{PBE} = -\frac{8}{9} \int dy\, y\, J^{PBE}(s, y). \tag{5.9}$$

We follow the idea of Heyd *et al.*[26] and implement the SR local exchange energy by screening the exchange hole in the calculation of the enhancement factor

$$F_x(s)^{PBE,SR} = -\frac{8}{9} \int dy\, y\, J^{PBE}(s, y) \times \mathrm{erfc}\left(\frac{\omega y}{k_F}\right) \tag{5.10}$$

with the local Fermi wavevector[b] k_F. The details of the implementation can be found

---

[a] reduced density gradient $s = \dfrac{|\nabla n|}{2 k_F n}$

[b] local Fermi wavevector $k_F = (3\pi^2 n)^{1/3}$
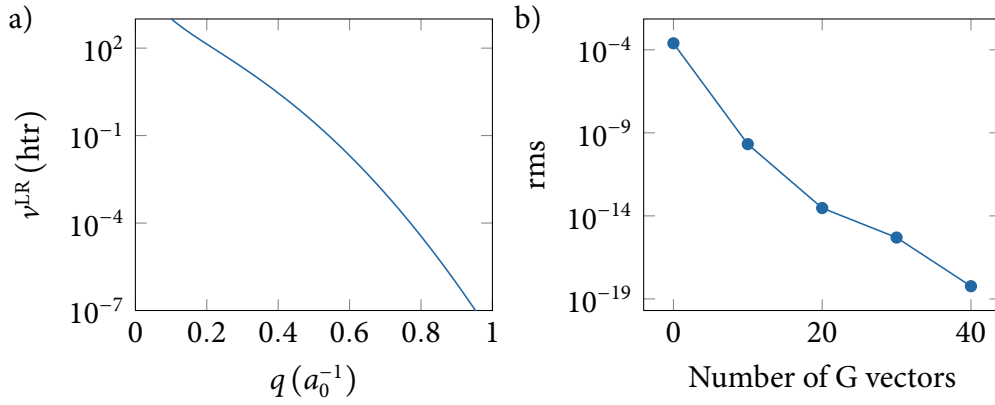
Figure 5.2: a) Long-range (LR) potential $v^{LR}(q)$ (cf. Eq. (5.12)), which is the Fourier transform of the difference of bare Coulomb and screened Coulomb potential, as function of $q = |q + G|$. b) Convergence of the root-mean-square (rms) deviation of the eigenvalues of Eq. (5.11) with respect to the number of plane waves used for the Fourier transformation. Illustrated using the example of cubic silicon (eight atoms per unit cell).

elsewhere.[132]

In Eq. (5.7), we separated the nonlocal exchange potential into the bare Coulomb potential V_x^{NL} and the LR component $V_x^{NL,LR}$. The first term is identical to Eq. (4.26) in the calculation of the PBE0 functional and evaluated efficiently employing the MPB. For the latter term, we utilize the quick convergence of the LR potential in reciprocal space

$$V_{x,nn'}^{NL,LR}(k) = \sum_m^{occ} \sum_q^{BZ} \sum_G \left\langle \phi_{nk}^\sigma \middle| \phi_{mk-q}^\sigma \zeta_{q+G} \right\rangle$$

$$\times \left\langle \zeta_{q+G} \middle| v^{LR} \middle| \zeta_{q+G} \right\rangle \left\langle \zeta_{q+G} \phi_{mk-q}^\sigma \middle| \phi_{n'k}^\sigma \right\rangle, \quad (5.11)$$

where $\zeta_{q+G}(r) = e^{i(q+G)\cdot r}/\sqrt{\Omega}$ is a plane wave normalized to the volume Ω of the unit cell. We employed additionally, the diagonality of the potential in the basis of plane waves

$$\left\langle \zeta_{q+G} \middle| v^{LR} \middle| \zeta_{q+G'} \right\rangle = \frac{4\pi}{|q + G|^2} e^{-|q+G|^2/4\omega^2} \delta_{G,G'}. \quad (5.12)$$

We show that this potential falls of quickly as a function of $q = |q + G|$ in Fig. 5.2a. Hence, the expression in Eq. (5.11) converges at small numbers of reciprocal lattice

vectors. We illustrate the convergence behavior of the root-mean-square (rms) deviation of the eigenvalues of $V_{x,nn'}^{\mathrm{NL,LR}}(\boldsymbol{k})$ in Fig. 5.2b using the example system of a cubic silicon unit cell (four primitive unit cells). Machine precision is achieved with as few as 40 plane waves which would translate to ten for a primitive unit cell containing two atoms. This behavior is essentially independent of the $\boldsymbol{q}$ point.[29]

To evaluate the Fourier transform of the wavefunction products, we introduce the MPB

$$\left\langle \phi_{nk}^{\sigma} \left| \phi_{mk-q}^{\sigma} \zeta_{q+G} \right\rangle = \sum_I \langle \phi_{nk}^{\sigma} | \phi_{mk-q}^{\sigma} M_{qI} \rangle \langle \tilde{M}_{qI} | \zeta_{q+G} \rangle. \tag{5.13}$$

This is advantageous as the first integrals on the right hand side are evaluated to calculate the bare Coulomb interaction (cf. Eq. (5.5)), hence, there is no computational overhead involved. Furthermore, in the calculation of the latter integrals the IR elements are trivial, as the biorthogonal set to these MPB functions are orthogonal to plane waves. As a consequence, we calculate the latter integrals only within the MT spheres

$$\langle \tilde{M}_{qI}^{\mathrm{MT}} | \zeta_{q+G} \rangle = \frac{1}{\sqrt{\Omega}} \int\limits_{\mathrm{MT}_I} \mathrm{d}^3 r \, R_I(|\boldsymbol{r} - \boldsymbol{r}_I|) Y_I^*(\widehat{\boldsymbol{r} - \boldsymbol{r}_I}) \, \mathrm{e}^{-\mathrm{i}\boldsymbol{q}\cdot\boldsymbol{r}_I} \, \mathrm{e}^{\mathrm{i}(\boldsymbol{q}+\boldsymbol{G})\cdot\boldsymbol{r}}$$

$$= \frac{4\pi \mathrm{i}^l}{\sqrt{\Omega}} Y_I^*(\widehat{\boldsymbol{q}+\boldsymbol{G}}) \, \mathrm{e}^{\mathrm{i}\boldsymbol{G}\cdot\boldsymbol{r}_I} \int\limits_0^{R_I^{\mathrm{MT}}} \mathrm{d}r \, r^2 R_I(r) \, \mathrm{j}_l(|\boldsymbol{q}+\boldsymbol{G}|), \tag{5.14}$$

where l is the angular moment of the MPB function with index I.

We note that Eq. (5.12) is divergent in the limit $\boldsymbol{q} + \boldsymbol{G} \to \boldsymbol{0}$.[29] Hence, we treat the $\boldsymbol{G} = \boldsymbol{0}$ part at the Γ point differently from the other reciprocal lattice vectors. The bare Coulomb potential contains an analogous divergent behavior,[33,125] which has to be treated separately as well (cf. Sec. 4.1). We can combine these two terms and, as it turns out, the result has a finite limit

$$\lim_{\boldsymbol{q}+\boldsymbol{G}\to\boldsymbol{0}} \frac{4\pi}{|\boldsymbol{q}+\boldsymbol{G}|^2} \left(1 - \mathrm{e}^{-|\boldsymbol{q}+\boldsymbol{G}|^2/4\omega^2} \right) = \frac{\pi}{\omega^2}. \tag{5.15}$$

We show a flowchart of a HSE calculation in `Fleur`[126] in Fig. 5.3. This figure is analogous to the earlier flowchart for the PBE0 calculation (cf. Fig. 4.1), where the red boxes indicate the changes. After the calculation of the nonlocal potential, we subtract the contribution of the LR potential according to Eq. (5.11). The divergence is not treated specifically anymore, as the divergent behavior of SR and LR contribution cancel each other (cf. Eq. (5.15)). For the core electrons, we replace the bare Coulomb exchange with the screened one. We correct the local potential employing the screened exchange hole (Eq. (5.10)) to calculate the enhancement factor and the corresponding local potential via the functional derivative of the energy (Eq. (5.8)).
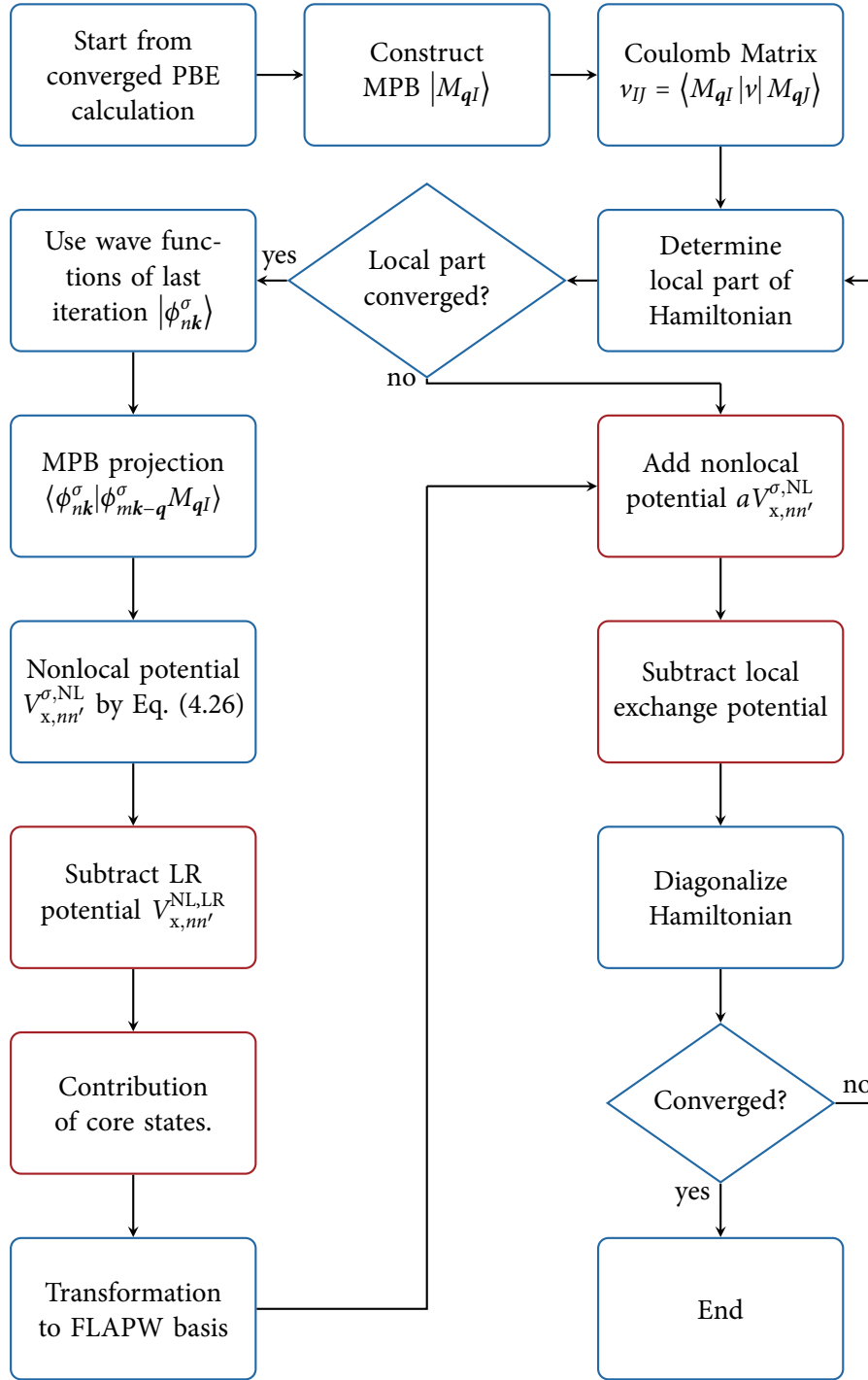
Figure 5.3: Flowchart of an HSE calculation within `Fleur`. The red boxes indicate changes with respect to a PBE0 calculation (cf. Fig. 4.1).

5.3   Total energy in hybrid functionals

In the evaluation of the total energy in hybrid functional calculations, we have to account for two contributions. Straightword is that a hybrid functional[20,24,26] modifies the exchange-correlation energy of the PBE functional E_x^{PBE} by addition of a nonlocal contribution E_x^{NL} and removal of a local part E_x^{L} (see Sec. 4.1)

$$E_{xc}^{hyb} = E_{xc}^{PBE} + a \left(E_x^{NL} - E_x^{L} \right). \tag{5.16}$$

For the PBE0 functional the nonlocal term E_x^{NL} is evaluated with the bare Coulomb potential and the local energy E_x^{L} is given by the PBE functional. In the HSE functional, the screened Coulomb potential as defined in Eq. (5.2) determines the nonlocal contribution E_x^{NL} and the local energy E_x^{L} is calculated according to Eq. (5.8) with the screened exchange hole (cf. Eq. (5.10)).[26,89]

   A second modification in the calculation of the total energy in hybrid functionals arises in the evaluation of the kinetic energy T. To improve the numerical stability of the implementation, it is not evaluated directly, because for the accurate calculation of the Laplace operator $\triangle$ the wave functions have to be smooth up to the second derivative. Instead, we evaluate the kinetic energy as difference of the sum of the eigenvalues and the expectation value of the potential (cf. Sec. 3.1)

$$T = \sum_{\sigma} \sum_{n\mathbf{k}} \left[\varepsilon_{n\mathbf{k}}^{\sigma} - \left\langle \phi_{n\mathbf{k}}^{\sigma} \left| \left(V_{\text{eff.}} - a V_x^{L} \right) \right| \phi_{n\mathbf{k}}^{\sigma} \right\rangle + a \sum_{m\mathbf{q}} \left\langle \phi_{n\mathbf{k}}^{\sigma} \phi_{m\mathbf{q}}^{\sigma} \left| v^{NL} \right| \phi_{m\mathbf{q}}^{\sigma} \phi_{n\mathbf{k}}^{\sigma} \right\rangle \right]. \tag{5.17}$$

We note that in this expression, the core states require a special treatment. In local exchange correlation functionals, the core wave functions are the solution of a radial Dirac equation (see Sec. 3.2). Hence, a necessary requirement for the construction of the core states is the availability of a local potential in the MT spheres. However, in hybrid functionals the key ingredient is the nonlocal HF exchange, so that such a local potential is not available and we cannot calculate the core wave functions. Thus, we treat the core states in the *frozen core approximation*, i.e., we fix the core wave functions to the result of a converged PBE calculation. As a consequence, the core states are no eigenfunctions of the hybrid functional Hamiltonian. Nevertheless, we incorporate the nonlocal exchange in the calculation of the total energy for all states, so that we get a consistent energy for the hybrid functional. On that account, we have to modify the calculation of the kinetic energy by limiting the contribution of the hybrid functional to valence states

$$T = \sum_{\sigma} \sum_{n\mathbf{k}} \left[\varepsilon_{n\mathbf{k}}^{\sigma} - \left\langle \phi_{n\mathbf{k}}^{\sigma} \left| \left(V_{\text{eff.}} - a_n V_x^{L} \right) \right| \phi_{n\mathbf{k}}^{\sigma} \right\rangle + a_n \sum_{m\mathbf{q}} \left\langle \phi_{n\mathbf{k}}^{\sigma} \phi_{m\mathbf{q}}^{\sigma} \left| v^{NL} \right| \phi_{m\mathbf{q}}^{\sigma} \phi_{n\mathbf{k}}^{\sigma} \right\rangle \right], \tag{5.18}$$

where

$$a_n = \begin{cases} a = {}^1\!/_4 & \text{for valence states and} \\ 0 & \text{for core states.} \end{cases}$$

(5.19)

5.4 Parallelization scheme

The evaluation of the nonlocal potential (Eq. (5.5)) is by far the most expensive part of the calculation. It consumes usually more than 90 percent of the computation time. Hence, calculations using hybrid functionals are typically one to two orders of magnitude more expensive than density functional theory (DFT) calculations employing local functionals. We easily identify the relevant part of the code, which we accelerate by parallelization. Nevertheless, the parallelization of hybrid functionals is not as straightforward as for local functionals. We note that Eq. (5.5) contains two separate loops over the k and q points within the Brillouin zone (BZ). To reduce the computational effort, we applied the spatial and time-reversal symmetries to restrict these summations to the irreducible BZ. However, there are less allowed symmetry operations in the inner loop, because the selection of one specific k point in the outer loop, distinguishes certain directions in the crystal. Consider for example a simple cubic unit cell, where the k vectors $k\widehat{x}$, $k\widehat{y}$, and $k\widehat{z}$ are equivalent by symmetry. However, if we have specified $k = k\widehat{x}$ in the outer k point summation, the q vector $q\widehat{x}$ is not equivalent to $k\widehat{y}$ and $k\widehat{z}$. For this reason the number of terms, which have to be evaluated, are different for all q points in the outer loop, and a simple parallelization over this loop is not possible.

k_1	k_2	k_3	k_4	k_5	k_6	k_7	k_8
CPU I		CPU II		CPU III	CPU IV	CPU V	CPU VI

Figure 5.4: Example of task distribution over six processes (CPU I–VI) of eight irreducible k points (k_i) which correspond to a Γ centered $4 \times 4 \times 4$ k-point mesh within a cubic unit cell. The number of q points within the inner loop in Eq. (5.5) is not the same for all k points. Hence, if the evaluation of the nonlocal potential takes longer at a certain k point it will be shared by several processes. This illustrates the complications in the communication pattern if synchronous communication is used as, for instance, process II will finish its share of k point 2 before process I arrives at the communication point.
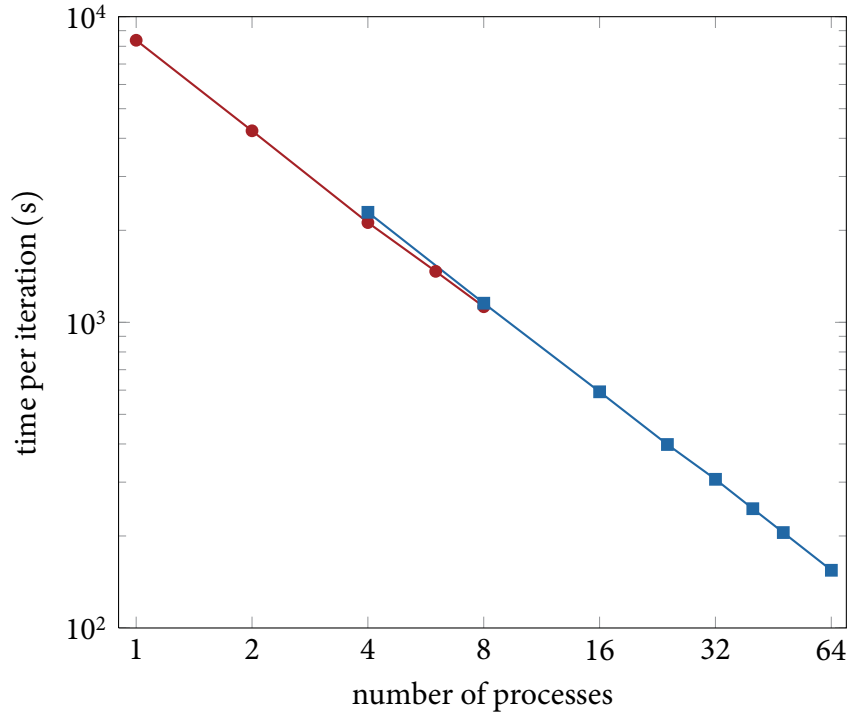
Figure 5.5: Improvement in execution time per nonlocal iteration by parallelization. We calculate bulk silicon with a $12 \times 12 \times 12$ **k**-point mesh increasing the number of processes on the local cluster (red) and on JuRoPA (blue). The code is slightly slower on JuRoPA and scales well with the number of processes. For comparison an ideal scaling (gray) is shown extrapolating from the time consumed by a single process calculation.

We circumvent this problem by sharing an equal amount of tasks to all processes. The total number N_t of tasks is

$$N_t = \sum_{k}^{\mathrm{BZ}} N_q(k), \tag{5.20}$$

where $N_q(k)$ is the symmetry-reduced number of **q** points necessary at a specific **k** point. If the number of tasks is no integral multiple of the number of processes, we assign one additional task to some processes to compensate for this. The consequence of this algorithm is an unequal amount of processes for the **k** points in the outer loop. The complications of this ansatz are illustrated in Fig. 5.4. Several processes have to evaluate only a small part of a specific **k** point. These processes would

have to wait for other ones which calculate a larger share. Hence, we arrange an asynchronous communication pattern. As the process with the smallest rank will be the last to complete the calculation of a specific k, we collect all necessary data on this process.

In addition to the nonlocal potential further computations are necessary at every k point. As pointed out in Fig. 5.3, this includes the core contribution, the transformation to the FLAPW basis, the subtraction of the local potential and the diagonalization of the Hamiltonian. In the current realization all these steps are done by only one process per k point. To reduce the communication overhead, we select the process with the smallest rank which received already all necessary information.

Figure 5.5 shows the time needed for a single iteration in which the nonlocal exchange potential is updated as function of the number of processes used for the calculation. We converged bulk silicon with the HSE hybrid functional on a $12 \times 12 \times 12$ k-point mesh which translate to 72 points in the irreducible BZ. The computation on the local cluster is slightly faster than on the JuRoPA supercomputer.[c] We find a great improvement in the execution speed up to 64 processes, which is close to the optimal behavior. In principle, in the theoretical limit of our parallelization method, the calculation of the nonlocal potential can be shared by more than 60000 processes. A reasonable practical constraint will be significantly lower. However, it turns out we cannot reach this limit as `Fleur`[126] is not suitable to treat more than one process per k point without the use of eigenvector parallelization, which is currently not integrated into our parallelization scheme.

5.5   Analysis of prototypical materials

We compare our results for the prototypical semiconductors (C in diamond structure, Si, and GaAs) and insulators (MgO, NaCl, and Ar) with previous works using plane wave[27] or Gaussian[131] basis sets in order to establish the correctness of our method and its implementation. In particular, we investigate the lattice constant, bulk moduli, and band transitions of these materials. The band transitions were calculated at the experimental lattice constant, which we took from Heyd and Scuseria.[136] We employ the common approximation of using the differences of Kohn-Sham eigenvalues at the respective k points to calculate the band-gap energies.

For all materials an $8 \times 8 \times 8$ k point mesh is sufficient to give an accurate description of the band transitions. In Fig. 5.6, we illustrate, as an example, the convergence

---

[c]Jülich Research on Petaflop Architectures: 2208 compute nodes with two Intel Xeon X5570 (Nehalem-EP) quad-core processors each.
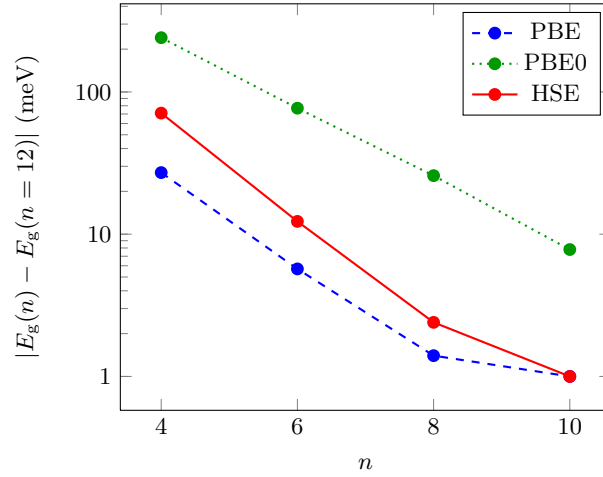
Figure 5.6: Convergence of the indirect $\Gamma \rightarrow X$ transition E_x in silicon with respect to the size of the *k*-point mesh *n*×*n*×*n*. The bare Coulomb potential in the PBE0 functional (green, dotted) requires a finer sampling to accurately describe the divergence near the Γ point. The screening of the Coulomb potential in HSE (red, solid) overcomes this problem, so that the overall convergence is similar to the PBE functional (blue, dashed).

of the indirect $\Gamma \rightarrow X$ transition in bulk silicon. HSE has a similar *k*-point convergence as the local PBE functional, whereas a significantly larger *k*-point mesh is necessary for the PBE0 functional. This behavior was also observed with other reciprocal space methods.[27] We attribute this to the nondivergent representation of the screened exchange potential (cf. Eq. (5.15)).[29] In methods employing a basis in the reciprocal space the favorable *k*-point convergence of the HSE functional leads to a shorter computation time with respect to PBE0.

In Table 5.1, we compare our results for the $\Gamma \rightarrow \Gamma$, $\Gamma \rightarrow X$, and $\Gamma \rightarrow L$ band transitions with experimental data and the implementation within the projector augmented wave (PAW) method.[27] We note a significant increase of the band-transition energies within the HSE functional. Local functionals systematically underestimate the band gap. Hence, as compared to PBE, the opening of the band gap within the HSE functional yields an improved agreement with experimental results. Especially the narrow gap semiconductors are accurately described with the HSE functional, whereas the larger band gaps are still underestimated. The values of the band transitions show only slight differences between the different applied methods. The deviations are somewhat larger in HSE than in PBE, though of the same order of magnitude.

Table 5.1: Kohn-Sham transition energies in eV obtained with the functionals PBE and HSE at experimental lattice constants compared with values from PAW calculations and experiment. An 8×8×8 k-point mesh was employed in our calculations.[a]

Functional		This work PBE	HSE	PAW[b] PBE	HSE	Expt.
GaAs	$\Gamma \to \Gamma$	0.54	1.43	0.56	1.45	1.52,[c] 1.63[d]
	$\Gamma \to X$	1.47	2.06	1.46	2.02	1.90,[c] 2.01,[d] 2.18[d]
	$\Gamma \to L$	1.01	1.78	1.02	1.76	1.74,[c] 1.84,[d] 1.85[d]
Si	$\Gamma \to \Gamma$	2.56	3.32	2.57	3.32	3.05,[e] 3.34–3.36[f], 3.4[d]
	$\Gamma \to X$	0.71	1.29	0.71	1.29	1.13,[f] 1.25[e]
	$\Gamma \to L$	1.54	2.24	1.54	2.24	2.06,[g] 2.40[d]
C	$\Gamma \to \Gamma$	5.60	6.98	5.59	6.97	7.3[c]
	$\Gamma \to X$	4.75	5.90	4.76	5.91	—
	$\Gamma \to L$	8.46	10.02	8.46	10.02	—
MgO	$\Gamma \to \Gamma$	4.77	6.49	4.75	6.50	7.7[h]
	$\Gamma \to X$	9.14	10.86	9.15	10.92	—
	$\Gamma \to L$	7.93	9.69	7.91	9.64	—
NaCl	$\Gamma \to \Gamma$	5.20	6.57	5.20	6.55	8.5[i]
	$\Gamma \to X$	7.58	9.05	7.60	8.95	—
	$\Gamma \to L$	7.30	8.66	7.32	8.67	—
Ar	$\Gamma \to \Gamma$	8.70	10.36	8.68	10.34	14.2[j]

[a] Reference 29.   [b] Reference 27.   [c] Reference 137.   [d] Reference 138.   [e] Reference 139.
[f] Reference 140. [g] Reference 141. [h] Reference 142. [i] Reference 143. [j] Reference 144.

In Table 5.2 and Table 5.3, we present the equilibrium lattice constant and the bulk modulus, respectively. We employ a fit to the Murnaghan equation[145] to evaluate these properties. We compare the results obtained with our implementation of the HSE functional[29] with experimental data and implementations using plane-wave (PAW)[27] and Gaussian basis sets.[131] We find a fine agreement between the three different methods. The deviations in the equilibrium lattice constant are smaller than 5 pm. The HSE functional improves the lattice constant and the bulk modulus for all materials but diamond with respect to the semilocal PBE functional.

Table 5.2: Optimized lattice constants in Å obtained with the PBE and the HSE functional.[a] In our work, an 8×8×8 k-point mesh was employed. Results are compared to experimental results and calculations using the HSE functional within a PAW[b] and a Gaussian[c] method.

Functional	This work		PAW[b]	Gaussian[c]	Expt.[d]
	PBE	HSE	HSE	HSE	—
GaAs	5.743	5.660	5.687	5.710	5.648
Si	5.472	5.441	5.435	5.451	5.430
C	3.571	3.549	3.549	3.557	3.567
MgO	4.265	4.217	4.210	4.222	4.207
NaCl	5.703	5.627	5.659	5.645	5.595

[a] Reference 29. [b] Reference 27. [c] Reference 131.
[d] Experimental data taken from Ref. 136.

Table 5.3: Bulk moduli in GPa obtained with the PBE and the HSE functional.[a] An 8×8×8 k-point mesh was employed in our calculations. Results are compared to experimental results and calculations using the HSE functional within a PAW method.[b]

Functional	This work		PAW[b]	Expt.[c]
	PBE	HSE	HSE	—
GaAs	64.5	79.2	70.9	75.6
Si	88.9	98.0	97.7	99.2
C	433	467	467	443
MgO	153	177	169	165
NaCl	21.3	28.8	24.5	26.6

[a] Reference 29. [b] Reference 27.
[c] Experimental data taken from Ref. 136.

Approximations to Hybrid Functionals

6.1   Computational effort

In recent years, hybrid functionals has been the subject of continuous scientific interest (cf. Fig. 6.1). In the 1990's, Becke[20] established the theoretical foundations, which motivate the intermixing of a certain fraction of nonlocal Hartree-Fock (HF) exchange with a local exchange correlation functional. With the advent of more powerful computers, hybrid functional calculations became feasible in periodic systems. They were successfully employed to describe the properties of molecules[127] and solids[128] Furthermore, they overcome[128–130] the band gap problem[122,123] of density functional theory (DFT). These successes animated the field, which is evidenced by the drastic increase of the number of publications since the early 2000's (see Fig. 6.1). By now, hybrid functionals are routinely applied to systems with correlated electrons using Gaussian,[127] plane wave[146], or full-potential linearized augmented-plane-wave (FLAPW)[33] basis sets. For details of the implementation in the FLAPW method, we refer to Chap. 3.

The evaluation of the nonlocal exchange potential is so expensive, that the use of these functionals is effectively restricted to a small number of atoms in the unit cell, despite of the increase of the computational power during the last decade. Several schemes to reduce the numerical demand have been described in the literature. A restriction of the Coulomb interaction to a certain range leads to screened exchange interaction and finally to an effectively screened potential as proposed by Heyd *et al.*.[26] Physically this corresponds to correlation effects within the electronic system, which screen the electron-electron interaction at large distances. The authors evaluated the necessary integrals in real space,[26] where they benefited from the finite length scale
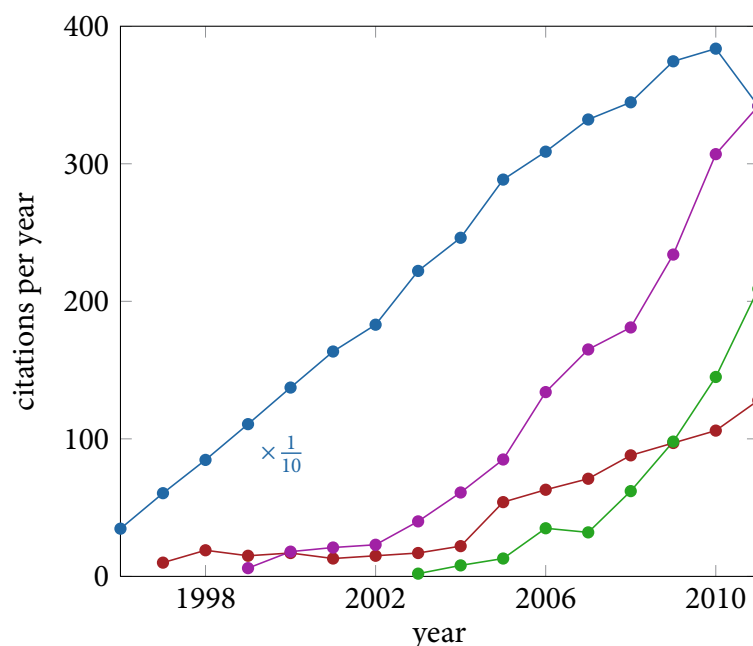
Figure 6.1: Citation analysis using *SciVerse Scopus* for four representative publications dealing with hybrid functionals. The citations of the seminal paper by Becke[23] (—•—) is scaled to 10% to fit on the same axis. The citations for the newer hybrid functionals—the PBE0 functional[24] (—•—), its implementation[127] in Gaussian (—•—), and the screened HSE[26] hybrid functional (—•—)—have increased strongly in the last five years.

of the interaction. Since then it has been shown[27,29] that the screening is beneficial for reciprocal-space methods as well, as, in comparison to the PBE0 functional, a smaller k-point sampling of the Brillouin zone (BZ) is sufficient. We have presented the implementation of the screened exchange in the FLAPW basis in Chap. 5.

An approach particularly suited for reciprocal-space methods was realized by Paier *et al.*.[27] The dispersion of the total energy mainly arises from the kinetic and the Hartree energy, whereas the exchange energy, which is by comparison small, has a smaller dispersion across the BZ. Within a basis set (in reciprocal space) the nonlocal exchange is given by two k-point summations over the BZ

$$E_{\mathrm{x}}^{\mathrm{HF}} = -\frac{1}{2} \sum_{n,m}^{\mathrm{occ.}} \sum_{k,q}^{\mathrm{BZ}} \left\langle \phi_{nk}\phi_{mq} \left| V^{\mathrm{NL}} \right| \phi_{mq}\phi_{nk} \right\rangle, \tag{6.1}$$

where ϕ_{nk} and ϕ_{mq} are Kohn-Sham wave functions with band indices n and m, re-

spectively. In this chapter, we suppress the spin indices, but a generalization to magnetic systems is straightforward. V^{NL} is the nonlocal interaction – the bare Coulomb interaction for the PBE0 functional[24] and the screened Coulomb interaction for the HSE functional.[26] Analogously, we find a second k-point summation in the calculation of the nonlocal exchange potential (cf. Eq. (4.26)). Paier *et al.*[27] proposed to restrict the inner q-point loop to a smaller mesh of points in the BZ and refer to this technique as *downsampling* of the nonlocal exchange. They demonstrate that in particular for the screened HSE[26] hybrid functional even an up to four times sparser q mesh yields accurate results. The same technique is not efficiently applicable to the PBE0[24] functional, where the accurate evaluation of the bare Coulomb potential requires a fine k-point sampling.

The most commonly used technique to treat correlated materials in DFT is the LDA+U method.[94] In this scheme an on-site Hubbard-like[97] term is included for the localized states (see reference 94 for more details). Although the Hubbard parameter U can be extracted from first principles methods by a constrained LDA[98,147] or a constrained random phase approximation (RPA)[100,148,149] calculation, one often chooses an appropriate U according to experimental observations. Rohrbach *et al.*[150] showed for the transition metal sulfides that a unique optimal value of U does not exist. Novák *et al.*[151] proposed an exchange functional that shares properties of the LDA+U method and the HF exchange. They approximate the nonlocal HF exchange of the correlated electrons by their on-site contributions

$$E_x^{HF} \approx -\frac{1}{2} \sum_{i,j,k,l} n_{i,l} n_{j,k} \left\langle \varphi_i \varphi_j \left| V^{NL} \right| \varphi_k \varphi_l \right\rangle, \tag{6.2}$$

where in contrast to Eq. (6.1) the bare Coulomb potential is restricted to two points in the same atomic sphere, the φ_i are localized auxiliary orbitals centered at a specific atom, and the $n_{i,l}$ is the density-matrix element of the localized orbitals i and l

$$n_{i,l} = \sum_m^{occ.} \sum_k^{BZ} \left\langle \phi_{mk} \middle| \varphi_i \right\rangle \left\langle \varphi_l \middle| \phi_{mk} \right\rangle. \tag{6.3}$$

As a double-counting correction E_{dc}, the exchange-correlation contribution of the correlated electrons is removed from the local density approximation (LDA) exchange-correlation energy. The total exchange-correlation energy has then the following form

$$E_{xc}^{on\text{-}site} = E_{xc}^{LDA} + E_x^{HF,on\text{-}site} - E_{xc}^{LDA}[n_{corr.}] \tag{6.4}$$

with the density of the correlated states

$$n_{corr.}(\boldsymbol{r}) = \sum_{i,l} n_{i,l} \varphi_i^*(\boldsymbol{r}) \varphi_l(\boldsymbol{r}). \tag{6.5}$$

Tran *et al.*[28] generalized this idea to the hybrid functionals replacing the terms in Eq. (6.4) with the corresponding ones of the hybrid functional. For instance, the approximated on-site PBE0 functional is calculated as

$$E_{\text{xc}}^{\text{PBE0,on-site}} = E_{\text{xc}}^{\text{PBE}} + a\left(E_{\text{x}}^{\text{HF,on-site}} - E_{\text{x}}^{\text{PBE}}[n_{\text{corr.}}]\right), \tag{6.6}$$

where the double-counting term is given as the exchange contribution of the correlated electrons in the PBE functional and the mixing parameter $a = 1/4$ is employed as in the full PBE0 functional.[24] Although a formal similarity with the nonlocal functionals exists, the on-site approximation to these functionals can produce drastically different results. For example, while the PBE0 functional predicts[152] a lattice constant of 4.40 Å and the fundamental band gap of 4.02 eV, the on-site approximation to the PBE0 functional yields[28] a significantly larger lattice constant of 4.51 Å and a drastically smaller band gap of 1.3 eV.

In spite of the fact that hybrid functionals have been investigated for almost 20 years, a detailed analysis of the importance of different contributions has not been done so far. In this chapter, we present a study based on the FLAPW method particularly suited for such an approach. The separation of the crystal into muffin-tin (MT) spheres centered at the atoms and the interstitial region (IR) in between leads directly to an evaluation of on-site, off-site, and interstitial contributions. In Sec. 6.2, we introduce different levels of approximations, where we successively replace nonlocal exchange terms by their local counterpart. We compare the effect of these approximations for two prototypical ionic materials (MnO and NiO) and covalent-bound materials (Si and GaAs) in Sec. 6.3. We draw our conclusions of this comparison in Sec. 6.5.

6.2   Discussion of different approximations

In Chap. 4, we introduced the evaluation of the nonlocal exchange potential $V_{\text{x},nn'}^{\text{NL}}(\boldsymbol{k})$ by the resolution of the identity with the *mixed product basis* (MPB)

$$V_{\text{x},nn'}^{\text{NL}}(\boldsymbol{k}) = -\sum_{m}^{\text{occ.}}\sum_{\boldsymbol{q}}^{\text{BZ}}\sum_{IJ}\left\langle \phi_{n\boldsymbol{k}}\middle|\phi_{m\boldsymbol{k}-\boldsymbol{q}}M_{\boldsymbol{q}I}\right\rangle v_{IJ}(\boldsymbol{q})\left\langle M_{\boldsymbol{q}J}\phi_{m\boldsymbol{k}-\boldsymbol{q}}\middle|\phi_{n'\boldsymbol{k}}\right\rangle, \tag{6.7}$$

where $v_{IJ}(\boldsymbol{q})$ is the Coulomb matrix

$$v_{IJ}(\boldsymbol{q}) = \left\langle M_{\boldsymbol{q}I}\middle|V_{\text{Coul}}\middle|M_{\boldsymbol{q}J}\right\rangle, \tag{6.8}$$

the $\phi_{n\boldsymbol{k}}$ are Kohn-Sham wave functions, the $M_{\boldsymbol{q}I}$ are MPB functions, n, n', and m are band indices, $\boldsymbol{k}$ and $\boldsymbol{q}$ are Bloch wavevectors, and

$$V_{\text{Coul}}(\boldsymbol{r}, \boldsymbol{r}') = \frac{1}{|\boldsymbol{r} - \boldsymbol{r}'|} \tag{6.9}$$

is the bare Coulomb potential. The nonlocal exchange energy is given by the sum of the diagonal elements and over the whole BZ

$$E_x^{\mathrm{NL}} = -\frac{1}{2} \sum_n^{\mathrm{occ.}} \sum_k^{\mathrm{BZ}} V_{x,nn}^{\mathrm{NL}}(\boldsymbol{k}).$$ (6.10)

In the PBE0 hybrid functional,[24] a fraction of $a = 1/4$ of the nonlocal exchange energy is added to the local PBE exchange-correlation functional.[14] To correct for double counting correction the same fraction a of semi-local PBE exchange[14] is removed (cf. Sec. 4.1).

$$E_{xc}^{\mathrm{PBE0}} = E_{xc}^{\mathrm{PBE}} + a\left(E_x^{\mathrm{NL}} - E_x^{\mathrm{PBE}}\right).$$ (6.11)

Within the FLAPW method,[31,32,117] we employ basis functions of atomic functions in the MT spheres which are matched to plane waves in the IR (see Chap. 3), so that the resulting basis function is differentiable at the MT boundary. The MPB is constructed to represent products of FLAPW basis functions[33,125,153] and consists of basis functions defined within the MT spheres and the IR. The strict separation of atomic centered parts and interstitial contributions allows us to investigate the importance of different terms in detail. The nonlocal energy is separated into four terms

$$E_x^{\mathrm{NL}} = E_{x,\mathrm{MT\text{-}MT}}^{\mathrm{NL}} + E_{x,\mathrm{MT\text{-}IR}}^{\mathrm{NL}} + E_{x,\mathrm{IR\text{-}IR}}^{\mathrm{NL}} + E_{x,\Gamma}^{\mathrm{NL}} :$$ (6.12)

The MT-MT term considers only the MT spheres and can be further separated into on-site and off-site contributions. The MT-IR term describes the interaction between the spheres and the IR. The IR-IR term is limited to IR basis functions. Finally, the Γ-point correction incorporates the analytical treatment of the divergence of the Coulomb potential in reciprocal space (cf. Chap. 4). The local exchange energy consists of MT and IR contribution

$$E_x^{\mathrm{PBE}} = E_{x,\mathrm{MT}}^{\mathrm{PBE}} + E_{x,\mathrm{IR}}^{\mathrm{PBE}}.$$ (6.13)

In the following, we will introduce several tiers, in which the energy difference of the PBE and PBE0 functional

$$\Delta E_x = E_{xc}^{\mathrm{PBE0}} - E_{xc}^{\mathrm{PBE}} = a\left(E_x^{\mathrm{NL}} - E_x^{\mathrm{PBE}}\right)$$ (6.14)

is replaced by approximations that are successively easier to evaluate. We estimate the computational cost of the different approximations comparing to them to conventional hybrid functional calculations. In these, almost the entire computation time is spent for the evaluation of the nonlocal exchange term. In our implementation, the evaluation of the overlap between the wave functions and the MPB accounts
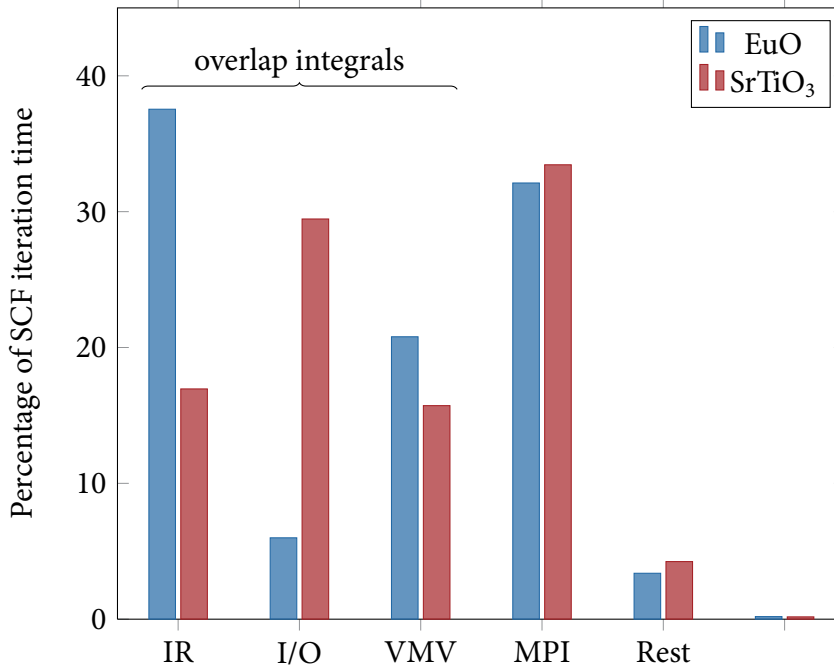
Figure 6.2: Computation-time distribution of several tasks in examplary EuO and SrTiO$_3$ hybrid-functional calculations. Roughly two thirds of the time are consumed by the calculation of the overlap integrals in the muffin-tin (MT) spheres, in the interstitial region (IR) and reading the wavefunctions from the harddisk. The vector-matrix-vector (VMV) multiplication accounts for another third of the time. The load imbalance in the MPI parallelization is responsible for a large part of the remainder. The rest of the time is spent for the common DFT calculation.

for roughly more expensive than the IR region overlap integrals. The sparse-matrix-vector multiplication accounts for another third. Everything else is considerably below 5% of the total time.

1 As a first approximation, we remove the IR-IR contribution of the nonlocal term and simultaneously the IR term in the local contribution. The exchange energy correction to the PBE functional is then given as

$$\Delta E_x^I = a \left(E_{x,\text{MT-MT}}^{\text{NL}} + E_{x,\text{MT-IR}}^{\text{NL}} + E_{x,\Gamma}^{\text{NL}} - E_{x,\text{MT}}^{\text{PBE}} \right). \qquad (6.15)$$

The physical motivation for this approximation is the small amount of the electric density that resides in the IR. Hence, we assume that the energy and eigenvalues

of the PBE0 functional will be accurately reproduced. The computational advantage of this approach amounts to approximately 15% of the total time, because we halve the time necessary to evaluate the sparse-matrix-vector multiplication by removing the IR-IR part.

2 In the second tier, we remove the IR contribution altogether

$$\Delta E_{\text{x}}^{\text{II}} = a \left(E_{\text{x,MT-MT}}^{\text{NL}} + E_{\text{x,}\Gamma}^{\text{NL}} - E_{\text{x,MT}}^{\text{PBE}} \right). \tag{6.16}$$

This approximation is more rigorous than the first one, as it removes the nonlocal interaction between the MT spheres and the IR region. If we employ this approximation, we could reduce the cost of the hybrid functional calculations by up to 40%. This results from a speed up in the matrix multiplication, where the neglect of the rectangular MT-IR part is advantageous, and we do not have to calculate the overlap integrals for the IR.

3 Within the third approximation, we restrict the MT contribution to on-site terms

$$\Delta E_{\text{x}}^{\text{III}} = a \left(E_{\text{x,MT-MT}}^{\text{NL,on-site}} - E_{\text{x,MT}}^{\text{PBE}} \right). \tag{6.17}$$

We note that with this restriction, the divergence of the Coulomb potential in reciprocal space disappears so that this energy contribution is not evaluated. While this has no effect in the computation time of the local part, the evaluation of the nonlocal part is drastically accelerated. We estimate that this approximation would reduce the computation time to same order of magnitude as typical LDA+U calculations.

4 Within the fourth tier, we focus only on specific localized orbitals φ_i. Resembling the work of Novák *et al.* [151] and Tran *et al.*,[28] we limit the description to localized d states

$$\Delta E_{\text{x}}^{\text{III}} = a \left(E_{\text{x,MT-MT}}^{\text{NL,on-site,}d} - E_{\text{x,MT}}^{\text{PBE,}d} \right). \tag{6.18}$$

In contrast to their work, we employ the MPB to evaluate the overlap integrals. The construction of the MPB ensures that these overlap integrals contain all d-state contributions in the wave functions. For the local exchange, we evaluate the PBE exchange energy for the density of the d electrons. An efficient implementation of this approximation would be as fast as the LDA+U method. The time difference to the third tier is hard to assess from our implementation of the hybrid functionals, as both methods would be approximately two orders of magnitude faster than the PBE0 functional.

A general problem of all these approximations is that nonlocal and local exchange are not treated on equal footing. In the local potential, the long-range nature of the Coulomb interaction is only included implicitly. In the LDA, the assumption of a homogeneous density allows for an analytical integration of the Coulomb interaction (cf. Eq. (2.37))

$$E_\mathrm{x} = \frac{1}{2} \iint \mathrm{d}^3 r \, \mathrm{d}^3 u \, \frac{n(\boldsymbol{r}) n_\mathrm{x}(\boldsymbol{r}, \boldsymbol{u})}{\boldsymbol{u}}, \qquad (6.19)$$

where n is the electronic density, n_x is the exchange hole, and $\boldsymbol{u} = \boldsymbol{r} - \boldsymbol{r}'$. In contrast, in the hybrid functionals the Coulomb interaction is evaluated explicitly for the HF exchange. If we impose restrictions to the region, where the HF exchange is evaluated, this would translate to a change in the strength of the local potential. However, it is not straightforward to translate the restriction imposed to the nonlocal Coulomb interaction to the local potential, because the analytical solution of the exchange integral in the local part is a direct consequence of the bare Coulomb potential. If a different nonlocal interaction, as introduced in the aforementioned approximations, is combined with an unsuitable local park, this will lead to a double-counting or a neglect of parts of the exchange interaction. To counteract these problems, one could refine the local energy imposing the same restrictions to the integrals in Eq. (6.19) as for the nonlocal part. However, then the six-dimensional integral would have to be calculated numerically, which would increase the computational cost drastically. Here, we limit ourselves to the simple approximations for the local contribution and reveal the resulting mismatch to the pure hybrid functional.

6.3   Application to prototypical materials

In the following, we analyze the two semiconductors Si and GaAs, which possess a diamond and a zincblende structure, respectively, and the two antiferromagnetic oxides MnO and NiO, which crystallize in a rock-salt unit cell. The antiferromagnetism of the latter two compounds is predicted by the Goodenough-Kanamori rules, [154,155] indicating that the magnetic moments in neighboring atoms with filled orbitals have an opposite alignment. This gives rise to a three -dimensional checkerboard- like arrangement of moments, the AFM-II structure. We perform all calculations at the experimental lattice constant and analyze different band transitions, magnetic moments where appropriate, and the orbital-resolved charge within the MT spheres. We calculate all band transition energies as differences of the respective Kohn-Sham eigenvalues. We define the magnetic moment as the difference of the two spin densities within a MT sphere, i.e., we neglect all contributions from the IR.

Table 6.1: We present the data for MnO: The smallest fundamental band gap Δ_{fund}, the smallest direct band gap Δ_{opt}, the magnetic moment per Mn atom m_{Mn}, and the number of d electrons of majority spin character within the MT spheres N_d is compared to theoretical and experimental results from the literature.

	Δ_{fund} (eV)	Δ_{opt} (eV)	m_{Mn} (μ_{B})	N_d
PBE0	3.73	4.37	4.63	4.92
Level I	3.78	4.39	4.62	4.91
Level II	3.01	3.72	4.61	4.92
Level III	1.98	2.66	4.64	4.93
Level IV	1.70	2.16	4.65	4.96
PBE	0.92	1.57	4.43	4.84
HSE	2.98	3.61	4.63	4.92
LDA + U	2.17	2.65	4.70	4.94
PBE + U	2.36	2.80	4.75	4.95
PBE0[a]	4.02		4.52	
HSE03[b]	2.8		4.52	
EXX[c]	3.80	4.21	4.60	
EXXc[c]	3.96	4.37	4.60	
B3LYP[d]	3.92		4.73	
on-site[e]	1.3	1.9	4.40	
LDA + U[e]	1.9	2.5	4.50	
Expt.	3.9[f]	2.0[g]	4.58,[h] 4.79[i]	

[a] Reference 152. [b] Reference 156. [c] Reference 121. [d] Reference 157. [e] Reference 28.
[f] Reference 158. [g] Reference 159. [h] Reference 160. [i] Reference 161.

The numerical convergence parameters are chosen to efficient values focusing more on the general trends in the different approximations and less on the exact values. These might change slightly with an increase of the numerical cutoffs, whereas the qualitative picture is well reproduced. We compare results for the PBE[14] and the PBE0[24] functional as well as for the different approximations introduced in the last section. We contrast these calculations to theoretical results from the literature. For comparison, we report experimental values where available.

Manganese Oxide (MnO)

For MnO, we present our results for the band transition energies, the magnetic moment per Mn atom, and the charge accumulated in d orbitals within the MT sphere

in Table 6.1. Within the PBE0 functional, direct and indirect band gap are drastically increased with respect to the corresponding PBE results. With the PBE0 (PBE) functional, we obtain a value of 3.73 eV (0.92 eV) for the fundamental band gap and a value of 4.37 eV (1.57 eV) for the smallest direct band gap which is accessible by optical experiments. The d electrons become more strongly localized in the PBE0 calculations, which is manifested in the increase of the magnetic moment per Mn atom from 4.43 μ_B to 4.63 μ_B and the charge accumulated in the d orbitals from 4.84 electrons to 4.92 electrons per spin channel. We get a somewhat smaller fundamental band gap than Franchini et $al.$,[152] which is a measure for size of the deviations induced by the reduced values of the numerical convergence parameter. The difference in the magnetic moment is probably related to a different size of the MT sphere. With the B3LYP hybrid functional a similar opening of the band gap is observed.[157] Employing the screened HSE hybrid functional yields an indirect band gap of 2.98 eV and a direct one of 3.61 eV. The same size of the magnetic moment and the same number of d electrons indicate that the charge localization is similar to the one obtained with the PBE0 functional. Employing the older HSE03 implementation, Marsman et $al.$[156] find a smaller band gap of 2.8 eV. The EXX functional,[121] where the nonlocal exchange is converted into an optimized local potential, results in similar band gaps and magnetic moments as our PBE0 results. We compare the hybrid functionals to DFT+U calculations, where the U and J values were determined by constrained RPA.[100] Adding the Hubbard-like term to the LDA calculation (U = 7.52 eV, J = 0.68 eV), we find an increased fundamental band gap of 2.17 eV and optical band gap of 2.65 eV. The charge is localized more strongly than in the hybrid functionals resulting in a higher magnetic moment. Starting from the PBE functional (U = 8.01 eV, J = 0.69 eV), the values increase to 2.36 eV and 2.80 eV for indirect and direct band gap, respectively, which is still somewhat smaller than the transitions predicted with hybrid functionals. The experimental results are inconsistent, because the optical band gap[159] of 2.0 eV is significantly smaller than the fundamental band gap[158] of 3.9 eV. The latter is best reproduced by the PBE0 functional, the former is closer to the PBE results.

Approximating the PBE0 functional with the expressions introduced in Sec. 6.2, we find that the first level reproduces the band transitions, the magnetic moment, and the number of electrons in the d states accurately. Though the second tier features a similar charge within the MT spheres, the band transitions are significantly reduces by ∼ 0.7 eV. For MnO the band transitions within the second approximation are surprisingly close to the results with the HSE functional. If we reduce the nonlocal exchange to on-site contributions (Level III), the band gap is further reduced to 1.98 eV and 2.66 eV for the fundamental and optical transition, respectively. However, this does not go along with a reduction of the charge at the atomic sites, which
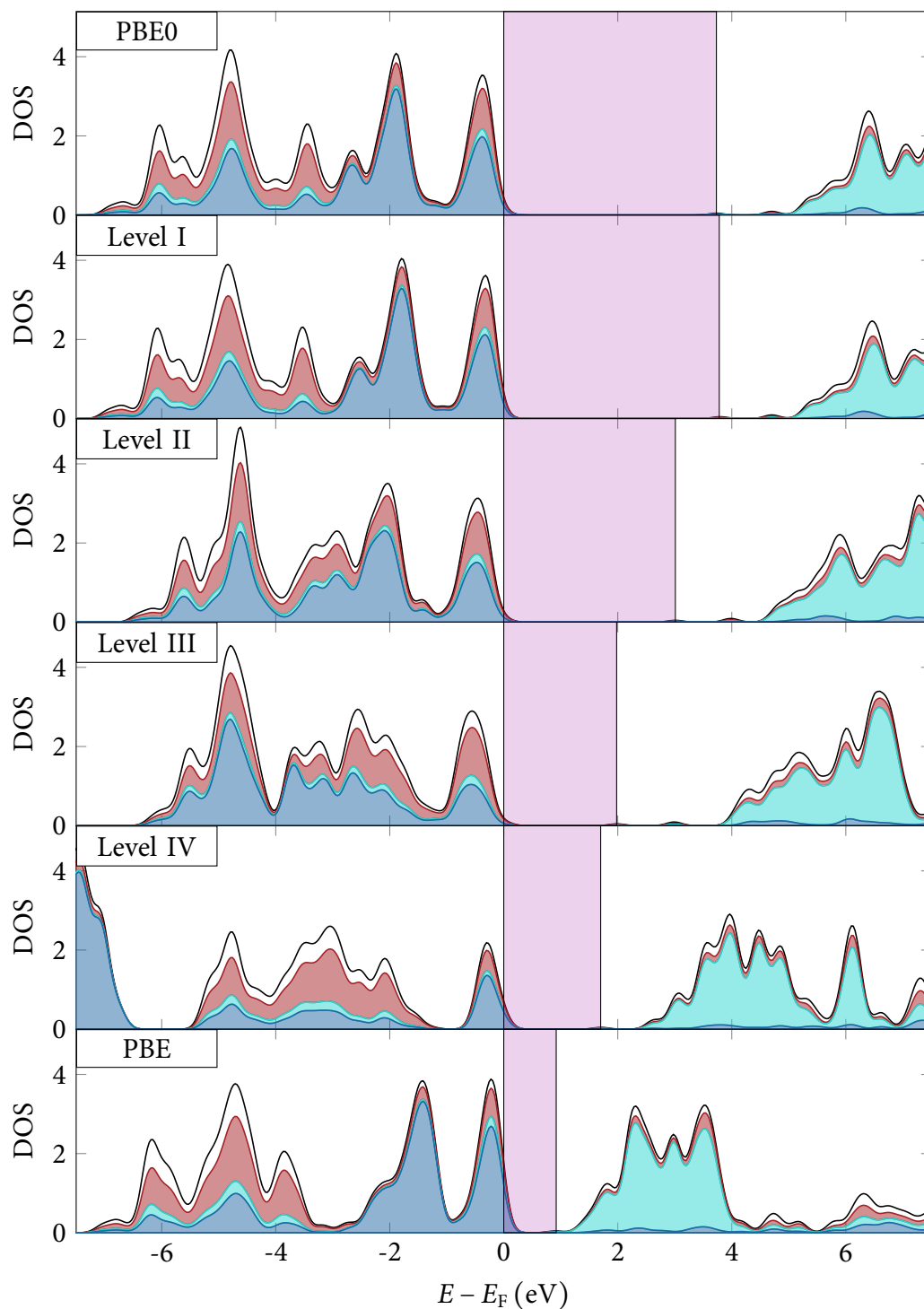
Figure 6.3: Comparison of l-projected density of states (DOS) for the spin-up channel in MnO using different approximations to the PBE0 functional. The blue contribution originates from the majority d orbitals of the Mn atom, the cyan contribution originates from the ones with the opposite spin direction. The red fraction is associated with the p orbitals of oxygen and the remainder to the total DOS consists mainly of charge in the interstitial region. The transparent purple area shows the region where no electronic states exist. The tails in the gap result from the Gaussian broadening.

is (albeit slightly) increased. As fourth tier, we limit the nonlocal exchange to the d states. The transitions shrink further to 1.70 eV (2.16 eV) for the fundamental (optical) band gap. The d electrons tend towards stronger localization. In comparison to the related DFT+U scheme, we observe band transitions that are similar or a bit smaller depending on the particular choice of the local functional and the values for the parameters U and J. The method of Tran *et al.*,[28] which employs a different kind of on-site projection functions but is otherwise identical to our fourth level, yields the smallest band transitions of all investigated techniques which go beyond the LDA and generalized gradient approximation (GGA) functionals.

Figure 6.3 visualizes the effect of the different approximations comparing the electronic density of states (DOS) of one spin channel. The area where no states appear becomes smaller the further we approximate the hybrid functional. Only the first level reproduces the band gap accurately. The DOS reveals that not only the sizes of the band transitions are modified. Starting from the second level of approximation the physics of the occupied states changes. The bandwidth of the p-d-hybridized states becomes narrower and the peaks more pronounced. In the fourth approximation the hybridization is almost lifted, and we identify separate O p and Mn d peaks. The hybridization disappears within the PBE functional as well, although the order of the peaks is different than in the fourth tier.

Nickel Oxide (NiO)

In Table 6.2, we compare the band transitions, number of occupied d states, and the magnetic moment of NiO obtained with the different approximations to the PBE0 functional with results from the literature. The bare PBE0 functional increases the direct and indirect band gap with respect to the PBE functional from 1.13 eV and 0.97 eV to 5.94 eV and 5.34 eV, respectively. This goes along with a growth of the magnetic moment from 1.38 μ_B to 1.67 μ_B, which is mainly driven by the decrease of the minority d charge from 3.49 to 3.29 electrons. In the B3LYP hybrid functional,[128,157] the fundamental band gap is significantly larger than in the local PBE functional, though not as large as in our PBE0 calculation. The magnetic moment predicted from B3LYP is identical to our results. In the LDA+U method the band gap opens as well.[28] The predicted value for the optical band gap of 4.0 eV is considerably smaller than our hybrid functional result. The magnetic moments of 1.64 μ_B and 1.90 μ_B measured in experiments,[160,165] matches well with the moments obtained in all the methods that go beyond PBE. The band transitions are inconsistent as the reported values of 4.0 eV[162] and 4.3 eV[163] for the fundamental band gap are larger than the optical band gap of 3.1 eV.[164] The PBE0 functional seems to overestimate the band gap by at least 1 eV.

Table 6.2: We present the data for NiO: The smallest fundamental band gap Δ_{fund}, the smallest direct band gap Δ_{opt}, the magnetic moment per Ni atom m_{Ni}, and the number of d electrons of minority spin character within the MT spheres N_d is compared to theoretical and experimental results from the literature.

	Δ_{fund} (eV)	Δ_{opt} (eV)	m_{Ni} (μ_{B})	N_d
PBE0	5.34	5.94	1.67	3.29
Level I	5.50	6.07	1.69	3.28
Level II	4.48	5.38	1.64	3.32
Level III	3.10	4.05	1.66	3.32
PBE	0.97	1.13	1.38	3.49
HSE03[a]	4.2		1.65	
B3LYP[b]	4.1		1.67	
B3LYP[c]	4.2		1.67	
on-site[d]	2.8	3.4	1.73	
LDA + U[d]	3.2	4.0	1.72	
Expt.	4.0,[e] 4.3[f]	3.1[g]	1.64,[i] 1.90[j]	

[a] Reference 156. [b] Reference 128. [c] Reference 157. [d] Reference 28. [e] Reference 162.
[f] Reference 163. [g] Reference 164. [i] Reference 165. [j] Reference 160.

We turn now to the effect of the approximations introduced in Sec. 6.2. For NiO, already the simplest approximation changes the band gap and the magnetic moment towards slightly larger values. The second level decreases the fundamental band gap to 4.48 eV and the direct one to 5.38 eV. The magnetic moment evaluated within the MT sphere shrinks due to a larger occupation of the minority d states. This effect on the magnetic moment is reversed in the third approximation although the occupation of the minority d states remains unchanged. Within the third tier, we obtain a significant reduction of the direct band gap to 4.05 eV and the indirect band gap to 3.10 eV. For the fourth approximation no self-consistent solution was found. Within the LDA+U method also only on-site contributions are considered, which are in addition limited to d electrons. The values obtained with the third approximation compare nicely to the LDA+U results of 4.0 eV and 3.2 eV, respectively. The on-site approximation of Tran *et al.*,[28] which incorporates nonlocal exchange only for d states predicts a fundamental band gap of 2.8 eV and an optical one of 3.4 eV, somewhat smaller than the band gap in the third tier. This difference might originate from the restriction to d levels in the on-site approximation of Tran *et al.*.[28]

In Fig. 6.4, we present the DOS of NiO obtained with different approximations to the PBE0 functional in comparison to the hybrid PBE0 functional and the local PBE
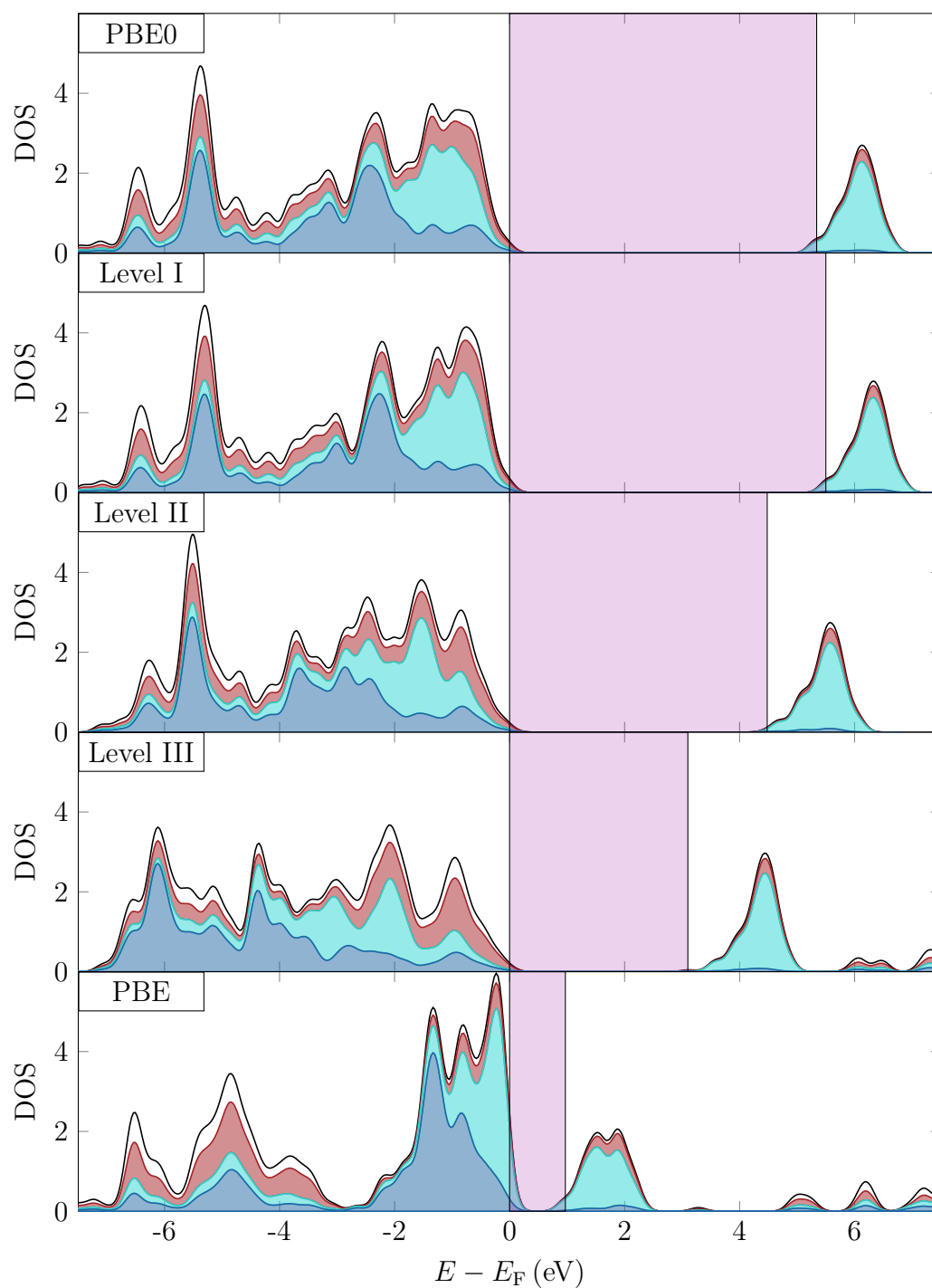
Figure 6.4: Comparison of *l*-projected density of states (DOS) for the spin-up channel in NiO using different approximations to the PBE0 functional. The blue contribution originates from the majority *d* orbitals of the Ni atom, the cyan contribution originates from the ones with the opposite spin direction. The red fraction is associated with the *p* orbitals of oxygen and the remainder to the total DOS consists mainly of charge in the interstitial region. The transparent purple area shows the region where no electronic states exist. The tails in the gap result from the Gaussian broadening.

functional. Within the PBE0 functional, we find a hybridization of the O $2p$ states with the Ni d states. The crystal field splits the d levels into t_{2g} and e_g. In the majority spin all d states are occupied, whereas only the t_{2g} ones are filled in the minority spin channel. The minority and majority states are separated by the exchange splitting so that the states close to the Fermi energy have mostly minority character. The minority e_g are separated from the t_{2g} states by a robust band gap of 5.34 eV. In the first level, this is reproduced accurately. All peaks in the conduction band are at the same positions as in the pure PBE0 functional. The major difference to the PBE0 functional is an increased band gap due to the shift of the unoccupied e_g peak towards higher energies. The second tier introduces more significant changes. The minority t_{2g} states acquire a broader band width, the peak of the majority e_g states is less pronounced, and the fundamental band gap shrinks by roughly 1 eV. Introducing the on-site approximation (Level III), the d states become stronger bound, hence the main contribution close to the Fermi energy comes from the O p states. All peaks associated to d states shrink in magnitude and move towards lower energies. The band gap is reduced to 3.10 eV. In the PBE functional only a very small hybridization of the O p and Ni d states is predicted. The oxygen levels are mainly distributed between -7 eV and -3 eV (relative to E_F), whereas the d levels reside between -2.5 eV and the Fermi energy. The band gap is reduced to roughly 1 eV, considerably smaller than calculated with any nonlocal functional.

Silicon (Si)

Table 6.3 collects the results for different band transitions, the lattice constant, and the bulk modulus of the silicon in the diamond structure. The application of the hybrid functionals PBE0 and HSE yields a significant increase in all band transitions with respect to the local PBE functional. The lattice constant is reduced, whereas the bulk modulus becomes larger. We attribute the small discrepancies with respect to results from the literature[27,29,33] to the slightly smaller values of the numerical cutoffs employed here. We find that the HSE functional accurately describes the experimental band transitions,[138–140] whereas the PBE0 functional yields a better agreement for the lattice constant and the bulk modulus.

We turn now to the approximations to the PBE0 functional. As for the oxides, the first approximation reproduces the band transitions of the PBE0 functional quite well. However, there is no systematic trend. While the $\Gamma \to$ X transition remains almost constant, the $\Gamma \to \Gamma$ transition decreases by 0.15 eV, and the $\Gamma \to$ L transition increases by 0.06 eV. Even though the band structure is close to the PBE0 functional, the structural properties are not reproduced. The lattice constant is increased almost to the value of the PBE functional and the bulk modulus is significantly overesti-

Table 6.3: Comparison of the theoretical and experimental results for different band transitions, the lattice constant a, and the bulk modulus B of silicon.

	$\Gamma \to \Gamma$ (eV)	$\Gamma \to X$ (eV)	$\Gamma \to L$ (eV)	a (Å)	B (GPa)
PBE0	4.00	1.96	2.92	5.439	99.3
Level I	3.85	1.95	2.98	5.460	115.8
Level II	3.30	1.19	2.15	5.455	80.1
Level III	2.49	0.37	1.14	$> 1.02 a_{\text{exp}}$	
Level IV	2.53	0.70	1.52	$> 1.02 a_{\text{exp}}$	
PBE	2.56	0.71	1.54	5.472	89.0
HSE	3.32	1.28	2.24	5.443	98.2
PBE0[a]	3.96	1.93	2.87		
PBE0[b]	3.97	1.93	2.88	5.433	99.0
HSE[c]	3.32	1.29	2.24	5.441	98.0
HSE[b]	3.32	1.29	2.24	5.451	97.7
Expt.	3.05,[d]	1.13,[e]	2.06,[g]	5.430[h]	99.2[h]
	3.34–3.36,[e]	1.25[d]	2.40[f]		
	3.4,[f]				

[a] Reference 33.   [b] Reference 27.   [c] Reference 29 (cf. Sec. 5.5).
[d] Reference 139.   [e] Reference 140.   [f] Reference 138.   [g] Reference 141.
[h] Experimental data taken from Ref. 136.

mated. In the second tier, the band gaps shrink to values approximately equal to the ones obtained with the HSE functional. However, the lattice constant is larger than the hybrid-functional prediction and the bulk modulus is even smaller than one obtained with the PBE functional. The on-site approximation (level III) performs worse than the PBE functional, the band transitions are underestimated, whereas the lattice constant resides above the investigated interval. In the fourth step, we restrict the exchange to the d states and recover the band transitions of the PBE functional. The lattice constant is still strongly overestimated, indicating that the ansatz for the total energy of this approach is not consistent (the nonlocal contribution of the d states does not compensate the local one).

In Fig. 6.5 the DOS of Si obtained with the HSE, the PBE0, and the PBE functional as well as all approximations is shown. We recognize that the valence DOS calculated with the PBE0 and the HSE functional are almost identical. The main difference lies in the gap, which is larger in the PBE0 functional. In hybrid functionals, the band width of the valence band is increased with respect to the band width obtained with the conventional PBE functional. Throughout the series of approximations in
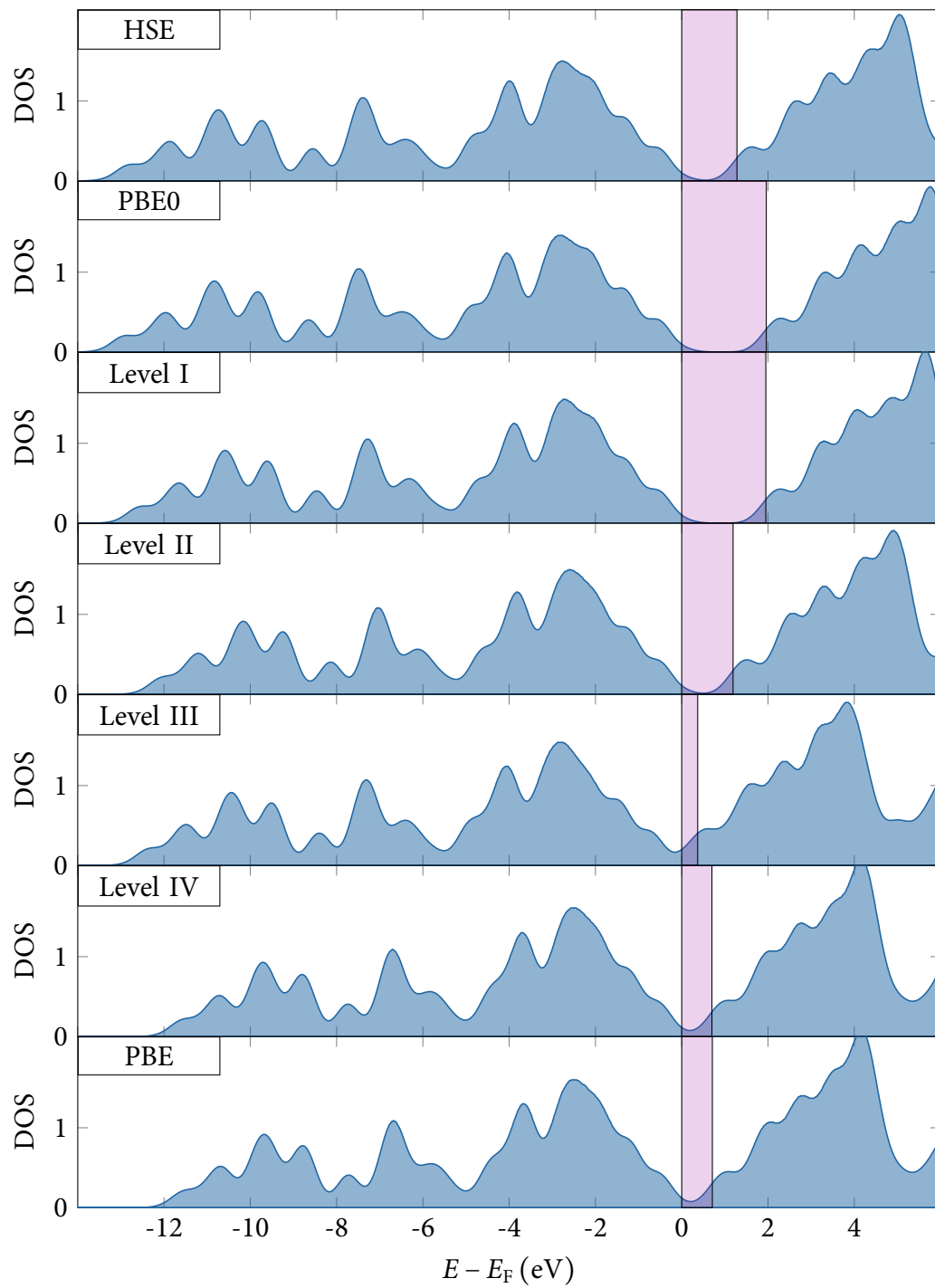
Figure 6.5: The densities of states (DOS) for bulk silicon calculated with the HSE, PBE0, and PBE exchange correlation functional is compared to the different approximations to the hybrid functionals. The purple area indicates the band gap region within which no electronic states exists. Any existing part within is an artifact of the Gaussian broadening used to construct the DOS.

Table 6.4: Comparison of the theoretical and experimental results for different band transitions and the position of the d states of Ga $\Delta_{d,\text{Ga}}$ with respect to the Fermi energy in GaAs.

	$\Gamma \rightarrow \Gamma$ (eV)	$\Gamma \rightarrow$ X (eV)	$\Gamma \rightarrow$ L (eV)	$\Delta_{d,\text{Ga}}$ (eV)
PBE0	1.95	2.72	2.35	-18.0
Level I	2.15	2.73	2.44	-17.7
Level II	1.24	1.84	1.62	-18.5
Level III	0.12	1.16	0.75	-19.1
Level IV	0.60	1.04	1.42	-22.0
PBE	0.47	1.47	0.75	-15.1
HSE	1.33	2.06	1.70	-18.0
PBE0[a]	2.02	2.69	2.38	
PBE0[b]	2.01	2.67	2.37	
HSE[c]	1.43	2.06	1.78	
HSE[b]	1.45	2.02	1.76	
Expt.[d]	1.63	2.01, 2.18	1.84, 1.85	-16.9
Expt.[e]	1.52	1.90	1.74	

[a] Reference 33. [b] Reference 27. [c] Reference 29 (cf. Sec. 5.5).
[d] Reference 138. [e] Reference 137.

particular the band gap and the band width decrease. The behavior is not monotonic, e.g., the band gap of the third tier is smaller than the one of the fourth approximation. We note that although the band transitions of the HSE functional are well reproduced by the second level, the band width is smaller.

Gallium Arsenide (GaAs)

We present the results for different band transitions of GaAs and the position of the d states of Ga in Table 6.4. The band gaps obtained with the PBE0 functional are approximately 1.5 eV larger than with the ones calculated with the PBE functional and are close to results from the literature obtained with the same functional.[27,33] The d orbitals of Ga are more strongly bound at -18.0 eV compared to the PBE functional (-15.1 eV). In the HSE functional, we find the d states at the same position as in the PBE0 functional. The band gap is considerably (~ 0.6 eV) smaller than the band gap obtained with PBE0. Nevertheless, it is still significantly larger than the PBE counterpart. The HSE results for these band transitions from the literature[27] and our results from Sec. 5.5 are somewhat larger, hence indicating the error associ-

ated to the reduced values of the numerical parameters. Comparing to experimental results,[137,138] we find that the HSE functional gives the best agreement of all the considered functionals.

We consider next the effect of the approximations. The first level yields band transitions in good agreement with the results of the PBE0 functional with a small increase in the absolute numbers. The d states of Ga are found at a somewhat higher energy. The second tier reduces the band gaps significantly to values approximately close to the ones obtained with the HSE functional. The binding energy of the d states increases to 18.5 eV. Within the third approximation, the band transitions are smaller than their PBE counterpart, while the d states of Ga are bound more strongly. Within the fourth level the order of the band transitions changes so that the $\Gamma \rightarrow X$ is smaller than $\Gamma \rightarrow L$, and the d states are even stronger bound.

In Fig. 6.6, we visualize the impact of the different approximations on the DOS of GaAs in contrast with the local PBE and the nonlocal HSE and PBE0 functional. We identify three major contributions to the valence band of GaAs in the selected energy range. The As s peak is situated at a binding energy of around 12 eV. Above, at an energy of ~ −7 eV, we see the corresponding s peak of Ga. The rest of the states below as well as above the Fermi energy have mainly p character from either of the atoms. With the HSE and PBE0 functional, the s peaks of both atoms are shifted downwards by ~ 1 eV and the band width of the p states below the Fermi energy is increased with respect to the PBE functional. In the PBE0 functional, the band gap obtains a large value of 1.95 eV, the HSE functional predicts a smaller band gap of 1.33 eV, and the PBE functional reduces it to merely 0.47 eV. Turning to the approximations, we recognize that the first level reproduces most properties of the PBE0 functional, albeit the Ga s peak is found at a higher energy and the band gap is increased by 0.2 eV. In the second tier, the band gap is reduced to 1.24 eV close to that of the HSE functional. Both s peaks are more loosely bound and the band width is slightly reduced compared to the hybrid functionals. Employing the third approximation (on-site HF only), the valence spectra is reproduced for the low lying As s states. The position of the Ga s and the band width of the p states is similar to the second tier. However, the band gap to the conduction band is significantly underestimated. In the fourth level, we almost recover the results of the PBE functional, although the details reveal a changed order in the band transitions (see Table 6.4).

6.4   k-point interpolation

An alternative approach to reduce the computational cost of hybrid functionals is related to the downsampling of the exchange potential. This was introduced by Paier
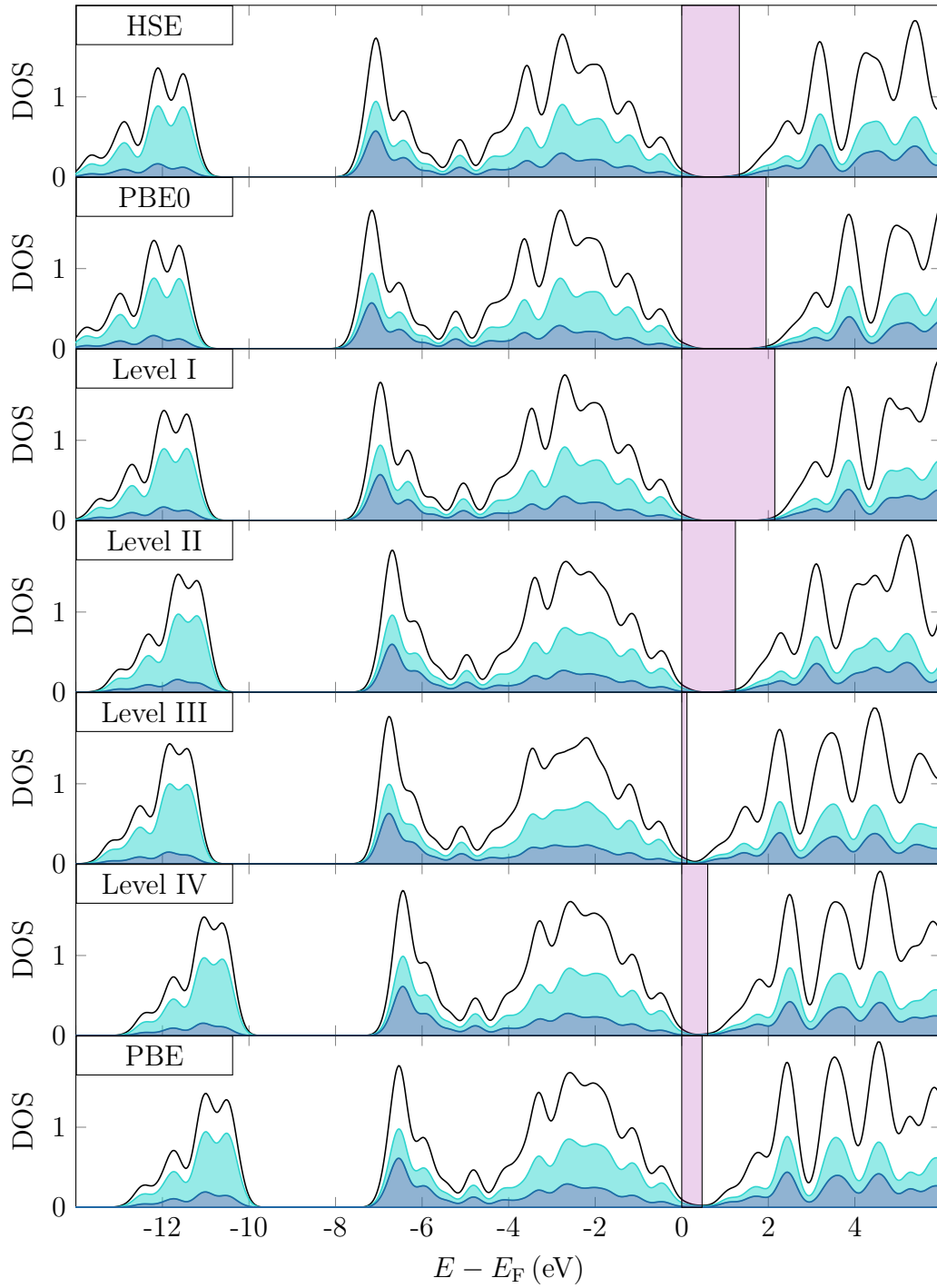
Figure 6.6: The densities of states (DOS) for bulk GaAs calculated with the HSE, PBE0, and PBE exchange correlation functional is compared to the different approximations to the hybrid functionals. The blue part shows the density located at Ga atoms, the cyan area represents the As atoms. The remainder to the total DOS (black) is situated within the interstitial region. The purple area indicates the band gap region within which no electronic states exists. The blue tails are related to the Gaussian broadening.

et al. [27] for the inner $\boldsymbol{q}$-point mesh of the nonlocal exchange, and we will examine the more rigorous downsampling of both $\boldsymbol{k}$- and $\boldsymbol{q}$-point mesh. The total contribution of the hybrid functional to the Hamiltonian is given as (cf. Eq. (4.15))

$$V_{\mathrm{x},\boldsymbol{GG'}}^{\mathrm{hyb.}}(\boldsymbol{k}) = \sum_{m}^{\mathrm{occ.}} \sum_{\boldsymbol{q}}^{\mathrm{BZ}} \left\langle \chi_{\boldsymbol{k+G}}\phi_{m\boldsymbol{q}} \left| V^{\mathrm{NL}} \right| \phi_{m\boldsymbol{q}}\chi_{\boldsymbol{k+G'}} \right\rangle - \left\langle \chi_{\boldsymbol{k+G}} \left| V^{\mathrm{L}} \right| \chi_{\boldsymbol{k+G'}} \right\rangle, \tag{6.20}$$

where $\chi_{\boldsymbol{k+G}}$ are FLAPW basis functions and V^{NL} and V^{L} correspond to the nonlocal and local potential, respectively. If we restrict the evaluation of this term to a reduced mesh of $\boldsymbol{k}$ points and evaluate the inner $\boldsymbol{q}$ summation on the same smaller mesh, we will gain a tremendous speed up. For example, reducing the $\boldsymbol{k}$-point mesh from $8 \times 8 \times 8$ to $4 \times 4 \times 4$ in $SrTiO_3$ reduces the computation time by a factor of 34. The physical motivation to restrict the evaluation of the exchange to a less precise mesh is that the exchange energy is a small quantity compared to the contribution of the kinetic energy and the electrostatic potential of the charge density. Nevertheless, we need an interpolation technique to evaluate the exchange potential at intermediate $\boldsymbol{k}$ points. We recall that two different types of basis functions exist (see Chap. 3): LAPW functions and local orbitals. For the former, we choose a linear interpolation technique. Let

$$\boldsymbol{k}^{\mathrm{int}} = a_1 \boldsymbol{k}_1 + a_2 \boldsymbol{k}_2, \tag{6.21}$$

where $\boldsymbol{k}_i$ are $\boldsymbol{k}$-points, for which the nonlocal exchange is evaluated directly, $\boldsymbol{k}^{\mathrm{int}}$ is the interpolated $\boldsymbol{k}$-point, and with the requirement that $a_1 + a_2 = 1$ and $0 \le a_i \le 1$. Then the interpolated potential is given by

$$V_{\mathrm{x},\boldsymbol{GG'}}^{\mathrm{hyb.}}(\boldsymbol{k}^{\mathrm{int}}) = \sum_{i=1}^{2} a_i V_{\mathrm{x},\boldsymbol{GG'}}^{\mathrm{hyb.}}(\boldsymbol{k}_i). \tag{6.22}$$

Due to the criterion $|\boldsymbol{k}+\boldsymbol{G}| \le G_{\mathrm{max}}$, the set of $\boldsymbol{G}$ vectors is different at different $\boldsymbol{k}$ points. Therefore, we restrict ourselves to those $\boldsymbol{G}$ points that are present at $\boldsymbol{k}_1, \boldsymbol{k}_2$, and the interpolated point $\boldsymbol{k}^{\mathrm{int}}$. Furthermore, we include a shift by an reciprocal lattice vector $\Delta\boldsymbol{G}_i$ to the $\boldsymbol{G}$ vectors if the path from $\boldsymbol{k}_i$ to $\boldsymbol{k}^{\mathrm{int}}$ crosses the boundary of the BZ. This corresponds to the requirement, that the length

$$\left| \Delta\boldsymbol{G}_i - \left(\boldsymbol{k}^{\mathrm{int.}} - \boldsymbol{k}_i \right) \right| \tag{6.23}$$

is minimized. This yields the following expression for the interpolated potential

$$V_{\mathrm{x},\boldsymbol{GG'}}^{\mathrm{hyb.}}(\boldsymbol{k}^{\mathrm{int}}) = \sum_{i=1}^{2} a_i V_{\mathrm{x},(\boldsymbol{G}+\Delta\boldsymbol{G}_i),(\boldsymbol{G'}+\Delta\boldsymbol{G}_i)}^{\mathrm{hyb.}}(\boldsymbol{k}_i). \tag{6.24}$$

For the local orbitals, we use a different scheme, in which the $\boldsymbol{k}$ dependence of the local orbitals is removed. In general, a local orbital can be written as

$$\chi_{\boldsymbol{k}+\boldsymbol{G}_{\text{lo}}}(\boldsymbol{r}) = \sum_{m=-l}^{l} M_{\boldsymbol{G}_{\text{lo}},m}(\boldsymbol{k}) f_m^{\text{lo}}(r), \tag{6.25}$$

with a $\boldsymbol{k}$-point independent radial function $f_m^{\text{lo}}(r)$, the angular momentum l of the local orbital and its magnetic quantum number m, and a matrix, which contains the $\boldsymbol{k}$-point dependence,

$$M_{\boldsymbol{G}_{\text{lo}},m}(\boldsymbol{k}) = e^{i(\boldsymbol{k}+\boldsymbol{G}_{\text{lo}})\cdot \boldsymbol{R}_a}\, Y_{lm}^{*}(\widehat{\boldsymbol{k}+\boldsymbol{G}}_{\text{lo}}), \tag{6.26}$$

with the position of the atom $\boldsymbol{R}_a$. $M_{\boldsymbol{G}_{\text{lo}},m}(\boldsymbol{k})$ is a square matrix, because exactly $(2l+1)$ different $\boldsymbol{G}^{\text{lo}}$ vectors are selected. These $\boldsymbol{G}^{\text{lo}}$ vectors correspond to "virtual" plane waves that are only employed in the construction of the local orbitals (see Sec. 3.4). We identify two cases:

1 We interpolate $V_{\text{x},\boldsymbol{GG}_{\text{lo}}}^{\text{hyb.}}(\boldsymbol{k}^{\text{int}})$, i.e., one basis function is an LAPW function associated with a plane wave of reciprocal lattice vector $\boldsymbol{G}$ and the other is a local orbital matched to a virtual plane wave characterized by $\boldsymbol{G}_{\text{lo}}$. Then the interpolated matrix is calculated as

$$V_{\text{x},\boldsymbol{GG}_{\text{lo}}}^{\text{hyb.}}(\boldsymbol{k}^{\text{int}}) = \sum_{i=1}^{2} a_i \sum_{m=-l}^{l} V_{\text{x},(\boldsymbol{G}+\Delta\boldsymbol{G}_i),\boldsymbol{G}_{\text{lo}}}^{\text{hyb.}}(\boldsymbol{k}_i) M_{\boldsymbol{G}_{\text{lo}},m}^{-1}(\boldsymbol{k}_i) M_{\boldsymbol{G}_{\text{lo}},m}(\boldsymbol{k}^{\text{int.}}). \tag{6.27}$$

The explicit $\boldsymbol{k}$-point dependence of the basis functions $\chi_{\boldsymbol{k}_i+\boldsymbol{G}_{\text{lo}}}$ is removed by the multiplication with the inverse of the matrix $M_{\boldsymbol{G}_{\text{lo}},m}(\boldsymbol{k}_i)$. The resulting term is then interpolated and the multiplication with the matrix $M_{\boldsymbol{G}_{\text{lo}},m}(\boldsymbol{k}^{\text{int.}})$ produces the correct $\boldsymbol{k}$-point dependence for the local orbital.

2 For $V_{\text{x},\boldsymbol{G}_{\text{lo}}\boldsymbol{G}_{\text{lo}}'}^{\text{hyb.}}(\boldsymbol{k}^{\text{int}})$ both basis functions are local orbitals characterized by $\boldsymbol{G}_{\text{lo}}$ and $\boldsymbol{G}_{\text{lo}}'$, respectively. We remove the $\boldsymbol{k}$-point dependence by multiplying the inverse matrices from left ($M_{\boldsymbol{G}_{\text{lo}},m}^{-1}(\boldsymbol{k}_i)$) and right ($M_{\boldsymbol{G}_{\text{lo}}',m'}^{-1}(\boldsymbol{k}_i)$), interpolate the result, and transform to the intermediate $\boldsymbol{k}$ point afterwards

$$V_{\text{x},\boldsymbol{G}_{\text{lo}}\boldsymbol{G}_{\text{lo}}'}^{\text{hyb.}}(\boldsymbol{k}^{\text{int}}) =$$
$$\sum_{i=1}^{2} a_i \sum_{m,m'} M_{\boldsymbol{G}_{\text{lo}},m}(\boldsymbol{k}^{\text{int.}}) M_{\boldsymbol{G}_{\text{lo}},m}^{-1}(\boldsymbol{k}_i) V_{\text{x},\boldsymbol{G}_{\text{lo}}\boldsymbol{G}_{\text{lo}}'}^{\text{hyb.}}(\boldsymbol{k}_i) M_{\boldsymbol{G}_{\text{lo}}',m'}^{-1}(\boldsymbol{k}_i) M_{\boldsymbol{G}_{\text{lo}}',m'}(\boldsymbol{k}^{\text{int.}}). \tag{6.28}$$
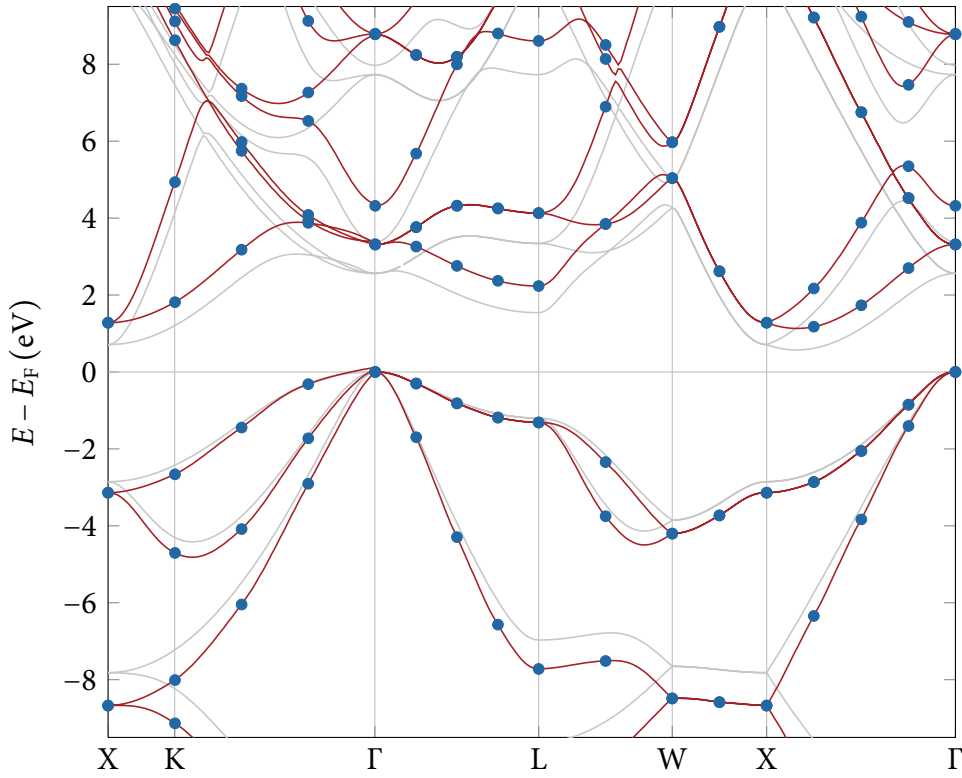
Figure 6.7: Electronic band structure of silicon generated by **k**-point interpolation (red) between the results of the HSE hybrid functional (blue). For comparison, we depict the results of a PBE calculation as a light-gray line.

As a first test of the accuracy of the $\boldsymbol{k}$-point interpolation, we investigate the band structure of silicon (cf. Fig. 6.7). The interpolated band structure shows a smooth behavior for the points between the exactly evaluated $\boldsymbol{k}$ points. A comparison with the PBE band structure shows that the interpolated HSE band structure displays the correct physical band dispersion. In particular, we shall discuss a few details. An important feature is the position of the conduction band mimimum, which is situated along the Γ-X direction and closer to X in the interpolated band structure and in the band structure obtained with the PBE functional. Consider also the second highest valence band state: Along the K-Γ direction (close to K) and along the L-W direction (close to W) the band is curved such that its minimum is below the exactly evaluated data points. A similar behavior is found in the local PBE functional as well. Hence, we attribute this curvature to the major energy contributions of the Hamiltonian (Coulomb potential, kinetic energy) and not to the interpolated one of the

hybrid functional. This qualitative agreement with the PBE band structure indicates that the linear interpolation of the nonlocal HSE potential is a viable ansatz.

Next, we try the same scheme for ZnO in the zincblende structure. Figure 6.8a) shows that the oxygen p bands directly below the Fermi energy display a smooth behavior whereas the zinc d states situated roughly 6 eV below the Fermi energy exhibit some unphysical irregularities. The interpolation of the LAPW basis functions fails for the localized states, because the expansion coefficients of the Kohn-Sham wave functions strongly differ at different k points. For more delocalized states, such as the s and p bands, the representation by LAPW at different k points is more similar, so that the interpolation scheme is applicable. As possible solution to this problem, we investigate a description of the localized states by local-orbital basis functions. These are interpolated by an explicit accounting of the k point dependence (see above). However, we note that this approach will cause problems in the electronic self consistency if the LAPW basis function and the local orbital one become linearly dependent. To avoid such problems, we choose a very large energy parameter for the LAPW basis functions. In Fig. 6.8b, we demonstrate that this avoids the unphysical irregularities in the d states of ZnO. The direct band gap at the Γ point is accurately reproduced, whereas the indirect L → Γ gap shrinks by 0.35 eV. The reduction of the band gap is caused by the decreased flexibility of the basis by the radical shift of the d energy parameter to high energies. Improving the flexibility by additional local orbitals restores the size of the band gap to the original value (see Fig. 6.8c).

Motivated by the accurate description of intermediate k points in the band structure, we apply the same scheme to a self-consistent calculation. As reference, we evaluate the eigenvalues of SrTiO$_3$ in a large $8 \times 8 \times 8$ k-point mesh. Then, we employ a small $4 \times 4 \times 4$ k-point mesh and interpolate the nonlocal potential for all k points that are present in the large mesh. We iterate the calculation in small mesh and subsequent interpolation of the nonlocal potential until a self consistent solution is reached. We note that for a general k^{int} several possible combinations of k_1 and k_2 that fulfill Eq. (6.21) exist. We restrict ourselves to one particular choice, where

$$k_{1,x} \leq k_x^{\text{int}} \leq k_{2,x}, \tag{6.29a}$$

$$k_{1,y} \leq k_y^{\text{int}} \leq k_{2,y}, \tag{6.29b}$$

$$k_{1,z} \leq k_z^{\text{int}} \leq k_{2,z}, \tag{6.29c}$$

and the length $|k_1 - k_2|$ is minimized. In Table 6.5, we show the differences in the eigenvalues between the small and the large k-point mesh. For the occupied states, we find an average deviation of 0.038 eV, which is almost constant for all k points in the BZ. For the k points, that are already present in the smaller mesh, the eigenval-
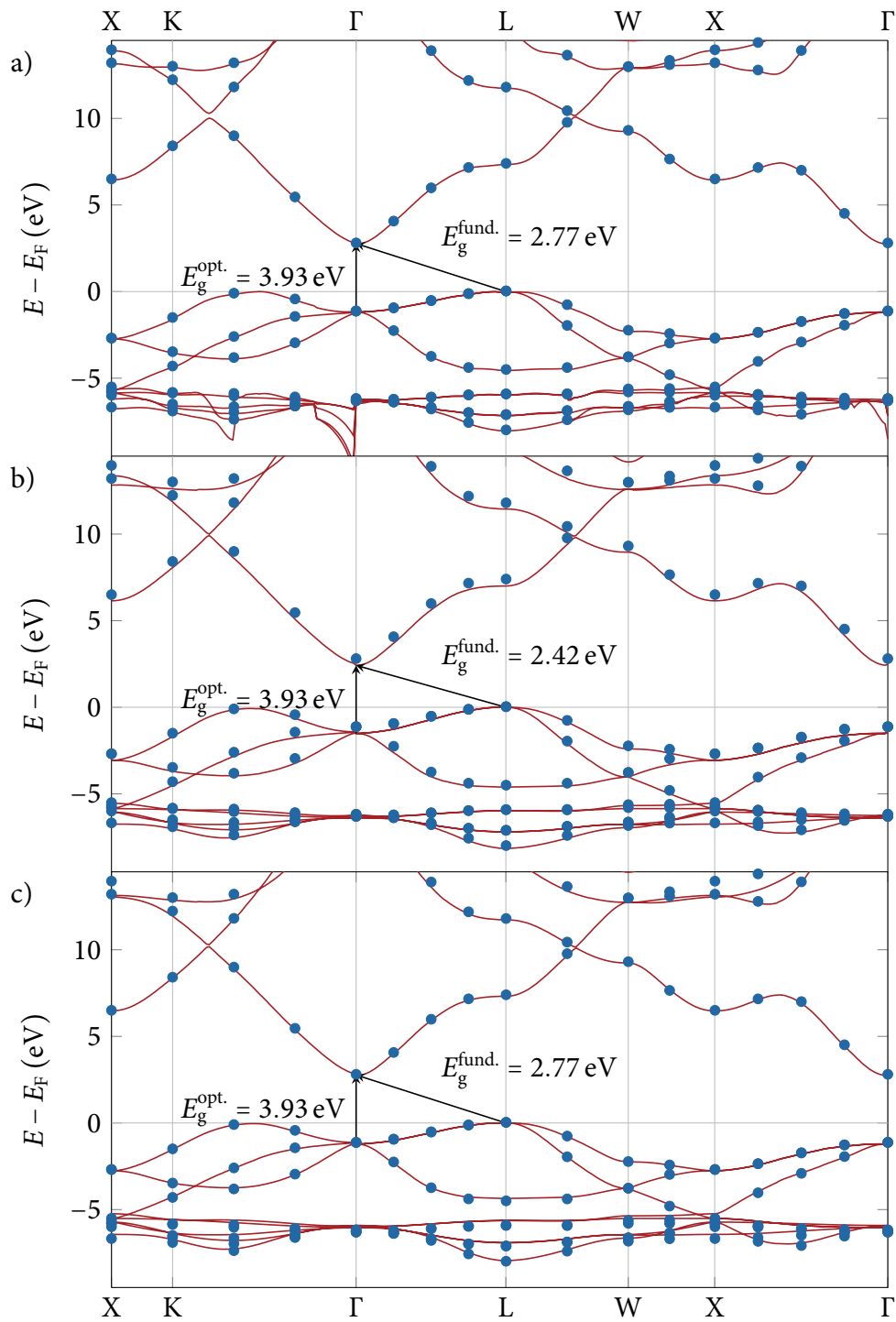
Figure 6.8: Electronic band structure of ZnO generated by **k**-point interpolation (red) between the results of the HSE hybrid functional (blue). The three figures differ by the basis functions employed to describe the Zn d states: (a) LAPW functions, (b) local orbitals for $3d$ states, and (c) local orbitals for $3d$ and $4d$ states.

Table 6.5: Interpolation for cubic $SrTiO_3$ from a $4 \times 4 \times 4$ to an $8 \times 8 \times 8$ $\boldsymbol{k}$-point mesh – The first 10 $\boldsymbol{k}$ points are present in both meshes, whereas the latter 25 ones are only present in the $8 \times 8 \times 8$ mesh. We show the mean error (ME) and the mean absolute error (MAE) of the eigenvalues of occupied and unoccupied states (relative to the Fermi energy). We compare the results of the interpolation with a full self-consistent result in the larger mesh. All $\boldsymbol{k}$ vectors are given in internal coordinates of the Brillouin zone.

$\boldsymbol{k}$-point			occupied states		unoccupied states	
			ME (eV)	MAE (eV)	ME (eV)	MAE (eV)
0	0	0	-0.000	0.038	-0.059	0.059
0	0	$1/4$	-0.006	0.036	-0.056	0.057
0	0	$1/2$	-0.010	0.039	-0.053	0.054
0	$1/4$	$1/4$	-0.009	0.036	-0.056	0.058
0	$1/4$	$1/2$	-0.012	0.039	-0.053	0.055
0	$1/2$	$1/2$	-0.013	0.041	-0.052	0.055
$1/4$	$1/4$	$1/4$	-0.011	0.038	-0.053	0.056
$1/4$	$1/4$	$1/2$	-0.013	0.039	-0.052	0.054
$1/4$	$1/2$	$1/2$	-0.014	0.040	-0.050	0.054
$1/2$	$1/2$	$1/2$	-0.014	0.040	-0.050	0.057
0	0	$1/8$	0.009	0.041	-0.072	0.072
0	0	$3/8$	0.002	0.035	-0.069	0.069
0	$1/8$	$1/8$	0.019	0.044	-0.079	0.079
0	$1/8$	$1/4$	0.053	0.062	-0.112	0.112
0	$1/8$	$3/8$	0.015	0.038	-0.075	0.075
0	$1/8$	$1/2$	0.000	0.037	-0.062	0.062
0	$1/4$	$3/8$	0.002	0.034	-0.064	0.064
0	$3/8$	$3/8$	0.013	0.035	-0.073	0.073
0	$3/8$	$1/2$	-0.001	0.036	-0.063	0.063
$1/8$	$1/8$	$1/8$	0.027	0.047	-0.090	0.090
$1/8$	$1/8$	$1/4$	0.012	0.038	-0.076	0.076
$1/8$	$1/8$	$3/8$	0.027	0.043	-0.083	0.083
$1/8$	$1/8$	$1/2$	0.012	0.036	-0.071	0.071
$1/8$	$1/4$	$1/4$	-0.000	0.035	-0.064	0.065
$1/8$	$1/4$	$3/8$	0.013	0.036	-0.073	0.073
$1/8$	$1/4$	$1/2$	-0.001	0.035	-0.062	0.063
$1/8$	$3/8$	$3/8$	0.025	0.040	-0.081	0.081
$1/8$	$3/8$	$1/2$	0.010	0.035	-0.071	0.071
$1/8$	$1/2$	$1/2$	-0.002	0.038	-0.059	0.059
$1/4$	$1/4$	$3/8$	-0.000	0.034	-0.063	0.064
$1/4$	$3/8$	$3/8$	0.012	0.035	-0.072	0.072
$1/4$	$3/8$	$1/2$	-0.001	0.034	-0.061	0.061
$3/8$	$3/8$	$3/8$	0.024	0.039	-0.081	0.081
$3/8$	$3/8$	$1/2$	0.011	0.035	-0.070	0.070
$3/8$	$1/2$	$1/2$	-0.001	0.036	-0.059	0.062
$\sum_{\boldsymbol{k}}^{\text{BZ}} \cdots$			0.005	0.038	-0.067	0.068

ues are decreased on average, whereas the eigenvalues are rather overestimated for k points that are only present in the larger mesh. For the unoccupied states, we find a systematic decrease in the eigenvalues of averaged 0.067 meV with some larger variations across the BZ than for the occupied states. The eigenvalues at k points of the $4 \times 4 \times 4$ mesh should not show differences to the reference calculation if we would calculate in a one-shot approach. Hence, the observed deviations are a consequence of the self-consistency cycle. They are smaller than the differences of the eigenvalues obtained at the interpolated k points. The systematic decrease of the eigenvalues of the unoccupied states leads to a decrease of the band gap from 3.33 eV in the reference calculation to 3.23 eV in the interpolated scheme. Hence, this scheme is no improvement over the smaller k-point mesh, where the band gap is 3.31 eV close to the one obtained with the large k-point mesh.

As perspective, we propose to improve the outlined k-point interpolation employing an more sophisticated scheme. A possible technique may be the employment of Wannier functions. Our implementation of the nonlocal exchange potential uses the wave functions in reciprocal space. A suitable alternative is the Wannier basis. Wannier functions are localized at specific sites $\boldsymbol{R}$

$$\phi_{n\boldsymbol{R}}^{\mathrm{W}}(\boldsymbol{r}) = \frac{1}{\sqrt{N}} \sum_{\boldsymbol{k}}^{\mathrm{BZ}} \mathrm{e}^{-\mathrm{i}\boldsymbol{k}\cdot\boldsymbol{R}} \, \phi_{n\boldsymbol{k}}(\boldsymbol{r}), \tag{6.30}$$

where N is the number of unit cells. Employing Wannier functions may be advantageous, because they contain the information of all k points in the BZ, whereas the direct interpolation considers only the k points closest to the intermediate one.

6.5 Conclusion

We have introduced four tiers as possible computationally less expensive alternatives to the nonlocal hybrid functionals. However, we find that no approximation is suited to reproduce the energies of the hybrid functionals, e.g., leading to a mismatch in the lattice constant of silicon. The error is more severe the more drastically we approximate the hybrid functionals. The band structure of the PBE0 functional could be approximated by the neglect of the pure IR contribution in nonlocal and local potential (first level). Surprisingly close agreement was found between the band transitions of the second tier (complete neglect of IR contribution) and the HSE functional, though deviations in details exist such as the position of low lying states and the band width. Although parts of the nonlocal exchange are included, the third approximation only occasionally provides an improvement over the local PBE functional, whereas it underperforms for the semiconductors. We have found no material where the fourth

level was useful. In conclusion, we find that the neglect of the IR-IR is an efficient approximation if one is only interested in the improvement of the band gap by hybrid functionals. The complete neglect of IR contributions may provide a faster implementation of a screened hybrid functional, though further investigation is necessary to reveal if the coincidence of the band transitions with the HSE functional is systematic or just a fortuitious case appearing in the selected materials. However, both approximations need to be refined if one is interested in total energies of hybrid functionals. The challenging task is the development of a consistent approximation to the local and nonlocal potential that avoids double counting and the neglect of relevant contributions.

We have demonstrated a technique to calculate the potential associated with the hybrid functional on a coarser mesh than the contributions of the kinetic energy and the electrostatic potential. This method is based on a linear interpolation of the matrix elements of the hybrid functional. It is particulary suitable for the evaluation of the electronic band structure of materials without localized states. Including additional local orbitals allows the interpolation scheme in compounds with localized d and f electrons. However, a significant effort of the user is required to make the calculation numerically stable, efficient, and accurate. Furthermore, the procedure is applicable in a self-consistent scheme, though in particular the eigenvalues of the unoccupied states are systematically underestimated. We encourage the community to refine the interpolation scheme, for example, by means of Wannier functions.

Rare Earth Compounds

7.1   Introduction

In this chapter, we present our results several rare earth compounds with a rock-salt structure. Our interest specifically focuses on the description of the $4f$ states of the rare earth atoms within these compounds. An accurate description of the position of these states is impossible with the conventional exchange-correlation function-als – the local density approximation (LDA) and the semilocal generalized gradient approximation (GGA). This failure is typically attributed to the spurious self inter-action which is present in all local functionals (cf. Sec. 2.5). Hence, one typically employs the DFT+U scheme,[94] where an on-site Hubbard-like term U is added to the Hamiltonian to correct the eigenvalue of the localized states. Although schemes to calculate this parameter have been established,[98–100] often its value is chosen to reproduce certain experimental observations, such as the lattice constant, the band gap, or the position of the localized states. However, Rohrbach *et al.*[150] showed at the example of the transition-metal monosulfides, that there is no unique choice of U, which reproduces all experimental values accurately. Thus, the predictive power of density functional theory (DFT) is limited as the quantitative and for some materials also the qualitative picture strongly depends on the chosen value of U. In this work, we demonstrate that hybrid functionals surmount these difficulties and provide an

accurate description of structural, magnetic, and electronic properties of rare earth materials.

We focus in particular on gadolinium nitride (GdN) and the europium chalcogenides (EuX, X = O, S, Se, or Te). The discovery of the europium chalcogenides dates back to the early 60s.[166–168] They crystallize in a rock-salt structure where the Eu atom has a half-filled $4f$ shell leading to a large magnetic moment of $7\,\mu_B$. All europium chalcogenides are semiconducting and the band gap increases from EuO (1.12 eV) to EuTe (2.0 eV).[49] As the $4f$ states are strongly localized the magnetic interaction between neighboring Eu atoms is of indirect kind.[169,170] The interaction with the nearest neighbors (nn) is ferromagnetic whereas the coupling to the next nearest neighbors (nnn) is of antiferromagnetic nature.[171] The nn interaction J_1 becomes 20 times weaker from EuO to EuTe and the nnn one J_2 increases slightly by an factor of two.[171] As a consequence, only EuO and EuS are strictly ferromagnetic below the Curie temperature, EuSe orders ferromagnetic or antiferromagnetic depending on the temperature, and EuTe is antiferromagnetic up to its Néel temperature.[171] First principles calculations based on an LSDA+U scheme[172] predict a decrease of both coupling constants J_1 and J_2 under isotropic stress.

Of special interest is EuO which can be grown epitaxially on Si,[43,44] GaN,[44] yttria-stabilized zirconia (YSZ)[45] and GaAs.[46] EuO and EuS show a large resistivity anomaly near the Curie temperature T_C,[173–178] which is attributed to the presence of "trap" states induced by oxygen vacancies. These trap states donate their electrons to the exchange split conduction band below T_C,[173,177] yielding a high spin-polarization perfectly suitable for efficient spin-filters in semiconductor devices.[47,48] Above the Curie temperature the exchange splitting vanishes and the trap states become occupied. Hence, the resistivity grows by several orders of magnitude. However, the highest Curie temperature T_C of 69 K for EuO[49] is too small for practical application. Fortunately, doping the sample with Gd increases the T_C up to 170 K.[51–54] A similar effect could be achieved by oxygen defects[50,51] or doping with La[55] or Ce.[56] Recently, Mairoser et al.[179] suggested a close connection of the T_C on the carrier density and showed that only a part of the dopants were activated.[179,180] In a theoretical analysis, Takahashi[181] proposed a model which confirms the growth of the Curie temperature upon the increase of the number of carriers in the conduction band. It was demonstrated[182] that the T_C of EuS can be increased by Gd doping, too. Theoretical calculations based on model calculations reproduced[183–186] the metal-insulator transition at the Curie temperature.

GdN crystallizes in the same structure as the europium chalcogenides. The electron configuration is isovalent to EuO, though in contrast to EuO the highest occupied states are of $2p$ character. The band gap is significantly smaller and whether there is one at all is still debated in the literature. There is experimental evidence for

semi-metallic single crystals[39] and insulating thin films.[187] Recent measurements find thin film samples of GdN which are degenerately doped semiconducting[36–38] or metallic[38] at low temperatures. In *ab initio* calculations employing an LSDA+U scheme, depending on the particular choice of the value U, semiconducting[34,35,188,189] as well as half-metallic[40,41] ground states were found.

The high saturation magnetic moment per Gd atom of 6.88 μ_B[190] makes GdN a promising material for future technological applications. The material is ferromagnetic with a Curie temperature of 58 K.[191] Recent measurements in thin films indicate[192] a slightly lower critical temperature of 37 K. GdN exhibits an anomaly in the resistivity close the phase transition[191] although it is less pronounced than in EuO.

In this chapter, we present our results for these rare earth compounds using the hybrid functionals HSE and PBE0. First, we describe the computational setup used for GdN as well as the EuX series in Sec. 7.2. In Sec. 7.3, the structural, electronic and magnetic ground state of GdN is examined. These results are part of our paper.[29] In the following sections, we compare the experimentally determined properties of EuO (Sec. 7.4), EuS (Sec. 7.5), EuSe (Sec. 7.6), and EuTe (Sec. 7.7) with the results of our DFT calculations. We analyze the systematical trends in the series in Sec. 7.8. Finally, we conclude our investigation of the rare earth compounds in Sec. 7.9.

7.2 Computational setup

We calculate the rare earth compounds in the rock-salt structure, with the room-temperature lattice constants of a_{GdN} = 4.988 Å,[193] a_{EuO} = 5.141 Å, a_{EuS} = 5.968 Å, a_{EuSe} = 6.195 Å, and a_{EuTe} = 6.598 Å.[171] At low temperatures the magnetic moments align, resulting in a ferromagnetic (FM) ground state (see Fig. 7.1) in all materials with the only exception of EuTe, which has an antiferromagnetic (AFM) ground state. In these materials, the following states are important: i) the $4f$ states of the rare earth ion, which are occupied only in the majority spin channel, and give rise to the large magnetic moment of 7 μ_B. ii) the s and p states for the nitrogen or the chalcogenide atom, which form the valence band. iii) the conduction band, which consist of the $5d$ and the $6s$ states of the rare earth ion. In addition to these states, we describe the $5s$ and the $5p$ states as local orbitals to avoid problems with semicore states.[118] To reduce the linearization error of the FLAPW method,[194,195] we increase the flexibility of the basis within the muffin-tin (MT) spheres by adding unoccupied local orbitals.[120]

We determined the numerical cutoff parameters by converging the energy difference between the experimental lattice constant and a 1% larger unit cell up to
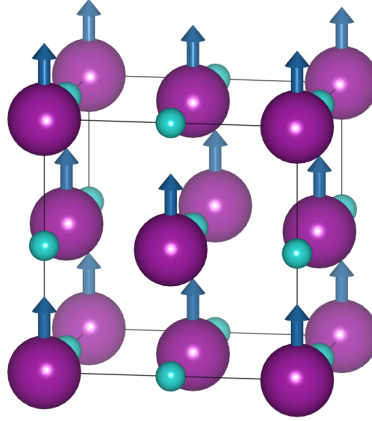
Figure 7.1: At low temperatures, GdN, EuO, EuS, and EuSe realize a ferromagnetic ground state in the rock-salt structure.

Table 7.1: Numerical parameters employed in the calculation of gadolinium nitride and the europium chalcogenides.

	GdN	EuO	EuS	EuSe	EuTe
$\boldsymbol{k}$-point mesh			$8\times8\times8$		
muffin-tin radii					
rare-earth cation (Gd, Eu)	$2.33\,a_0$	$2.60\,a_0$	$3.08\,a_0$	$2.85\,a_0$	$2.80\,a_0$
anion (N, O, S, Se, Te)	$1.95\,a_0$	$2.16\,a_0$	$2.41\,a_0$	$2.85\,a_0$	$2.80\,a_0$
plane-wave cutoffs					
FLAPW basis	$4.9\,a_0^{-1}$	$4.3\,a_0^{-1}$	$4.5\,a_0^{-1}$	$4.7\,a_0^{-1}$	$4.3\,a_0^{-1}$
mixed product basis (MPB)	$3.6\,a_0^{-1}$	$3.1\,a_0^{-1}$	$3.6\,a_0^{-1}$	$3.0\,a_0^{-1}$	$3.4\,a_0^{-1}$
angular-momentum cutoffs					
cation, FLAPW basis	12	14	12	14	14
anion, FLAPW basis	10	8	10	14	14
cation, MPB	6	6	6	6	6
anion, MPB	4	4	4	4	4
local orbitals, cation			$5s, 5p, 7s, 7p, 6d, 5f$		
local orbitals, anion	$3s, 3p,$	$3s, 3p,$	$4s, 4p,$	$5s, 5p,$	$6s, 6p,$
	$4d, 5f$	$4d, 5f$	$4d, 5f$	$5d, 5f$	$6d, 5f$
number of bands	200	240	270	260	240
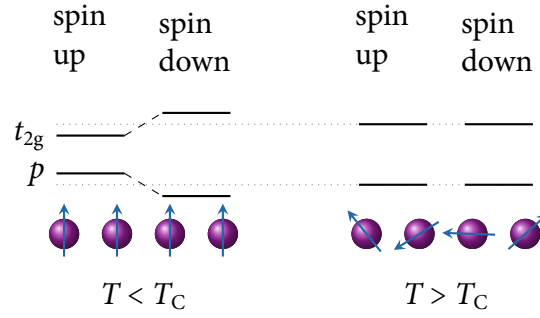
Figure 7.2: Schematic picture of the paramagnetic approximation:[188] Below the Curie temperature T_C (left), the magnetic moments are aligned which yields a small magnetic polarization of the p and t_{2g} levels for the different spin channels. Increasing the temperature above T_C, the moments rotate randomly, so that in average the polarization of the p and t_{2g} states disappears.

1 meV. In particular, we optimized the FLAPW basis set as well as the *mixed product basis* (MPB) with respect to the size of the k-point mesh, the plane-wave and angular-momentum cutoffs, the included unoccupied local orbitals and the number of bands (cf. Chap. 4). We list the converged parameters for the primitive unit cell consisting of two atoms in Table 7.1. For the larger unit cells involved in the anti-ferromagnetic calculations, we adjusted the k-point mesh so that the k-point density remains the same. In addition, we increased the number of bands according to the increase in the number of electrons.

We fit total energies obtained for different lattice constants to a Murnaghan equation of state[145] to determine the theoretically optimized lattice constant and the bulk modulus. We approximate the real eigenvalues by their Kohn-Sham counterpart (see Sec. 4.1). Hence, we calculate the direct and indirect band transitions as energy difference of Kohn-Sham eigenvalues at the same, and at two different k points, respectively. The paramagnetic configuration is more difficult to assess from first principles, as the thermal fluctuations driving the ferromagnetic to paramagnetic transition are not included in the calculation. To compare to experimental results which are obtained at room temperature, Larson *et al.*[188] developed a practical approximation to extract the paramagnetic state from DFT results. We illustrate the idea in Fig. 7.2. Below the phase transition temperature T_C the moments of the rare-earth $4f$ states are aligned. Each moment induces a small polarization on the d-t_{2g} levels and the p states. At temperatures above T_C, the moments of the rare-earth atoms fluctuate randomly which yields an overall vanishing magnetization. The magnetic
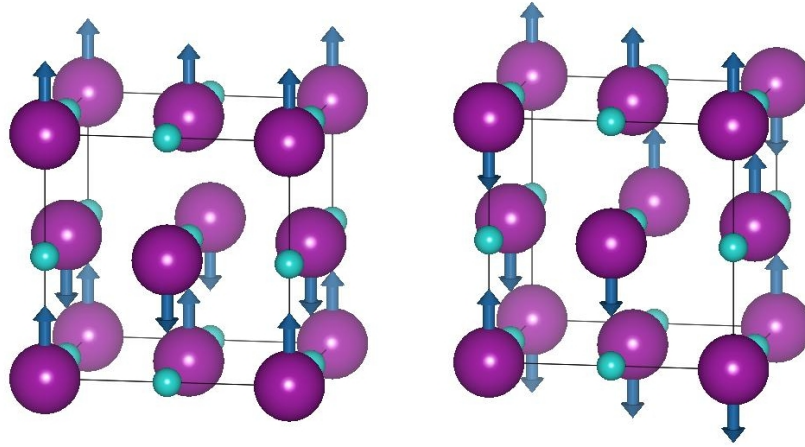
Figure 7.3: Antiferromagnetic unit cells: On the left the AFM-I structure is shown, where the magnetic moment alternates along the crystallographic [001] direction. In the AFM-II structure (right), the magnetic moment flips in neighboring planes orthogonal to the crystallographic [111] direction.

polarization induced on the other states disappears. Thus, the approximate eigenvalue of a particular state above the Curie temperature is given by the average of the corresponding spin-up and spin-down energies in the ferromagnetic phase.[29,188]

From first principles, we determine the critical temperature by mapping total energies onto a classical Heisenberg spin Hamiltonian

$$\mathcal{H} = -\frac{1}{2} \sum_i \boldsymbol{S}_i \left(J_1 \sum_{j=\text{nn}} \boldsymbol{S}_j + J_2 \sum_{j=\text{nnn}} \boldsymbol{S}_j \right) \tag{7.1}$$

with normalized spin vectors $\boldsymbol{S}_i$ and $\boldsymbol{S}_j$ including nn and nnn interaction. The corresponding coupling constants J_1 (nn) and J_2 (nnn) favor ferromagnetism, if they are positive and antiferromagnetism otherwise.[29] Following the work of Duan *et al.*,[196] we evaluate the coupling constants by calculating the unit cells depicted in Fig. 7.3. The energy difference between FM and AFM configuration is directly related to the coupling constants. In the first structure (AFM-I), the magnetic moments are ordered ferromagnetically in planes orthogonal to the [001] direction, whereas neighboring planes are coupled antiferromagnetically. The second structure (AFM-II) is defined analogously by planes orthogonal to the [111] direction. We evaluate both structures in their primitive unit cell, which has a twice as large volume as that of the primitive unit cell of the FM structure. The energy of the FM state is addition-

ally evaluated for the structure of the AFM configurations, to ensure a reliable total energy difference.

Employing the classical Heisenberg spin Hamiltonian (Eq. (7.1)) to these structures, we obtain the following expressions for the energy differences between FM and AFM structure

$$\Delta E_{\mathrm{I}} = E_{\mathrm{AFM,I}} - E_{\mathrm{FM,I}} \quad = 8J_1 \quad \text{and} \tag{7.2a}$$

$$\Delta E_{\mathrm{II}} = E_{\mathrm{AFM,II}} - E_{\mathrm{FM,II}} = 6J_1 + 6J_2. \tag{7.2b}$$

From these equations obtaining the coupling constants J_1 and J_2 is straightforward. With these coupling constants, we have access to the determination of the critical temperature T_{C} by three different methods:

Mean field approximation (MFA) assumes that the effect on a single spin can be condensed into an average field.[154] The probability of obtaining a certain spin state S is proportional to the Boltzmann factor $\exp[-E/k_{\mathrm{B}}T]$. Without external field, the energy is given as

$$E = \frac{1}{2}(J_1 N_{\mathrm{nn}} + J_2 N_{\mathrm{nnn}})\overline{S} \cdot S, \tag{7.3}$$

with the mean spin $\overline{S}$, the number of nn N_{nn}, and the number of nnn N_{nnn}. For a classical spin this leads to an implicit equation for the average spin $\overline{S}$

$$\overline{S} = \mathrm{L}\left[\frac{1}{2k_{\mathrm{B}}T}(J_1 N_{\mathrm{nn}} + J_2 N_{\mathrm{nnn}})\overline{S}\right], \tag{7.4}$$

with the Langevin function L. We expand the right-hand side to determine the smallest temperature for which a non-zero solution for $\overline{S}$ exists and find

$$T_{\mathrm{C}}^{\mathrm{MFA}} = \frac{J_{\mathrm{eff.}}^{\mathrm{MFA}}}{3k_{\mathrm{B}}}, \tag{7.5}$$

with an effective coupling constant $J_{\mathrm{eff.}}^{\mathrm{MFA}} = N_{\mathrm{nn}}J_1 + N_{\mathrm{nnn}}J_2 \overset{\mathrm{fcc}}{=} 12J_1 + 6J_2$, which subsumes the interaction of all other spins.

Random phase approximation Taking into account magnetic excitations, Bogoliubov and Tyablikov[197] developed the random phase approximation (RPA) that yields[198] a Curie temperature of

$$T_{\mathrm{C}}^{\mathrm{RPA}} = \frac{J_{\mathrm{eff.}}^{\mathrm{RPA}}}{3k_{\mathrm{B}}}. \tag{7.6}$$

This equation is formally similar to the MFA (Eq. (7.5)) and the details of the approximation are combined into a modified effective coupling constant

$$J_{\text{eff.}}^{\text{RPA}} = \left[\int_{\text{BZ}} \mathrm{d}^3 q \, \frac{1}{J(\boldsymbol{0}) - J(\boldsymbol{q})} \right]^{-1}, \tag{7.7}$$

where the integral is evaluated on a discrete mesh of $\boldsymbol{q}$ points within the Brillouin zone (BZ),[29,121] and $J(\boldsymbol{q})$ is the Fourier transform of the exchange coupling constants

$$J(\boldsymbol{q}) = \sum_{\text{nn}} J_1 \, \mathrm{e}^{\mathrm{i}\boldsymbol{q}\cdot\boldsymbol{R}_{\text{nn}}} + \sum_{\text{nnn}} J_2 \, \mathrm{e}^{\mathrm{i}\boldsymbol{q}\cdot\boldsymbol{R}_{nnn}}, \tag{7.8}$$

with the positions of nn $\boldsymbol{R}_{\text{nn}}$ and of nnn $\boldsymbol{R}_{\text{nnn}}$.

Monte Carlo simulation The third employed method is a Monte-Carlo (MC) simulation,[199] which we apply to a $20{\times}20{\times}20$ supercell ($N_{\text{tot}} = 8000$ spins) initialized with random magnetic moments. A sampling step consists of the successive random selection of N_{tot} spins (a spin may be selected more than once). The selected spin will be changed to a different state, with a probability of $p = \mathrm{e}^{-\Delta E / k_{\text{B}} T}$, where ΔE is the energy difference between the current and the new state. Hence, if the new state is energetically favorable ($\Delta E < 0$), the spin will be modified certainly. After 5000 of these sampling steps, we determine the total magnetization M of the simulation box and the specific heat C. We repeat this procedure for different temperatures and determine the Curie temperature by the disappearance of the magnetization and a peak in the specific heat in the $M - T$ and $C - T$ plots, respectively.

7.3 Gadolinium nitride

We turn to the results for bulk GdN. In Table 7.2, we show some of the available experimental data[189–191,193,202,203] and theoretical results obtained with the LSDA+U method[188,189,200] and the B3LYP functional[42] in comparison to our HSE hybrid functional calculations.[29] The experimental lattice constant of 4.988 Å is accurately predicted by the parameter-free HSE functional (4.967 Å). The small discrepancy might arise from thermal expansion, as the theoretical result corresponds to a temperature of 0 K. To our knowledge the linear expansion coefficient α of GdN is unknown. If we employ the thermal expansion coefficient of related EuO ($\alpha = 13 \cdot 10^{-13}\,\text{K}^{-1}$), we obtain an estimate of 4.969 Å at 0 K in almost perfect agreement with our result of 4.967 Å. This highlights the advantage of the hybrid functional approach over

Table 7.2: We compare our results for GdN obtained with the HSE functional[29] with experimental and theoretical works from the literature. The columns in that the lattice constant is printed in gray the band gaps and the magnetic moment are calculated at the experimental lattice constant. In the other columns, the theoretically optimized lattice constants was employed.

	HSE this work		Ref. 200[a]	LSDA+U Ref. 188[b]	Ref. 189[b]	B3LYP Ref. 42[c]	Expt.
lattice constant (Å)	4.988	4.967	4.92	5.08	4.988	5.05	4.988[d]
bulk modulus (GPa)		164		150		159	192[e]
magnetic moment (μ_B)	6.99	6.99		6.93		7.0	6.88[f]
direct gap at X							
below T_C (eV)	0.90	0.85	−0.16		0.91	1.18	0.90[g]
above T_C (eV)	1.17	1.11	0.10	0.98	1.30	1.77	1.31[g]
indirect gap $\Gamma \rightarrow$ X							
below T_C (eV)	0.01	−0.06	−0.45	0.14	0.43	0.72	
above T_C (eV)	0.90	0.85	−0.13	0.69	0.98	1.47	
position of 4f peak							
majority (eV)	−6.00	−6.00	−7.8	−8.1		−6.3	−7.8[h]
minority (eV)	6.05	6.05	6.6	5.0	4.8	5.5	5.5 to 6.1[i]

[a] U optimized for bulk Gd (Ref. 201). [b] U chosen to reproduce the experimental bandgap of paramagnetic GdN. [c] We compare to the insulating solution, which is most similar to our results. [d] Reference 202; at room temperature. [e] Reference 193. [f] Reference 190. [g] Reference 189. [h] Reference 191. [i] Reference 203; measured for GdX (X = P, As, Sb, and Bi).
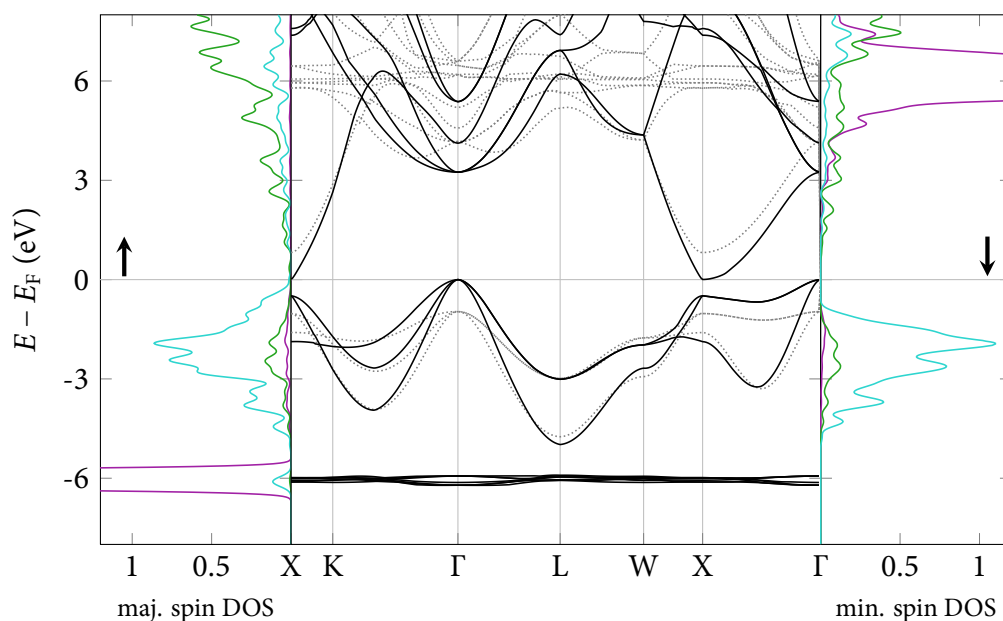
Figure 7.4: Results for GdN obtained with the HSE functional at the experimental lattice constant. The orbital- and spin-resolved density of states (DOS) shows the Gd 4f and 5d states as purple and green lines, respectively. The cyan lines represent the N 2p states. In the electronic band structure in the center features the majority (black, solid) and the minority (gray, dotted) bands.

the LSDA+U method, in which a change of the parameter U strongly impacts the predicted lattice constant. Depending on the choice of U an underestimation of the lattice constant (4.92 Å)[41] or an overestimation (5.08 Å)[188] is observed. Within the B3LYP hybrid functional, which does not improve the lattice constant of solids over the PBE functional,[204] three different states are observed.[42] Two of the states are semi-metallic in either majority or minority spin channel and close in energy. In both cases the 4f states of Gd hybridize with the 2p states of N and the lattice constant is significantly larger than in experiment. Only the third, insulating solution is similar to our theoretical results. Thus, we compare only to this state in Table 7.2, though it is considerably higher in energy ($\sim$ 2.4 eV) in B3LYP.[42]

We focus now on the electronic properties of GdN. In Fig. 7.4, we present[29] the band structure of GdN calculated at the experimental lattice constant of 4.988 Å. The flat features at −6 eV and +6 eV illustrate the strong localization of the 4f states in the majority and minority spin channel, respectively. The position of the 4f states agrees well with available experimental data for the occupied states −7.8 eV[191] and

for the typical position of the unoccupied ones 5.5 – 6.1 eV in the Gd pnictides.[203] This presents a significant improvement over the local PBE functional,[14] where the majority $4f$ state is found at −3.1 eV. In the B3LYP hybrid functional[42] the positions of the $4f$ states (−6.3 eV and 5.5 eV) are similar as in our calculations. A better agreement can be obtained in LSDA+U schemes,[188,189] where the position of this state is directly controlled by the optimized choice of U (cf. Table 7.2).

An extensive discussion in the literature focuses on the electronic structure at low temperatures. Figure 7.4 reveals an intriguing feature in the vicinity of the Fermi level. The N occupied $2p$ states at the Γ point have almost the same energy as the unoccupied Gd $5d$ states at the X point. Hence, tiny changes in the structure induced by dopants or defects may turn the material either semiconducting or semi-metallic, which explains the experimental evidence for both configurations.[36–39,187] Our results indicate a tiny indirect band gap of 0.01 eV in the majority spin channel at the experimental lattice constant. Employing the quasiparticle self-consistent GW method, Chantis et al.[205] predict a similar band gap of 0.05 eV. We find that a small decrease of the lattice constant, which is probably within the range of thermal expansion, is sufficient to close this gap, so that the material becomes semi-metallic. Formally defining the "band gap" as difference of the eigenvalue of the $5d$ states at X and the $2p$ at Γ, we obtain a negative value. The gap in the minority spin channel amounts to 1.5 eV, so that we expect no qualitative change upon doping. Experimentally accessible by optical excitations are only the direct band transitions, of which the smallest one appears at the X point. We predict a direct band gap of 0.90 eV and 0.85 eV in the majority channel at the experimental lattice constant and the theoretically optimized one, respectively. Considering the systematic difficulties of predicting band gaps with DFT,[122,123] both values are in very good agreement with the experimental observation[189] of 0.90 eV. Comparing to previous theoretical results in Table 7.2, we find a good agreement with the results where the U parameter was chosen to reproduce the experimental band gap.[188,189] The indirect band gap obtained with these schemes is, however, larger than the one we obtain. Duan et al.[41] find a half-metallic solution, which undergoes subsequent phase transitions to semi-metallic and semiconducting under isotropic expansion. In contrast to our results, where a small change of the lattice constant by 0.5% induced a transition, Duan et al.[41] determine the boundary of the semi-metallic to semiconducting phase transition at a 14% enlarged lattice constant. The hybrid B3LYP functional yields[42] a non-ground-state solution with a related band structure, although all band transitions are significantly larger than in our calculations.

At room temperature, the coupling between the $4f$ magnetic moments is overcome by thermal fluctuations. We compare our results to the experiments conducted at the room temperature using the paramagnetic approximation (see above). All

Table 7.3: Energy differences ΔE (meV) between FM and AFM configuration according to Eq. (7.2), magnetic coupling constants J_1 and J_2 (meV), and Curie temperature T_C (K) for bulk GdN. The Curie temperature is determined with the mean-field approximation (MFA), the random-phase approximation (RPA), and a Monte-Carlo (MC) simulation.

	ΔE_I	ΔE_II	J_1	J_2	T_C^MFA	T_C^RPA	T_C^MC
This work	8.8	7.6	1.09	0.17	55	42	45
Duan et al.[a]	6.7	4.2	0.84	−0.14	36	26	28
Mitra et al.[b]	3.4	0.4	0.42	−0.36	11	5	6

[a] Reference 196.   [b] Reference 206.

band transitions in the paramagnetic phase shift towards larger values. The magnitude of the shift for the direct band gap ~ 0.27 eV is comparable to the experimentally observed one of 0.41 eV. The deviation is overestimated, as we do not account for the effect of thermal expansion of the lattice in DFT. Comparing the band transitions at the theoretically optimized lattice constant with the ones obtained in the experimental structure, we can estimate the magnitude of the thermal effects to enlarge the shift by ~ 0.06 eV. We stress that this accurate description of the experimental values is achieved without a tunable parameter. In contrast, the LSDA+U calculations either show a significantly larger deviation[41,200] or choose the parameter U such that the experimental band gap is reproduced.[188,189]

Next, we consider the magnetic properties of GdN. In particular, we focus on the Curie temperature, which is experimentally found at $T_C = 58$ K.[193] Below this temperature the magnetic moments of the Gd atoms align ferromagnetically. The magnetic moment per Gd atom amounts to $6.88\,\mu_\mathrm{B}$ determined from the saturation magnetic moment.[190] We obtain a total magnetic moment of $7\,\mu_\mathrm{B}$ which originates mainly in the Gd f states. Comparing the HSE to the PBE functional,[29] we observe an increase of the Gd $4f$ moment by $90\,\mathrm{m}\mu_\mathrm{B}$ from $6.78\,\mu_\mathrm{B}$ to $6.87\,\mu_\mathrm{B}$, a decrease of the Gd $5d$ moment by $20\,\mathrm{m}\mu_\mathrm{B}$ from $90\,\mathrm{m}\mu_\mathrm{B}$ to $70\,\mathrm{m}\mu_\mathrm{B}$, and an increase of the N $2p$ moment, which is aligned antiparallel to the Gd $4f$ moment, by $20\,\mathrm{m}\mu_\mathrm{B}$, from $-100\,\mathrm{m}\mu_\mathrm{B}$ to $-120\,\mathrm{m}\mu_\mathrm{B}$. We conclude that the magnetic moment of Gd is in good agreement with the experimental observation (see Table 7.2).

In Table 7.3, we compare our results for the energy differences, the coupling constants, and the Curie temperature with results from the literature.[196,206] We find that the HSE hybrid functional increases the energy differences between FM and AFM configuration by roughly 2 meV compared to the LSDA+U calculation of Duan et al..[196] The differences are even larger comparing our results to the ones obtained

by Mitra and Lambrecht.[206] These larger values give a stronger calculated nn coupling and a qualitative difference in the nnn coupling. While we find a coupling favoring an FM alignment, the nnn interaction favors an AFM configuration in the LSDA+U results. The larger coupling constants in hybrid functionals lead to a higher Curie temperature in closer agreement to experimental observations. We obtain a Curie temperature of 55 K in the MFA, which is reduced to 42 K or 45 K employing the RPA or a MC simulation, respectively. There are several possible sources os errors:[29] (i) The convergence of the total energy up to 1 meV translates to a difference in the Curie temperature of 3 K. (ii) The neglect of third nearest neighbor interactions amounts to a change in the Curie temperature of below 1 K. We base this estimation employing the coupling constants of Duan *et al.*.[196] The comparison of the MC result incorporating or neglecting third nearest neighbor exchange gives rise to the same Curie temperature of 28 K. (iii) The systematic error due to the selection of a specific exchange-correlation functional is difficult to assess, because the exact solution is computationally too expensive for systems containing more than a few electrons. Experimental observations of the Curie temperature report values of 37 K,[192] 58 K,[191,193] 68 K,[36] and 69 K,[207] where the absolute value varies depending on film thickness, strain, grain size, stoichiometry, and N vacancies.[208,209] Considering the range of experimental observations and the small error bars associated with the theoretical results, we conclude that our results[29] are in very good agreement with the experimental situation.

7.4 Europium oxide

In this section, we present our results for bulk EuO. In Table 7.4, we compare the results of our hybrid-functional calculations with theoretical[172,210] and experimental[171,211,212] ones from the literature. We obtain a lattice constant of 5.120 Å, which matches accurately the experimental one of 5.127 Å[211] obtained at 4.2 K. Within the LSDA+U approach the lattice constants (5.14 Å[210] and 5.1578 Å[172]) are closer to the room-temperature lattice constant of 5.141 Å.[171] Our prediction for the bulk modulus matches the experimental values (considering their variations).

Next, we turn to the electronic structure. In Fig. 7.5, we depict the electronic band structure of EuO obtained with Wannier interpolation[213–215] of the screened HSE functional at the theoretically optimized lattice constant of 5.120 Å. In the majority spin channel the smallest band gap is of indirect nature between the Γ and the X point. The transition occurs between the occupied 4f and the unoccupied 5d states. In the minority spin channel the 4f levels are unoccupied, so that the band gap is a direct one between the filled oxygen 2p and empty europium 5d band. The

Table 7.4: Comparison of our results with the PBE0 and HSE hybrid functional for EuO with those from LSDA+U calculations and experiment. The theoretical results are evaluated at the room temperature lattice constant, except for the optimized lattice constant and the bulk modulus.

	this work			Expt.
	PBE0	HSE	LSDA+U	
lattice constant (Å)	5.120	5.120	5.14,[a] 5.1578[b]	5.141,[c,d] 5.127[e]
bulk modulus (GPa)	95.8	93.0		91 to 110[e]
$f \to$ CB (eV)			0.7[b,f]	1.12[c,f]
$\Gamma \to \Gamma$	2.13	1.42	0.64[a]	
$\Gamma \to$ X	0.91	0.23	0.98[a]	
X $\to$ X	1.17	0.36	1.17[a]	
$p \to$ CB (eV)	4.71	4.02	3.8,[a] 3.5[b]	3.9 to 4.1[e]
bandwidth p (eV)	2.26	2.23	2.0,[a] 1.9[b]	3.0[c]
magnetic moment (μ_B)	6.90	6.90		6.80[f]
J_1 (meV)	2.37	2.52	1.95,[a] 1.79[b]	1.44 to 2.04[e]
J_2 (meV)	0.80	0.89	0.60,[a] 0.52[b]	-0.30 to $+0.70$[e]
T_C (K)	107	115	85,[h] 78[i]	64.2[d], 69.1 to 70.3[e]

[a] Reference 210. [b] Reference 172. [c] Reference 171. [d] At room temperature. [e] Reference 211 and references therein. [f] Position in reciprocal space not specified. [g] Reference 212. [h] Monte-Carlo simulation based on coupling constants of Ref. 210. [i] Monte-Carlo simulation based on coupling constants of Ref. 172.

exchange splitting, which averages to 0.9 eV for the 5d and 0.1 eV for the 2p states, is induced by the magnetic moment of the 4f electrons. The band structure obtained with the PBE0 functional shares the features of the HSE-functional one, except that the conduction band in PBE0 is shifted upwards by 0.7 eV. The smallest direct band transition, which is comparable to optical experiments, is found at the X points and amounts to 1.02 eV and 0.36 eV for PBE0 and HSE, respectively. Hence, the experimental band gap of 1.12 eV[171] is underestimated. If we account for the disappearance of the magnetic polarization above the Curie temperature (see Fig. 7.2), the paramagnetic direct band gaps amount to 1.56 eV (PBE0) and 0.88 eV (HSE). Within the LSDA+U scheme incorporating a Hubbard U for f and d states, a qualitatively different behavior is found: Larson and Lambrecht[210] find that the smallest band gap is of direct nature and resides at the Γ point. Both calculations agree that the main contribution of the conduction band edge near the Γ-point is of 6s character, whereas the 5d
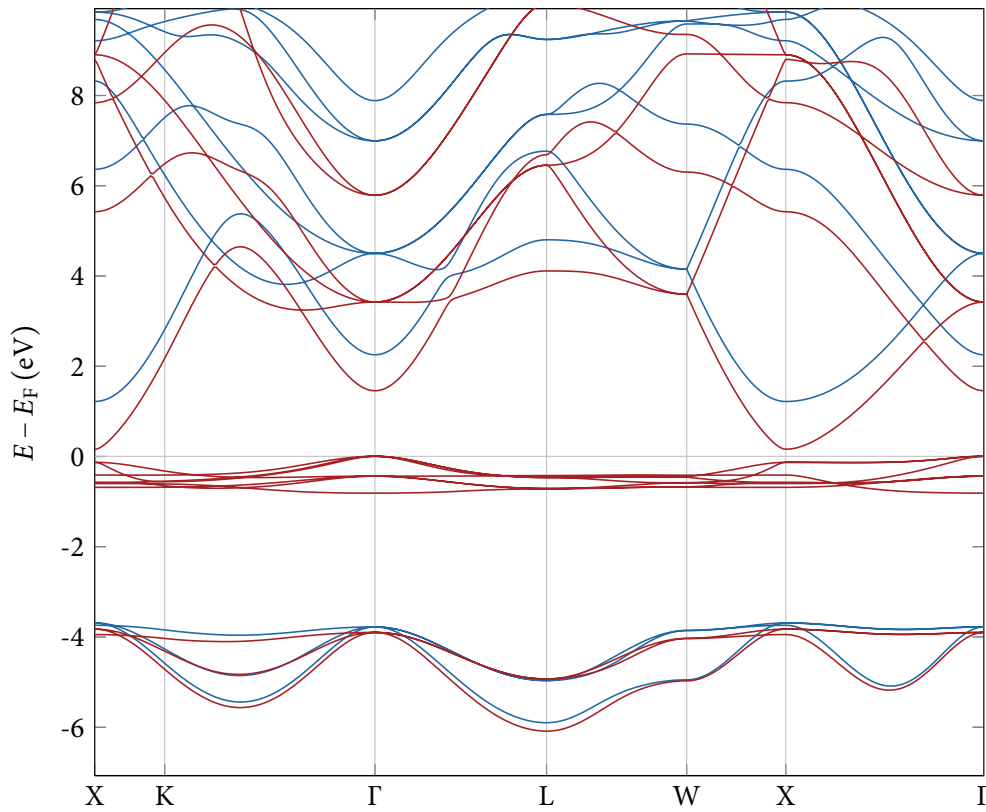
Figure 7.5: Electronic band structure of EuO at the theoretically optimized lattice constant for the HSE hybrid functional. The red lines show the spectrum of the majority states, whereas the minority states are shown in blue.

character is dominant at the X point. Experimental observations[171] suggest, that the transition occurs between $4f$ and $5d$ states, and hence, support our calculations. The energy of the $2p$-to-conduction-band transition is significantly larger with hybrid functionals than with the LSDA+U method. Although the larger value, in particular with the HSE functional of 4.02 eV is in agreement with experimental observations of 3.9 to 4.1 eV,[193] the removal of the magnetic polarization at room temperature would increase our values further, overestimating the experimental situation. Investigating the bandwidth of the $2p$ states, which is experimentally 3.0 eV, we find that all DFT results provide underestimating results. Within the hybrid functional calculations, we obtain slightly larger values of 2.26 eV (PBE0) and 2.23 eV (HSE) than in the LSDA+U method.

Finally, we consider the magnetic properties of EuO. The total magnetic moment

inside the MT sphere of Eu is $6.9\,\mu_B$ close to experimental saturation magnetization of $6.8\,\mu_B$ per Eu atom. As discussed in Sec. 7.2, the coupling constants J_1 and J_2 are determined from energy differences of FM and two AFM configurations. The obtained values of J_1 = 2.37 meV (PBE0) and J_1 = 2.52 meV (HSE) are larger than in the LSDA+U method and in experiment (1.44 meV to 2.04 meV).[193] We observe an analogous overestimation of the second coupling constant J_2, where the experimental range (-0.30 meV to $+0.70$ meV)[193] is exceeded by the hybrid functional calculations (0.80 meV and 0.89 meV for PBE0 and HSE, respectively). The LSDA+U method predicts a coupling constant at the upper end of the experimental range. The larger coupling constants give rise to an overestimation of the Curie temperature. Within the MC simulation, we find a transition at 107 K (PBE0) and 115 K (HSE), whereas the experimental value is close to 70 K.[193] If we employ the coupling constants obtained in the LSDA+U scheme,[172,210] we find a Curie temperature of 74 K to 85 K depending on the specific value of U.

We conclude that the hybrid functionals provide an accurate description of the electronic, structural and magnetic properties of EuO. In contrast to the LSDA+U method no tunable parameter is optimized to achieve this agreement.

7.5   Europium sulfide

The next compound in the europium chalcogenide series is EuS. In Table 7.5, we list the experimental[171,211,212] and numerical[210] results from the literature and compare to the values we obtain with the hybrid functionals PBE0 and HSE. Our DFT calculations as well as the ones of Larson and Lambrecht[210] obtain very similar lattice constants of 5.97 Å close to the room-temperature lattice constant of 5.968 Å.[171] The bulk modulus of 52.6 GPa and 52.3 GPa for PBE0 and HSE, respectively, is situated within the interval of experimental observations between 50 GPa and 61 GPa.[211]

Turning to the electronic structure, we find a fundamental indirect $\Gamma \to X$ band gap of 1.43 eV (PBE0) and 0.74 eV (HSE), in contrast to the LSDA+U results,[210] in which the fundamental gap is of direct nature. In experiment,[171] an optical gap of 1.65 eV is observed, which is a transition between $4f$ and $5d$ states. In the numerical results, the direct transition between states of this orbital character is found at the X point. In the ferromagnetic phase, it amounts to 1.68 eV (0.99 eV) with the PBE0 (HSE) functional. The LSDA+U result[210] for the direct $X \to X$ transition of 2.89 eV is significantly larger than the experimental gap. In the paramagnetic phase, the magnetic polarization of the d states is removed, so that the band gap is increased to 1.99 eV and 1.29 eV in the PBE0 and HSE functional, respectively. All in all, the hybrid functionals improve the agreement with the experimental gap of 1.65 eV in

Table 7.5: Comparison of our results with the PBE0 and HSE hybrid functional for EuS with those from LSDA+U calculations and experiment. The theoretical results are evaluated at the room temperature lattice constant, except for the optimized lattice constant and the bulk modulus.

	this work		LSDA+U^a	Expt.
	PBE0	HSE		
lattice constant (Å)	5.969	5.970	5.97	5.968,[b,c] 5.951[d]
bulk modulus (GPa)	52.6	52.3		50 to 61[d]
$f \to$ CB (eV)				1.65[b,e]
$\Gamma \to \Gamma$	3.22	2.52	1.75	
$\Gamma \to$ X	1.43	0.74	2.49	
X $\to$ X	1.68	0.99	2.89	
$p \to 5d/6s$ (eV)	4.17	3.47	3.3	2.3[d]
bandwidth p (eV)	2.30	2.25	1.7	2.3[b]
magnetic moment (μ_B)	6.97	6.97		6.87[f]
J_1 (meV)	0.86	0.91	0.62	0.54 to 0.64[d]
J_2 (meV)	−0.16	−0.11	−0.68	−0.16 to −0.34[d]
T_C (K)	28	31	8[g]	16.3 to 16.6[d]

[a] Reference 210.   [b] Reference 171.   [c] At room temperature.   [d] Reference 211 and references therein.   [e] Position in reciprocal space not specified.   [f] Reference 212.   [g] Néel temperature based on Monte-Carlo simulation employing the coupling constants of Ref. 210.

the paramagnetic phase. The transition from the lower lying 3p states to the conduction band is significantly overestimated by all theoretical methods. An inclusion of the paramagnetic approximation would increase this mismatch further. The experimental bandwidth of 2.3 eV is quite accurately described by the hybrid functional approach. The LSDA+U method estimates[210] a smaller bandwidth of 1.7 eV.

Next, we focus on the magnetic structure of EuS. The theoretical magnetic moment of EuS is 7 μ_B. Almost all of this originates in the spin polarization of 6.97 μ_B within the Eu-MT sphere. The experimental magnetic moment[212] of 6.87 μ_B is close to the theoretical estimate. The experimental coupling constant between nn J_1, which lies in the range of 0.54 meV to 0.64 meV, is overestimated by approximately 0.3 meV in hybrid functionals. The LSDA+U result[210] of 0.62 meV is within the experimental range. The nnn interaction J_2 favors antiferromagnetism and amounts to −0.16 meV (PBE0) and −0.11 meV (HSE), which is close to the experimental observations of −0.16 meV to −0.34 meV.[211] The by-far larger value of $J_2 = -0.68$ meV obtained with

Table 7.6: Comparison of our results with the PBE0 and HSE hybrid functional for EuSe with those from LSDA+U calculations and experiment. The theoretical results are evaluated at the room temperature lattice constant, except for the optimized lattice constant and the bulk modulus.

	this work			Expt.
	PBE0	HSE	LSDA+U^a	
lattice constant (Å)	6.194	6.195	6.20	6.195,^{b,c} 6.176^d
bulk modulus (GPa)	47.1	46.7		48 to 53^d
$f \rightarrow$ CB (eV)				1.80^{b,e}
$\Gamma \rightarrow \Gamma$	2.92	2.25	1.50	
$\Gamma \rightarrow$ X	1.58	0.91	2.71	
X $\rightarrow$ X	1.90	1.22	3.14	
$p \rightarrow$ CB (eV)	3.98	3.30	2.4	2.1^b
bandwidth p (eV)	2.33	2.28	2.3	2.2^b
magnetic moment (μ_B)	6.95	6.95		6.70^f
J_1 (meV)	0.57	0.50	0.30	0.35^b, 0.30^d
J_2 (meV)	−0.35	−0.50	−0.92	−0.30,^{b} −0.24^d
T_C (K)	12	4^g		2.8^b
T_N (K)		4^g	15^h	4.6^b

^{a} Reference 210. ^{b} Reference 171. ^{c} At room temperature. ^{d} Reference 211 and references therein. ^{e} Position in reciprocal space not specified. ^{f} Reference 212. ^{g} Starting point will determine, if system relaxes to FM or AFM configuration. ^{h} Monte-Carlo simulation based on coupling constants of Ref. 210.

the LSDA+U approach[210] leads to the incorrect prediction of an AFM ground state with a Néel temperature of 8 K. In hybrid functionals, the FM ground state is realized. However, the large estimated nn coupling gives rise to an overestimation of the experimental Curie temperature of 16.3 K to 16.6 K.[211] In a MC simulation, we find a transition at 28 K and 31 K with the PBE0 and the HSE functional, respectively.

7.6 Europium selenide

Now, we consider the results for EuSe. In Table 7.6, we compare our hybrid functional calculations with the LSDA+U ones by Larson and Lambrecht[210] and experimental results from the literature.[171,211,212] We find a small overestimation of the experimental liquid-helium lattice constant of 6.176 Å by all numerical works. All

theoretical values are in a very close range to each other and reproduce the room-temperature lattice constant. The obtained bulk modulus of 47.1 GPa (PBE0) and 46.7 GPa is slightly below the range of 48 GPa to 53 GPa observed in experiment.[211]

Next, we focus on the electronic structure of EuSe, in particular the magnitude and nature of the band gap. In optical emission experiments only direct transitions are observable. Wachter[171] suggest that the onset of the absorption corresponds to a transition from the occupied $4f$ states to the unoccupied $5d$ ones. In the LSDA+U method employing a U for f and d states, the smallest band gap occurs at the Γ point, between $4f$ and $6s$ niveaus. In hybrid functional calculations the fundamental band gap is an indirect transition between Γ and X. The lowest-energy optical transition is found at the X point and the character of the states matches the experimental observations. The size of the optical band gap in the PBE0 and the HSE functional amounts to 1.90 eV and 1.22 eV, respectively. To compare to the room-temperature experiments, we include the paramagnetic approximation (see Sec. 7.2). The random alignment of the magnetic moments removes the magnetic polarization of the states increasing the optical band gap to 2.18 eV (1.49 eV) for PBE0 (HSE). The experimental band gap of 1.80 eV[171] is reproduced approximately by both hybrid functionals. The lower lying $4p$ states are separated by 3.98 eV (PBE0) and 3.30 eV. Thus, they are bound much stronger than in the LSDA+U scheme[210] (2.4 eV) and in experiment[171] (2.1 eV). This overestimation increases further if we incorporate the paramagnetic approximation to simulate the room-temperature experiments. The band width of the p states is close to the experimental value of 2.2 eV in all numerical calculations.

The magnetic properties of EuSe are listed in Table 7.6. The experimental magnetic moment of $6.7\,\mu_B$[212] is close to the theoretical moment of $7\,\mu_B$ of which $6.95\,\mu_B$ resides inside the Eu-MT sphere. Experimentally the coupling between nn (J_1) and nnn (J_2) is approximately of the same size but of opposite sign, i.e., the nn favor a FM environment whereas the nnn prefer an AFM alignment. This balance is only predicted by the screened HSE hybrid functional, although the coupling strength of 0.50 meV is larger than the experimental one of roughly 0.3 meV. Within the PBE0 functional the absolute value of $J_2 = -0.35$ meV is smaller than the one of $J_1 = 0.57$ meV. In the LSDA+U method the AFM coupling is strongly preferred, because the size of $J_2 = -0.92$ meV is approximately three times larger than the nn coupling $J_1 = 0.30$ meV. In a MC simulation, this leads to a FM arrangement in PBE0 with an ordering temperature of $T_C = 12$ K and an AFM structure in LSDA+U ordering at $T_N = 15$ K. In experiment as well as in the HSE calculations two stable solutions are found. In HSE the ordering appears at 4 K and the random starting point of the MC simulation determines if the system becomes FM or AFM. Experimentally, two successive orderings take place: At the Néel temperature of 4.6 K EuSe adopts an AFM structure that is supplanted by a FM ordering below $T_C = 2.8$ K.

Table 7.7: Comparison of our results with the PBE0 and HSE hybrid functional for EuTe with those from LSDA+U calculations and experiment. The theoretical results are evaluated at the room temperature lattice constant, except for the optimized lattice constant and the bulk modulus.

	this work			Expt.	
	PBE0	HSE	LSDA+U^a		
lattice constant (Å)	6.592	6.600	6.60	$6.598,^{b,c}$	6.576^d
bulk modulus (GPa)	78.5	78.6			36 to 40^d
$f \to$ CB (eV)					$2.00^{b,e}$
$\Gamma \to \Gamma$	3.40	2.70	1.96		
$\Gamma \to$ X	1.67	1.01	2.92		
X $\to$ X	2.19	1.49	3.58		
$p \to$ CB (eV)	3.64	2.96	2.4		2.3^b
bandwidth p (eV)	2.30	2.30	2.1		2.3^b
magnetic moment (μ_B)	6.95	6.97			
J_1 (meV)	0.32	0.34	-0.008		0.08 to 0.27^d
J_2 (meV)	-0.57	-0.56	-1.06		-0.41 to 0.58^d
T_N (K)	8	8	17^f		9.6^b

^{a} Reference 210. ^{b} Reference 171. ^{c} At room temperature. ^{d} Reference 211 and references therein. ^{e} Position in reciprocal space not specified. ^{f} Monte-Carlo simulation based on coupling constants of Ref. 210.

Concluding, we emphasize the improvement of the results obtained with hybrid functionals over previous LSDA+U results. The band transitions adopt a qualitative different nature in agreement with experimental results and the obtained magnetic interactions explain the experimental competition of FM and AFM configuration. The lattice constants are accurately reproduced with overall slightly smaller deviations than the ones obtained in the LSDA+U approach.

7.7   Europium telluride

The EuX compound with the largest chalcogenide atom is EuTe. We present its structural, electronic, and magnetic properties obtained with the hybrid functional calculations in Table 7.7. We compare to LSDA+U[210] and experimental[171,211] results from the literature. The lattice constant of EuTe is experimentally 6.576 Å at 4.2 K and 6.598 Å at room temperature and the numerical results are close to the latter one.

The PBE0 lattice constant of 6.592 Å is slightly smaller than the value of 6.600 Å obtained with the LSDA+U method[210] and the HSE functional. The bulk modulus is strongly overestimated by hybrid functionals. It amounts to 78.5 GPa (78.6 GPa) in PBE0 (HSE), whereas experimentally values between 36 GPa and 40 GPa have been reported.[211]

We turn now to the electronic structure of EuTe. In hybrid functionals, the fundamental band gap is an indirect transition between Γ and X, which amounts to 1.67 eV and 1.01 eV with the PBE0 and HSE functional, respectively. EuTe exhibits the smallest direct band gap of 2.19 eV (PBE0) and 1.49 eV (HSE) at the X point. In contrast to these results, in an LSDA+U approach[210] the fundamental band gap is a direct one of 1.96 eV at the Γ point. In experiments the optical transition occurs between the 4f and the 5d states of Eu. Investigating the orbital character of the different bands, we find that the lowest lying band at the Γ point is formed by 6s orbitals, whereas the 5d contribution dominates at the X point. Thus, we conclude that the hybrid-functional description surpasses the LSDA+U one. To compare to the absolute value of the experimental band gap, we employ the paramagnetic approximation (see Sec. 7.2). The exchange splitting, which amounts to roughly 0.4 eV, is removed by the randomly oriented magnetic moments of the Eu atoms, thus, increasing the direct band gap to 2.42 eV (PBE0) and 1.71 eV (HSE). The experimental observation[171] of 2.0 eV is close to the HSE result. The transition from the 5d niveaus to the conduction band is overestimated by hybrid-functional calculations. Experiments report a value of 2.3 eV, whereas a PBE0 (HSE) calculation results in a transition of 3.64 eV (2.96 eV). This overestimation would increase further, if we incorporate the paramagnetic approximation. The experimental bandwidth of the Telluride 5p levels of 2.3 eV is reproduced by our calculations.

Experimentally, EuTe realizes an AFM-II ground state with a Néel temperature of 9.6 K.[171] This order is driven by a nnn coupling constant, which favors an antiparallel alignment and stronger than the nn coupling. The nn coupling constant of 0.32 meV (PBE0) and 0.34 meV (HSE) is larger than the experimentally observed one of 0.08 meV to 0.27 meV. The nnn interaction is at the upper end of the experimental range of −0.41 meV to −0.58 meV. A different picture emerges from the LSDA+U approach:[210] The nn coupling vanishes almost completely and favors an AFM configuration and the nnn coupling is almost twice as large as the one obtained with hybrid functionals. As a consequence, the Néel temperature is overestimated in an MC simulation. In contrast, if we employ the results of the hybrid-functional calculations, we find a Néel temperature of 8 K. The precision of 1 meV in the energy differences corresponds to a possible error of 3 K. Hence, the mismatch between our first principles calculation and experiment is below the numerical and experimental errors.

7.8   Trends in the series

Of technological interest are systematic changes in material properties upon substituting one chalcogenide atom for another. Understanding these trends facilitates the design of desired functionalities by selective choice of the anion. Employing a mixture of different chalcogenides increases the possible phase space. In this section, we will illustrate the experimental trends that are captured by hybrid-functional DFT. This provides a comprehensive review of where these novel functionals supplant conventional DFT+U approaches and where these approaches are complementing each other.

In Table 7.8, we collect the results we obtained with the hybrid functionals for the europium chalcogenides and compare to available experimental data.[171,211] Increasing the size of the anion gives rise to larger lattice constants. This trend in sign and magnitude is accurately captured by DFT. Except for EuO the numerical results overestimate the experimental lattice constant slightly by an amount similar to the thermal expansion from 4.2 K to room-temperature. Throughout the series the experimental bulk modulus decreases from (101 ± 10) GPa in EuO to (38 ± 2) GPa in EuTe. For the first three compounds, the bulk modulus obtained with PBE0 and HSE is in good agreement with the experiment data, though systematically towards the bottom of the experimental range. However, hybrid functionals exhibit a strong overestimation of the bulk modulus for EuTe.

Next, we focus on the electronic structure and realize two experimental trends. The first one is illustrated in Fig. 7.6: The optical gap to the conduction band increases from 1.12 eV in EuO to 2.00 eV in EuTe. The FM gap predicted by PBE0 functional is close to the experimental results. Incorporating the paramagnetic approximation increases the gap to overestimating values. The HSE functional provides smaller band gaps, which approach the experimental value in the paramagnetic approximation. For all materials, hybrid functionals predict a transition from f to d levels, in agreement with experimental observations and in contrast to LSDA+U calculations.[210] The second trend (cf. Table 7.8) is the reduction of the gap between the valence p electrons and the conduction band from the value of 4.0 eV in EuO to 2.3 eV in EuS and to 2.1 eV in EuSe. For EuTe, a the band gap enlarges to 2.3 eV. In Fig. 7.6, we depict the position of the p state relative to the $4f$ band. In both hybrid functional, the position of the p is almost identical. Compared to the experiment, both functionals underestimate the loosening of the binding of these states across the series. We note, that DFT yields an almost constant bandwidth of the p states, which amounts to roughly 2.3 eV. In contrast, EuO exhibits a larger bandwidth of 3.0 eV in experiments.[171]

Throughout the series, the magnetic coupling between the nn Eu $4f$ moments

Table 7.8: Collection of our hybrid functional results for the europium chalcogenide series and comparison to available experimental data.[a] All results other than the lattice constant a and the bulk modulus B are given for the experimental room temperature lattice constant. The bandwidth (BW) of the $2p$ states and the direct band transitions are calculated as differences of Kohn-Sham eigenvalues.

	EuO			EuS			EuSe			EuTe		
	PBE0	HSE	Expt.	PBE0	HSE	Expt.	PBE0	HSE	Expt.	PBE0	HSE	Expt.
a (Å)	5.120	5.120	5.127	5.969	5.970	5.951	6.194	6.195	6.176	6.592	6.600	6.576
B (GPa)	95.8	93.0	101	52.6	52.3	56	47.1	46.7	51	78.5	78.6	38
$f \to$ CB (eV)	1.02	0.36	1.12	1.68	0.99	1.65	1.90	1.22	1.80	2.19	1.49	2.00
$p \to$ CB (eV)	4.71	4.02	4.0	4.17	3.47	2.3	3.98	3.30	2.1	3.64	2.96	2.3
BW_p (eV)	2.26	2.23	3.0	2.30	2.25	2.3	2.33	2.28	2.2	2.30	2.30	2.3
J_1 (meV)	2.37	2.52	1.74	0.86	0.91	0.59	0.57	0.50	0.33	0.32	0.34	0.18
J_2 (meV)	0.80	0.89	0.20	−0.16	−0.11	−0.25	−0.35	−0.50	−0.27	−0.57	−0.56	−0.50
T_C^{MFA} (K)	128	138		36	40		18	12		2	3	
T_C^{MC} (K)	107	115		28	31		12	4				
$T_C^{\mathrm{exp.}}$ (K)			69.7			16.5			2.8			
T_N^{MFA} (K)	−19	−21		4	3		8	12		13	13	
T_N^{MC} (K)										8	8	
$T_N^{\mathrm{exp.}}$ (K)									4.6			9.6

[a] Experimental data taken from Ref. 171, Ref. 211, and references therein. If more than one value is available the average value is depicted.
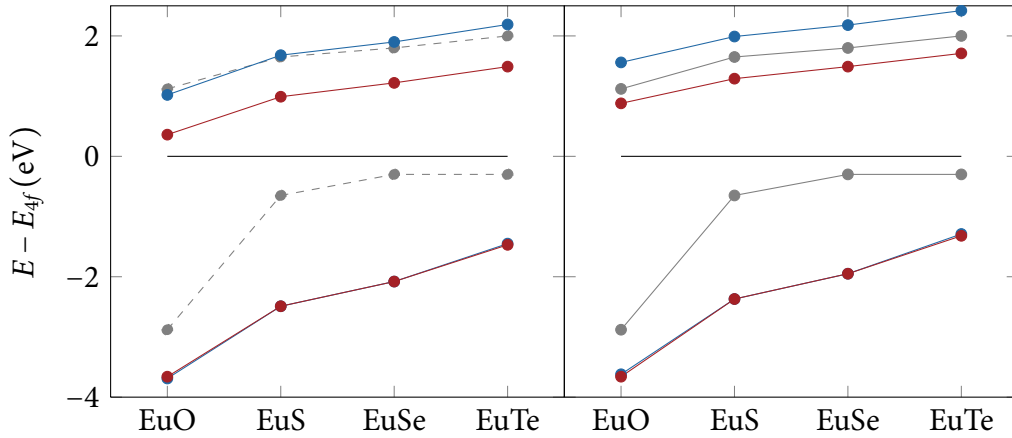
Figure 7.6: Comparison of the Kohn-Sham eigenvalues of the top of the p states (below 0), the top of the valence band (black line), and the bottom of the $5d$ states (above 0) at the X point with experimental results (gray line). The eigenvalues obtained with PBE0 (blue) and HSE (red) are shown on the left side. Including the paramagnetic approximation yields the picture on the right side. The experiments are performed at room temperature (right side). On the left side, we show the same data as dashed line, because the experimental paramagnetic configuration does not directly correspond to the ferromagnetic configuration in the DFT calculations.

weakens. The nnn coupling changes from favoring FM in EuO to favoring AFM in EuS and increases in strength for EuSe and EuTe. Though the absolute value of the coupling is overestimated except for the nnn coupling in EuS, this qualitative trend is well captured by hybrid functionals. Hence, we reproduce the experimental transition from a FM ground state for EuO and EuS, to an ambiguous one in EuSe, and to an AFM one in EuTe. In contrast, LSDA+U calculations predict[210] an AFM state for EuS and overestimate the Néel temperature for EuSe and EuTe. Comparing the different techniques, we find that the MFA to the critical temperature overestimates the more precise value of the MC simulation. However for EuSe, several MC simulations are necessary to reveal whether FM or AFM are stable, as the obtained magnetic state is dependent on the seeding of the random number generator.

7.9   Summary

In this chapter, we applied our implementation of the nonlocal hybrid functionals in the full-potential linearized augmented-plane-wave (FLAPW) method to GdN and

the EuX (X = O, S, Se, and Te) series. For GdN, we find[29] a ground state close to a phase transition: Depending on small changes in the lattice constant, a semi-metallic or semiconducting state is observed. Taking into account the effect of thermal expansion, the theoretically optimized lattice constant fits exactly to the experimental value. We obtained an electronic structure that reproduces the experimentally known band transitions. The magnetic interactions were accurately described as indicated by the good agreement of the theoretical Curie temperature of 45 K (MC simulation) and the experimental value of 58 K.

The investigation of the europium chalcogenides revealed that hybrid functionals successfully predict lattice constants, band transitions and magnetic interactions of these compounds, at least to the accuracy of the LSDA+U method, however without the adjustable U-parameter. For several properties, in particular the nature of the direct band gap and the magnetic interactions, the hybrid functionals provide a better agreement with experimental results.

We emphasize that the employment of hybrid functionals removes an important obstacle in the calculation of the properties of rare-earth materials – the determination of the optimal value for U in a DFT+U scheme. Hence, hybrid functionals facilitate genuine *ab initio* calculations of compounds with strongly localized states. We anticipate their application to the investigation of the subtle dependence of the physical properties of rare-earth compounds on strain, on dopants, on defect concentration, and on the composition of heterostructures.[29]

Cubic Perovskites

8.1   Introduction

For several years, perovskites are investigated as exemplary oxides in which the subtle differences in the composition and lattice parameters can strongly impact the material properties. Historically, the mineral $CaTiO_3$ was named *perovskite* after the Russian mineralogist Perovski. As many materials exhibit the same chemical com-
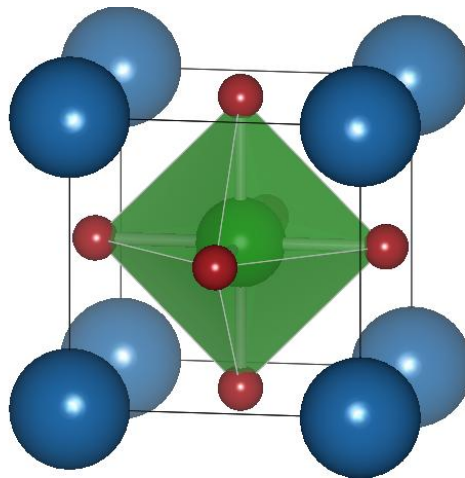
Figure 8.1: Ideal simple ABO_3 cubic perovskite structure. The A-site atoms are shown in blue, the B-site ones in green, and the oxygen atoms in red. The oxygen atom are connected to emphasize the oxygen octahedron.

position ABX_3 as $CaTiO_3$, the name was generalized to all of these materials. Two classes of perovskites can be identified: i) The A and B site are occupied by anion and the X site is occupied by large cations. ii) The A and the B site are occupied by a large cation and the X site by small anions (O, Fl, Cl). Here, we will restrict us to those materials, where the X site is occupied by oxygen atoms. The ideal perovskite structure, which is depicted in Fig. 8.1, exhibits a simple cubic unit cell, where the corners are occupied by A atoms, the center by a B atom, and the face centers by oxygen atoms. Most perovskites show deviations from the perfect cubic unit cell at low temperatures.[a] Frequently these distortions influence the shape or position of the oxygen octahedra.

Perovskites provide a wide variety of material properties, which is driven by the huge number of possible combinations of A- and B-site ions. The potential of inter-mixture of different perovskites, doping of the A and B site, and the combination to heterostructures increases the variation possibilities further. This rich phase-space provides an intriguing area of research motivated by fundamental as well as techno-logical interests. For example, thin films of $La_xCa_{1-x}MnO_3$ show a colossal magneto resistance,[216] which holds out the prospect of more accurate magnetic sensors. The phase diagram of this material shows a metal-to-insulator transition at half mix-ing,[217] from which fundamental insight in the physics of this transition is obtained. At the same mixture the compound changes from an antiferromagnetic (AFM) to a ferromagnetic (FM) arrangement indicating the delicate competition of super and double exchange in doped perovskites. The rare-earth nickelates ($RNiO_3$) exhibit a metal-insulator transition, which is determined by the strength of the coupling of neighboring Ni atoms.[218,219] The bond angle of the Ni-O-Ni bond increases with the size of the rare-earth ion. As a consequence, the coupling between neighboring Ni atoms strengthens, which gives rise to a higher critical temperature for the metal-insulator transition. At low temperatures neighboring Ni ions become nonequiva-lent, which is driven by charge or orbital order.[219] If both order patterns are present, this may give rise to multiferroicity.[220]

In multiferroic materials, a permanent magnetic moment and a permanent elec-tric polarization coexist.[1] A magneto-electric coupling of these orders would enable the electric control of the magnetic ground-state and vice versa the magnetic control of the electric polarization.[2] Even if both orders are present, the coupling between them may be vanishing by symmetry.[221] One distinguishes *proper* and *improper* mul-tiferroicity.[220] In proper multiferroics, both ferroelectric and ferromagnetic order are stable independent of each other so that the coupling between both orders is

---

[a]Naturally, *low temperature* is only a relative expression. For some systems *low* might be as large as several hundreds of K.

usually weak. In improper multiferroics, the presence of order allows the establishment of the other one so that both critical temperatures coincide. These materials are characterized by the strong coupling between both orders, however, their critical temperature is usually very low. Perovskite materials play an important role in this area of research, because several of the model ferroelectrics such as $BaTiO_3$ and $KNbO_3$ have a perovskite structure. However, in these materials, the emptiness of all d orbitals at the B-site atom, the so-called d^0-*ness*, is important for the ferroelectric distortion.[222] Hence, either the magnetic moment has to originate from the A site or a different mechanism has to drive ferroelectricity. The latter is present in the famous $BiFeO_3$ compound, in which the lone-pair electrons of Bi yield the ferroelectric polarization and the magnetic moment originates from the Fe atoms.[57] Ležaić and Spaldin[223] predicted that the combination of the lone-pair-driven ferroelectricity with a mixture of $3d$ and $5d$ materials on the B site gives rise to higher critical temperatures. An example for a material, in which the magnetism originates from the A site, is $EuTiO_3$. Fennie and Rabe[59] suggested that a AFM to FM transition is induced by switching the polarization in strained samples. An important concept for tuning the material properties of perovskites is the so called *strain engineering*. By growing $SrTiO_3$ on $DyScO_3$, Haeni *et al.*[58] induced a strain in the sample turning the material ferroelectric.

The influence of external strain is one of the fields, in which density functional theory (DFT) may direct experiments to the right combination of materials. "Growing" the sample with a different lattice constant is trivial in the numerical methods, whereas it requires cumbersome fine tuning in experiment. However, common exchange-correlation functionals underestimate (LDA) or overestimate (GGA) the lattice constant. Thus, the various theoretically-predicted strain-dependent transitions may appear at a different strain value in experiments. This is a significant limitation of the predictive power of DFT, because the range of possible misfit strains in experiment is limited to roughly three per cent. Furthermore, if one is interested in the optical properties of perovskites, local exchange-correlation functionals do not include a derivative discontinuity[122,123] and underestimate the band transitions drastically. The source of these discrepancies includes the spurious self interaction (see Sec. 2.5) present in local exchange correlation functionals. As hybrid functionals[23,24,26] partly correct for the self interaction via the inclusion of Hartree-Fock (HF) exchange, we expect an improved description of perovskites.

In fact, Heifets *et al.*[224] found an improved description of the termination of the $SrTiO_3$ surface employing the hybrid functionals B3LYP and B3PW. Piskunov *et al.*[225] successfully employed the same hybrid functionals to determine the bulk properties of cubic unit cells of the prototypical titanates $SrTiO_3$, $BaTiO_3$, and $PbTiO_3$. In particular, the lattice constant, elastic constants, and the optical band gap could be

accurately reproduced. The surface termination of these compounds was explored later,[226] providing a good agreement with experimentally determined lattice and optical properties. The B3PW hybrid functional yields an accurate characterization of the antiferrodistortive phase of bulk $SrTiO_3$ in particular the c/a ratio and the rotation of the oxygen octahedra.[227] Investigating $LaMnO_3$, Muñoz *et al.*[228] found a strong dependence of band gap on amount of HF exchange, where the B3LYP functional and the 35% Fock exchange provided a quantitative good agreement to the experimental values. Bilc *et al.*[229] sound a word of caution as in their investigation of $BaTiO_3$ and $PbTiO_3$ the hybrid functionals B3LYP and B1 underperform the local Wu-Cohen (WC) functional,[230] which is optimized for perovskites. Furthermore, the tetragonality is overestimated with nonlocal functionals, which is directly related to the ferroelectric polarization. They suggest the construction of the B1-WC functional,[229] which provides accurate lattice constants for several perovskite materials. Wahl *et al.*[231] found a very accurate description of $SrTiO_3$ and $BaTiO_3$ by the HSE and this B1-WC hybrid functional. In particular the latter yields "exceptionally good ferroelectric displacements and polarizations."[231] Recently, the HSE hybrid functional has been applied to $BiFeO_3$ and $HoMnO_3$.[232] The obtained structural properties agree well with the experimental results and the band transition could reproduce the precise results of the *GW* method. Evarestov[233] examined the BaBO$_3$ series (B = Ti, Zr, Hf) with the parameter-free PBE0 functional and was able to reproduce the experimental lattice constant, cohesive energy, and band gap accurately.

In this chapter, we systematically investigate the performance of the HSE hybrid functional for a series of cubic perovskites and compare to the results of the local PBE functional. Specifically, we have calculated the theoretically optimized lattice constant and the fundamental and optical band gap for $KNbO_3$, $KTaO_3$, $NaNbO_3$, $BaHfO_3$, $BaSnO_3$, $BaTiO_3$, $BaZrO_3$, $CaSnO_3$, $CaTiO_3$, $CaZrO_3$, $CdTiO_3$, $SrHfO_3$, $SrSnO_3$, $SrTiO_3$, $SrZrO_3$, $PbSnO_3$, $PbTiO_3$, $PbZrO_3$, and $LaAlO_3$. We describe the general procedure to set up these structures in Sec. 8.2. Overall, we find that the HSE functional improves the lattice constant with respect to results of local exchange correlation functionals. We illustrate this in Sec. 8.3. We discuss the compensation of the underestimation of the band gap in PBE functional by the inclusion of HF exchange in Sec. 8.4. Finally, we conclude this chapter in Sec. 8.5.

8.2   Computational setup

In this section, we describe the computational setup common to all investigated perovskites. We calculate the ground state of all perovskite by means of DFT. We employ the precise all-electron full-potential linearized augmented-plane-wave (FLAPW)

basis set[31,32,117] as realized in the `Fleur` code.[126] We describe the Kohn-Sham wave functions by a Γ-point-centered $6\times6\times6$ $\boldsymbol{k}$-point mesh and add one additional unoccupied local orbital[120] for each l channel from s to f to improve the description of the conduction band by reducing the linearization error of the FLAPW basis.[119] For some materials, further local orbitals are included to describe semicore states. In these cases, we increase the number of bands employed in the calculation of the hybrid functionals, so that 10 bands per electron are considered. The material-specific numerical parameters, such as the muffin-tin (MT) radius, are listed in the appendix (see Sec. B).

With these parameters, we evaluate the total energy of unit cells at different lattice constants close to the theoretically optimized lattice constant. For each investigated lattice constant, we converge a calculation with the local generalized gradient approximation (GGA) functional PBE.[14] Then, we start the convergence of the nonlocal screened Heyd-Scuseria-Ernzerhof (HSE) hybrid functional[26] from the resulting density and wave functions. The energies E obtained with both functionals are fitted to a Murnaghan equation of state[145]

$$E(V) = E_0 + \frac{B_0 V}{B_0'}\left(\frac{(V_0/V)^{B_0'}}{B_0' - 1} + 1\right) - \frac{B_0 V_0}{B_0' - 1}, \tag{8.1}$$

where E_0 is the ground state energy, V is the volume of the unit cell, V_0 is the volume of the ground-state unit cell, B_0 is the bulk modulus, and B_0' is the derivative of the bulk modulus with respect to the external pressure. The four quantities E_0, V_0, B_0, and B_0' are fitted to the obtained energies, and in the cubic symmetry of these perovskites the determination of the theoretically optimized lattice constant a_0 is straightforward

$$a_0 = \sqrt[3]{V_0}. \tag{8.2}$$

For the calculation of the band gap, we consider the differences of Kohn-Sham eigenvalues. We note that in principle only the fundamental band gap is well defined quantity in the realm of DFT (see Sec. 4.1). Nevertheless, to compare to experimental results obtained with optical excitations, we determine the direct band gap by the differences at specific $\boldsymbol{k}$-points as well. This corresponds to the neglect of excitonic effects.

8.3 Lattice optimization

In Table 8.1, we present our results for the lattice constants of the investigated cubic perovskites in comparison to theoretical and experimental works from the literature. We visualize our data in Fig. 8.2. First, we focus on our GGA calculations

Table 8.1: Lattice constant (Å) obtained with the local PBE and the nonlocal HSE functional in comparison to experimental and theoretical results from the literature.

	This work		Literature		
	PBE	HSE	LDA	GGA	Expt.
I–V compounds					
$KNbO_3$	4.013	3.992	3.956[a]	4.028[a]	4.016[a]
$KTaO_3$	4.032	4.007	3.938[a]	4.033[a]	3.983[a]
$NaNbO_3$	3.975	3.940	3.914[a]	3.952[b]	3.937[a]
II–IV compounds					
$BaHfO_3$	4.201	4.168	4.12[c]	4.20[c]	4.172[d]
$BaSnO_3$	4.176	4.127	4.059[e]	4.192[e]	4.124[f]
$BaTiO_3$	4.011	3.979	3.947[a]	4.028[a]	4.000[a]
$BaZrO_3$	4.221	4.193	4.152[a]	4.207[a]	4.193[a]
$CaSnO_3$	4.038	4.005	3.965[g]		3.947[h,†]
$CaTiO_3$	3.874	3.848	3.809[a]	3.88[i]	3.836[a]
$CaZrO_3$	4.139	4.111		4.138[j]	4.012[k]
$CdTiO_3$	3.873	3.840	3.809[l]	3.888[l]	3.800[a]
$SrHfO_3$	4.139	4.109	4.069[a]	4.157[m]	4.087[n,†]
$SrSnO_3$	4.106	4.051		4.111[o]	4.025[p]
$SrTiO_3$	3.931	3.900	3.862[a]	3.941[a]	3.905[a]
$SrZrO_3$	4.169	4.151	4.10[q]	4.18[q]	4.101[a]
$PbSnO_3$	4.123	4.070			4.070[r]
$PbTiO_3$	3.968	3.930	3.888[a]	3.965[a]	3.969[a]
$PbZrO_3$	4.187	4.155	4.115[a]	4.18[s]	4.133[a]
III–III compounds					
$LaAlO_3$	3.811	3.782	3.739[t]	3.810[t]	3.791[u]
ME[v]	0.049	0.015	−0.033	0.049	
MAE[w]	0.049	0.025	0.037	0.050	
rms[x]	0.058	0.036	0.050	0.059	

[†] Experimentally noncubic structure.
[a] Reference 60 and references therein. [b] Reference 234. [c] Reference 235. [d] Reference 236.
[e] Reference 237. [f] Reference 238. [g] Reference 239. [h] Reference 240. [i] Reference 241.
[j] Reference 242. [k] Reference 243. [l] Reference 244. [m] Reference 245. [n] Reference 246.
[o] Reference 247. [p] Reference 248. [q] Reference 249. [r] Reference 250. [s] Reference 251.
[t] Reference 252. [u] Reference 253.
[v] Mean error. [w] Mean absolute error. [x] Root mean square.
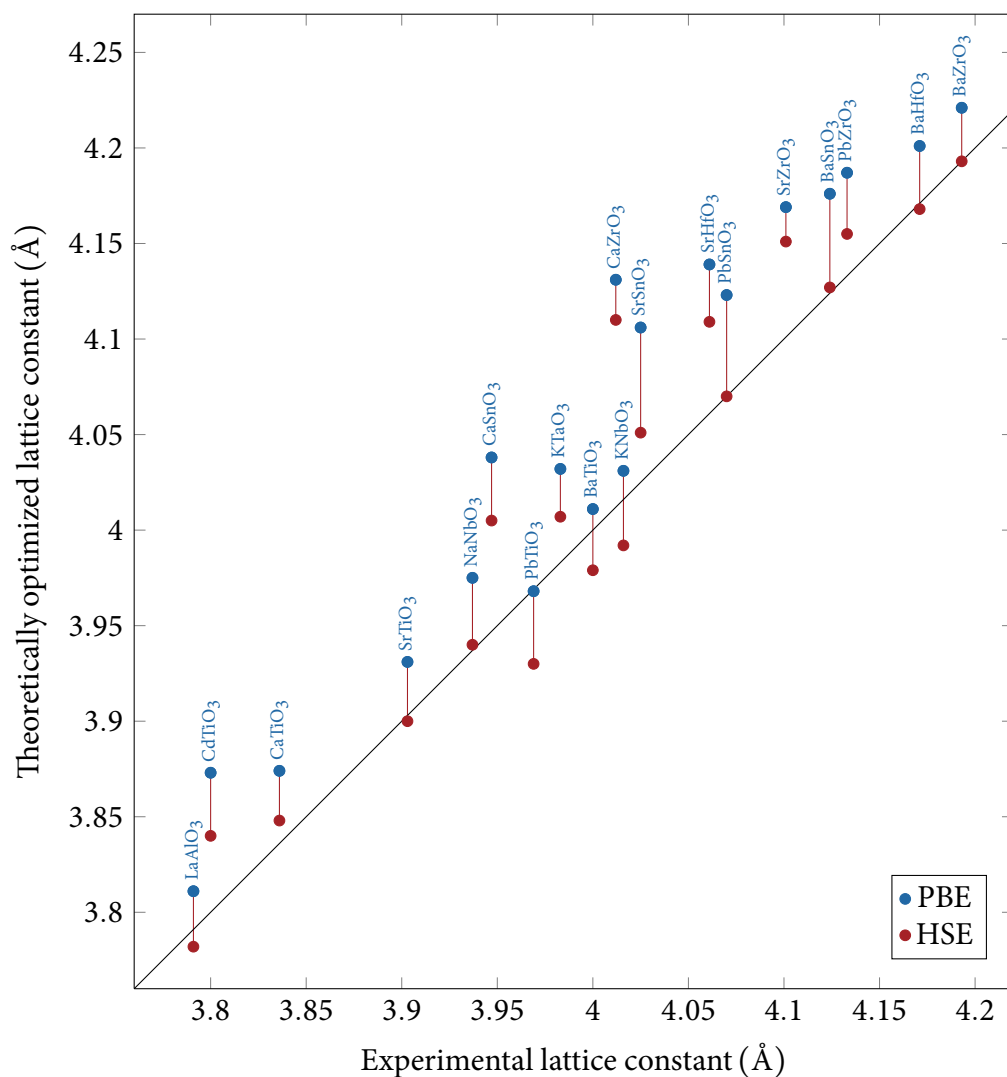
Figure 8.2: Comparison of experimental and theoretically optimized lattice constant for a series of cubic perovskites. The results obtained with the local PBE and the nonlocal HSE functional are shown in blue and red, respectively. The black diagonal line indicates the ideal prediction, where theory and experiment coincide.

employing the PBE[14] functional. Overall, the obtained lattice constants are in good agreement with the experimental ones with the largest overestimation of roughly 3% for $CaZrO_3$. We find similar lattice constants as in other numerical works from the literature, which employ a GGA functional as well. As a trend, PBE overestimates the lattice constant of perovskites by 0.05 Å on average, which results in the mean error (ME) being almost identical to the mean absolute error (MAE). In contrast to this the local density approximation (LDA) with the exceptions of $CaSnO_3$ and $CdTiO_3$ underestimates the lattice constant of the selected materials. The MAE is smaller than the one associated with the GGA functionals.

Next, we turn to the results of our hybrid functional calculations. For most materials the lattice constants are most accurately predicted with the HSE functional. Considering only our data, the PBE functional yields a lattice constant in better agreement with experimental observations only for three ($KNbO_3$, $BaTiO_3$, and $PbTiO_3$) out of 19 materials. If we include the LDA and GGA results from the literature, the HSE functional predicts the most accurate lattice constant for the majority of the materials. We find a reduction of the MAE and the root-mean-square (rms) from 0.049 Å (0.037 Å) and 0.058 Å (0.050 Å) in the PBE (LDA) functional to 0.025 Å and 0.036 Å, respectively. The positive sign of the ME indicates, that in average the HSE functional overestimates the lattice constant, though this trend is not as systematic as for the LDA and GGA functionals. Comparing the results for the II-IV compounds, we find that the lattice constant difference between PBE and HSE is always the smallest for the Zr cation and the largest for Sn one. The change associated with the Ti and Hf cation is comparable. We extract a similar order from the lattice constants considering different A site ions. In the majority of the cases the difference of the lattice constant between the PBE and the HSE functional exhibits the largest value for a Pb cation. For Ca and Sr ions, we find a significantly smaller impact of the hybrid functional. The Ba cation is in between these extrem cases. The notable exception to this rule is $SrSnO_3$, for which the reduction of the lattice constant in hybrid functionals is the largest of all investigated materials.

From the differences in the lattice constants, we extract the relative size of the ions for the A site r_A

$$r_K > r_{Nb} \quad \text{and} \quad r_{Ba} > r_{Pb} > r_{Sr} > r_{Ca} > r_{Cd} \qquad (8.3)$$

and for the B site r_B

$$r_{Ta} > r_{Nb} \quad \text{and} \quad r_{Zr} > r_{Hf} > r_{Sn} > r_{Ti}, \qquad (8.4)$$

which matches the experimental descending order of these ionic radii.[254] Assuming a hard-sphere model, the ionic radius of the B-site ion r_B and the radius of the oxygen

ion r_O determine the lattice constant

$$a_0^B = 2r_B + 2r_O. \tag{8.5}$$

Replacing one B-site ion with another one, the lattice constant changes by

$$a_0^{B'} - a_0^B = 2(r_{B'} - r^B). \tag{8.6}$$

Hence, we can evaluate the ion size relative to one specific B-site cation (Zr) and compare to experimental results. In principle, this value should be independent of the A-site ion. With the HSE functional, we find that the Hf, Sn, and Ti ion are (1.7 ± 0.6) pm, (4.5 ± 0.9) pm, and (12.5 ± 2.1) pm smaller than the Zr ion, respectively. The respective experimental differences[254] of 1 pm, 3 pm, and 11.5 pm compare well to our data.

    The determination of the lattice constants of the perovskites is subject to several approximations. A fundamental one is related to the selection of a specific exchange-correlation functional. As the true functional is unknown, the deviation to the precise result associated to the exchange-correlation functional is not assessable. Furthermore, many of these perovskites realize distortions from the cubic structure which is the ground state at high temperatures. In general, if we include distortions from the perfect cubic symmetry, the crystal will reduce its volume. The most common displacements in the perovskite structure are Jahn–Teller (JT) deformations or rotations of the oxygen octahedra. Additionally, temperature effects and in particular the movement of the ions is neglected in DFT. Employing the thermal expansion coefficient of $SrTiO_3$, which is between $2.16 \cdot 10^{-5}\,\mathrm{K}^{-1}$ and $2.82 \cdot 10^{-5}\,\mathrm{K}^{-1}$,[255] we find that neglect of thermal expansion leads to the underestimation of the experimental room-temperature lattice constant by less than 0.01 Å. Even in low-temperature experiments, zero-point fluctuations will take place, which are removed via the Born-Oppenheimer approximation[76] in DFT. These fluctuations tend to increase the lattice constant due to the inharmonicity of the potential.

8.4 Band transitions in perovskites

The electronic band structures of the investigated perovskite materials share many common features. In Fig. 8.3, we illustrate prototypically the band structure for $SrTiO_3$ and $PbTiO_3$. All materials in this study have either a completely empty or a completely filled d shell, so that the valence states consist of the oxygen p levels. The top of the valence band is extremely flat in particular between the M and the R point with an energy difference of only 0.09 eV in $SrTiO_3$. In most compounds, the
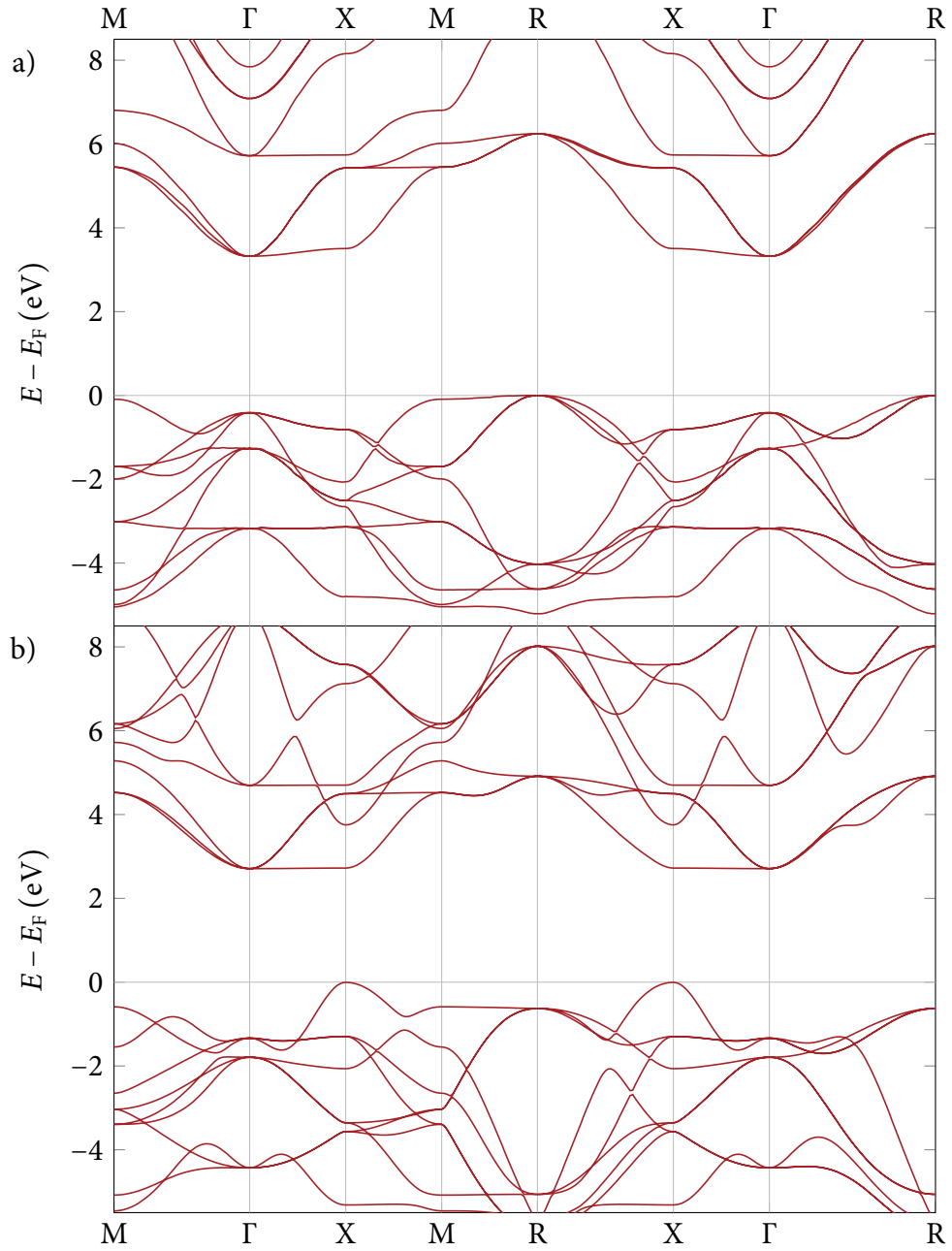
Figure 8.3: Electronic band structure obtained with the HSE hybrid functional for the two prototypical perovskites $SrTiO_3$ (a) and $PbTiO_3$ (b).

Table 8.2: Direct and indirect band gap obtained with the local PBE and the nonlocal HSE functional in comparison to optical absorption experiments.

	Fundamental gap			Optical gap			
	PBE	HSE	transition[†]	PBE	HSE	k point[†]	Expt.
I–V compounds							
$NaNbO_3$	1.69	2.95	$R \to \Gamma$	2.48	3.83	Γ	3.4[a]
$KNbO_3$	1.51	2.72	$R \to \Gamma$	2.17	3.44	Γ	3.3[a]
$KTaO_3$	2.23	3.57	$R \to \Gamma$	2.84	4.22	Γ	3.79[a]
II–IV compounds							
$BaHfO_3$	3.66	5.17	$R \to \Gamma$	3.78	5.35	Γ	4.8[b]
$BaSnO_3$	0.99	2.67	$R \to \Gamma$	1.47	3.11	Γ	3.4[c]
$BaTiO_3$	1.78	3.14	$R \to \Gamma$	1.93	3.27	Γ	3.2[a]
$BaZrO_3$	3.22	4.67	$R \to \Gamma$	3.46	4.99	Γ	5.3[d]
$CaSnO_3$	2.61	4.37	$R \to \Gamma$	3.68	5.46	Γ	4.4[e]
$CaTiO_3$	1.99	3.46	$R \to \Gamma$	2.43	3.97	Γ	3.57[f]
$CaZrO_3$	3.46	5.00	$R \to \Gamma$	3.64	5.36	Γ	5.2[g]
$CdTiO_3$	0.16	1.61	$M \to \Gamma$	0.81	2.36	Γ	2.7[h]
$SrHfO_3$	3.87	5.42	$R \to \Gamma$	4.01	5.67	Γ	6.07[i]
$SrSnO_3$	1.79	3.53	$R \to \Gamma$	2.65	4.38	Γ	4.1[j]
$SrTiO_3$	1.87	3.29	$R \to \Gamma$	2.24	3.69	Γ	3.43[a]
$SrZrO_3$	3.44	4.93	$R \to \Gamma$	3.68	5.29	Γ	5.6[k]
$PbSnO_3$	1.51	3.17	$M \to \Gamma, X \to \Gamma$	2.61	4.14	Γ, X	2.8[l]
$PbTiO_3$	1.64	2.72	$X \to \Gamma$	1.65	2.73	X	3.4[d]
$PbZrO_3$	2.45	3.47	$M \to X, X \to X$	2.45	3.47	X	3.7[d]
III–III compounds							
$LaAlO_3$	3.51	4.84	$R \to \Gamma$	3.66	5.03	Γ	5.6[m]
ME[n]				−1.38	0.10		
MAE[o]				1.38	0.43		
rms[p]				1.46	0.53		

[†] If more than one transition or k-point are present, the first item corresponds to the PBE result and the second on the HSE functional.
[a] Reference 256. [b] Reference 257. [c] Reference 258. [d] Reference 259. [e] Reference 260.
[f] Reference 261. [g] Reference 262. [h] Reference 263. [i] Reference 264. [j] Reference 265.
[k] Reference 266. [l] Reference 267. [m] Reference 268.
[n] Mean error. [o] Mean absolute error. [p] Root mean square.

eigenvalue close to R point constitutes the absolute maximum of the valence band. In the compounds that contain Pb, the p states exhibit a higher value near the X point. The bottom of the conduction band consists of the t_{2g} states of the transition metal ion, if the d states are empty. The edge of the conduction band is found as flat feature between the Γ and the X point. For all materials except for $PbZrO_3$, the absolute minimum resides at the Γ point. For materials, where the d shell of the B-site ion is filled, the lowest unoccupied state has s character and exhibits an almost parabolic behavior near the Γ point.

In Table 8.2, we list the obtained direct and indirect band gaps for the 19 investigated perovskites. In average, the direct (indirect) band gap obtained with the nonlocal HSE functional is $[1.48 \pm 0.21]$ eV ($[1.44 \pm 0.21]$ eV) larger than the PBE one. Particularly interesting are the Pb based compounds, where the application of the hybrid functionals changes the position of the fundamental band gap. Neglecting excitonic effects, the direct band gap can be related to optical absorption measurements. Overall, we find a drastic improvement of the predicted band transition energies. In the PBE functional, the MAE and the rms amount to 1.38 eV and 1.46 eV, respectively. The ME has the same absolute value as the MAE and a negative sign indicating that the PBE functional underestimates the band gap for all compounds. In the HSE functional the MAE (rms) is 0.43 eV (0.53 eV), which represents an improvement by roughly a factor of three compared to the PBE results. For the HSE functional the ME is much smaller than the MAE. This indicates that the sign of the error between predicted and experimental value is not the same for all materials.

The prediction of band transitions in DFT is limited by the following approximations: i) Although the fundamental band gap is in principle an observable quantity (see Sec. 4.1), local functionals suffer from the lack of a derivative discontinuity.[122,123] This leads to the systematic underestimation of the band gap by local functionals. ii) DFT is an effective one-particle theory, so that the many-body effects associated with the optical excitation, in particular, the binding of the electron and hole to an exciton, are not captured. Hence, the experimentally measured transition is lowered by the binding energy, so that DFT will overestimate the optical transition. iii) We did not account for the optical matrix element between valence and conduction band. Some transitions will be strongly suppressed, if the dipole operator between initial and final state vanishes. Thus, the experimentally observed lowest transition may be not between the band edges. iv) Finally, the noncubic ground-state structure at low temperatures, the neglect of thermal expansion, and the omission of zero-point fluctuations has an indirect effect on the band transitions caused by the relaxation of the lattice.

8.5 Conclusion

We demonstrated that the application of the HSE hybrid functional improves the structural as well as the electronic properties of a benchmark set of 19 cubic perovskites. The lattice constants are improved by roughly a factor of two compared to the local exchange correlation functional. While the PBE (LDA) functional provide systematically too large (small) lattice constants, the HSE functional predicts lattice constants smaller than the PBE functional and larger than the LDA one. There is no systematic trend in the HSE lattice constant, though, in average, a small overestimation is found, which may be associated to thermal expansion or other relaxations. Employing hybrid functionals for the calculation of the band transitions, we find a systematic opening of the optical band gaps by (1.48 ± 0.21) eV, which compensates for the systematic underestimation of 1.38 eV in PBE. As a consequence, the MAE is more than three times smaller in the HSE functional as compared to the PBE one.

Lead Chromate

9.1   Introduction

PbCrO$_3$ (PCO) was synthesized for the first time by DeVries and Roth[62]. They reported a cubic perovskite structure with a lattice constant of 4.0 Å and a G-type antiferromagnetic (AFM) order of the Cr ions.[61] Later, Chamberland and Moeller[63] examined the conductivity of PCO and found a semiconducting state with an activation energy of 0.27 eV. From an anomaly in the conductivity at 100 K, they suggest a possible phase transition at that temperature. The Néel temperature is difficult to determine as the magnetism cannot be easily fitted to a Brillouin function.[63] Depending on the method used the Néel temperature is found to be either 160 K[63] or 240 K.[61] The magnetic moment of the Cr ions is estimated to be either 1.9 μ_B[61] or 2.5 μ_B.[66] These measurements suggested a Pb^{2+}Cr^{4+}O$_3^{2-}$ valence.

Only in the last years, PCO gained a renewed interest and several interesting properties were found. Arévalo-López and Alario-Franco[64] found that in off-stoichiometric Pb$_{1-x}$CrO$_{3-x}$ the lead ions move by approximately 0.29 Å from their high symmetry position. By using electron energy loss spectroscopy (EELS) in this compound, the valence of the Cr ion was first determined[269] to be 4+ and later refined[65] to 3.5+. A recent study of the magnetic structure[66] found the Néel temperature at 245 K. They proposed a non-collinear state superposed to the G-type AFM state leading to weak ferromagnetism. Between 185 K and 62 K a spin-reorientation appears. Xiao *et al.*[67] investigated the effect of pressure on PCO and found a phase

transition at a compressive pressure of 1.2 – 1.6 GPa. The high-pressure phase is cubic, too, and has a roughly 10% smaller volume than the low pressure phase. Komarek *et al.*[270] point out that PCO is very different to the $CaCrO_3$ and $SrCrO_3$ compounds despite their similar chemical composition. PCO is insulating and exhibits a G-type AFM order, whereas $CaCrO_3$ and $SrCrO_3$ are metallic and order in a C-type AFM order. Furthermore, they investigated the thermal expansion of PCO and found an almost linear behavior down to 0 K, where the extrapolated lattice constant amounts to 3.995 Å. Arévalo-López and Alario-Franco[271] found a strong preference for a cubic arrangement in mixed compounds of $PbB_{1-x}Cr_xO_3$ (B = Ti or V). At an amount of x = 30 − −40% Cr ions, the space group P4mm of bulk $PbTiO_3$ and $PbVO_3$ is replaced with the cubic P$m\bar{3}m$ one.

PCO was considered in several density functional theory (DFT) studies. However, none of them were able to get the semiconducting ground state. The earliest work by Jaya *et al.*[68] was based on a linearized muffin-tin orbital (LMTO) basis set. They found a good agreement with the experimental magnetic moment and a strong hybridization of the Cr-3d and O-2p states. Recently, Wang *et al.*[69] considered the effect of intermixing of Pb and Cr ions using a projector augmented wave (PAW) method. They used a DFT+U approach with values for U between 0 and 6 eV. Independent of the used exchange-correlation functional and the value of U, the obtained lattice constant is much smaller than in experiment. The ground-state is metallic for reasonable values of U. Ganesh and Cohen[70] investigated a displacement of the Pb ions using a PAW method and a DFT+U approach, too. They found a favorable polar shift along the crystallographic (001)-direction which disappears upon reduction of the volume by 20%. They associate these two phases with the high pressure and low pressure phase predicted by Xiao *et al.*.[67] Both phases are metallic independent of the value of U. The low pressure phase is tetragonal with a gigantic distortion of c/a ~ 0.88. Yıldırım *et al.*[272] investigated surfaces of PCO employing a GGA+U scheme. They found a strong dependence of the equilibrium properties on the Hubbard-parameter U and could not reproduce the insulating ground state.

A simple consideration of the energy diagram in Fig. 9.1 reveals, that the experimentally suggested perfect cubic perovskite structure in combination with the 4+ oxidation state of Cr cannot yield an insulating ground state. In a perfect cubic perovskite structure, the three t_{2g} levels are degenerate. Hence, the two electrons of the Cr^{4+} ion would only result in a two-third filling of this band. The symmetry of the crystal must allow for a splitting of the t_{2g} levels, so that the resulting state can be semiconducting. Roth and DeVries noted small discrepancies in the observed scattering amplitude compared to the expected value for a perfectly cubic perovskite, "which may be due to small deformations of the oxygen octahedron sufficient to lift the orbital degeneracy."[61]
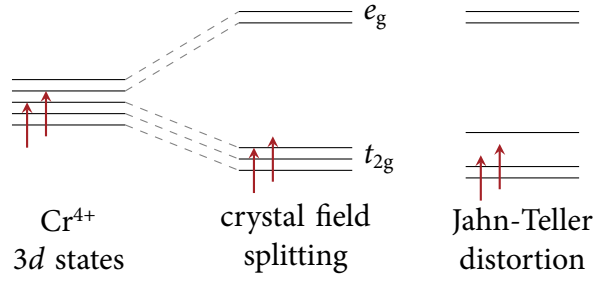
Figure 9.1: Energy diagram of PbCrO$_3$: The five $3d$ states split under the influence of the octahedral crystal field into two e_g states and three t_{2g}. For the Cr^{4+} ion the latter ones are occupied by two electrons. As experimentally a semiconducting state is observed, the symmetry has to be lowered (e.g. by a Jahn-Teller distortion) so that the three t_{2g} levels split.

In this chapter, we will investigate the effect of deformations of the oxygen octahedra. A combination of Jahn–Teller (JT) distortions and tilting of the oxygen octahedra allows by symmetry for 44 different space groups.[273] We evaluate the total energy for PCO in every one of these space groups and determine the ground-state structure. In the isovalent BiFeO$_3$, the lone-pair electrons of Bi drive a ferroelectric distortion.[57] To account for this possibility, we include a polar displacement in all of the examined structures. Depending on the size of the Hubbard parameter U, we find two different deformations, which minimize the energy of the system. At small values of U, JT distortions are the dominating mechanism whereas a rotation of the octahedra leads to lower energies for large values of U. Both structures exhibit a small band gap reproducing thereby the experimentally observed semiconducting nature of this material for the first time in DFT calculations. We examine both types of distortions closely to determine the origin of the gap. The JT distortions split the Cr t_{2g} states as depicted in Fig. 9.1 giving rise to an orbitally ordered state. The inclusion of oxygen octahedra rotation leads to a charge order on the Pb site and a +3 oxidation state on Cr with completely filled t_{2g} states. The results of these DFT+U calculations depends strongly on the choice of the Hubbard-parameter U. Hence, we perform hybrid-functional calculations on the obtained ground-state structures to motivate an optimized choice for the value of U.

This chapter is structured as follows: In Sec. 9.2, we introduce the considered lattice distortions. We describe the setup of the unit cell and the computational details in Sec. 9.3. The results of these calculations are presented in Sec. 9.4. We focus on the two insulating states in the next two sections. In Sec. 9.5, we describe the state driven
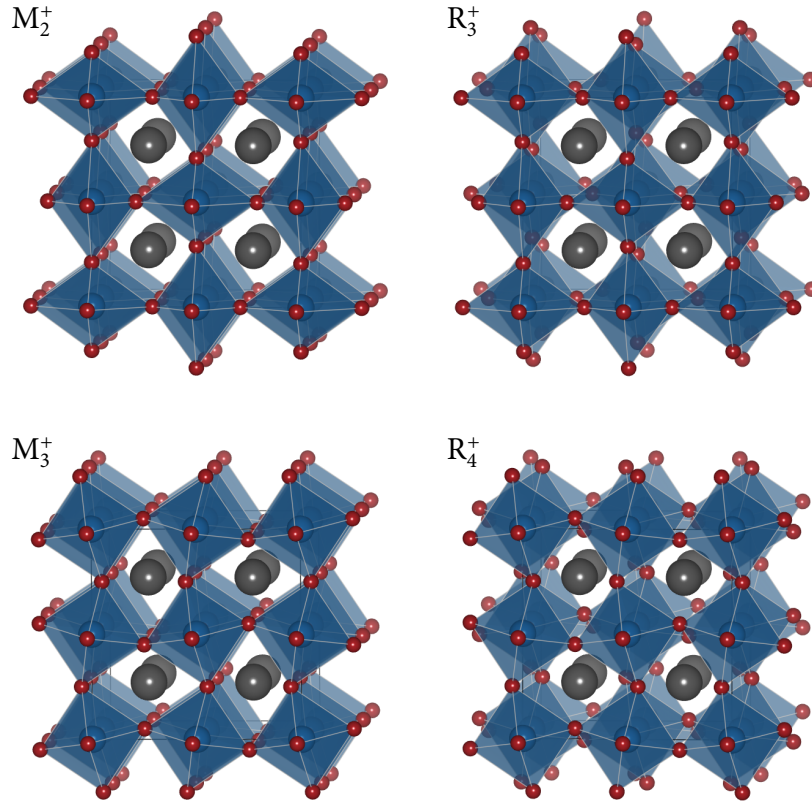
Figure 9.2: Common distortions of the oxygen octahedra in perovskite materials. Each distortion mode is labeled by the irreducible representation it belongs to. Jahn–Teller deformations and oxygen cage rotations are shown in the first and second row, respectively. In plane, neighboring octahedra have opposite deformations. Out of plane, the octahedra ordering pattern is either "in-phase" (M_2^+ and M_3^+ mode) or "out-of-phase" (R_3^+ and R_4^+ mode).

by JT distortions. In Sec. 9.6, we focus on the effect of oxygen rotations. We illustrate the U dependence of these two structures in Sec. 9.7 and discuss the consequences of hybrid-functional calculations. Finally, we draw our conclusions in Sec. 9.8.

9.2   Octahedral tilting and Jahn–Teller distortions

A distortion of the oxygen cage in PCO was already suggested by Roth and DeVries,[61] yet neither experimentally nor theoretically investigated so far. The Cr^{4+} ion is JT active, so we expect an elongation of some of the Cr-O bonds and a subsequent shrinking of several of the other ones. All these distortions can be decomposed into three modes which belong to the irreducible representations Γ_3^+, M_2^+, and R_3^+. The Γ_3^+ mode is two dimensional where these degrees of freedom correspond to the c/a and b/a ratio different from 1. Hence, in a cubic crystal the amplitude of the Γ_3^+ mode is zero, so that we do not include it in our study.

The other two modes can exist in a cubic crystal with nonzero amplitude. We visualize a one dimensional representative of these modes in the upper part of Fig. 9.2. In plane, a selected oxygen octahedron is elongated along one axis defining consequently the shrinking of its neighbors along this axis. This leads to a checkerboard-like arrangement of the octahedra. Out of plane, the stacking in the M_2^+ mode is in-phase (neighboring cages have the same distortion), whereas the R_3^+ mode shows an out-of-phase pattern (neighboring cages have the opposite distortion). A single oxygen octahedron can be elongated along three axes, so that these JT modes are three dimensional. Hence, any possible M_2^+ mode can be represented in a combination of elongations along the three coordinate axes. However, in the case of the R_3^+ mode this representation is reducible to a two dimensional one, because the elongation along one particular axis can be expressed by elongations along the other two axes.

In addition to these JT modes, we consider rotations of the oxygen octahedra, because they are the most common distortion in perovskite materials and possibly influence the JT distortion.[274] All possible rotations can be realized as a combination of two modes which correspond to the irreducible representations M_3^+ and R_4^+. We show two simple representatives of these modes in the lower part of Fig. 9.2. The ordering is analogous to the JT distortions. In plane, we see a checkerboard-like setup, as the rotation of one oxygen octahedron is directly linked to its neighbors. Out of plane, the M_3^+ mode describes an in-phase ordering, while an out-of-phase arrangement is found in the R_4^+ mode.

In the following, we will consider all possible combinations of JT modes and oxygen cage tilting. This was investigated in much detail by Carpenter and Howard.[273] They found that a combination of these modes leads to 44 space groups. In our study, we considered the 42 space groups depicted in Table 9.1. We will describe in the next section, how we generated the primitive unit cell and which numerical parameters were chosen for the calculation.

Table 9.1: Carpenter and Howard [273] found 44 space groups accessible by a perovskite system in which a tilting of the oxygen octahedra (M_3^+ and R_4^+ mode) is combined with a JT distortion (Γ_3^+, M_2^+ and R_3^+ mode). We do not depict the two space groups, which differ from the simple cubic one only by a c/a or a b/a ratio different from 1.

Mode	no JT	M_2^+	R_3^+
no tilt	221 $Pm\bar{3}m$	127 $P4/mbm$	140 $I4/mcm$
		139 $I4/mmm$	139 $I4/mmm$
		204 $Im\bar{3}$	69 $Fmmm$
		71 $Immm$	
M_3^+	127 $P4/mbm$	55 $Pbam$	135 $P4_2/mbc$
	139 $I4/mmm$	74 $Imma$	126 $P4/nnc$
	204 $Im\bar{3}$	87 $I4/m$	48 $Pnnn$
	71 $Immm$	12 $C2/m$	
R_4^+	140 $I4/mcm$	135 $P4_2/mbc$	72 $Ibam$
	74 $Imma$	63 $Cmcm$	
	167 $R\bar{3}c$	15 $C2/c$	
	12 $C2/m$	14 $P2_1/c$	
	2 $P\bar{1}$	2 $P\bar{1}$	
M_3^+, R_4^+	63 $Cmcm$	52 $Pnna$	15 $C2/c$
	62 $Pnma$	62 $Pnma$	14 $P2_1/c$
	11 $P2_1/m$	86 $P4_2/n$	2 $P\bar{1}$
	137 $P4_2/nmc$		68 $Ccca$

9.3   Computational setup

We generate the unit cells according to the spacegroups in Table 9.1. In several cases the symmetry of the space group allows for additional shifts of the other atoms. To investigate all possible modes at these sites, we make use of the program Isotropy. [275] Figure 9.3 shows the input and output of this investigation. In this case we will assume that in the simple perovskite unit cell, Pb occupies the Wyckoff position b, Cr the Wyckoff position a, and O the Wyckoff position d. With this assignment, we find six modes for Pb (Γ_4^-, R_5^+, X_1^+, X_5^+, M_2^-, and M_5^-) as well as six modes for Cr (Γ_4^-, R_4^-, X_3^-, X_5^-, M_3^-, and M_5^-). In addition, we find the displacements of the atoms when the mode is present in the crystal.

```
*value parent 221
*value wyckoff a b
*value kdegree 0
*show irrep
*show subgroup
*show microscopic vector
*display distortions
Irrep (ML) Point        Projected Vectors
GM4-       (0,0,0)      (1,0,0), (0,1,0), (0,0,1)
GM4-       (1/2,1/2,1/2)(1,0,0), (0,1,0), (0,0,1)
R5+        (1/2,1/2,1/2)(0,0,1), (1,0,0), (0,1,0)
           (3/2,3/2,3/2)(0,0,-1), (-1,0,0), (0,-1,0)
R4-        (0,0,0)      (0,0,1), (1,0,0), (0,1,0)
           (1,1,1)      (0,0,-1), (-1,0,0), (0,-1,0)
X1+        (1/2,1/2,1/2)(0,1,0), (0,0,1), (1,0,0)
           (1/2,1/2,3/2)(0,1,0), (0,0,-1), (1,0,0)
           (1/2,3/2,1/2)(0,-1,0), (0,0,1), (1,0,0)
           (1/2,3/2,3/2)(0,-1,0), (0,0,-1), (1,0,0)
           (3/2,1/2,1/2)(0,1,0), (0,0,1), (-1,0,0)
           (3/2,1/2,3/2)(0,1,0), (0,0,-1), (-1,0,0)
           (3/2,3/2,1/2)(0,-1,0), (0,0,1), (-1,0,0)
           (3/2,3/2,3/2)(0,-1,0), (0,0,-1), (-1,0,0)
X5+        (1/2,1/2,1/2)(1,0,-1), (-1,0,-1), (-1,1,0), (-1,-1,0), (0,-1,1), (0,-1,-1)
           (1/2,1/2,3/2)(1,0,-1), (-1,0,-1), (1,-1,0), (1,1,0), (0,-1,1), (0,-1,-1)
           (1/2,3/2,1/2)(-1,0,1), (1,0,1), (-1,1,0), (-1,-1,0), (0,-1,1), (0,-1,-1)
           (1/2,3/2,3/2)(-1,0,1), (1,0,1), (1,-1,0), (1,1,0), (0,-1,1), (0,-1,-1)
           (3/2,1/2,1/2)(1,0,-1), (-1,0,-1), (-1,1,0), (-1,-1,0), (0,1,-1), (0,1,1)
           (3/2,1/2,3/2)(1,0,-1), (-1,0,-1), (1,-1,0), (1,1,0), (0,1,-1), (0,1,1)
           (3/2,3/2,1/2)(-1,0,1), (1,0,1), (-1,1,0), (-1,-1,0), (0,1,-1), (0,1,1)
           (3/2,3/2,3/2)(-1,0,1), (1,0,1), (1,-1,0), (1,1,0), (0,1,-1), (0,1,1)
X3-        (0,0,0)      (0,1,0), (0,0,1), (1,0,0)
           (0,0,1)      (0,1,0), (0,0,-1), (1,0,0)
           (0,1,0)      (0,-1,0), (0,0,1), (1,0,0)
           (0,1,1)      (0,-1,0), (0,0,-1), (1,0,0)
           (1,0,0)      (0,1,0), (0,0,1), (-1,0,0)
           (1,0,1)      (0,1,0), (0,0,-1), (-1,0,0)
           (1,1,0)      (0,-1,0), (0,0,1), (-1,0,0)
           (1,1,1)      (0,-1,0), (0,0,-1), (-1,0,0)
X5-        (0,0,0)      (1,0,-1), (1,0,1), (-1,1,0), (1,1,0), (0,-1,1), (0,1,1)
           (0,0,1)      (1,0,-1), (1,0,1), (1,-1,0), (-1,-1,0), (0,-1,1), (0,1,1)
           (0,1,0)      (-1,0,1), (-1,0,-1), (-1,1,0), (1,1,0), (0,-1,1), (0,1,1)
           (0,1,1)      (-1,0,1), (-1,0,-1), (1,-1,0), (-1,-1,0), (0,-1,1), (0,1,1)
           (1,0,0)      (1,0,-1), (1,0,1), (-1,1,0), (1,1,0), (0,1,-1), (0,-1,-1)
           (1,0,1)      (1,0,-1), (1,0,1), (1,-1,0), (-1,-1,0), (0,1,-1), (0,-1,-1)
           (1,1,0)      (-1,0,1), (-1,0,-1), (-1,1,0), (1,1,0), (0,1,-1), (0,-1,-1)
           (1,1,1)      (-1,0,1), (-1,0,-1), (1,-1,0), (-1,-1,0), (0,1,-1), (0,-1,-1)
M2-        (1/2,1/2,1/2)(0,0,1), (1,0,0), (0,1,0)
           (3/2,1/2,1/2)(0,0,-1), (1,0,0), (0,-1,0)
           (1/2,3/2,1/2)(0,0,-1), (-1,0,0), (0,1,0)
           (1/2,1/2,3/2)(0,0,1), (-1,0,0), (0,-1,0)
M3-        (0,0,0)      (0,0,1), (1,0,0), (0,1,0)
           (1,0,0)      (0,0,-1), (1,0,0), (0,-1,0)
           (0,1,0)      (0,0,-1), (-1,0,0), (0,1,0)
           (0,0,1)      (0,0,1), (-1,0,0), (0,-1,0)
M5-        (0,0,0)      (1,0,1), (1,0,-1), (1,1,0), (-1,1,0), (0,1,1), (0,-1,1)
           (1,0,0)      (-1,0,-1), (-1,0,1), (-1,-1,0), (1,-1,0), (0,1,1), (0,-1,1)
           (0,1,0)      (1,0,1), (1,0,-1), (-1,-1,0), (1,-1,0), (0,-1,-1), (0,1,-1)
           (0,0,1)      (-1,0,-1), (-1,0,1), (1,1,0), (-1,1,0), (0,-1,-1), (0,1,-1)
M5-        (1/2,1/2,1/2)(1,0,1), (-1,0,1), (1,1,0), (1,-1,0), (0,1,1), (0,1,-1)
           (3/2,1/2,1/2)(-1,0,-1), (1,0,-1), (-1,-1,0), (-1,1,0), (0,1,1), (0,1,-1)
           (1/2,3/2,1/2)(1,0,1), (-1,0,1), (-1,-1,0), (-1,1,0), (0,-1,-1), (0,-1,1)
           (1/2,1/2,3/2)(-1,0,-1), (1,0,-1), (1,1,0), (1,-1,0), (0,-1,-1), (0,-1,1)
```

Figure 9.3: Excerpt of input and output of Isotropy.[275]

```
*value parent 221
*value wyckoff d
*value irrep m2+
*show irrep
*show subgroup
*show microscopic vector
*display distortions
Irrep (ML) Point      Projected Vectors
M2+        (1/2,0,0) (1,0,0),  (0,0,0),  (-1,0,0)
           (3/2,0,0) (-1,0,0), (0,0,0),  (1,0,0)
           (1/2,1,0) (-1,0,0), (0,0,0),  (-1,0,0)
           (1/2,0,1) (1,0,0),  (0,0,0),  (1,0,0)
           (0,0,1/2) (0,0,0),  (0,0,-1), (0,0,1)
           (1,0,1/2) (0,0,0),  (0,0,-1), (0,0,-1)
           (0,1,1/2) (0,0,0),  (0,0,1),  (0,0,1)
           (0,0,3/2) (0,0,0),  (0,0,1),  (0,0,-1)
           (0,1/2,0) (0,-1,0), (0,1,0),  (0,0,0)
           (1,1/2,0) (0,1,0),  (0,1,0),  (0,0,0)
           (0,3/2,0) (0,1,0),  (0,-1,0), (0,0,0)
           (0,1/2,1) (0,-1,0), (0,-1,0), (0,0,0)
```

Figure 9.4: Excerpt of input and output of ISOTROPY.[275]

In a similar fashion, we determine the displacements of the oxygen atoms in the crystal. In Fig. 9.4, we show for example the determination of the shifts of the oxygen atoms in the M_2^+ mode. Analogously, we find the distortions in the R_3^+, in the M_3^+, and in the R_4^+ mode. It is noteworthy, that we limited ourselves to modes which can be represented within a unit cell of $2\times2\times2$ primitive cubic unit cells.

To analyze which modes are allowed in a specific subgroup, we use another tool of the ISOTROPY[275] software. Figure 9.5 illustrates, using the example of the space group 68 *Ccca*, how we determine the allowed deformations. For this, we need only the basis and the origin of the subgroup relative to the parent space group. These are given in the work of Carpenter and Howard.[273] Of all these possible deformations, we consider those that yield a microscopic displacement of the Pb or the Cr atoms. Hence, in the specific example depicted in Fig. 9.5, we consider only the X_5^+ mode with an order parameter $(a, a, 0, 0, -a, a)$. Examining all the spacegroups listed in Table 9.1, we find that the only modes which may be present for the Pb ions are R_5^+, X_1^+, and X_5^+, though not all of these modes are allowed for all spacegroups. Further-

```
*value parent 221
*value subgroup 68
*value basis 2,2,0 -2,2,0 0,0,2
*value origin 0,0,0
*display directions
Irrep (ML) Dir               Subgroup      Size
GM1+        (a)              221 Pm-3m      1
GM3+        (a,0)            123 P4/mmm     1
GM5+        (a,0,0)          65 Cmmm        1
R2+         (a)              226 Fm-3c      2
R3+         (0,a)            140 I4/mcm     2
R4+         (a,0,0)          140 I4/mcm     2
X2+         (0,a,0)          131 P4_2/mmc   2
X3+         (a,b,a)          126 P4/nnc     8
X4+         (a,0,a)          125 P4/nbm     4
X5+         (a,a,0,0,-a,a)   129 P4/nmm     4
M1+         (a,0,0)          123 P4/mmm     2
M3+         (0,a,a)          139 I4/mmm     4
M4+         (a,b,-b)         139 I4/mmm     4
M5+         (0,0,0,a,0,0)    140 I4/mcm     4
```

Figure 9.5: Excerpt of input and output of ISOTROPY.[275]

more, in none of these structures a movement of the Cr atom is allowed by symmetry. To ensure that the latter constraint is not too restrictive, we repeated the above procedure taking into account an explicit symmetry breaking by a polar Γ_4^- distortion at the Cr site. This distortion may be induced by the lone-pair electrons of the Pb ion.

The unit cells given by Carpenter and Howard[273] which correspond to the spacegroups in Table 9.1 are generally not the primitive unit cell of the respective structure. In addition, PCO is a G-type antiferromagnet,[61] hence the magnetic unit cell might be larger than the crystallographic one. To find the primitive unit cell, we use this algorithm:

1 We select a trial lattice vector a_t that is a linear combination of the lattice vectors of the simple cubic perovskite unit cell. We start using the smallest possible vectors and proceed to larger ones. If one or more lattice vectors were already found, we require that the new one is linearly independent.

2 We calculate the displacement caused by all modes allowed in the crystal for the

five reference atoms in the simple perovskite unit cell. In order to achieve this, we multiply the specific order parameter of the mode with the displacements as found in Fig. 9.3 and Fig. 9.4.

3 We repeat the calculation of the displacement for test unit cell that is translated by $\boldsymbol{a}_t$ with respect to the reference unit cell. If the magnetic moment and the displacement are identical for the corrsponding atoms in the test and the reference unit cell, then $\boldsymbol{a}_t$ is a valid lattice vector of the primitive unit cell.

4 If we have found three lattice vectors, we are done with the determination of the primitive cell, otherwise we proceed with step 1.

5 As a final step, we analyze which atoms are present within the primitive unit cell. We invert the matrix built by the three lattice vectors and calculate the internal coordinates for all 40 atoms of the $2\times2\times2$ unit cell. Removing the duplicates, we have the positions of the atoms for the space group.

Once the primitive unit cell is initialized with some small distortions, we perform first-principles DFT calculations to establish the ground state of all these different structures employing a multi-code approach. The most time-consuming part of the calculation is the relaxation of the shape of the unit cell and the atoms within. For this step, we apply the PAW method,[111,276] which is faster than all-electron methods at the cost of being less precise. During the relaxation, we employ a plane-wave cutoff of 600 eV. The Pb $5d$ as well as the Cr $3p$ states are treated as valence states. For the exchange-correlation functional, we chose the local PBE functional and add an on-site Hubbard-like term[94] to describe the localized nature of the Cr d states. We vary the U value between 2 eV and 4 eV and selected a value of $J = 1$ eV. We analyze all relaxed structures with the tools provided by the Bilbao Crystallographic Server,[277,278] in particular *Amplimodes*,[279] to investigate which modes remain after relaxation. The specific value of U changes which structure has the lowest energy of all investigated structures. We examine the U dependence of these two structures in more detail.

The relaxed structures are further processed in the precise all-electron full-potential linearized augmented-plane-wave (FLAPW) method[31,32,117] as realized in the `Fleur` code.[126] We cross-check the energy differences obtained with the PAW method, investigate the origin of the insulating state, and determine the ferroelectric polarization if present. For this study, we make use of the Wannier90 interface,[215,280] which allows us to construct Wannier functions from the obtained Kohn-Sham wavefunctions. Furthermore, we investigate the resulting structures in more detail using the HSE06 functional,[26,131] from which we extract a trend for the value of the Hubbard U.

9.4 Ground state investigation

In this section, we analyze the results of the relaxation. We calculated the 42 different structures depicted in Table 9.1 and determine the total energy and the relaxed structure. In Fig. 9.6, we illustrate the stable (black) and unstable (gray) spacegroups. A space group can not be stable, if a stable subgroup exists, so that a symmetry breaking would lower the total energy. Furthermore, we investigate the symmetry of the relaxed structure with Isotropy[275] and *Amplimodes*.[279] If the symmetry has increased during the relaxation, we indicate this by a green arrow pointing to the appropriate supergroup. In this case the structure with the higher symmetry yields the same total energy at a reduced computational time, so that we limit ourselves to this more symmetric space groups in the remainder of this chapter. A lot of subgroups with JT distortions (illustrated by the red and blue area in Fig. 9.6) relax to supergroups without JT distortion, so that in general the JT distortions are suppressed by the presence of a tilting of the oxygen octahedra. The three notable exceptions are the *Imma* ($a^0b^0c^+$), the *I4/m* ($a^+a^+c^0$), and the *C2/c* ($a^+b^-c^0$) structure. The rest of the stable spacegroups includes either only JT distortions ($I4/mmm$, $Im\bar{3}$, $I4/mcm$, and $I4/mmm$) or only tilting of the oxygen octahedra ($P4_2/nmc$, $C2/c$, and $P2_1/m$). The energetic order of these structures depends on the value of the Hubbard U. The pure JT distortion is favored for small values of U, whereas the rotation of the oxygen octahedra is more stable at larger values of U. Common to all these structures is the significant energy decrease of > 100 meV compared to the simple cubic arrangement. Furthermore, we determine a stabilization of a polar Γ_4^- mode at the Cr site, if we allow for the corresponding symmetry breaking. Next, we focus on the electronic properties of the stable structures and find that the inclusion of a JT mode as well as the rotation of the oxygen octahedra gives rise to the opening of a band gap at a certain value of U. To emphasize this in more detail, we concentrate on two prototypical structures for these relaxations. In Sec. 9.5, we illustrate the structure $P4/mbm$ in which the JT distortions are responsible for the transition to the insulating state. This structure exhibits the lowest total energy at small values of the Hubbard U. In the $P4_2/nmc$ structure, which has the lowest energy at large values of U, the oxygen octahedra rotate about all three axes and a charge order of the Pb ions drives the transition. We will discuss this in Sec. 9.6.

9.5 Splitting of t_{2g} levels by Jahn-Teller distortion

Keeping the volume of the unit cell fixed to the experimental value during the relaxation, we find the energetic minimum of the $P4/mbm$ structure (space group 127,
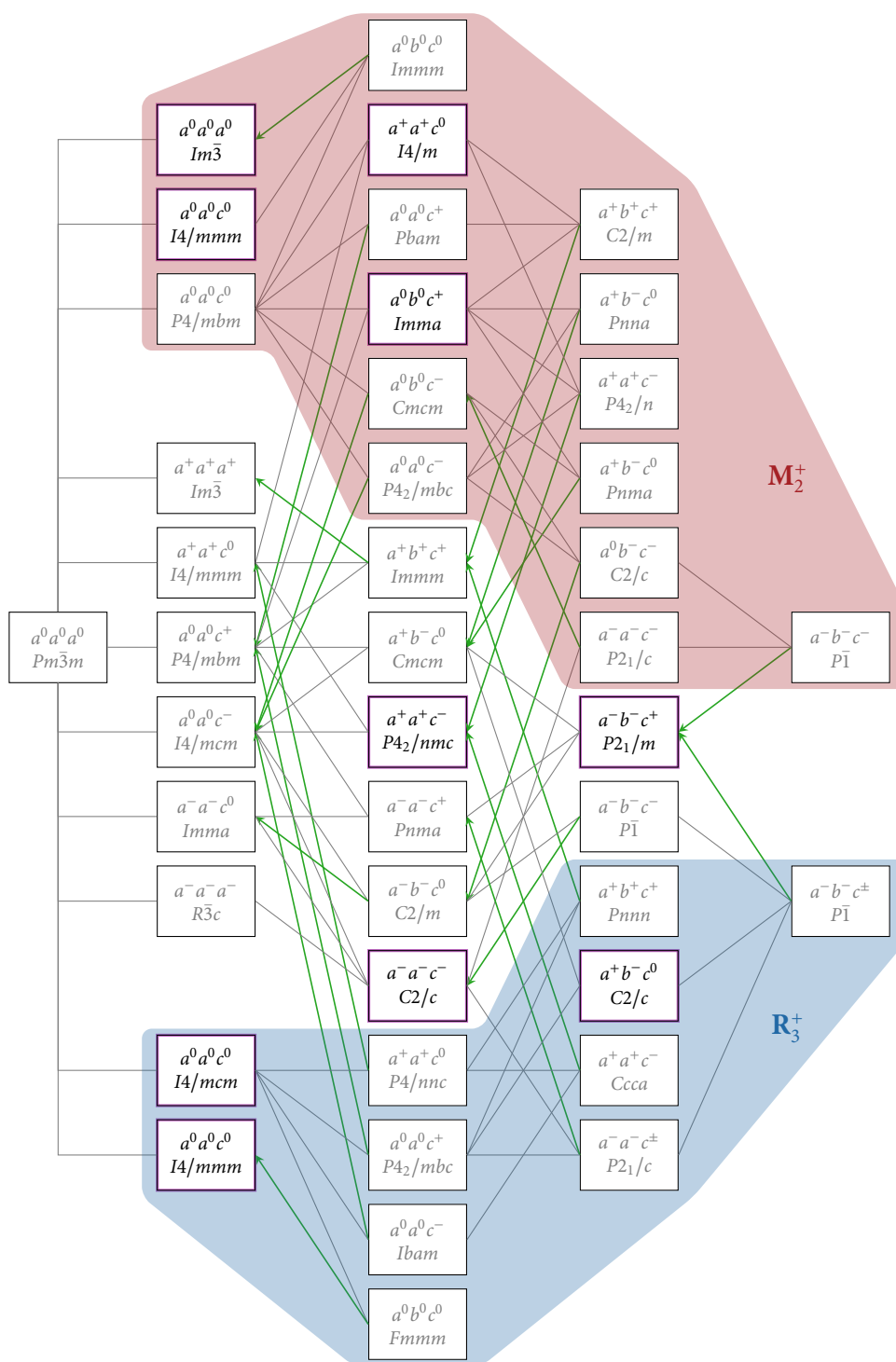
Figure 9.6: Relaxation of PbCrO$_3$ with a Hubbard $U = 4$ eV: The structures are labeled in Glazer notation[281] and the Hermann-Mauguin notation of the space group. All possible group-subgroup connections are visualized by gray lines or green arrows. A purple frame (a gray color of the label) indicates the structure is (not) stable. A structure is not stable, if either a stable subgroup exists or the structure relaxes along the green arrows to a supergroup. The red and blue area illustrate the presence of the respective Jahn-Teller mode. In the area in between only tilts of the oxygen octahedra are present.
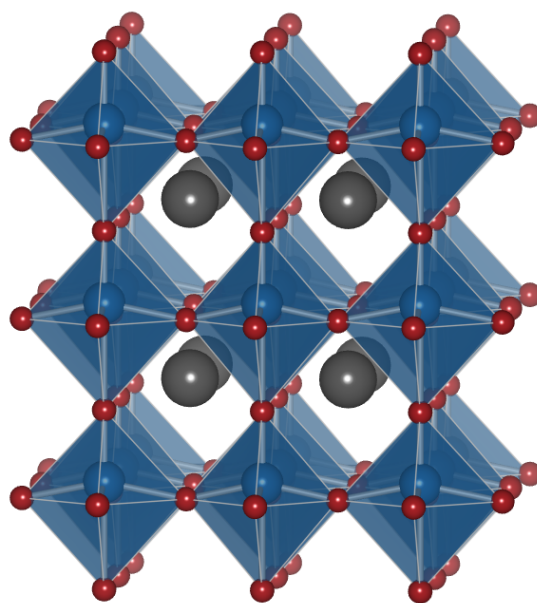
Figure 9.7: Relaxed *P4bm* structure with experimental unit-cell volume.

Glazer notation[281] $a^0a^0c^0$). Allowing for a polar displacement breaks the symmetry of the crystal further so that the relaxed compound exhibits a *P4bm* (space group 100) structure as depicted in Fig. 9.7. This structure differs from the simple cubic unit cell by three distortions: The Γ_4^- mode shifts the positive ions Pb and Cr with respect to the negative oxygen ions in *z* direction and gives rise to an electric polarization. In planes orthogonal to the *z* axis, the R_3^+ JT mode elongates the oxygen octahedra in a checkerboard pattern. Both modes break the symmetry as the *z* axis is distinguishable from the other axes. As a consequence the structure exhibits a *c/a* ratio, which amounts to a value larger than 110%. The absolute amount depends on the size of the Hubbard-*U* parameter (see Sec. 9.7). If we relax the volume of the unit cell, the experimental volume of $64\,\text{Å}^3$ is overestimated by 7%. Although an overestimation of the volume is a typical feature of the generalized gradient approximation (GGA) functionals (see Sec. 8.3), we would expect a better description by the PBE functional. More important is the large *c/a* ratio which does not agree at all with the cubic structure observed in experiment. We point out that Ganesh and Cohen[70] found a strong length difference of the three crystal axes, too, however with a *c/a* ratio of 88%. The coherent movement of the cations, which is associated to the polar Γ_4^- mode, is experimentally not observed. While the displacement of the Pb ion appears to be oriented randomly in experiment,[64,66] the Cr ion resides in the
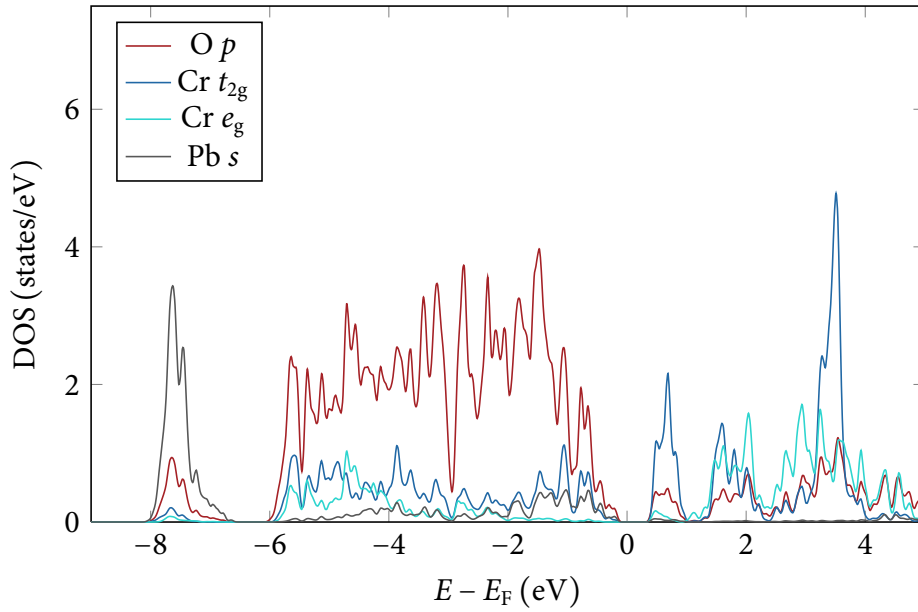
Figure 9.8: Electronic DOS of one spin channel in the *P4bm* structure. The valence band consists of Pb s (gray) and a hybridization of O p (red) and Cr t_{2g} states (blue). The unoccupied band is built by a single t_{2g}, the e_g (cyan) and the minority d states.

center of the oxygen octahedron.[61,62]

We turn to the analysis of the electronic properties of this structure. The orbital-decomposed electronic density of states (DOS) for one spin channel[a] is depicted in Fig. 9.8. The Pb s orbitals are situated approximately 7.7 eV below the Fermi energy. The band between −6 eV and the Fermi energy is built by a hybridization of Cr d and O p states. Above the Fermi energy the lowest unoccupied state has t_{2g} character. At even higher energies reside the e_g states and the unoccupied d states of the spin-down Cr ion. Investigating the unoccupied state more closely, we find an orbital order of the the hole state. We evaluate the Wannier functions[280] for the lowest unoccupied state, which provide a prominent illustration of this orbital order. In Fig. 9.9, we recognize that the empty orbital alternates in plane between d_{xz} and d_{yz}. Out of plane the stacking is in phase. The origin of this particular orbital order is the following: The large off-centering of the Cr ion in combination with the large c/a ratio favors the occupation of the d_{xy} orbital over the other two t_{2g} ones similar as in $PbVO_3$.[282,283] The – in comparison – smaller JT distortion in plane, splits the energy of the remaining d orbitals. Hence, the occupation of the orbitals follows the checkerboard

---

[a]Due to the AFM arrangement both spin channels are equivalent.
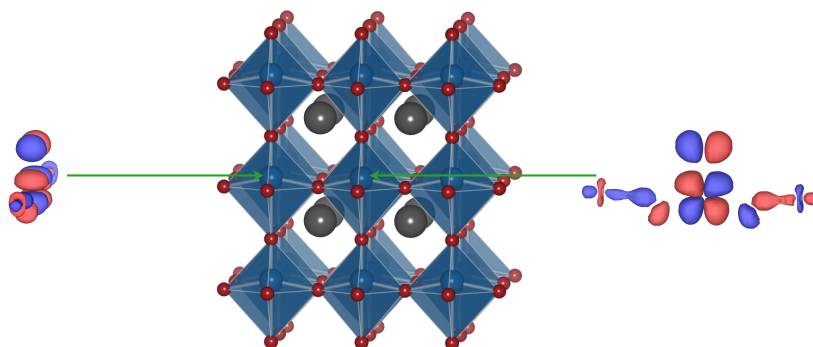
Figure 9.9: Wannier functions for the unoccupied levels directly above the Fermi energy reveal a checkerboard orbital order in the structure.

pattern established by the R_3^+ JT mode. A construction of the Wannier functions for all occupied states allows the calculation of the electric polarization of this structure. The sum of electronic ($11.2\,\mu C/cm^2$) and ionic ($42.8\,\mu C/cm^2$) polarization yields a total polarization of $54.0\,\mu C/cm^2$.

Finally, we considered the effect of oxygen defects, which are commonly present in perovskites. Removing a single oxygen out of the 40 atoms unit cell corresponds to a defect concentration of 4.2%. This defect causes a symmetry break, so that all axes are nonequivalent. The corresponding c/a and c/b ratio amount to 1.09 and 1.06, respectively, in better agreement with experiments. The volume of the structure shrinks by roughly 7%, which corresponds roughly to the overestimation of the defect-free structure. Furthermore, we obtain a mixed valency of Cr^{3+} and Cr^{4+} ions, which was also observed in recent experiments.[65] However, the inclusion of a single defect introduces a magnetic moment on the Cr ions, because the AFM order does not follow the local charge order induced by the defect. From the investigation of a $2 \times 2 \times 2$ unit cell, we can not conclude whether this problem would persist in a real crystal, where the defects are randomly distributed or if it is an artifact originating in the small size of the calculational unit cell.

9.6 Charge order in oxygen-octahedra tilt structure

The $P4_2/nmc$ structure (space group 137) incorporating only oxygen tilts relaxes into the $P4_2mc$ (space group 105) structure (see Fig. 9.10), if we allow for polar displacements. The Glazer notation[281] $a^+a^+c^-$ of this structure reveals the distortions associated to tilting of the oxygen octahedra. The octahedra rotate by an equal amount
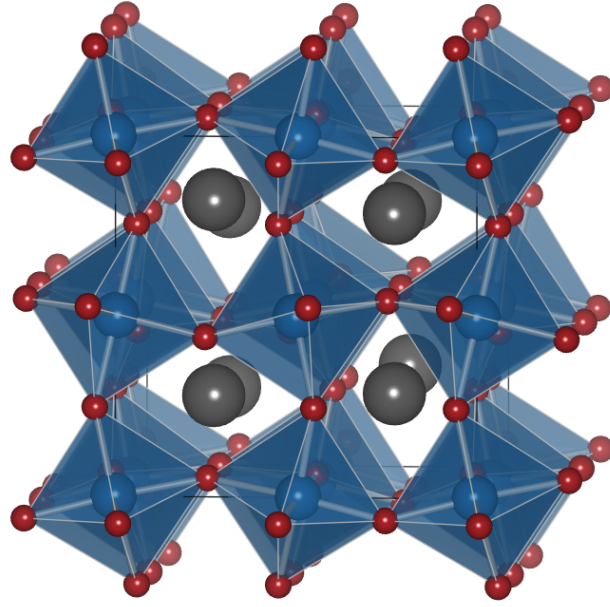
Figure 9.10: Relaxed $P4_2mc$ structure with experimental unit-cell volume.

about x and y axis with an in-phase ordering perpendicular to these axes. The rotation about the z axis is slightly smaller and the neighboring layers have an out-of-phase stacking. In addition to these rotations and the polar displacement, the reduced symmetry allows for further modes (M_5^-, M_2^-, M_4^+, X_5^+, X_4^-, and X_3^-) to be established. The amplitude of these distortions is a factor 5 to 20 smaller than the amplitude of the tilting modes R_4^+ and M_3^+. The amplitude of the polar displacement is larger than any of those additional modes but of the same order of magnitude. This structure exhibits a c/a ratio of 0.998, which is almost identical to the value of the cubic structure. This value decreases with the increase of the value of the Hubbard U, what will be discussed in more detail in Sec. 9.7. The volume of the unit cell is significantly smaller (6%) than the experimentally observed one, which is astonishing as GGA functionals tend to overestimate the lattice constant. The same behavior was found in other numerical calculations for the simple cubic unit cell.[69,70] A detailed investigation of the distortion with *Amplimodes*[279] reveals that the polar Γ_4^- mode mainly shifts the Pb atoms with respect to the oxygens, whereas the Cr atoms hardly shift at all. As several of the modes with smaller amplitude act on the Pb ions as well (X_5^+, M_2^-, and M_5^-), this may explain why experimentally a random displacement of the Pb ions is seen,[64] in particular taking into account that phase boundaries and defects destroy the long-range order.
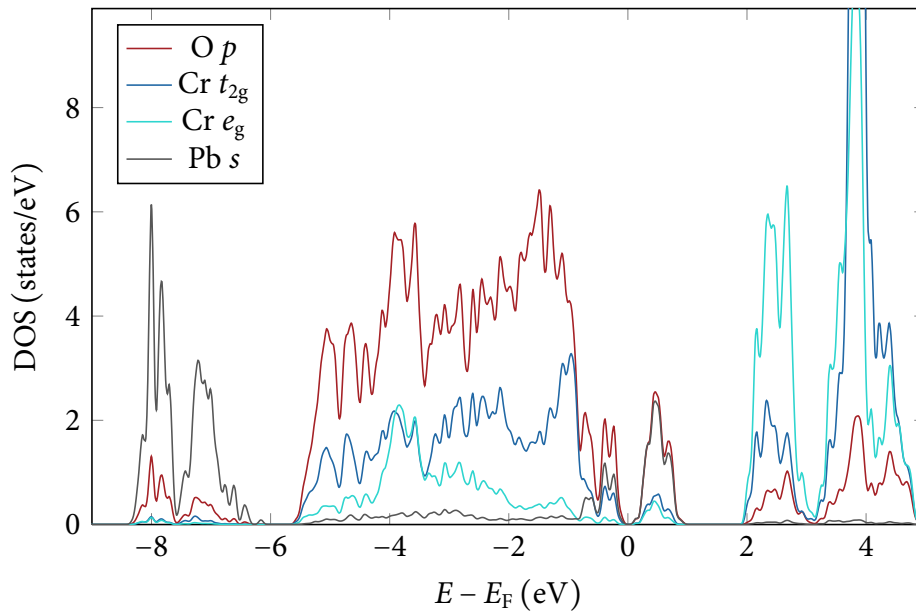
Figure 9.11: Electronic DOS of one spin channel in the $P4_2mc$ structure. The oxygen p states (red) hybridize with the Cr t_{2g} states (blue). The Cr e_g states are shown in cyan and the Pb s states in gray.
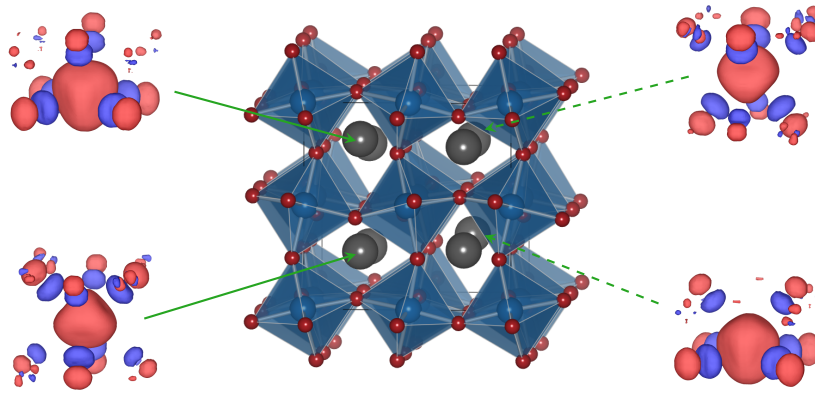
Figure 9.12: Wannier functions for the unoccupied levels directly above the Fermi energy localized at particular Pb^{4+} sites. The dashed arrows indictate that the functions are centered at the rear Pb ions, whereas solid lines are associated with the front Pb ions.

The electronic properties of this structure are illustrated by the DOS in Fig. 9.11. We recognize that the symmetry of the crystal makes two types of Pb atoms distinguishable, which gives rise to two separate $6s$ peaks at $8\,\text{eV}$ and $7.2\,\text{eV}$ below the Fermi energy. The valence band consists mainly of a hybridization of O $2p$ and Cr t_{2g} states, however the edge of the valence band has a notable contribution of Pb s character. A hybridized band of Pb s and O p states, which includes contribution of one particular Pb type, forms a band approximately $0.5\,\text{eV}$ above the Fermi energy. At a higher energy of roughly $2\,\text{eV}$ the unoccupied e_g and the minority d states reside. We realize that this electronic arrangement is incompatible with the simple energy diagram as proposed in Fig. 9.1. Instead it corresponds to a charge order of the Pb atoms, where a hybridized $6s2p$ state donates the electrons to completely fill the Cr t_{2g} levels of the majority spin. A nice visualization of this gap state is provided by the calculation of the Wannier functions for the first unoccupied bands depicted in Fig. 9.12. The Pb ions form columns of Pb^{4+} and Pb^{2+}, so that the Wannier functions are localized in these columns. Even the Pb^{4+} ions differ from each other, which is revealed by the hybridization of the Wannier functions. Two of the Pb ions shift upwards strongly from their high symmetry position and as a consequence the s state only hybridizes with the in-plane oxygens and two of the ones above. For the second type of Pb^{4+} ions, the rotation of the oxygen octahedra moves the in-plane oxygens away from the Pb ions, so that its s state hybridizes with all of the out-of-plane oxygens. This electronic arrangement is incompatible with the experimental observations. The measurement of the magnetic moment[61,66] and the EELS spectrum[64,65] suggest a formal charge of the Cr ion of 4+ or 3.5+. Hence, the Pb ion should exhibit a formal charge of 2+ or 2.5+ to compensate the formal charge of 2− of the three oxygen ions. We emphasize the difficulty to determine the charge attributed to a specific atom in a real material. As illustrated by the DOS, the s state of "Pb^{4+}" is mostly filled, which would not be the case if the real charge on the Pb^{4+} ion would correspond to the formal one. The Wannier functions and the DOS indicate that the lowest conduction band state is rather a combination of Pb s and O p states, which is not modeled by the simple ionic picture of formal charges. Finally, we employ a Wannier construction to all occupied states to evaluate the contributions of electronic ($3.1\,\mu\text{C/cm}^2$) and ionic ($17.7\,\mu\text{C/cm}^2$) polarization, which amount to a total polarization of $20.8\,\mu\text{C/cm}^2$.

The inclusion of an oxygen defect per 40 atoms unit-cell yields an *increase* of volume by roughly 1%, so that it agrees better with the experimental volume. The three lattice vectors remain at almost cubic ($a : b : c = 1.001 : 0.995 : 1.003$) although the deviations are slightly larger than in the defect-free structure. The excess electrons induced by the defect move to one of the Pb^{4+} ions resulting in a formal 2+ charge, the formal charge of the Cr ions remains unchanged.
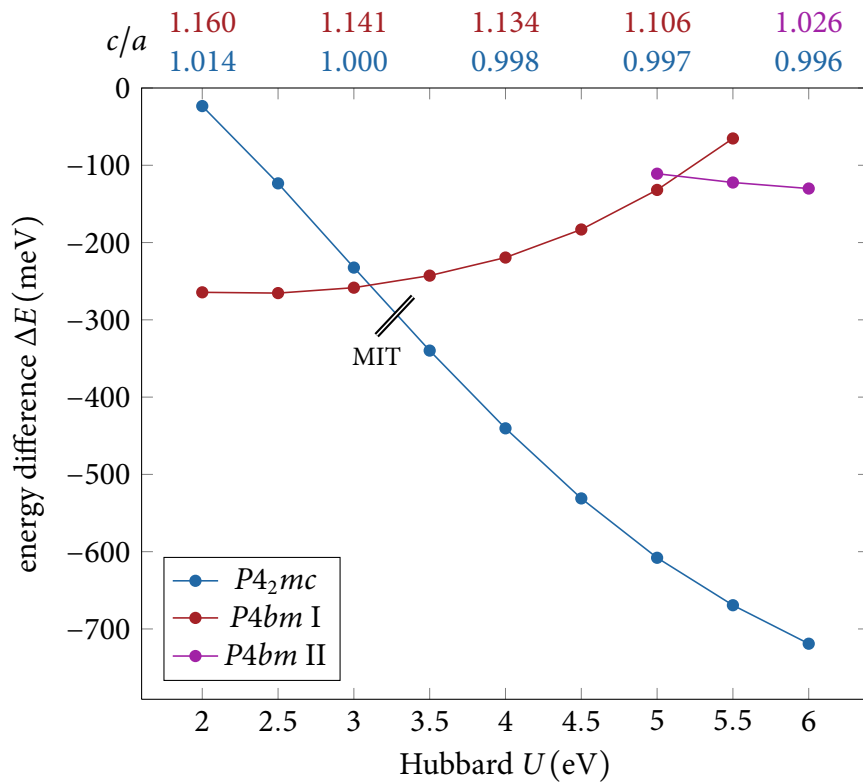
Figure 9.13: Energy difference ΔE of distorted structure with respect to simple cubic one as function of the Hubbard U applied in the DFT+U scheme. The $P4bm$ structure exhibits a phase transition to a different structural arrangement at $U = 5.2$ eV. The $P4_2mc$ structure shows a metal-insulator transition (MIT) at $U = 3.3$ eV. Above the plot, the c/a ratio of the structures at different values of U is shown.

9.7 Comparison DFT+U and hybrid functionals

The properties of the relaxed solutions vary strongly with the chosen value of the Hubbard U. In this section, we analyze trends for the two prototypical structures discussed in the last two sections. In Fig. 9.13, we depict the energetic competition between the two structures in comparison to the simple cubic structure. At small values of U the strongly tetragonal $P4bm$ structure is roughly 260 meV per formula unit (f.u.) more favorable than an undistorted arrangement. Increasing the value of U lead to a decrease of the c/a ratio and the energy difference to the cubic structure. At a value of $U = 5$ eV a metastable metallic structure exist, which has a significantly smaller c/a ratio. For even larger values of U the metallic structure becomes more
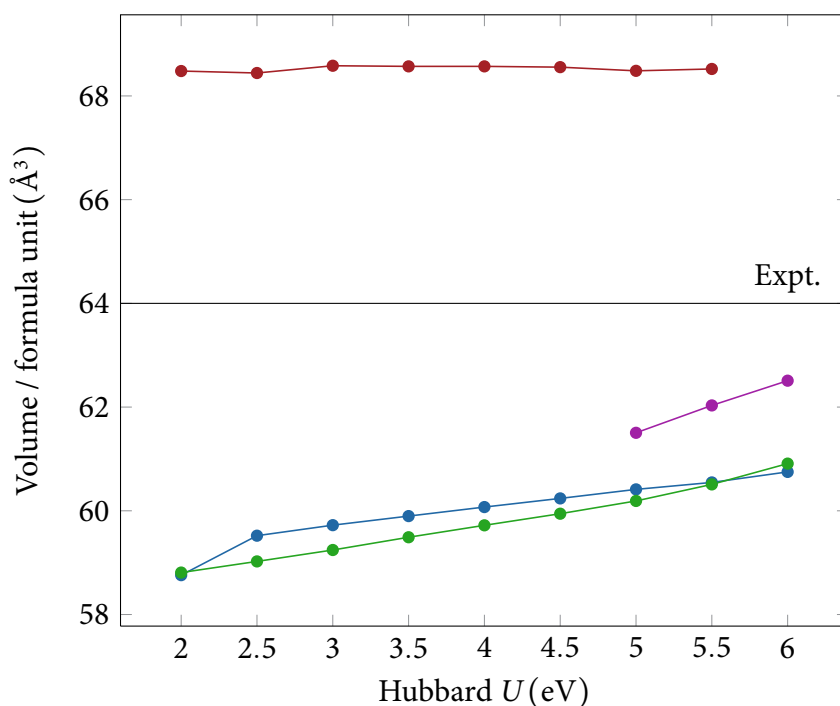
Figure 9.14: Comparison of the U dependence of the volume in the simple cubic (—●—), in the $P4_2mc$ (—●—), and in the $P4bm$ structure. The latter has two solutions, an insulating one (—●—) at small values of U and a metallic one (—●—) at large values of U. As reference the experimental unit-cell volume is depicted as black line.

stable than the insulating one. This new structure is characterized by a single Γ_4^- mode, i.e., the JT distortion disappears during the relaxation. We recall that the polar displacement in addition to the large c/a ratio were responsible for the opening of the band gap, so that it is straightforward that the disappearance of these features yields a metallic solution. At a U of 2 eV, the $P4_2mc$ structure is only slightly favorable compared to the simple cubic state. Increasing the value of U yields a stabilization of this structure which results in a transition from the $P4mb$ structure to the $P4_2mc$ one at $U > 3$ eV. In parallel to the lowering in energy the structure becomes continuously closer to an insulating state until a metal-insulator transition occurs. For all values of $U \geq 3.5$ eV a band gap is found.

Next, we focus on the change of the volume with the chosen value of U (see Fig. 9.14). The volume of the $P4bm$ structure is almost independent of U and significantly larger than the experimental volume. At large values of U the transition to the metallic solution occurs with a smaller volume than the experimental one. The

unit cell of the $P4_2mc$ structure increases monotonically with the applied value of U. At small values of U the obtained volume is roughly 8% smaller than the experimental volume, whereas the difference is only 5% at the largest investigated value of U. We note that the large volume underestimation is also observed in the simple cubic arrangement (see Fig. 9.14 and Ref. 69). Ganesh and Cohen[70] proposed that a similar transition between the large tetragonal unit cell and the cubic unit cell corresponds to the experimental observation of a volume collapse under pressure.[67] However, in their calculation both solutions are metallic, whereas our distortions reproduce the experimental observation of a semiconducting ground state.

Figure 9.15 illustrates the impact of the Hubbard U on the electronic DOS. In the $P4_2mc$ structure, increasing the value of U the t_{2g} states move downwards. As a consequence, they are closer in energy to the oxygen p levels leading to a stronger hybridization. Furthermore, the unoccupied d states shift towards higher energy. The $6s2p$-hybrid peak has a small hybridization with the t_{2g} states that weakens as these states are pushed downwards by a larger value of U, which leads to the opening of a small band gap. We realize a second $6s2p$-hybrid peak directly below the Fermi energy, which is separated more clearly at a larger value of U. The effect of the Hubbard U on the d electrons is similar in the $P4bm$ structure. At small values of U the average of the t_{2g} states is above the average of the p states. Increasing the U shifts the occupied t_{2g} states downwards. The hybridization is maximized, when the average position of t_{2g} and p band coincide. The empty t_{2g} state directly above the Fermi energy does not shift significantly with the applied U, yet, its width decreases. The unoccupied d states are moved to higher energies by the increase of the value of U. Common to both structures is that the position of the remaining peaks, in particular the Pb s one, are hardly influenced by the change of U. This is a direct consequence of the construction of the DFT+U method.[94] As the Hubbard U is only applied to states of a particular orbital character, the rest of the spectrum is altered only via indirect effects.

The strong dependence of the relative stability and the volume of the structures on the specific value of the Hubbard U limits the predictive power of DFT. Hence, we investigated both structures with the Heyd-Scuseria-Ernzerhof (HSE) hybrid functional,[26] which yields parameter-free results. However, the computational expense of hybrid functionals effectively limits such an investigation to an electronic self consistency, so that we have to start from the relaxed structures of a DFT+U calculation. In Fig. 9.15, we compare the electronic DOS obtained with the hybrid functional to the results of the DFT+U scheme. We find the occupied $p - d$ hybridized states in the $P4_2mc$ structure between 6.5 eV and 1 eV below the Fermi energy. Hence, the position of the bands is best described by a large value of U. However, if we consider the position of the centers of the peaks, a smaller U agrees better, because the max-

$P4_2mc$ $P4bm$

$E - E_{\mathrm{F}}$ (eV) $E - E_{\mathrm{F}}$ (eV)
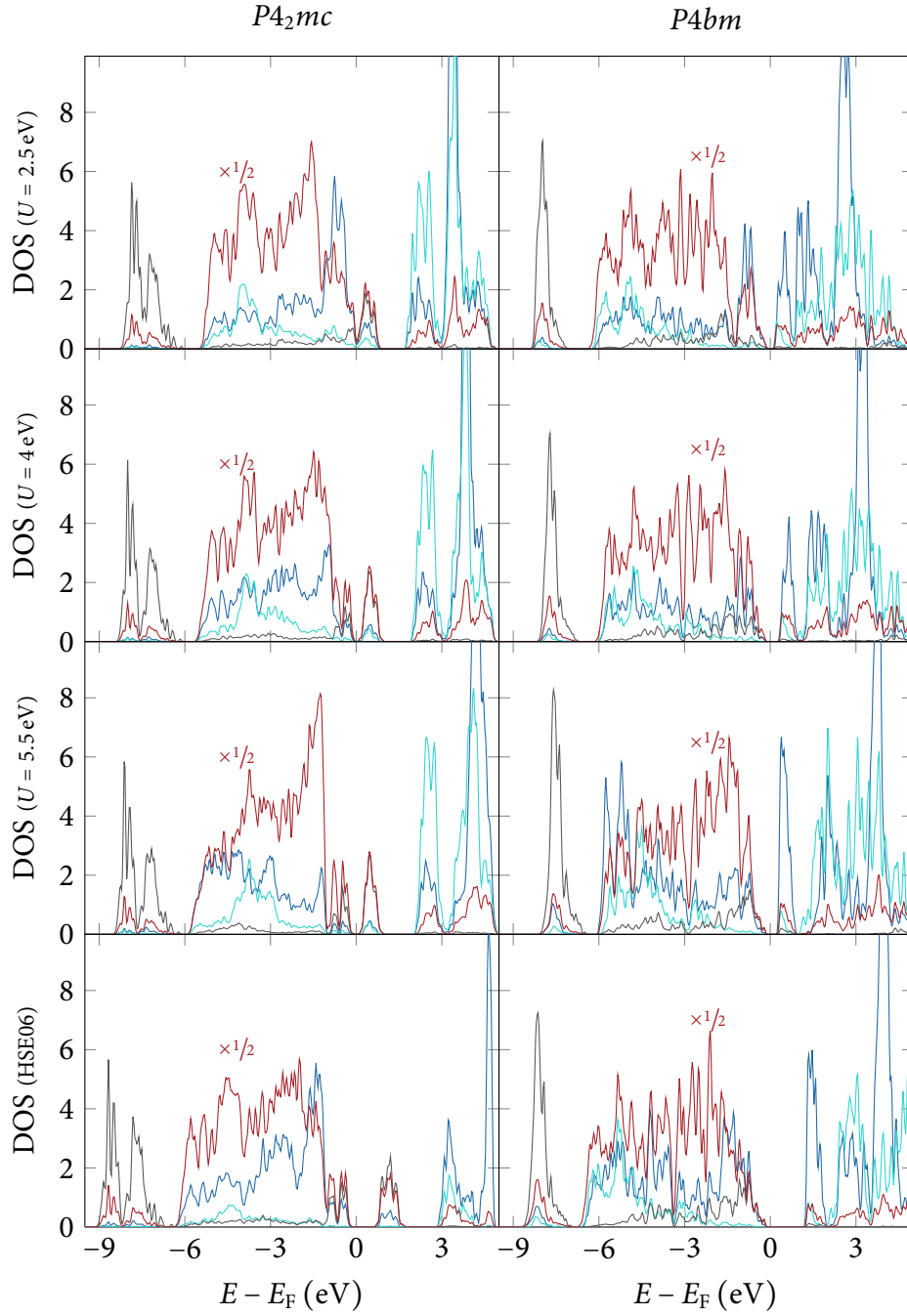
Figure 9.15: Illustration of changes in the orbital resolved electronic DOS associated to the Hubbard U parameter for 40 atoms unit cell of PbCrO$_3$ in the prototypical $P4_2mc$ (left) and $P4bm$ (right) structure. For comparison, we depict the result of a HSE hybrid functional calculation. We show the contribution of the Pb s (gray), the Cr e_{g} (blue), the Cr e_{g} (cyan), and the O p (red) states. The latter is scaled by $1/2$ to make the scale of all states more similar.

imum of the *d* states is above the maximum of the *p* states. The states closest to the Fermi energy are of hybrid O *p* and Pb *s* nature, where the band gap is significantly increased compared to all DFT+*U* results. The unoccupied *d* states are shifted to roughly 1 eV higher energies and their localization is drastically reduced, which is illustrated by the decrease of the peak height. Next, we turn to the *P4bm* structure. The part of the valence band built from Cr *d* and O *p* states is situated at energies between −7 eV and the Fermi energy. The position of the peaks is best described by an intermediate *U* of roughly 4 eV. The unoccupied t_{2g} states are shifted to an approximately 1 eV higher energy increasing the band gap above all of the DFT+*U* results. The unoccupied e_g states are affected more than the minority t_{2g} states. Similar to the *P4$_2$mc* structure, the binding of the Pb *s* state increases by 0.5 eV.

No unique value of *U* is sufficient to describe the results of the hybrid functionals. To reproduce the hybridization of Cr *d* and O *p* electrons a value of *U* between 3 and 4 eV would be optimal, whereas the reproduction of the band gap requires a significantly larger value of *U*. We encourage the development of more efficient implementations of the hybrid functionals that allow for a consistent investigation of PCO.

9.8   Summary

In this chapter, we have analyzed the properties of the perovskite $PbCrO_3$ within a DFT+*U* approach and have compared the results for the relaxed structures with the ones obtained with the HSE hybrid functional. We have investigated 42 possible combinations of tilts and JT distortions of the oxygen octahedra. Of all considered structures only a few turn out to be stable. We have chosen two prototypical representatives that exhibit the lowest total energy at small and large values of *U*, respectively, and have determined their properties in detail. Most importantly, both structures allow for the insulating ground state that is experimentally observed, but could not be reproduced by previous DFT calculations from the literature.[68–70] The opening of the band gap is driven by different mechanisms in the two structures. In the *P4bm* structure, which consist of a polar displacement of the Pb and Cr ions and JT distortions, the symmetry is broken such that the t_{2g} levels split in three different states. This results in an orbitally-ordered structure. The *P4$_2$mc* structure is characterized by rotations of the oxygen octahedra around all three axes and an off-centering of the Pb atoms. The charge in this structure is redistributed such that the t_{2g} states are completely filled and an empty $6s2p$ hybridized state is unoccupied. Both structures show some discrepancies to the experimental results, most notably the large c/a ratio and the volume overestimation in the *P4bm* structure and

the magnetic moment and the volume underestimation in the $P4_2mc$ structure. We have shown that the inclusion of oxygen defects partially overcomes this discrepancies. The properties as well as the stability of both structures is subject to significant changes under the applied value of the Hubbard U. We have outlined that although the hybrid functional approach yields the same qualitative electronic structure, there are prominent changes in the quantitative properties such as the position of peaks, the charge localization, and the strength of the hybridization. No unique choice of U is appropriate to reproduce the results of the hybrid functional calculation. Hence, we propose improving the speed of the hybrid functionals to allow for a parameter-free investigation of $PbCrO_3$.

Concluding, we find an insulating ground state, if the simple cubic symmetry is broken and DFT reveals that such a symmetry breaking can be realized by tilting and JT distortion of the oxygen octahedra and polar displacements. We note that the presence of polar distortions has not been experimentally observed and encourage the community to confirm our prediction of a microscopically noncubic polar structure.

Conclusion

This work is motivated by investigating and pushing the limits of the predictive power
of density functional theory (DFT) in the design of new functional materials. The
only approximation in DFT is the choice of the appropriate exchange-correlation
functional. We have discussed and have investigated some of the limitations of con-
ventional local exchange correlation functionals. The most commonly used alterna-
tive – the DFT+U method[94] – relies on adjustable parameters that are often chosen to
reproduce experimental results. In this thesis, we have implemented and investigated
the Heyd-Scuseria-Ernzerhof (HSE) functional[26] that incorporates a certain fraction
of screened nonlocal exchange. The specifications of the HSE functional are mate-
rial independent, hence, the predictive power surpasses the DFT+U approach. We
have employed the precise all-electron full-potential linearized augmented-plane-
wave (FLAPW) method as realized in the `Fleur` code,[126] in which the wave func-
tions are represented in a basis of numerical radial function times a spherical har-
monic in muffin-tin (MT) spheres surrounding the nuclei and plane waves in the
interstitial region (IR). The product of two wave functions, which is evaluated for
the nonlocal exchange, is evaluated via the resolution of the identity with an auxiliary
basis.[33] In this thesis, we have extended the implementation of Betzinger *et al.*[33] suit-
able for the Coulomb potential to any arbitrary potential, which is a pure function of
the distance, in particular the screened Coulomb potential. The screened interaction
is separated into the bare Coulomb potential and a long-range part, where the for-
mer is evaluated with a sparse-matrix technique similar to the PBE0 functional[33] and
for the latter we have exploited the fast converging Fourier series.[29] The reduction
of the k-point summations to the symmetry-irreducible parts gives rise to different
computational cost for the individual k points. This is taken into account explic-
itly in our parallelization scheme of the nonlocal potential so that we can achieve
parallelization efficiencies of more than 99%.

We have investigated possible approximations to develop faster implementation
of hybrid functionals. The FLAPW naturally separates the contributions of the non-
local functional into IR-IR, IR-MT, and MT-MT part. The MT-MT part can be fur-
ther divided into on-site and off-site terms. A systematic removal of the smaller
contributions to the hybrid functionals yields four tiers between the nonlocal PBE0
functional[24] and the local PBE functional.[14] In the first tier, the nonlocal functional

is not incorporated for the IR-IR part. This approximation yields accurate band gaps almost identical to the PBE0 functional. Removing the IR-MT contribution (second tier) from the nonlocal functional, we find band transitions that are surprisingly close to HSE functional. The stronger approximations, in which only on-site MT contributions are considered, produce no reasonable results for the band gaps in particular for the semiconductors Si and GaAs. Though the first two tiers yield acceptable band transitions, the total energy of the PBE0 functional is not reproduced. The construction of the PBE0 hybrid functional ensures that local and nonlocal part are treated on an equal footing. By approximating the hybrid functional, the violation of this delicate balance gives rise to the mismatch in the total energy. Additionally, we have considered the possibility of reducing the k-point summations in the calculation of the nonlocal potential through an interpolation scheme. This technique is suited in particular to evaluate the electronic band structure of materials, where the assignment of the intermediate k points to the ones in the coarse mesh is straightforward. Applying this method also to the self-consistent field cycle currently demands fine tuning of the user. We propose the implementation of a Wannier-interpolation technique to ease these requirements.

We have employed our implementation to investigate rare earth compounds, in particular the europium chalcogenides (EuX; X = O, S, Se, and Te) and gadolinium nitride (GdN). The lattice constant of all these materials is accurately predicted by hybrid functionals. For the ground state of GdN contradictory experimental evidence for semiconducting[36–38,187] as well as semi-metallic[38,39] properties has been reported. Our investigation reveals a transition between these two states induced by small changes in the lattice constant, which may explain the variety of the experimental observations. The magnetic coupling between neighboring Gd atoms is of ferromagnetic nature. Fitting our results to a classical Heisenberg model, we have obtained a Curie temperature of 45 K in a Monte-Carlo simulation in good agreement to the experimental one of 58 K.[191] In the EuX series, the PBE0 and the HSE hybrid functional overestimate and underestimate the experimental band gap, respectively. Nevertheless, in contrast to a DFT+U scheme, the qualitative nature of the experimental band transition is reproduced. Hybrid functionals yield a slightly stronger magnetic coupling between neighboring Eu atoms resulting in higher critical temperatures in particular for EuO and EuS. They capture the transition from a ferromagnetic to an antiferromagnetic configuration across the series. In all the investigated rare earth compounds, the particular choice of the Hubbard parameter U strongly impacts the results of a DFT+U calculation. We have shown that hybrid functionals present a parameter-free alternative with at least the same accuracy as sophisticated DFT+U calculations.

As second application, we have systematically analyzed the performance of the

HSE hybrid functional for simple perovskite oxides. The common local exchange-correlation functionals, namely the local density approximation (LDA) and the generalized gradient approximation (GGA), tend to underestimate and overestimate the lattice constants of perovskites, respectively. Generally, the lattice constant obtained with the HSE functional is between those values. Thus, this screened nonlocal functional provides the smallest mean average error of all the investigated functionals. Local functionals lack the derivative discontinuity associated with small changes of the number of particles. As a consequence, all PBE results for the direct and indirect band transitions are too small. Including the small fraction of Hartree-Fock (HF) exchange opens the band gap so that the HSE functional yields a much better agreement with the experimental observations.

Finally, we have performed a detailed investigation of $PbCrO_3$ (PCO). The experiments suggest that PCO is a semiconducting perovskite crystallizing in the ideal simple cubic structure.[61–63] However, we have argued that by simple symmetry consideration these two features are incompatible. In a simple cubic perovskite, the three t_{2g} states are degenerate, hence, the occupation of these states with two d electrons of Cr cannot result in a semiconducting state. Many perovskites exhibit a structural distortion by tilting or Jahn–Teller (JT) deformation of the oxygen octahedra. Carpenter and Howard[273] point out that a construction including combinations of these distortions leads to 42 different space groups. In addition, we have included a polar distortion along the z axis, which frequently occurs driven by the lone-pair $6s$ electrons at the Pb site. Relaxing all these structures in a DFT+U scheme, we have found several possible stable structures. For the first time, we have achieved an agreement of the experimental semiconductivity and *ab initio* results. We have identified two mechanisms that result in the opening of a band gap. PCO in the *P4bm* space group is characterized by a large c/a ratio and an off-centering of the Cr ions along the z axis similar to $PbVO_3$.[282,283] An additional JT deformation of the octahedra in the xy plane splits the t_{2g} states in three distinct levels. The d_{xy} orbital is occupied at all sites and the d_{yz} and d_{zx} orbitals realize a checkerboard orbital order in the xy plane. The volume of this structure is larger than the experimentally observed one and the large c/a ratio does not match the experimental cubic structure. The second mechanism occurs in a structure that exhibits the $P4_2mc$ space group and is dominated by large tilts of the oxygen octahedra. As a consequence, the Pb atoms are nonequivalent with respect to symmetry so that a charge order is allowed. We have found that a hybrid state of Pb $6s$ and O $2p$ electrons is unoccupied in half of the Pb ions. The excess electrons fill the t_{2g} states in the majority spin channel giving rise to an overall insulating structure. Although a c/a ratio is allowed in this structure, the actual value of 0.998 is close to the one of a cubic structure. However, the obtained volume is significantly smaller than the experimental one and the magnetic moment at the Cr

site is too large. The disadvantage of the DFT+U approach is the strong dependence of energetic order, structural and electronic properties on the specific choice of the value of U. Unfortunately, a thorough investigation employing hybrid functionals is computationally too demanding. Hence, we have evaluated properties of the relaxed structures using the HSE hybrid functional and have compared them to results with different choices for U. Common to both structures is the opening of the band gap with respect to the DFT+U results and a stronger binding of the Pb s states. However, the hybridization of the d-p valence band and the position of the unoccupied d states cannot be described by a single optimal value of U. As future work, we propose to develop a faster implementation of the hybrid functionals to examine all structures independent of an adjustable parameter. Although the ultimate ground state is not unambiguously identified, our investigations of PCO strongly suggest the presence of microscopic distortion of the simple cubic arrangement. In our calculations, a polar distortion is stable, which leads to a multiferroic ground state. Analyzing the microscopic properties of PCO experimentally especially in single crystals, would bring valuable insights into which of the outlined mechanisms is adapted in practice. We hope that our findings will stimulate such studies in the future.

Appendix

A   Atomic Units

Atomic units were introduced by Hartree[78] and provide a convenient formulation for the Schrödinger equation, the Coulomb potential, and many other equations in condensed matter physics.[77] The idea of atomic units is to measure physical quantities in terms of fundamental constants, so that these fundamental constants become equal to unity. In particular the mass m_e and charge e of an electron, Planck's constant $\hbar$ the Coulomb constant $1/4\pi\varepsilon_0$ and the Boltzmann constant k_B define the length,

Table A.1: In this thesis, we express all quantities in atomic units unless stated otherwise. Here, we present the conversion factors for the five fundamental physical dimensions and the energy.

Dimension	Atomic units	SI units	other units
length	$a_0 = \dfrac{4\pi\varepsilon_0\hbar^2}{m_e e^2}$	$5.292 \cdot 10^{-11}$ m	0.5292 Å
time	$\dfrac{(4\pi\varepsilon_0)^2\hbar^3}{m_e e^4}$	$2.419 \cdot 10^{-17}$ s	
mass	m_e	$9.109 \cdot 10^{-31}$ kg	
charge	e	$1.602 \cdot 10^{-19}$ C	
temperature	$\dfrac{m_e e^4}{(4\pi\varepsilon_0\hbar)^2 k_B}$	$3.158 \cdot 10^{5}$ K	
energy	$\mathrm{htr} = \dfrac{m_e e^4}{(4\pi\varepsilon_0\hbar)^2}$	$4.360 \cdot 10^{-18}$ J	27.211 eV

time, mass, charge, and temperature dimension and thus all the derived units (cf. Table A.1).

B   Numerical parameters for perovskite calculation

In Table A.2, we present the numerical settings employed in the calculation of the simple cubic perovskites (Chap. 8). Common to all materials is the $6\times6\times6$ $\boldsymbol{k}$-point mesh and the $l_{\max} = 4$ for the *mixed product basis* (MPB) and all atoms. For different ABO$_3$ compounds, the local orbitals employed at a particular site (A or B) are usually independent of the atom at the other site, e.g. for all B = Ti 5s, 3p, 5p, 4d, and 5f local orbitals are included. The only exception to this rule is CaSnO$_3$, where the 4p states of Sn are described as core states in contrast to the other Sn perovskites.

Table A.2: Numerical configuration of the perovskite calculations.

material ABO_3	R^{MT} (a$_0$)			G_{max} (a$_0^{-1}$)		l cutoff			local orbitals[a]		N_{bands}
	A	B	O	χ_G	M_G	A	B	O	A	B	
I–V compounds											
$NaNbO_3$	2.80	2.31	1.30	4.5	4.0	10	8	6	$4s, 2p, 4p, 4d, 5f$	$6s, 4p, 6p, 5d, 5f$	360
$KNbO_3$	2.80	2.36	1.33	4.7	3.9	10	8	6	$3s, 5s, 3p, 5p, 4d, 5f$	$6s, 4p, 6p, 5d, 5f$	380
$KTaO_3$	2.80	2.34	1.32	4.8	4.0	10	8	6	$3s, 5s, 3p, 5p, 4d, 5f$	$7s, 5p, 7p, 6d, 6f$	380
II–IV compounds											
$BaHfO_3$	2.80	2.45	1.38	4.3	3.8	10	10	6	$5s, 7s, 5p, 7p, 6d, 5f$	$5s, 7s, 5p, 7p, 6d, 5f$	480
$BaSnO_3$	2.80	2.42	1.36	4.7	3.8	10	10	6	$5s, 7s, 5p, 7p, 6d, 5f$	$6s, 6p, 4d, 6d, 5f$	420
$BaTiO_3$	2.80	2.35	1.33	4.4	3.9	10	8	6	$5s, 7s, 5p, 7p, 6d, 5f$	$5s, 3p, 5p, 4d, 5f$	380
$BaZrO_3$	2.80	2.47	1.39	4.2	3.7	10	10	6	$5s, 7s, 5p, 7p, 6d, 5f$	$6s, 4p, 6p, 5d, 5f$	380
$CaSnO_3$	2.80	2.23	1.26	4.7	4.2	10	10	6	$3s, 5s, 3p, 5p, 4d, 5f$	$6s, 6p, 5d, 5f$	420
$CaTiO_3$	2.80	2.23	1.26	4.7	4.2	10	8	6	$3s, 5s, 3p, 5p, 4d, 5f$	$5s, 3p, 5p, 4d, 5f$	380
$CaZrO_3$	2.80	2.36	1.33	4.7	3.9	10	8	6	$3s, 5s, 3p, 5p, 4d, 5f$	$6s, 4p, 6p, 5d, 5f$	380
$CdTiO_3$	2.80	2.23	1.26	4.7	4.2	10	8	6	$6s, 6p, 5d, 5f$	$5s, 3p, 5p, 4d, 5f$	400
$SrHfO_3$	2.80	2.39	1.35	4.4	3.9	10	8	6	$4s, 6s, 4p, 6p, 5d, 5f$	$5s, 7s, 5p, 7p, 6d, 5f$	540
$SrSnO_3$	2.80	2.16	1.53	4.4	3.9	10	8	6	$4s, 6s, 4p, 6p, 5d, 5f$	$6s, 6p, 4d, 6d, 5f$	420
$SrTiO_3$	2.80	2.29	1.29	4.6	4.1	10	8	6	$4s, 6s, 4p, 6p, 5d, 5f$	$5s, 3p, 5p, 4d, 5f$	380
$SrZrO_3$	2.80	2.40	1.36	4.6	3.9	10	10	6	$4s, 6s, 4p, 6p, 5d, 5f$	$6s, 4p, 6p, 5d, 5f$	380
$PbSnO_3$	2.80	2.39	1.35	4.7	3.9	10	8	6	$7s, 7p, 5p, 7d, 6f$	$6s, 6p, 4d, 6d, 5f$	460
$PbTiO_3$	2.80	2.33	1.32	4.5	4.0	10	8	6	$7s, 7p, 5d, 7d, 6f$	$5s, 3p, 5p, 4d, 5f$	420
$PbZrO_3$	2.80	2.43	1.37	4.3	3.8	10	10	6	$7s, 7p, 5d, 7d, 6f$	$6s, 4p, 6p, 5d, 5f$	420
III–III compounds											
$LaAlO_3$	2.80	2.23	1.26	4.7	4.2	10	8	6	$5s, 7s, 5p, 7p, 6d, 5f$	$4s, 4p, 4d, 5f$	320

[a] In all compounds $3s, 3p, 4d, 5f$ local orbitals are employed for oxygen.

Bibliography

[1]   H. Schmid. *Multi-ferroic magnetoelectrics.* Ferroelectrics **162**, 317 (1994).

[2]   N. A. Spaldin and M. Fiebig. *The Renaissance of Magnetoelectric Multiferroics.* Science **309**, 391 (2005).

[3]   N. A. Spaldin and W. E. Pickett. *Computational design of multifunctional materials.* J. Solid State Chem. **176**, 615 (2003).

[4]   P. Hohenberg and W. Kohn. *Inhomogeneous Electron Gas.* Phys. Rev. **136**, B864 (1964).

[5]   W. Kohn and L. J. Sham. *Self-Consistent Equations Including Exchange and Correlation Effects.* Phys. Rev. **140**, A1133 (1965).

[6]   J. P. Perdew and K. Schmidt. *Jacob's ladder of density functional approximations for the exchange-correlation energy.* AIP Conference Proceedings **577**, 1 (2001).

[7]   U. von Barth and L. Hedin. *A local exchange-correlation potential for the spin polarized case.* J. Phys. C: Solid State Phys. **5**, 1629 (1972).

[8]   O. Gunnarsson and B. I. Lundqvist. *Exchange and correlation in atoms, molecules, and solids by the spin-density-functional formalism.* Phys. Rev. B **13**, 4274 (1976).

[9]   D. M. Ceperley and B. J. Alder. *Ground State of the Electron Gas by a Stochastic Method.* Phys. Rev. Lett. **45**, 566 (1980).

[10]   S. H. Vosko, L. Wilk, and M. Nusair. *Accurate spin-dependent electron liquid correlation energies for local spin density calculations: a critical analysis.* Can. J. Phys. **58**, 1200 (1980).

[11]   J. P. Perdew and A. Zunger. *Self-interaction correction to density-functional approximations for many-electron systems.* Phys. Rev. B **23**, 5048 (1981).

[12] J. P. Perdew and Y. Wang. *Accurate and simple analytic representation of the electron-gas correlation energy.* Phys. Rev. B **45**, 13244 (1992).

[13] J. P. Perdew, J. A. Chevary, S. H. Vosko, K. A. Jackson, M. R. Pederson, D. J. Singh, and C. Fiolhais. *Atoms, molecules, solids, and surfaces: Applications of the generalized gradient approximation for exchange and correlation.* Phys. Rev. B **46**, 6671 (1992).

[14] J. P. Perdew, K. Burke, and M. Ernzerhof. *Generalized Gradient Approximation Made Simple.* Phys. Rev. Lett. **77**, 3865 (1996).

[15] Y. Wang and J. P. Perdew. *Spin scaling of the electron-gas correlation energy in the high-density limit.* Phys. Rev. B **43**, 8911 (1991).

[16] A. D. Becke. *Density-functional exchange-energy approximation with correct asymptotic behavior.* Phys. Rev. A **38**, 3098 (1988).

[17] C. Lee, W. Yang, and R. G. Parr. *Development of the Colle-Salvetti correlation-energy formula into a functional of the electron density.* Phys. Rev. B **37**, 785 (1988).

[18] S. Kümmel and L. Kronik. *Orbital-dependent density functionals: Theory and applications.* Rev. Mod. Phys. **80**, 3 (2008).

[19] J. Tao, J. P. Perdew, V. N. Staroverov, and G. E. Scuseria. *Climbing the Density Functional Ladder: Nonempirical Meta⊠Generalized Gradient Approximation Designed for Molecules and Solids.* Phys. Rev. Lett. **91**, 146401 (2003).

[20] A. D. Becke. *A new mixing of Hartree–Fock and local density-functional theories.* J. Chem. Phys. **98**, 1372 (1993).

[21] A. Heßelmann and A. Görling. *Random phase approximation correlation energies with exact Kohn-Sham exchange.* Mol. Phys. **108**, 359 (2010).

[22] A. D. Becke. *Density-functional thermochemistry. IV. A new dynamical correlation functional and implications for exact-exchange mixing.* J. Chem. Phys. **104**, 1040 (1996).

[23] A. D. Becke. *Density-functional thermochemistry. III. The role of exact exchange.* J. Chem. Phys. **98**, 5648 (1993).

[24] J. P. Perdew, M. Ernzerhof, and K. Burke. *Rationale for mixing exact exchange with density functional approximations.* J. Chem. Phys. **105**, 9982 (1996).

[25] J. A. Pople, M. Head-Gordon, D. J. Fox, K. Raghavachari, and L. A. Curtiss. *Gaussian-1 theory: A general procedure for prediction of molecular energies.* J. Chem. Phys. **90**, 5622 (1989).

[26] J. Heyd, G. E. Scuseria, and M. Ernzerhof. *Hybrid functionals based on a screened Coulomb potential.* J. Chem. Phys. **118**, 8207 (2003).

[27] J. Paier, M. Marsman, K. Hummer, G. Kresse, I. C. Gerber, and J. G. Ángyán. *Screened hybrid density functionals applied to solids.* J. Chem. Phys. **124**, 154709 (2006). *ibid.* **124**, 249901 (2006).

[28] F. Tran, P. Blaha, K. Schwarz, and P. Novák. *Hybrid exchange-correlation energy functionals for strongly correlated electrons: Applications to transition-metal monoxides.* Phys. Rev. B **74**, 155108 (2006).

[29] M. Schlipf, M. Betzinger, C. Friedrich, M. Ležaić, and S. Blügel. *HSE hybrid functional within the FLAPW method and its application to GdN.* Phys. Rev. B **84**, 125142 (2011).

[30] M. Weinert. *Solution of Poisson's equation: Beyond Ewald-type methods.* J. Math. Phys. **22**, 2433 (1981).

[31] M. Weinert, E. Wimmer, and A. J. Freeman. *Total-energy all-electron density functional method for bulk solids and surfaces.* Phys. Rev. B **26**, 4571 (1982).

[32] H. J. F. Jansen and A. J. Freeman. *Total-energy full-potential linearized augmented-plane-wave method for bulk solids: Electronic and structural properties of tungsten.* Phys. Rev. B **30**, 561 (1984).

[33] M. Betzinger, C. Friedrich, and S. Blügel. *Hybrid functionals within the all-electron FLAPW method: Implementation and applications of PBE0.* Phys. Rev. B **81**, 195117 (2010).

[34] W. R. L. Lambrecht. *Electronic structure and optical spectra of the semimetal ScAs and of the indirect-band-gap semiconductors ScN and GdN.* Phys. Rev. B **62**, 13538 (2000).

[35] D. B. Ghosh, M. De, and S. K. De. *Electronic, magnetic, and optical properties of Gd monopnictides: An LDA+U study.* Phys. Rev. B **72**, 045140 (2005).

[36] S. Granville, B. J. Ruck, F. Budde, A. Koo, D. J. Pringle, F. Kuchler, A. R. H. Preston, D. H. Housden, N. Lund, A. Bittar, G. V. M. Williams, and H. J. Trodahl. *Semiconducting ground state of GdN thin films.* Phys. Rev. B **73**, 235335 (2006).

[37] B. M. Ludbrook, I. L. Farrell, M. Kuebel, B. J. Ruck, A. R. H. Preston, H. J. Trodahl, L. Ranno, R. J. Reeves, and S. M. Durbin. *Growth and properties of epitaxial GdN.* J. Appl. Phys. **106**, 063910 (2009).

[38] M. Scarpulla, C. Gallinat, S. Mack, J. Speck, and A. Gossard. *GdN (111) heteroepitaxy on GaN (0001) by N_2 plasma and NH_3 molecular beam epitaxy.* J. Cryst. Growth **311**, 1239 (2009).

[39] P. Wachter and E. Kaldis. *Magnetic interaction and carrier concentration in GdN and $GdN_{1-x}O_x$.* Solid State Commun. **34**, 241 (1980).

[40] C. M. Aerts, P. Strange, M. Horne, W. M. Temmerman, Z. Szotek, and A. Svane. *Half-metallic to insulating behavior of rare-earth nitrides.* Phys. Rev. B **69**, 045115 (2004).

[41] C.-G. Duan, R. F. Sabiryanov, J. Liu, W. N. Mei, P. A. Dowben, and J. R. Hardy. *Strain Induced Half-Metal to Semiconductor Transition in GdN.* Phys. Rev. Lett. **94**, 237201 (2005).

[42] K. Doll. *Electronic structure of GdN, and the influence of exact exchange.* J. Phys.: Condens. Matter **20**, 075214 (2008).

[43] T. J. Konno, N. Ogawa, K. Wakoh, K. Sumiyama, and K. Suzuki. *Synthesis and Magnetic Properties of Non-Equilibrium Eu-Rich EuO Thin Films.* Japanese Journal of Applied Physics **35**, 6052 (1996).

[44] A. Schmehl, V. Vaithyanathan, A. Herrnberger, S. Thiel, C. Richter, M. Liberati, T. Heeg, M. Rockerath, L. F. Kourkoutis, S. Muhlbauer, P. Boni, D. A. Muller, Y. Barash, J. Schubert, Y. Idzerda, J. Mannhart, and D. G. Schlom. *Epitaxial integration of the highly spin-polarized ferromagnetic semiconductor EuO with silicon and GaN.* Nat. Mater. **6**, 882 (2007).

[45] R. Sutarto, S. G. Altendorf, B. Coloru, M. Moretti Sala, T. Haupricht, C. F. Chang, Z. Hu, C. Schüßler-Langeheine, N. Hollmann, H. Kierspel, J. A. Mydosh, H. H. Hsieh, H.-J. Lin, C. T. Chen, and L. H. Tjeng. *Epitaxy, stoichiometry, and magnetic properties of Gd-doped EuO films on YSZ (001).* Phys. Rev. B **80**, 085308 (2009).

[46] A. G. Swartz, J. Ciraldo, J. J. I. Wong, Y. Li, W. Han, T. Lin, S. Mack, J. Shi, D. D. Awschalom, and R. K. Kawakami. *Epitaxial EuO thin films on GaAs.* Appl. Phys. Lett. **97**, 112509 (2010).

[47] X. Hao, J. S. Moodera, and R. Meservey. *Spin-filter effect of ferromagnetic europium sulfide tunnel barriers.* Phys. Rev. B **42**, 8235 (1990).

[48] T. S. Santos and J. S. Moodera. *Observation of spin filtering with a ferromagnetic EuO tunnel barrier.* Phys. Rev. B **69**, 241203 (2004).

[49] A. Mauger and C. Godart. *The magnetic, optical, and transport properties of representatives of a class of magnetic semiconductors: The europium chalcogenides.* Phys. Rep. **141**, 51 (1986).

[50] O. Massenet, Y. Capiomont, and N. V. Dang. *Effects of high nonstoichiometry on EuO properties.* J. Appl. Phys. **45**, 3593 (1974).

[51] T. Matsumoto, K. Yamaguchi, M. Yuri, K. Kawaguchi, N. Koshizaki, and K. Yamada. *Preparation of Gd-doped EuO_{1-x} thin films and the magnetic and magneto-transport properties.* J. Phys.: Condens. Matter **16**, 6017 (2004).

[52] M. W. Shafer and T. R. McGuire. *Studies of Curie-Point Increases in EuO.* J. Appl. Phys. **39**, 588 (1968).

[53] K. Y. Ahn and T. R. McGuire. *Magnetic and Magneto-optic Properties of EuO Films Doped with Trivalent Rare-Earth Oxide.* J. Appl. Phys. **39**, 5061 (1968).

[54] H. Ott, S. J. Heise, R. Sutarto, Z. Hu, C. F. Chang, H. H. Hsieh, H.-J. Lin, C. T. Chen, and L. H. Tjeng. *Soft x-ray magnetic circular dichroism study on Gd-doped EuO thin films.* Phys. Rev. B **73**, 094407 (2006).

[55] H. Miyazaki, H. J. Im, K. Terashima, S. Yagi, M. Kato, K. Soda, T. Ito, and S. Kimura. *La-doped EuO: A rare earth ferromagnetic semiconductor with the highest Curie temperature.* Appl. Phys. Lett. **96**, 232503 (2010).

[56] P. Liu, J. Tang, J. A. C. Santana, K. D. Belashchenko, and P. A. Dowben. *Ce-doped EuO: Magnetic properties and the indirect band gap.* J. Appl. Phys. **109**, 07C311 (2011).

[57] J. Wang, J. B. Neaton, H. Zheng, V. Nagarajan, S. B. Ogale, B. Liu, D. Viehland, V. Vaithyanathan, D. G. Schlom, U. V. Waghmare, N. A. Spaldin, K. M. Rabe, M. Wuttig, and R. Ramesh. *Epitaxial $BiFeO_3$ Multiferroic Thin Film Heterostructures.* Science **299**, 1719 (2003).

[58] J. H. Haeni, P. Irvin, W. Chang, R. Uecker, P. Reiche, Y. L. Li, S. Choudhury, W. Tian, M. E. Hawley, B. Craigo, A. K. Tagantsev, X. Q. Pan, S. K. Streiffer,

L. Q. Chen, S. W. Kirchoefer, J. Levy, and D. G. Schlom. *Room-temperature ferroelectricity in strained SrTiO₃*. Nature **430**, 758 (2004).

[59] C. J. Fennie and K. M. Rabe. *Magnetic and Electric Phase Control in Epitaxial EuTiO₃ from First Principles*. Phys. Rev. Lett. **97**, 267602 (2006).

[60] K. M. Rabe and P. Ghosez. *First-Principles Studies of Ferroelectric Oxides*. In *Physics of Ferroelectrics*, edited by K. M. Rabe, C. H. Ahn, and J.-M. Triscone (Springer, Berlin, 2007).

[61] W. L. Roth and R. C. DeVries. *Crystal and Magnetic Structure of PbCrO₃*. J. Appl. Phys. **38**, 951 (1967).

[62] R. C. DeVries and W. L. Roth. *High-pressure Synthesis of PbCrO₃*. J. Am. Ceram. Soc. **51**, 72 (1968).

[63] B. L. Chamberland and C. W. Moeller. *A study on the PbCrO₃ perovskite*. J. Solid State Chem. **5**, 39 (1972).

[64] A. M. Arévalo-López and M. A. Alario-Franco. *On the structure and microstructure of PbCrO₃*. Journal of Solid State Chemistry **180**, 3271 (2007).

[65] A. M. Arévalo-López and M. A. Alario-Franco. *Reliable Method for Determining the Oxidation State in Chromium Oxides*. Inorg. Chem. **48**, 11843 (2009). PMID: 19928981.

[66] A. M. Arévalo-López, A. J. Dos santos Garíca, and M. A. Alario-Franco. *Antiferromagnetism and Spin Reorientation in PbCrO₃*. Inorg. Chem. **48**, 5434 (2009).

[67] W. Xiao, D. Tan, X. Xiong, J. Liu, and J. Xu. *Large volume collapse observed in the phase transition in cubic PbCrO₃ perovskite*. Proc. Nat. Acad. Sci. USA **107**, 14026 (2010).

[68] S. Jaya, R. Jagadish, R. Rao, and R. Asokamani. *Electronic structure of the perovskite oxides SrCrO₃ and PbCrO₃*. Mod. Phys. Lett. B **6**, 103 (1992).

[69] B.-T. Wang, W. Yin, W.-D. Li, and F. Wang. *First-principles DFT+U study of structural and electronic properties of PbCrO₃*. arXiv:1012.0143v1 [cond-mat.str-el] (2011).

[70] P. Ganesh and R. E. Cohen. *Orbital ordering, ferroelasticity, and the large pressure-induced volume collapse in PbCrO₃*. Phys. Rev. B **83**, 172102 (2011).

[71] P. A. M. Dirac. *Quantum mechanics of many-electron systems.* Proc. R. Soc. Lond. A **123**, 714 (1929).

[72] K. Burke and friends. *The ABC of DFT* (2011). `http://dft.uci.edu/materials/bookABCDFT/gamma/g1.pdf`.

[73] W. Kohn. *Nobel Lecture: Electronic Structure of Matter - Wave Functions and Density Functionals* (2011). `http://www.nobelprize.org/nobel_prizes/chemistry/laureates/1998/kohn-lecture.html`.

[74] J. P. Perdew and S. Kurth. *Density Functionals for Non-relativistic Coulomb Systems in the New Century.* In *A Primer in Density Functional Theory*, edited by C. Fiolhais, M. A. L. Marques, and F. Nogueira, chapter 1, 1–55 (Springer, Berlin, 2003).

[75] K. Capelle. *A bird's-eye view of density-functional theory* (2006). arXiv:cond-mat/0211443v5 [cond-mat.mtrl-sci].

[76] M. Born and R. Oppenheimer. *Zur Quantentheorie der Molekeln.* Ann. d. Phys. **389**, 457 (1927).

[77] wikipedia.org. *Atomic units* (2011). `http://en.wikipedia.org/wiki/Atomic_units`.

[78] D. R. Hartree. *The Wave Mechanics of an Atom with a Non-Coulomb Central Field. Part I. Theory and Methods.* Mathematical Proceedings of the Cambridge Philosophical Society **24**, 89 (1928).

[79] M. Levy. *Electron densities in search of Hamiltonians.* Phys. Rev. A **26**, 1200 (1982).

[80] J. Harris and R. O. Jones. *The surface energy of a bounded electron gas.* Journal of Physics F: Metal Physics **4**, 1170 (1974).

[81] D. C. Langreth and J. P. Perdew. *Exchange-correlation energy of a metallic surface: Wave-vector analysis.* Phys. Rev. B **15**, 2884 (1977).

[82] J. Harris. *Adiabatic-connection approach to Kohn-Sham theory.* Phys. Rev. A **29**, 1648 (1984).

[83] P. Güttinger. *Das Verhalten von Atomen im magnetischen Drehfeld.* Z. Phys. **73**, 169 (1932).

[84] H. Hellmann. *Einführung in die Quantenchemie* (Franz Deuticke, Leipzig, 1937).

[85] R. P. Feynman. *Forces in Molecules.* Phys. Rev. **56**, 340 (1939).

[86] J. P. Perdew and Y. Wang. *Accurate and simple density functional for the electronic exchange energy: Generalized gradient approximation.* Phys. Rev. B **33**, 8800 (1986).

[87] P. R. Antoniewicz and L. Kleinman. *Kohn-Sham exchange potential exact to first order in $\rho(\mathbf{K})/\rho_0$.* Phys. Rev. B **31**, 6779 (1985).

[88] E. H. Lieb and S. Oxford. *Improved lower bound on the indirect Coulomb energy.* International Journal of Quantum Chemistry **19**, 427 (1981).

[89] M. Ernzerhof and J. P. Perdew. *Generalized gradient approximation to the angle- and system-averaged exchange hole.* J. Chem. Phys. **109**, 3313 (1998).

[90] E. Engel. *Orbital-Dependent Functionals for the Exchange-Correlation Energy: A Third Generation of Density Functionals.* In *A Primer in Density Functional Theory*, edited by C. Fiolhais, M. A. L. Marques, and F. Nogueira, chapter 2, 56–143 (Springer, Berlin, 2003).

[91] A. Ruzsinszky, J. P. Perdew, G. I. Csonka, O. A. Vydrov, and G. E. Scuseria. *Spurious fractional charge on dissociated atoms: Pervasive and resilient self-interaction error of common density functionals.* J. Chem. Phys. **125**, 194112 (2006).

[92] A. Filippetti and N. A. Spaldin. *Self-interaction-corrected pseudopotential scheme for magnetic and strongly-correlated systems.* Phys. Rev. B **67**, 125109 (2003).

[93] J. C. Slater. *A Simplification of the Hartree-Fock Method.* Phys. Rev. **81**, 385 (1951).

[94] V. I. Anisimov, F. Aryasetiawan, and A. I. Lichtenstein. *First-principles calculations of the electronic structure and spectra of strongly correlated systems: the LDA+U method.* J. Phys.: Condens. Matter **9**, 767 (1997).

[95] F. Aryasetiawan and O. Gunnarsson. *The GW method.* Rep. Prog. Phys. **61**, 237 (1998).

[96] J. Harl and G. Kresse. *Accurate Bulk Properties from Approximate Many-Body Techniques.* Phys. Rev. Lett. **103**, 056401 (2009).

[97] J. Hubbard. *Electron Correlations in Narrow Energy Bands.* Proc. R. Soc. Lond. A **276**, 238 (1963).

[98] P. H. Dederichs, S. Blügel, R. Zeller, and H. Akai. *Ground States of Constrained Systems: Application to Cerium Impurities.* Phys. Rev. Lett. **53**, 2512 (1984).

[99] M. Cococcioni and S. de Gironcoli. *Linear response approach to the calculation of the effective interaction parameters in the LDA+U method.* Phys. Rev. B **71**, 035105 (2005).

[100] E. Şaşıoğlu, C. Friedrich, and S. Blügel. *Effective Coulomb interaction in transition metals from constrained random-phase approximation.* Phys. Rev. B **83**, 121101 (2011).

[101] H. Hellmann. *A New Approximation Method in the Problem of Many Electrons.* J. Chem. Phys. **3**, 61 (1935).

[102] E. Fermi. *Motion of neutrons in hydrogenous substances.* Ricerca Scientifica **7**, 13 (1936).

[103] J. C. Slater. *Wave Functions in a Periodic Potential.* Phys. Rev. **51**, 846 (1937).

[104] J. Korringa. *On the calculation of the energy of a Bloch wave in a metal.* Physica **13**, 392 (1947).

[105] W. Kohn and N. Rostoker. *Solution of the Schrödinger Equation in Periodic Lattices with an Application to Metallic Lithium.* Phys. Rev. **94**, 1111 (1954).

[106] P. Mavropoulos and N. Papanikolaou. *The Korringa-Kohn-Rostoker (KKR) Green Function Method I. Electronic Structure of Periodic Systems.* In *Computational Nanoscience: Do It Yourself!*, edited by J. Grotendorst, S. Blügel, and D. Marx, volume 31 of *NIC Series*, 85–129 (Forschungszentrum Jülich, Jülich, 2006).

[107] D. R. Hamann, M. Schlüter, and C. Chiang. *Norm-Conserving Pseudopotentials.* Phys. Rev. Lett. **43**, 1494 (1979).

[108] A. Zunger and M. L. Cohen. *First-principles nonlocal-pseudopotential approach in the density-functional formalism: Development and application to atoms.* Phys. Rev. B **18**, 5449 (1978).

[109] G. P. Kerker. *Non-singular atomic pseudopotentials for solid state applications.* J. Phys. C **13**, L189 (1980).

[110] D. Vanderbilt. *Soft self-consistent pseudopotentials in a generalized eigenvalue formalism.* Phys. Rev. B **41**, 7892 (1990).

[111] P. E. Blöchl. *Projector augmented-wave method.* Phys. Rev. B **50**, 17953 (1994).

[112] V. Blum, R. Gehrke, F. Hanke, P. Havu, V. Havu, X. Ren, K. Reuter, and M. Scheffler. *Ab initio molecular simulations with numeric atom-centered orbitals.* Comput. Phys. Commun. **180**, 2175 (2009).

[113] J. C. Slater. *An Augmented Plane Wave Method for the Periodic Potential Problem.* Phys. Rev. **92**, 603 (1953).

[114] P. Kurz. *Non-Collinear Magnetism at Surfaces and in Ultrathin Films.* Ph.D. thesis, RWTH Aachen, Institut für Festkörperphysik, Forschungszentrum Jülich (2000).

[115] S. Blügel and G. Bihlmayer. *The Full-Potential Linearized Augmented Plane Wave Method.* In *Computational Nanoscience: Do It Yourself!*, edited by J. Grotendorst, S. Blügel, and D. Marx, volume 31 of *NIC Series*, 85–129 (Forschungszentrum Jülich, Jülich, 2006).

[116] O. K. Andersen. *Linear methods in band theory.* Phys. Rev. B **12**, 3060 (1975).

[117] E. Wimmer, H. Krakauer, M. Weinert, and A. J. Freeman. *Full-potential self-consistent linearized-augmented-plane-wave method for calculating the electronic structure of molecules and surfaces: O_2 molecule.* Phys. Rev. B **24**, 864 (1981).

[118] D. Singh. *Ground-state properties of lanthanum: Treatment of extended-core states.* Phys. Rev. B **43**, 6388 (1991).

[119] G. Michalicek, M. Betzinger, C. Friedrich, and S. Blügel. in preparation (2012).

[120] M. Betzinger, C. Friedrich, S. Blügel, and A. Görling. *Local exact exchange potentials within the all-electron FLAPW method and a comparison with pseudopotential results.* Phys. Rev. B **83**, 045105 (2011).

[121] M. Betzinger. *Orbital-dependent exchange-correlation functionals in density-functional theory realized by the FLAPW method.* Ph.D. thesis, RWTH Aachen (2011).

[122] L. J. Sham and M. Schlüter. *Density-Functional Theory of the Energy Gap*. Phys. Rev. Lett. **51**, 1888 (1983).

[123] J. P. Perdew and M. Levy. *Physical Content of the Exact Kohn-Sham Orbital Energies: Band Gaps and Derivative Discontinuities*. Phys. Rev. Lett. **51**, 1884 (1983).

[124] B. G. Janesko, T. M. Henderson, and G. E. Scuseria. *Screened hybrid density functionals for solid-state chemistry and physics*. Phys. Chem. Chem. Phys. **11**, 443 (2009).

[125] C. Friedrich, A. Schindlmayr, and S. Blügel. *Efficient calculation of the Coulomb matrix and its expansion around k = 0 within the FLAPW method*. Comput. Phys. Commun. **180**, 347 (2009).

[126] http://www.flapw.de (????).

[127] C. Adamo and V. Barone. *Toward reliable density functional methods without adjustable parameters: The PBE0 model*. J. Chem. Phys. **110**, 6158 (1999).

[128] T. Bredow and A. R. Gerson. *Effect of exchange and correlation on bulk properties of MgO, NiO, and CoO*. Phys. Rev. B **61**, 5194 (2000).

[129] J. Muscat, A. Wander, and N. Harrison. *On the prediction of band gaps from hybrid functional theory*. Chemical Physics Letters **342**, 397 (2001).

[130] W. Perger. *Calculation of band gaps in molecular crystals using hybrid functional theory*. Chem. Phys. Lett. **368**, 319 (2003).

[131] A. V. Krukau, O. A. Vydrov, A. F. Izmaylov, and G. E. Scuseria. *Influence of the exchange screening parameter on the performance of screened hybrid functionals*. J. Chem. Phys. **125**, 224106 (2006).

[132] J. Heyd and G. E. Scuseria. *Assessment and validation of a screened Coulomb hybrid density functional*. J. Chem. Phys. **120**, 7274 (2004).

[133] F. Tran and P. Blaha. *Implementation of screened hybrid functionals based on the Yukawa potential within the LAPW basis set*. Phys. Rev. B **83**, 235118 (2011).

[134] O. A. Vydrov and G. E. Scuseria. *Assessment of a long-range corrected hybrid functional*. J. Chem. Phys. **125**, 234109 (2006).

[135] T. M. Henderson, A. F. Izmaylov, G. E. Scuseria, and A. Savin. *The importance of middle-range Hartree-Fock-journal article exchange for hybrid density functionals.* J. Chem. Phys. **127**, 221103 (2007).

[136] J. Heyd and G. E. Scuseria. *Efficient hybrid density functional calculations in solids: Assessment of the Heyd–Scuseria–Ernzerhof screened Coulomb hybrid functional.* J. Chem. Phys. **121**, 1187 (2004).

[137] K.-H. Hellwege, O. Madelung, M. Schulz, and H. Weiss (editors). *Numerical Data and Functional Relationships in Science and Technology*, volume 17 & 22 of *Landolt-Börnstein - Group III Condensed Matter* (Springer, New York, 1982).

[138] T. Chiang and F. J. Himpsel. *Band structure and core levels of tetrahedrally-bonded semiconductors.* In *Electronic Structure of Solids: Photoemission Spectra and Related Data*, edited by A. Goldmann and E.-E. Koch, volume 23a of *Landolt-Börnstein - Group III: Condensed Matter* (Springer, Berlin, 1989).

[139] J. E. Ortega and F. J. Himpsel. *Inverse-photoemission study of Ge(100), Si(100), and GaAs(100): Bulk bands and surface states.* Phys. Rev. B **47**, 2130 (1993).

[140] M. Welkowsky and R. Braunstein. *Interband Transitions and Exciton Effects in Semiconductors.* Phys. Rev. B **5**, 497 (1972).

[141] R. Hulthén and N. G. Nilsson. *Investigation of the second indirect transition of silicon by means of photoconductivity measurements.* Solid State Commun. **18**, 1341 (1976).

[142] S. Adachi. *Optical Properties of Crystalline and Amorphous Semiconductors: Numerical Data and Graphical Information* (Kluwer Academic, Dordrecht, 1999).

[143] R. T. Poole, J. Liesegang, R. C. G. Leckey, and J. G. Jenkin. *Electronic band structure of the alkali halides. II. Critical survey of theoretical calculations.* Phys. Rev. B **11**, 5190 (1975).

[144] R. J. Magyar, A. Fleszar, and E. K. U. Gross. *Exact-exchange density-functional calculations for noble-gas solids.* Phys. Rev. B **69**, 045111 (2004).

[145] F. Murnaghan. *The Compressibility of Media under Extreme Pressures.* Proc. Nat. Acad. Sci. USA **30**, 244 (1944).

[146] J. Paier, R. Hirschl, M. Marsman, and G. Kresse. *The Perdew-Burke-Ernzerhof exchange-correlation functional applied to the G2-1 test set using a plane-wave basis set.* J. Chem. Phys. **122**, 1 (2005).

[147] V. I. Anisimov and O. Gunnarsson. *Density-functional calculation of effective Coulomb interactions in metals.* Phys. Rev. B **43**, 7570 (1991).

[148] F. Aryasetiawan, M. Imada, A. Georges, G. Kotliar, S. Biermann, and A. I. Lichtenstein. *Frequency-dependent local interactions and low-energy effective models from electronic structure calculations.* Phys. Rev. B **70**, 195104 (2004).

[149] F. Aryasetiawan, K. Karlsson, O. Jepsen, and U. Schönberger. *Calculations of Hubbard U from first-principles.* Phys. Rev. B **74**, 125106 (2006).

[150] A. Rohrbach, J. Hafner, and G. Kresse. *Electronic correlation effects in transition-metal sulfides.* J. Phys.: Condens. Matter **15**, 979 (2003).

[151] P. Novák, J. Kuneš, L. Chaput, and W. E. Pickett. *Exact exchange for correlated electrons.* Phys. Status Solidi B **243**, 563 (2006).

[152] C. Franchini, V. Bayer, R. Podloucky, J. Paier, and G. Kresse. *Density functional theory study of MnO by a hybrid functional approach.* Phys. Rev. B **72**, 045132 (2005).

[153] C. Friedrich, S. Blügel, and A. Schindlmayr. *Efficient implementation of the GW approximation within the all-electron FLAPW method.* Phys. Rev. B **81**, 125102 (2010).

[154] J. B. Goodenough. *Magnetism And The Chemical Bond* (Interscience-Wiley, New York, 1963).

[155] J. B. Goodenough. *Goodenough-Kanamori rule.* Scholarpedia **3**, 7382 (2008).

[156] M. Marsman, J. Paier, A. Stroppa, and G. Kresse. *Hybrid functionals applied to extended systems.* J. Phys.: Condens. Matter **20**, 064201 (2008).

[157] X. Feng. *Electronic structure of MnO and CoO from the B3LYP hybrid density functional method.* Phys. Rev. B **69**, 155107 (2004).

[158] J. van Elp, R. H. Potze, H. Eskes, R. Berger, and G. A. Sawatzky. *Electronic structure of MnO.* Phys. Rev. B **44**, 1530 (1991).

[159] D. R. Huffman, R. L. Wild, and M. Shinmei. *Optical Absorption Spectra of Crystal-Field Transitions in MnO.* J. Chem. Phys. **50**, 4092 (1969).

[160] A. K. Cheetham and D. A. O. Hope. *Magnetic ordering and exchange effects in the antiferromagnetic solid solutions $Mn_xNi_{1-x}O$*. Phys. Rev. B **27**, 6964 (1983).

[161] B. E. F. Fender, A. J. Jacobson, and F. A. Wedgwood. *Covalency Parameters in MnO, α-MnS, and NiO*. J. Chem. Phys. **48**, 990 (1968).

[162] S. Hüfner, J. Osterwalder, T. Riesterer, and F. Hulliger. *Photoemission and inverse photoemission spectroscopy of NiO*. Solid State Commun. **52**, 793 (1984).

[163] G. A. Sawatzky and J. W. Allen. *Magnitude and Origin of the Band Gap in NiO*. Phys. Rev. Lett. **53**, 2339 (1984).

[164] R. J. Powell and W. E. Spicer. *Optical Properties of NiO and CoO*. Phys. Rev. B **2**, 2182 (1970).

[165] H. A. Alperin. J. Phys. Soc. Japan Suppl. B **17**, 12 (1962).

[166] B. T. Matthias, R. M. Bozorth, and J. H. Van Vleck. *Ferromagnetic Interaction in EuO*. Phys. Rev. Lett. **7**, 160 (1961).

[167] T. R. McGuire, B. E. Argyle, M. W. Shafer, and J. S. Smart. *Ferromagnetism in divalent europium salts*. Appl. Phys. Lett. **1**, 17 (1962).

[168] K. Ahn and J. Suits. *Preparation and properties of EuO films*. IEEE Trans. Magn. **3**, 453 (1967).

[169] T. Kasuya. *s-f Exchange Interactions And Magnetic Semiconductors*. Crit. Rev. Solid State Sci. **3**, 131 (1972).

[170] A. Mauger. *Indirect exchange in europium chalcogenides*. Phys. Status Solidi B **84**, 761 (1977).

[171] P. Wachter. *The Optical Electrical And Magnetic Properties of Europium Chalcogenides and the Rare Earth Pnictides*. Crit. Rev. Solid State Sci. **3**, 189 (1972).

[172] N. J. C. Ingle and I. S. Elfimov. *Influence of epitaxial strain on the ferromagnetic semiconductor EuO: First-principles calculations*. Phys. Rev. B **77**, 121202 (2008).

[173] M. R. Oliver, J. A. Kafalas, J. O. Dimmock, and T. B. Reed. *Pressure Dependence of the Electrical Resistivity of EuO*. Phys. Rev. Lett. **24**, 1064 (1970).

[174] M. R. Oliver, J. O. Dimmock, A. L. McWhorter, and T. B. Reed. *Conductivity Studies in Europium Oxide*. Phys. Rev. B **5**, 1078 (1972).

[175] Y. Shapira and T. B. Reed. *Resistivity and Hall Effect of EuS in Fields up to 140 kOe*. Phys. Rev. B **5**, 4877 (1972).

[176] J. B. Torrance, M. W. Shafer, and T. R. McGuire. *Bound Magnetic Polarons and the Insulator-Metal Transition in EuO*. Phys. Rev. Lett. **29**, 1168 (1972).

[177] Y. Shapira, S. Foner, and T. B. Reed. *EuO. I. Resistivity and Hall Effect in Fields up to 150 kOe*. Phys. Rev. B **8**, 2299 (1973).

[178] Y. Shapira, S. Foner, R. L. Aggarwal, and T. B. Reed. *EuO. II. Dependence of the Insulator-Metal Transition on Magnetic Order*. Phys. Rev. B **8**, 2316 (1973).

[179] T. Mairoser, A. Schmehl, A. Melville, T. Heeg, L. Canella, P. Böni, W. Zander, J. Schubert, D. E. Shai, E. J. Monkman, K. M. Shen, D. G. Schlom, and J. Mannhart. *Is There an Intrinsic Limit to the Charge-Carrier-Induced Increase of the Curie Temperature of EuO?* Phys. Rev. Lett. **105**, 257206 (2010).

[180] T. Mairoser, A. Schmehl, A. Melville, T. Heeg, W. Zander, J. Schubert, D. E. Shai, E. J. Monkman, K. M. Shen, T. Z. Regier, D. G. Schlom, and J. Mannhart. *Influence of the substrate temperature on the Curie temperature and charge carrier density of epitaxial Gd-doped EuO films*. Appl. Phys. Lett. **98**, 102110 (2011).

[181] M. Takahashi. *Origin of Anomalous Magnetization Curve of Electron-Doped EuO*. J. Phys. Soc. Jpn. **80**, 075001 (2011).

[182] S. Kar, W. L. Boncher, D. Olszewski, N. Dollahon, R. Ash, and S. L. Stoll. *Gadolinium Doped Europium Sulfide*. J. Am. Chem. Soc. **132**, 13960 (2010).

[183] R. Schiller, W. Müller, and W. Nolting. *Kondo lattice model: Application to the temperature-dependent electronic structure of EuO(100) films*. Phys. Rev. B **64**, 134409 (2001).

[184] P. Sinjukow and W. Nolting. *Metal-insulator transition in EuO*. Phys. Rev. B **68**, 125107 (2003).

[185] P. Sinjukow and W. Nolting. *Fully self-consistent determination of transport properties in Eu-rich EuO*. Phys. Rev. B **69**, 214432 (2004).

[186] M. Arnold and J. Kroha. *Simultaneous Ferromagnetic Metal-Semiconductor Transition in Electron-Doped EuO*. Phys. Rev. Lett. **100**, 046404 (2008).

[187] J. Q. Xiao and C. L. Chien. *Proximity Effects in Superconductor/Insulating-Ferromagnet NbN/GdN Multilayers*. Phys. Rev. Lett. **76**, 1727 (1996).

[188] P. Larson, W. R. L. Lambrecht, A. Chantis, and M. van Schilfgaarde. *Electronic structure of rare-earth nitrides using the LSDA+U approach: Importance of allowing 4f orbitals to break the cubic crystal symmetry*. Phys. Rev. B **75**, 045114 (2007).

[189] H. J. Trodahl, A. R. H. Preston, J. Zhong, B. J. Ruck, N. M. Strickland, C. Mitra, and W. R. L. Lambrecht. *Ferromagnetic redshift of the optical gap in GdN*. Phys. Rev. B **76**, 085211 (2007).

[190] D. X. Li, Y. Haga, H. Shida, and T. Suzuki. *Magnetic properties of ferromagnetic GdN*. Physica B: Condensed Matter **199-200**, 631 (1994).

[191] F. Leuenberger, A. Parge, W. Felsch, K. Fauth, and M. Hessler. *GdN thin films: Bulk and local electronic and magnetic properties*. Phys. Rev. B **72**, 014427 (2005).

[192] H. Yoshitomi, S. Kitayama, T. Kita, O. Wada, M. Fujisawa, H. Ohta, and T. Sakurai. *Optical and magnetic properties in epitaxial GdN thin films*. Phys. Rev. B **83**, 155202 (2011).

[193] U. Rössler and D. Strauch. *Group IV Elements, IV-IV and III-V Compounds. Part a - Lattice Properties*, volume 41A1a of *Landolt-Börnstein - Group III Condensed Matter* (Springer, Berlin, 2001).

[194] C. Friedrich, A. Schindlmayr, S. Blügel, and T. Kotani. *Elimination of the linearization error in GW calculations based on the linearized augmented-plane-wave method*. Phys. Rev. B **74**, 045104 (2006).

[195] E. E. Krasovskii. *Accuracy and convergence properties of the extended linear augmented-plane-wave method*. Phys. Rev. B **56**, 12866 (1997).

[196] C.-G. Duan, R. F. Sabiryanov, W. N. Mei, P. A. Dowben, S. S. Jaswal, and E. Y. Tsymbal. *Magnetic ordering in Gd monopnictides: Indirect exchange versus superexchange interaction*. Appl. Phys. Lett. **88**, 182505 (2006).

[197] N. N. Bogoliubov and S. V. Tyablikov. Dokl. Akad. Nauk SSSR **126**, 53 (1959).

[198] U. Nowak. *Localized Moments: Finite Temperature*. In *Magnetism goes Nano*, edited by S. Blügel, T. Brückel, and C. M. Schneider, volume 26 of *Matter and Materials*, A3.1 (Forschungszentrum Jülich, Jülich, 2005).

[199] K. Binder and D. W. Heermann. *Monte Carlo Simulation in Statistical Physics An Introduction* (Springer, Berlin, 2010).

[200] C.-G. Duan, R. F. Sabirianov, W. N. Mei, P. A. Dowben, S. S. Jaswal, and E. Y. Tsymbal. *Electronic, magnetic and transport properties of rare-earth monopnictides.* J. Phys.: Condens. Matter **19**, 315220 (2007).

[201] B. N. Harmon, V. P. Antropov, A. I. Liechtenstein, I. V. Solovyev, and V. I. Anisimov. *Calculation of magneto-optical properties for 4f systems: LSDA + Hubbard U results.* J. Phys. Chem. Solids **56**, 1521 (1995). Proceedings of the 1994 Conference on Magneto-optic Materials.

[202] R. C. Brown and N. J. Clark. *Composition limits and vaporization behaviour of rare earth nitrides.* J. Inorg. Nucl. Chem. **36**, 2507 (1974).

[203] H. Yamada, T. Fukawa, T. Muro, Y. Tanaka, S. Imada, S. Suga, D.-X. Li, and T. Suzuki. *XPS and X-BIS Studies of Gd Monopnictides.* J. Phys. Soc. Jpn. **65**, 1000 (1996).

[204] J. Paier, M. Marsman, and G. Kresse. *Why does the B3LYP hybrid functional fail for metals?* J. Chem. Phys. **127**, 024103 (2007).

[205] A. N. Chantis, M. van Schilfgaarde, and T. Kotani. *Quasiparticle self-consistent GW method applied to localized 4f electron systems.* Phys. Rev. B **76**, 165126 (2007).

[206] C. Mitra and W. R. L. Lambrecht. *Magnetic exchange interactions in the gadolinium pnictides from first principles.* Phys. Rev. B **78**, 134421 (2008).

[207] K. Khazen, H. J. von Bardeleben, J. L. Cantin, A. Bittar, S. Granville, H. J. Trodahl, and B. J. Ruck. *Ferromagnetic resonance study of GdN thin films with bulk and extended lattice constants.* Phys. Rev. B **74**, 245330 (2006).

[208] K. Senapati, T. Fix, M. E. Vickers, M. G. Blamire, and Z. H. Barber. *Structural evolution and competing magnetic orders in polycrystalline GdN films.* Phys. Rev. B **83**, 014403 (2011).

[209] A. Punya, T. Cheiwchanchamnangij, A. Thiess, and W. R. L. Lambrecht. *First-principles Study of Nitrogen Vacancies in GdN.* MRS Proceedings **1290**, mrsf10-1290-i04-04 (2011).

[210] P. Larson and W. R. L. Lambrecht. *Electronic structure and magnetism of europium chalcogenides in comparison with gadolinium nitride.* J. Phys.: Condens. Matter **18**, 11333 (2006).

[211] U. Köbler and C. Sauer. *Rare earth compounds with elements of group VI (O, S, Se, Te).* In *Magnetic and Other Properties of Oxides and Related Compounds - Part C*, volume 12 of *Landolt-Börnstein - Group III Condensed Matter* (Springer, Berlin, 1982).

[212] T. R. McGuire and M. W. Shafer. *Ferromagnetic Europium Compounds.* J. Appl. Phys. **35**, 984 (1964).

[213] N. Marzari and D. Vanderbilt. *Maximally localized generalized Wannier functions for composite energy bands.* Phys. Rev. B **56**, 12847 (1997).

[214] J. R. Yates, X. Wang, D. Vanderbilt, and I. Souza. *Spectral and Fermi surface properties from Wannier interpolation.* Phys. Rev. B **75**, 195121 (2007).

[215] F. Freimuth, Y. Mokrousov, D. Wortmann, S. Heinze, and S. Blügel. *Maximally localized Wannier functions within the FLAPW formalism.* Phys. Rev. B **78**, 035120 (2008).

[216] S. Jin, T. H. Tiefel, M. McCormack, R. A. Fastnacht, R. Ramesh, and L. H. Chen. *Thousandfold Change in Resistivity in Magnetoresistive La-Ca-Mn-O Films.* Science **264**, 413 (1994).

[217] A. Moreo, S. Yunoki, and E. Dagotto. *Phase Separation Scenario for Manganese Oxides and Related Materials.* Science **283**, 2034 (1999).

[218] M. L. Medarde. *Structural, magnetic and electronic properties of* $RNiO_3$ *perovskites (R = rare earth).* J. Phys.: Condens. Matter **9**, 1679 (1997).

[219] G. Catalan. *Progress in perovskite nickelate research.* Phase Transitions **81**, 729 (2008).

[220] S.-W. Cheong and M. Mostovoy. *Multiferroics: a magnetic twist for ferroelectricity.* Nat. Mater. **6**, 13 (2007).

[221] W. Eerenstein, N. D. Mathur, and J. F. Scott. *Multiferroic and magnetoelectric materials.* Nature **442**, 759 (2006).

[222] N. A. Hill. *Why Are There so Few Magnetic Ferroelectrics?* J. Phys. Chem. B **104**, 6694 (2000).

[223] M. Ležaić and N. A. Spaldin. *High-temperature multiferroicity and strong magnetocrystalline anisotropy in 3d-5d double perovskites.* Phys. Rev. B **83**, 024410 (2011).

[224] E. Heifets, R. I. Eglitis, E. A. Kotomin, J. Maier, and G. Borstel. *Ab initio modeling of surface structure for SrTiO₃ perovskite crystals.* Phys. Rev. B **64**, 235417 (2001).

[225] S. Piskunov, E. Heifets, R. I. Eglitis, and G. Borstel. *Bulk properties and electronic structure of SrTiO₃, BaTiO₃, PbTiO₃ perovskites: an ab initio HF/DFT study.* Comp. Mater. Sci. **29**, 165 (2004).

[226] S. Piskunov, E. Kotomin, E. Heifets, J. Maier, R. Eglitis, and G. Borstel. *Hybrid DFT calculations of the atomic and electronic structure for ABO₃ perovskite (0 0 1) surfaces.* Surf. Sci. **575**, 75 (2005).

[227] E. Heifets, E. Kotomin, and V. A. Trepakov. *Calculations for antiferrodistortive phase of SrTiO₃ perovskite: hybrid density functional study.* J. Phys.: Condens. Matter **18**, 4845 (2006).

[228] D. Muñoz, N. M. Harrison, and F. Illas. *Electronic and magnetic structure of LaMnO₃ from hybrid periodic density-functional theory.* Phys. Rev. B **69**, 085115 (2004).

[229] D. I. Bilc, R. Orlando, R. Shaltaf, G.-M. Rignanese, J. Íñiguez, and P. Ghosez. *Hybrid exchange-correlation functional for accurate prediction of the electronic and structural properties of ferroelectric oxides.* Phys. Rev. B **77**, 165107 (2008).

[230] Z. Wu and R. E. Cohen. *More accurate generalized gradient approximation for solids.* Phys. Rev. B **73**, 235116 (2006).

[231] R. Wahl, D. Vogtenhuber, and G. Kresse. *SrTiO₃ and BaTiO₃ revisited using the projector augmented wave method: Performance of hybrid and semilocal functionals.* Phys. Rev. B **78**, 104116 (2008).

[232] A. Stroppa and S. Picozzi. *Hybrid functional study of proper and improper multiferroics.* Phys. Chem. Chem. Phys. **12**, 5405 (2010).

[233] R. A. Evarestov. *Hybrid density functional theory LCAO calculations on phonons in Ba(Ti,Zr,Hf)O₃.* Phys. Rev. B **83**, 014105 (2011).

[234] R. Machado, M. Sepliarsky, and M. G. Stachiotti. *Relative phase stability and lattice dynamics of NaNbO₃ from first-principles calculations.* Phys. Rev. B **84**, 134107 (2011).

[235] N. Guang-Xin and W. Yuan-Xu. *First-principles study of the (001) surface of cubic PbHfO₃ and BaHfO₃.* Chinese Phys. B **18**, 1194 (2009).

[236] W. Pies and A. Weiss. *e1468, XVII.3 Oxo-compounds of hafnium (oxohafnates).* In *Crystallography, Structure and Morphology · Crystal Structure Data of Inorganic Compounds · Key Elements: d9-, d10-, d1_d3-, f-Elements*, edited by K.-H. Hellwege and A. M. Hellwege, volume 7e of *Landolt-Börnstein - Group III Condensed Matter*, chapter XVII.3 Oxo-compounds of hafnium (oxohafnates) (Springer, Berlin, 1977).

[237] A. Bouhemadou and K. Haddadi. *Structural, elastic, electronic and thermal properties of the cubic perovskite-type BaSnO₃.* Solid State Sci. **12**, 630 (2010).

[238] Y. Hinatsu. *Electron Paramagnetic Resonance Spectra of Pr⁴⁺ in BaCeO₃, BaZrO₃, BaSnO₃, and Their Solid Solutions.* J. Solid State Chem. **122**, 384 (1996).

[239] D. Cherrad, D. Maouche, M. Reffas, and A. Benamrani. *Structural, elastic, electronic and optical properties of the cubic perovskites CaXO₃ (X = Hf and Sn).* Solid State Commun. **150**, 350 (2010).

[240] J. Zhao, N. L. Ross, and R. J. Angel. *Tilting and distortion of CaSnO₃ perovskite to 7 GPa determined from single-crystal X-ray diffraction.* Phys. Chem. Miner. **31**, 299 (2004).

[241] Y. X. Wang, M. Arai, T. Sasaki, and C. L. Wang. *First-principles study of the (001) surface of cubic CaTiO₃.* Phys. Rev. B **73**, 035411 (2006).

[242] Z. Hou. *Ab initio calculations of elastic modulus and electronic structures of cubic.* Physica B: Condensed Matter **403**, 2624 (2008).

[243] A. Rabenau. *Perowskit- und Fluoritphasen in den Systemen ZrO₂-LaO₁,₅-MgO und ZrO₂-LaO₁,₅-CaO.* Z. Anorg. Allg. Chem. **288**, 221 (1956).

[244] H. Moriwake, A. Kuwabara, C. A. J. Fisher, H. Taniguchi, M. Itoh, and I. Tanaka. *First-principles calculations of lattice dynamics in CdTiO₃ and CaTiO₃: Phase stability and ferroelectricity.* Phys. Rev. B **84**, 104114 (2011).

[245] Z. Feng, H. Hu, S. Cui, C. Bai, and H. Li. *First-principles study of electronic structure, chemical bonding, and optical properties of cubic SrHfO₃*. J. Phys. Chem. Solids **70**, 412 (2009).

[246] J. Guevara, S. Cuffini, Y. Mascarenhas, R. Carbonio, J. A. Alonso, M. Fernandez, P. de la Presa, A. Ayala-Morales, and A. L. Garcia. *The Structure of Orthorhombic Hafniates by Neutron Powder Diffraction and Perturbed-Angular-Correlation Spectroscopy (PAC)*. Materials Science Forum **278-281**, 720 (1998).

[247] I. Shein, V. Kozhevnikov, and A. Ivanovskii. *First-principles calculations of the elastic and electronic properties of the cubic perovskites SrMO₃ (M = Ti, V, Zr and Nb) in comparison with SrSnO₃*. Solid State Sci. **10**, 217 (2008).

[248] H. D. Megaw. *Crystal structure of double oxides of the perovskite type*. Proc. Phys. Soc. **58**, 133 (1946).

[249] Y. X. Wang and M. Arai. *First-principles study of the (001) surface of cubic SrZrO₃*. Surf. Sci. **601**, 4092 (2007).

[250] W. Pies and A. Weiss. *d3141, XII.1.1.1 Simple oxo-compounds of tin without H₂O (simple stannates)*. In *Crystallography, Structure and Morphology · Crystal Structure Data of Inorganic Compounds · Key Elements: Ge, Sn, Pb*, edited by K.-H. Hellwege and A. M. Hellwege, volume 7e of *Landolt-Börnstein - Group III Condensed Matter*, chapter XVII.3 Oxo-compounds of hafnium (oxohafnates) (Springer, Berlin, 1986).

[251] J. Baedi, S. M. Hosseini, A. Kompany, and E. A. Kakhki. *Structural, electronic and optical properties of lead zirconate*. Phys. Status Solidi B **245**, 2572 (2008).

[252] B. Wu, M. Zinkevich, F. Aldinger, and W. Zhang. *Ab initio structural and energetic study of LaMO₃ (M = Al, Ga) perovskites*. J. Phys. Chem. Solids **68**, 570 (2007).

[253] A. Nakatsuka, O. Ohtaka, H. Arima, N. Nakayama, and T. Mizota. *Cubic phase of single-crystal LaAlO₃ perovskite synthesized at 4.5GPa and 1273K*. Acta Crystallog. E **61**, i148 (2005).

[254] R. D. Shannon. *Revised effective ionic radii and systematic studies of interatomic distances in halides and chalcogenides*. Acta Cryst. **32**, 751 (1976).

[255] D. de Ligny and P. Richet. *High-temperature heat capacity and thermal expansion of SrTiO₃ and SrZrO₃ perovskites*. Phys. Rev. B **53**, 3013 (1996).

[256] H. Dittrich, N. Karl, S. Kück, and H. Schock. *I-V-VI3 compounds*. In *Ternary Compounds and Organic Semiconductors*, edited by O. Madelung, volume 41E of *Landolt-Börnstein: Numerical Data and Functional Relationships in Science and Technology* (Springer, Berlin, 2000).

[257] O. Fursenko, J. Bauer, G. Lupina, P. Dudek, M. Lukosius, C. Wenger, and P. Zaumseil. *Optical properties and band gap characterization of high dielectric constant oxides*. Thin Solid Films **in press** (2011).

[258] G. Larramona, C. Gutierrez, I. Pereira, M. R. Nunes, and F. M. A. da Costa. *Characterization of the mixed perovskite $BaSn_{1-x}Sb_xO_3$ by electrolyte electroreflectance, diffuse reflectance, and X-ray photoelectron spectroscopy*. J. Chem. Soc., Faraday Trans. 1 **85**, 907 (1989).

[259] J. Robertson. *Band offsets of wide-band-gap oxides and implications for future electronic devices*. In *Papers from the international conference on silicon dielectric interfaces*, volume 18, 1785–1791 (AVS, 2000).

[260] H. Mizoguchi and P. M. Woodward. *Electronic Structure Studies of Main Group Oxides Possessing Edge-Sharing Octahedra: Implications for the Design of Transparent Conducting Oxides*. Chem. Mater. **16**, 5233 (2004).

[261] K. Ueda, H. Yanagi, H. Hosono, and H. Kawazoe. *Study on electronic structure of $CaTiO_3$ by spectroscopic measurements and energy band calculations*. J. Phys.: Condens. Matter **11**, 3535 (1999).

[262] S. Yamaguchi, K. Kobayashi, T. Higuchi, S. Shin, and Y. Iguchi. *Electronic transport properties and electronic structure of $InO_{1.5}$-doped $CaZrO_3$*. Solid State Ionics **136-137**, 305 (2000).

[263] O. I. Prokopalo, E. G. Fesenko, M. A. Malitskaya, Y. M. Popov, and V. G. Smotrakov. *Photoelectric phenomena in single crystals of some perovskite oxides*. Ferroelectrics **18**, 99 (1978).

[264] C. Rossel, M. Sousa, C. Marchiori, J. Fompeyrine, D. Webb, D. Caimi, B. Mereu, A. Ispas, J. Locquet, H. Siegwart, R. Germann, A. Tapponnier, and K. Babich. *$SrHfO_3$ as gate dielectric for future CMOS technology*. Microelectron. Eng. **84**, 1869 (2007).

[265] W. Zhang, J. Tang, and J. Ye. *Photoluminescence and photocatalytic properties of $SrSnO_3$ perovskite*. Chem. Phys. Lett. **418**, 174 (2006).

[266] Y. S. Lee, J. S. Lee, T. W. Noh, D. Y. Byun, K. S. Yoo, K. Yamaura, and E. Takayama-Muromachi. *Systematic trends in the electronic structure parameters of the 4d transition-metal oxides SrMO₃ (M = Zr, Mo, Ru, and Rh)*. Phys. Rev. B **67**, 113101 (2003).

[267] D. Chen, S. Ouyang, and J. Ye. *Photocatalytic Degradation of Isopropanol Over PbSnO₃ Nanostructures Under Visible Light Irradiation*. Nanoscale Research Letters **4**, 274 (2009).

[268] P. W. Peacock and J. Robertson. *Band offsets and Schottky barrier heights of high dielectric constant oxides*. J. Appl. Phys. **92**, 4712 (2002).

[269] A. M. Arévalo-López, E. Castillo-Martínez, and M. A. Alario-Franco. *Electron energy loss spectroscopy in ACrO₃ (A = Ca, Sr and Pb) perovskites*. J. Phys.: Condens. Matter **20**, 505207 (2008).

[270] A. C. Komarek, T. Möller, M. Isobe, Y. Drees, H. Ulbrich, M. Azuma, M. T. Fernández-Díaz, A. Senyshyn, M. Hoelzel, G. André, Y. Ueda, M. Grüninger, and M. Braden. *Magnetic order, transport and infrared optical properties in the ACrO₃ system (A = Ca, Sr, and Pb)*. Phys. Rev. B **84**, 125114 (2011).

[271] A. M. Arévalo-López and M. A. Alario-Franco. *Structural Percolation in the PbM$_{1-x}$M$'_x$O₃ (M, M′ = Ti, Cr, and V) Perovskites*. Inorg. Chem. **50**, 7136 (2011).

[272] H. Yıldırım, S. Ağduk, and G. Gökoğlu. *Electronic structure of antiferromagnetic PbCrO₃ (0 0 1) surfaces*. J. Alloys Compd. **509**, 9284 (2011).

[273] M. A. Carpenter and C. J. Howard. *Symmetry rules and strain/order-parameter relationships for coupling between octahedral tilting and cooperative Jahn–Teller transitions in ABX3 perovskites. I. Theory*. Acta Cryst. B **65**, 134 (2009).

[274] T. Mizokawa, D. I. Khomskii, and G. A. Sawatzky. *Interplay between orbital ordering and lattice distortions in LaMnO₃, YVO₃, and YTiO₃*. Phys. Rev. B **60**, 7309 (1999).

[275] H. T. Stokes, D. M. Hatch, and B. J. Campbell. *ISOTROPY* (2007). http://stokes.byu.edu/isotropy.html.

[276] G. Kresse and J. Furthmüller. *Efficient iterative schemes for ab initio total-energy calculations using a plane-wave basis set*. Phys. Rev. B **54**, 11169 (1996).

[277] M. I. Aroyo, J. M. Perez-Mato, C. Capillas, E. Kroumova, S. Ivantchev, G. Madariaga, A. Kirov, and H. Wondratschek. *Bilbao Crystallographic Server: I. Databases and crystallographic computing programs.* Z. Kristallogr. **221**, 15 (2006).

[278] M. I. Aroyo, A. Kirov, C. Capillas, J. M. Perez-Mato, and H. Wondratschek. *Bilbao Crystallographic Server. II. Representations of crystallographic point groups and space groups.* Acta Cryst. A **62**, 115 (2006).

[279] D. Orobengoa, C. Capillas, M. I. Aroyo, and J. M. Perez-Mato. AMPLIMODES: *symmetry-mode analysis on the Bilbao Crystallographic Server.* J. Appl. Crystallogr. **42**, 820 (2009).

[280] A. A. Mostofi, J. R. Yates, Y.-S. Lee, I. Souza, D. Vanderbilt, and N. Marzari. *wannier90: A tool for obtaining maximally-localised Wannier functions.* Computer Physics Communications **178**, 685 (2008).

[281] A. M. Glazer. *The classification of tilted octahedra in perovskites.* Acta Cryst. B **28**, 3384 (1972).

[282] R. V. Shpanchenko, V. V. Chernaya, A. A. Tsirlin, P. S. Chizhov, D. E. Sklovsky, E. V. Antipov, E. P. Khlybov, V. Pomjakushin, A. M. Balagurov, J. E. Medvedeva, E. E. Kaul, and C. Geibel. *Synthesis, Structure, and Properties of New Perovskite $PbVO_3$.* Chem. Mater. **16**, 3267 (2004).

[283] K. Oka, I. Yamada, M. Azuma, S. Takeshita, K. H. Satoh, A. Koda, R. Kadono, M. Takano, and Y. Shimakawa. *Magnetic Ground-State of Perovskite $PbVO_3$ with Large Tetragonal Distortion.* Inorg. Chem. **47**, 7355 (2008). PMID: 18642895.

Acknowlegdments

In the last three years, I have experienced a continous support by a great number of people, for which I am deeply thankful.

First, I like to thank my supervisor Jun.-Prof. Dr. Marjana Ležaić for giving me the oppurtunity to write this thesis in the *Computational Nanoferronics Laboratory*, for introducing me to intriguing topic of multiferroic oxides, for her constructive suggestions, for the interesting scientific discussions, and for opening me many possiblities. Without you this work would not have been possible.

I am very grateful to Prof. Dr. Carsten Honerkamp for being the second referee of this thesis.

I would also like to thank Prof. Dr. Stefan Blügel, who has taken me into the Peter-Grünberg institute, spured my work by his everlasting energy, and provided insightful comments to the implementation and acceleration of the hybrid functionals.

Next, I thank Dr. Christoph Friedrich and Dr. Markus Betzinger for their support in the implementation of the HSE hybrid functionals and for proof-reading my thesis.

I express my gratidue to Prof. Dr. Silivia Picozzi for organizing the Aquifer program, where I had the chance to meet and discuss with PhD students from all over the world. I would also like to acknowledge my fellow Aquiferians, who made this such a great time.

I thank Prof. Dr. Manuel Bibes and Prof. Dr. Frédéric Petroff for organizing the ISOE at the lovely Cargése and the other attendees of the school in particular Greta, Carmen, Paolo, Heberton, Wolfgang, Peiman, Roman, and Vikas.

My former and current office mates Ali, David, Andreas, Andreas, Gregor, and Aaron, I would like to thank for the intersting discussion, their help in the small but tedious details, and for proof-reading my thesis.

The rest of the institute, I thank for scientific discussions, for the social events, and the warm welcome in the institute. In particular, I would express my gratitude to Alex and the IAS Allstars for the weekly soccer games and the board-game enthusiasts Alex, Timo, Gregor, Aaron, Adam, Julian, and Andreas for the occasional board game party.

I am indebted to Ute Winkler, the soul of our institute, for the smooth organisation of all the necessary administration issues.

Finally, I thank with all my heart my family and my girlfriend for the moral support during the last years.

Schriften des Forschungszentrums Jülich
Reihe Schlüsseltechnologien / Key Technologies

Schriften des Forschungszentrums Jülich
Reihe Schlüsseltechnologien / Key Technologies

Weitere *Schriften des Verlags im Forschungszentrum Jülich* unter
http://wwwzb1.fz-juelich.de/verlagextern1/index.asp

JÜLICH
FORSCHUNGSZENTRUM